ile Copy
Do not remove.

DOE/ER-0045/6

Alloy Development for Irradiation Performance

Quarterly Progress Report
For Period Ending March 31, 1981

U.S. Department of Energy
Office of Fusion Energy

Printed in the United States of America. Available from
National Technical Information Service
U.S. Department of Commerce
5285 Port Royal Road, Springfield. Virginia 22161
NTIS price codes — Printed Copy: A13 Microfiche A01

DOE/ER-0045/6
Distribution
Category
uc-20, 20c

ALLOY DEVELOPMENT FOR IRRADIATION PERFORMANCE QUARTERLY PROGRESS REPORT FOR PERIOD ENDING MARCH 31, 1981

ARGONNE NATIONAL LABORATORY

GENERAL ATOMIC COMPANY

HANFORD ENGINEERING DEVELOPMENT LABORATORY

McDONNELL DOUGLAS ASTRONAUTICS COMPANY

MASSACHUSETTS INSTITUTE OF TECHNOLOGY

NAVAL RESEARCH LABORATORY

OAK RIDGE NATIONAL LABORATORY

SANDIA NATIONAL LABORATORIES

WESTINGHOUSE FUSION POWER SYSTEMS

Date Published: July **1981**

Prepared by
OAK RIDGE NATIONAL LABORATORY
Oak Ridge, Tennessee 37830
operated by
UNION CARBIDE CORPORATION
for the
DEPARTMENT OF ENERGY
Under Contract No. W-7405-eng-26

Reports previously issued in this series are as follows:

DOE/ET-0058/1	Period Ending March 31, 1978
DOE/ET-0058/2	Period Ending June **30,** 1978
DOE/ET-0058/3	Period Ending September 30, 1978
DOE/ET-0058/4	Period Ending December 31, 1978
DOE/ET-0058/5	Period Ending March 31, 1979
DOE/ET-0058/6	Period Ending June 30, 1979
DOE/ET-0058/7	Period Ending September 30, 1979
DOE/ER-0045/1	Period Ending December 31, 1979
DOE/ER-0045/2	Period Ending March 31, 1980
DOE/ER-0045/3	Period Ending June 30, 1980
DOE/ER-0045/4	Period Ending September 30, 1980
DOE/ER-0045/5	Period Ending December 31, 1980

FOREWORD

This report is the thirteenth in a series of Quarterly Technical Progress Reports on *"Alloy Development for Irradiation Performance"* (ADIP), which is one element of the Fusion Reactor Materials Program, conducted in support of the Magnetic Fusion Energy Program of the U.S. Department of Energy. Other elements of the Materials Program are

- *Damge Analysis and Fundamental Studies (DAFS)*
- *Plasma-Materials Interaction (PMI)*
- *Special-Purpose Materiats (SPM)*

The first seven reports in this series are numbered DOE/ET-0058/1 through 7. This report is the sixth in a new numbering sequence that begins with DOE/ER-0045/1.

The ADIP program element is a national effort composed of contributions from a number of National Laboratories and other government laboratories, universities, and industrial laboratories. It was organized by the Materials and Radiation Effects Branch, Office of Fusion Energy, DOE, and a Task Group on *Alloy Development for Irmdiation Performance,* which operates under the auspices of that Branch. The purpose of this series of reports is to provide a working technical record of that effort for the use of the program participants, for the fusion energy program in general, and for the Department of Energy.

This report is organized along topical lines in parallel to a Program Plan of the same title so that activities and accomplishments may be followed readily relative to that Program Plan. Thus, the work of a given laboratory may appear throughout the report. Chapters 1, 2, 8, and 9 review activities on analysis and evaluation, test methods development, status of irradiation experiments, and corrosion testing and hydrogen permeation studies, respectively. These activities relate to each of the alloy development paths. Chapters 3, 4, 5, 6, and 7 present the ongoing work on each alloy development path. The Table of Contents is annotated for the convenience of the reader.

This report has been compiled and edited under the guidance of the Chairman of the Task Group on *Alloy Development for Irmdiation Performance.* E. E. Bloom, Oak Ridge National Laboratory, and his efforts and those of the supporting staff of ORNL and the many persons who made technical contributions are gratefully acknowledged. T. C. Reuther, Materials and Radiation Effects Branch, is the Department of Energy Counterpart to the Task Group Chairman and has responsibility for the ADIP Program within DOE.

Klaus M. Zwilsky, Chief
Materials and Radiation Effects Branch
Office of Fusion Energy

CONTENTS

1. ANALYSIS AND EVALUATION STUDIES

1.1 MATERIALS HANDBOOK FOR FUSION ENERGY SYSTEMS

J. W. Davis (McDonnell Douglas Astronautics Company - St. Louis) and T. K. Bierlein (Hanford Engineering Development Laboratory)

1.1.1 ADIP Task

Task Number 1.A.1 - Define material property requirements and make structural life predictions.

1.1.2 Objective

To provide an authoritative and consistent source of material property data for use by the fusion energy community in conceptual designs, safety analysis, and performance/verification.

1.1.3 Summary

The first publication package of data sheets for the MHFES has been released and the second publication package will be ready for release in the next month. The first publication package contains revisions in the handbook format along with procedures for incorporating data sheets in the handbook and data sheets on the effect of irradiation on the fatigue strength of 20% cold worked stainless steel. The second publication package will contain data sheets on fatigue crack growth of 20% cold worked stainless steel, electrical resistivity of stainless steel, and tritium permeability of stainless steel. Data sheets should also be available on the properties of G-10CR glass laminate which is used in superconducting magnets. Work is currently underway to develop data sheets on ferritic steels, solid tritium breeding compounds, carbon and graphite, liquid lithium, and irradation induced swelling and creep of 20% cold worked stainless steel. At the present time we have targeted mid-summer for release of these data sheets.

1.1.4 Progress and Status

In the process of requesting inputs to the handbook it became apparent that in some instances the data base was inadequate to develop a handbook data page. However, the design projects still needed the data

and were unable to wait for a testing program to be undertaken to fill the data voids. The solution to meeting the projects data needs and still reflect the weakness in the data base was to create two separate page classifications for the handbook, INTERIM and PERMANENT. Pages for which a fully validated or adequate data base is not available will be designated as INTERIM PAGES. These pages will be subjected to a less extensive review than the PERMANENT PAGES. INTERIM PAGES will be imprinted with an "INTERIM PAGE" stamp at the top of the data page to indicate this classification. PERMANENT PAGES will be those pages which have been prepared from an adequate data base and have received the standard review and approval. Since the majority of the pages planned for the handbook will be permanent pages no special stamp will be used for pages in this classification.

It is currently planned that the data pages, whether INTERIM or PERMANENT, will be prepared by an authorized DOE/OFE task group, subtask group/working group, project designer, or an individual with the proper expertise. The candidate pages, along with their supporting documentation and recommended classification (INTERIM or PERMANENT) will then be submitted by the originators to the coordinator of the MHFES. Those data pages prepared by an individual will first be referred by the coordinator to one of the DOE/OFE authorized groups for review. After this review the coordinator will then direct the review according to one of the following procedures, depending upon page classification.

1.1.5 Permanent Page Review/Approval

The coordinator of the MHFES reviews the candidate pages for completeness and submits them to the Analysis and Evaluation (A&E) Task Group for review and approval. The A&E Task Group will be responsible for performing the final review and approval of all PERMANENT pages prior to publication in the MHFES. The review results are reported to the coordinator via a ballot which is provided to each A&E Task Group member along with the candidate data pages. Thirty working days are allowed for the A&E Task Group ballot response. The ballot provides a uniform and concise record of MHFES page transactions and will be used in all Review/Approval responses. The ballot allows for three responses (1) Approval (comments

optional), (2) Disapproval (written explanation required), or (3) Abstain (reason stated). The coordinator subsequently reviews all ballots and comments and either revises the data pages personnally or returns them along with the disapproval ballots to the originator(s) for resolution. The revised pages are then returned to the coordinator for concurrence. The coordinator will, as necessary, direct and participate in discussions between the A&E Task Group and the data page originators until in the coordinator's judgement all objections have been sufficiently resolved. The coordinator will then release the data pages for publication.

1.1.6 Interim Page Review/Approval

The coordinator reviews the INTERIM pages for completeness and submits the pages along with a ballot to a limited number of A&E Task Group members or to individuals who are not members of the A&E Task Group but who have the required expertise. The primary purpose of this review is to verify the usefulness of the data and the consistency of the assumptions regarding the use of the data. Ten working days are allowed for the ballot response. The coordinator of the MHFES will then take the resulting comments, revise the data pages, as required, and release them for publication in the Handbook as INTERIM pages. If major revisions are required, the comments and accompanying data pages will be returned to the originators for action and resolution prior to release for publication in the MHFES.

Currently all of the data sheets in the review cycle along with the approved data sheets have been processed as permanent data pages. The approved data sheets cover the "effect of irradiation on the elevated temperature fatigue strength of 20% cold worked stainless steel." The data sheets that have passed task group review and have been submitted to the A&E Task Group for final review are Electrical Resistivity and tritium permeability of 20% cold worked stainless steel and properties of G-10Cr epoxy-glass laminates. The data sheets that are in preparation and review within the task groups and are close to the point that they can be submitted to the handbook coordinator for final review cover the following topics: (1) changes in mechanical properties due to irradiation; (2) effect of helium and displacement damage on swelling, and (3) irradiation creep. All of these are for 20% cold worked 316 stainless steel.

2. TEST MATRICES AND METHODS DEVELOPMENT

2.1 STATUS OF MFE-5 IN-REACTOR FATIGUE CRACK GROWTH EXPERIMENT - A. M. Ermi (Hanford Engineering Development Laboratory).

2.1.1 ADIP Task

ADIP Task I.B.l, "Fatigue Crack Growth in Austenitic Alloys" (Path A).

2.1.2 Objectives

An apparatus has been developed to perform an in-reactor fatigue crack propagation test on the Path A Reference Alloy. Effects of dynamic irradiation on crack growth behavior will be evaluated by comparing the results with those of unirradiated and postirradiated tests.

2.1.3 Summary

The in-reactor fatigue crack propagation test was halted after an apparent lengthening in the specimen chain had occurred. The experiment was removed from the ORR and shipped back to HEDL for examination. The thermal control test at HEDL, duplicating the in-reactor test, was concluded and is also awaiting specimen examination.

2.1.4 Progress and Status

2.1.4.1 Introduction

Fatigue crack propagation (FCP) in the first wall of a magnetic fusion reactor may be a limiting quantity governing reactor lifetimes. Previous studies of irradiation effects on FCP have all been conducted out of reactor on materials preirradiated in the unstressed condition. The ORR-MET-5 experiment was designed to investigate FCP during irradiation, where dynamic irradiation may effect crack growth characteristics.

2.1.4.2 In-Reactor FCP Test at ORNL

The in-reactor fatigue machine[1,2] was inserted into the ORR during the November 1980 end-of-cycle shutdown. The system had been operating smoothly, cycling a chain of eight 20% cold-worked 316 stainless steel specimens at 1 cycle/min and at a peak temperature of 460°C.[3] However, when the reactor was brought up to power after routine refueling in late January 1981, and the cycling continued, it was observed that the desired triangular waveform previously obtained (Figure 2.1.1) had been replaced with a truncated waveform (Figure 2.1.2). The maximum achievable load was only ~55% of the prior peak load.

A series of tests on the assembly and support equipment were performed both during full reactor power and during shutdown. Results of these tests were: (1) All instruments, strain gauges and the bellows cycling system were functioning as intended; and (2) The truncated waveforms were a result of chain lengthening, which caused the bellows to reach its full stroke before the full load could be transmitted to the specimens.

The assembly containing the specimens was removed from the experiment at ORNL, and shipped to HEDL in March. Preparations for sodium removal and specimen examination are underway.

2.1.4.3 Thermal Control Test at HEDL

The thermal control tests was initiated at HEDL two months after startup of the in-reactor test. This test paralleled the ORR test, duplicating the temperature and cycling history. When the in-reactor test was removed, the thermal control test was continued until it had achieved the same number of cycles. Preparations are also underway for sodium removal and specimen examination of the control test.

2.1.5 Future Work

A facility is being prepared to perform the task of sodium removal from both the in-reactor assembly and the thermal control test. Specimen examination including crack length measurements will follow.

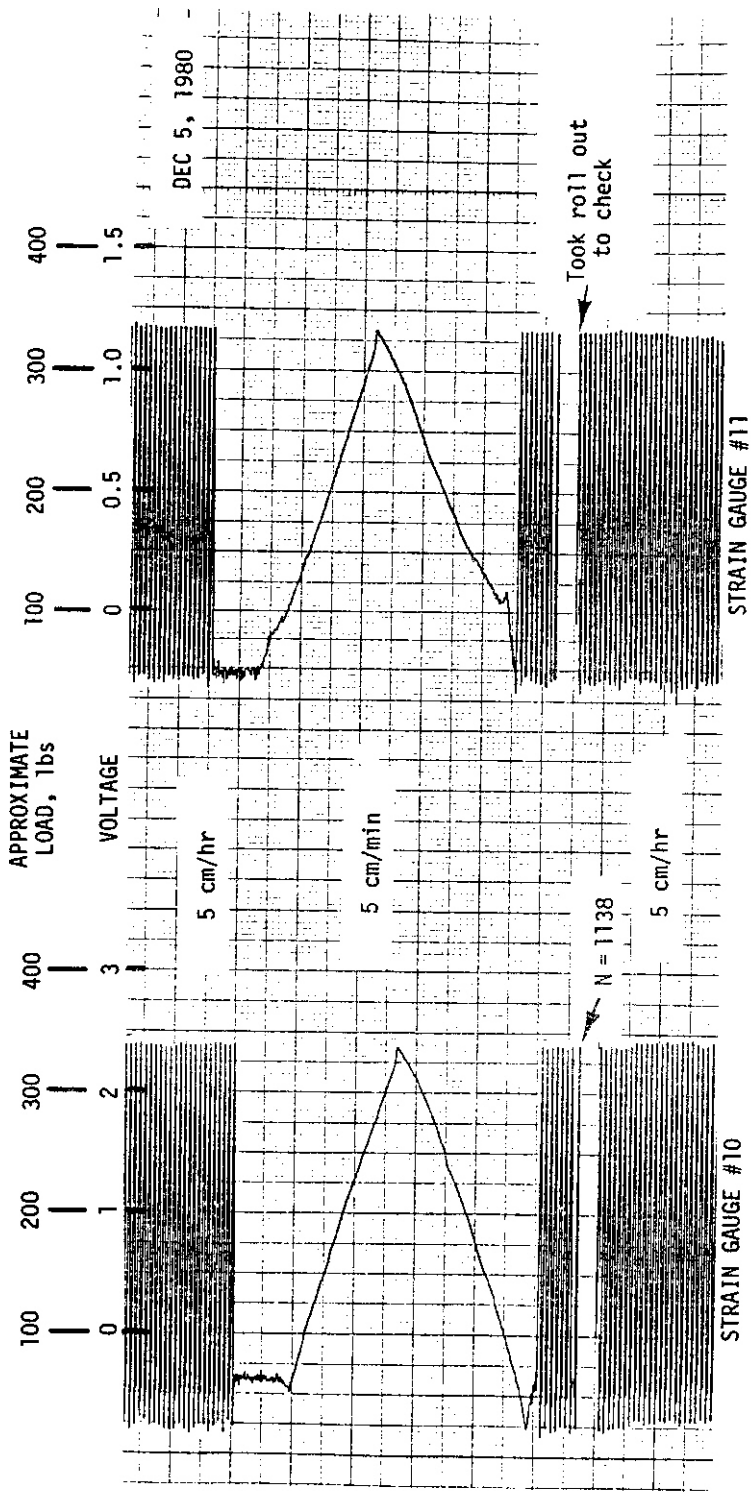

FIGURE 2.1.1 Typical Strain Gauge Outputs at a Frequency of 1 cycle/min.

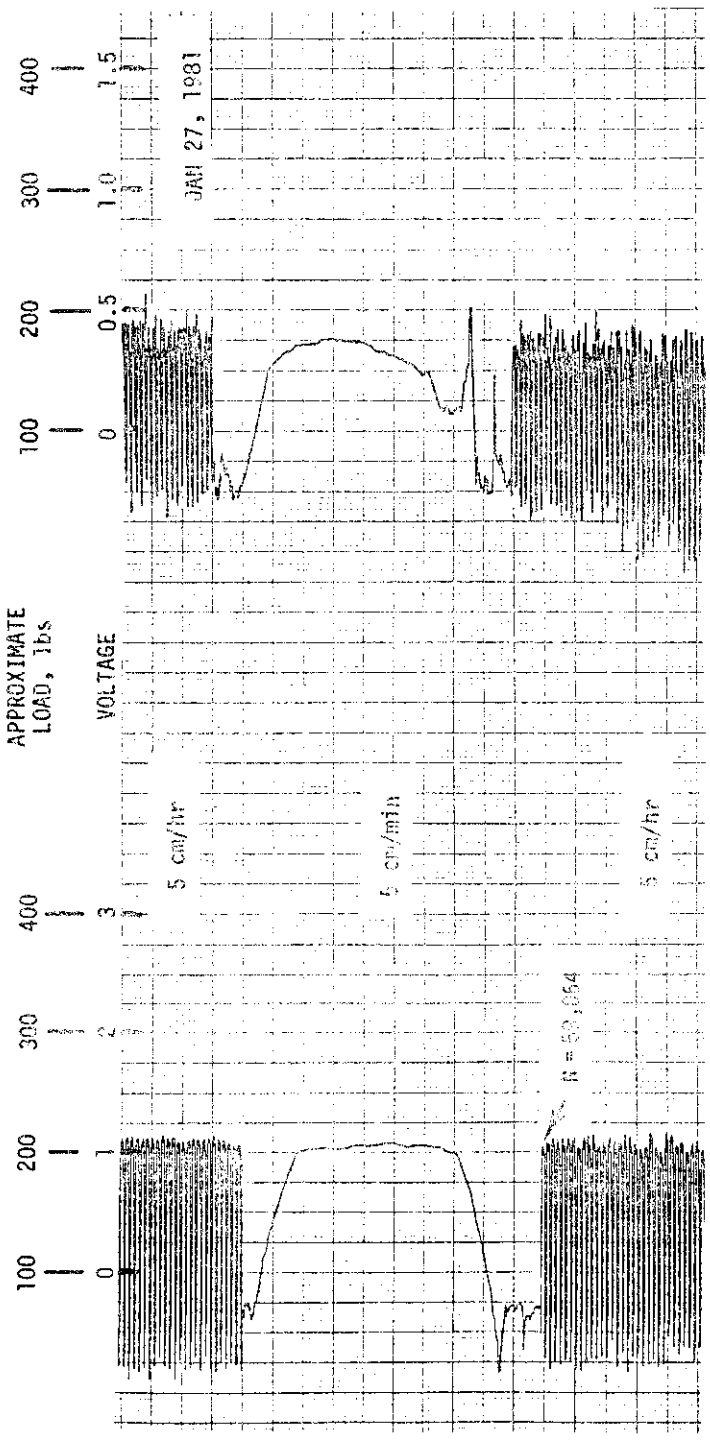

FIGURE 2.1.2 Truncated Strain Gauge Outputs at a Frequency of 1 cycle/min.

2.1.6 References

1. A. M. Ermi, "Status of an In-Reactor Fatigue Crack Growth Experiment," *ADIP Quarterly Progress Report, June 30, 1979,* DOE/ET-0058/6, pp. 28-34.
2. A. M. Ermi, "Results of Prototypic Testing for the MFE-5 In-Reactor Fatigue Crack Propagation Experiment," *ADIP Quarterly Progress Report, September 30, 1979,* DOE/ET-0058/7, pp. 50-65.
3. A. M. Ermi, "Status of MFE-5 In-Reactor Fatigue Crack Growth Experiment," *ADIP Quarterly Progress Report, December 31, 1980,* DOE/ER-0045/5.

2.2 NEUTRONIC CALCULATIONS FOR THE CONCEPTUAL DESIGN OF AN IN-REACTOR SOLID BREEDER EXPERIMENT, TRIO-01 — R. A. Lillie, R. L. Childs, and T. A. Gabriel (Oak Ridge National Laboratory)

2.2.1 ADIP Task

ADIP Task I.A.2, Define Test Matrices and Test Procedures.

2.2.2 Objective

The objective of these neutronic calculations is to provide tritium production and heat generation rates for the irradiation of solid tritium breeding materials in the Oak Ridge Research Reactor (ORR). These calculations will guide the design of the reactor irradiation experiment.

2.2.3 Summary

A technical memorandum covering this work has been completed and printed.[1]

2.2.4 Progress and Status

A technical memorandum covering this work has been completed and printed.[1]

The detailed calculations described previously[2] have not been completed due to a delay in the transfer of funds.* These calculations which are also described below will be completed during the next quarter.

2.2.5 Future Work

The VENTURE calculations to determine the changes in the poolside fluxes due to the presence of the TRIO-01 experiment will be repeated using the recently processed lithium cross sections. These calculations will be performed using the modified geometry, containing γ-$LiAlO_2$ at 60% of its theoretical density of 2.615 Mg/m^3. In addition to obtaining the poolside flux changes, this calculation will provide better estimates of the neutron fluxes around the experiment. With the results, additional

---

*Funding for the neutronics calculations for the design of the TRIO-01 experiment was not received during the period ending March 31, 1981, and the detailed calculations were temporarily halted.

two-dimensional transport calculations will be performed to determine the asymmetric tritium production and heating rates that are expected to occur with the experiment located in the ORR reactor core position A2.

2.2.6 References

1. R. A. Lillie, R. L. Childs, and T. A. Gabriel, *Neutronic Calculations for the Conceptual Design of an In-Reactor Solid Breeder Experiment, TRIO-01,* ORNL/TM-7758 (March 1981).
2. R. A. Lillie, R. L. Childs, and T. A. Gabriel, "Neutronic Calculations for the Conceptual Design of an In-Reactor Solid Breeder Experiment, TRIO-01," *ADIP Quart. Prog. Rep. Dec. 31, 1980,* DOE/ER-0045/5, pp. 10-14.

2.3 NEUTRONIC CALCULATIONS IN SUPPORT OF THE ORR-MFE-4 SPECTRAL TAILORING EXPERIMENT — R. A. Lillie, R. L. Childs, and T. A. Gabriel (Oak Ridge National Laboratory)

2.3.1 ADIP Task

ADIP Task I.A.2, Define Test Matrices and Test Procedures.

2.3.2 Objective

The objective of this work is to provide the neutronic design for materials irradiation experiments in the Oak Ridge Research Reactor (ORR). Spectral tailoring to control the fast and thermal neutron fluxes is required to provide the desired displacement and helium production rates in alloys containing nickel.

2.3.3 Summary

Three-dimensional neutronic calculations[1,2] are being carried out to follow the irradiation environment of the ORR-MFE-4A experiment. These calculations currently cover 19 ORR reactor cycles, corresponding to 131,543 MW h. This exposure has resulted in a thermal fluence of 4.05×10^{25} neutrons/m^2, a total fluence of 1.21×10^{26} neutrons/m^2, and a calculated response in type 316 stainless steel of 3.07 dpa and 21.01 at. ppm He (not inrluding 2.0 at. ppm He from ^{10}B). Using these data and previous calculations, real time projections have been made to estimate the dates that core pieces should be changed and the first samples removed.

The calculations required to validate the reduction of gamma heating rates within the OKR-MFE-4A experimental capsule due to the use of thermal flux reducing core pieces have been completed.[3-5] These calculations predict substantial decreases in the heating rates that are unavoidable since they are caused by the thermal flux reductions that are required to maintain the desired ratio of helium prodURtion to displarement damage over the lifetime of the experiment.

2.3.4 Progress and Status

The real time projections of the helium prodURtion and displarement damage levels based on rurrent calrulated data are given in Fig. 2.3.1.

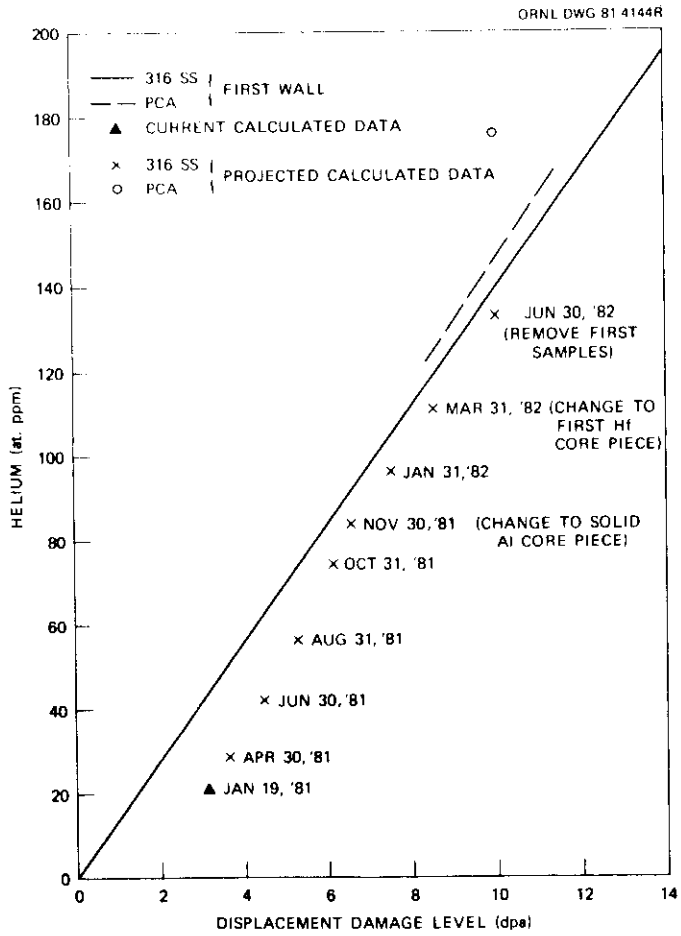

Fig. 2.3.1. Current and Projected Helium and Displacement Damage Levels in the ORR-MFE-4A Experiment.

The data reflect all refueling and extended shutdown times as of January 19, 1981. Using these data, the insertion of the solid aluminum core piece will not be required until the end of November 1981. In addition, the first samples will be removed sometime around June 30, 1982. These last two dates take into account that the ORR-MFE-4A experiment was not in the ORR from January 19, 1981, to March 19, 1981.

The predicted relative thermal flux and relative gamma heating using three methods of calculation for several core piece configurations are presented in Figs. 2.3.2 and 2.3.3, respectively. All three methods employed the one-dimensional model described previously.[4] A neutron source spectrum obtained from an earlier three-dimensional ORR calculation[2] was placed at the outer edge of the fuel surrounding the experiment

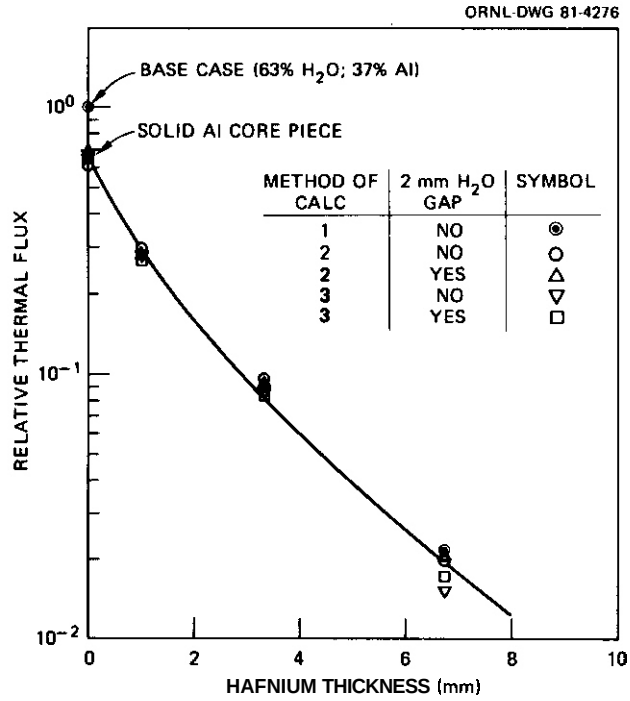

Fig. 2.3.2. Predicted Relative Thermal Flux in the ORR-MFE-4A Experiment for Several Core Piece Compositions.

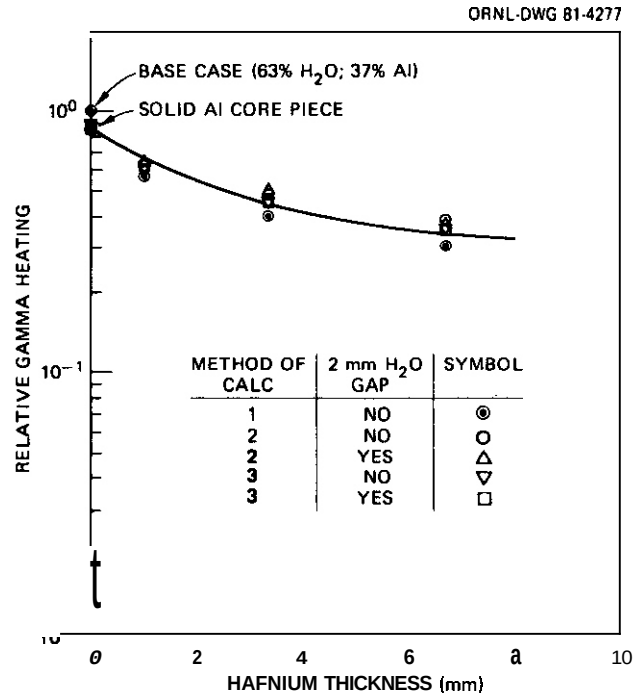

Fig. 2.3.3. Predicted Relative Gamma Heating in the ORR-MFE-4A Experiment for Several Core Piece Compositions.

and a reflected boundary condition was impcsed upon the gammas at the source location in method 1. Method 2 differed from method 1 in that a gamma source spectrum obtained from the base case calculation was employed in the succeeding calculations, thus preventing a reduction in the number of gammas incident on the outer edge of the fuel as the core piece composition is changed. In method 3, the outer radius of the fuel required for criticality was determined in the base case calculation and a fuel concentration search was performed tc maintain criticality in the succeeding calculations, This procedure allowed the loss of fissions in the fuel surrounding the experiment, due to the thermal flux reductions, to be compensated by increased fissions elsewhere.

The data presented in Figs. 2.3.1 and 2.3.3 indicate that all three methods yield essentialiy the same results, In addition, the calculations performed using methods 2 and 3 were carried out both with and without a 2 mm water gap surrounding the experimental capsule and no appreciable differences resultet for any of the core piece compositions. These results give a strong indication that reductions in gamma heating rates are unavoidable since they are caused by the thermal flux reductions that must be obtained to maintain the desired ratios of helium production to displacement damage over the lifetime of the experiment.

As a final note, all three methods of calculation predict a relative gamma heating reduction of approximately 13% with the insertion of the solid aluminum core piece, is excellent agreement with the 14% reduction measured in the ORR.[6]

2.3.5 Future Work

The three-dimensional calculations that monitor the radiation environment of the ORR-MFE-4A experiment will- rontinue with each reactor cycle.

2.3.6 References

1. D. K. Vondy, T. B. Fowler, and G. W. Cunningham, *VENTURE, A Code Block for Solving Multigroup Neutron Problems Applying Fine-Diffusion-Theory Approximations to Neutron Transport,* ORNL-5062 (October 1975).

2. T. A. Gabriel, R. A. Lillie, B. L. Bishop, and R. L. Childs, "Neutronic Calculations in Support of the ORR-MFE-4A Spectral Tailoring Experiment," *ADIP Quart. Prog. Rep. June 30, 1960,* DOE/ER-0045/3, pp. 7–9.

3. W. W. Engle, Jr., *A User's Manual for ANISN, A One-Dimensionit Discrete Ordinates Code with Anisotropic Scattering,* K–1693 (1967).

4. T. A. Gabriel, R. A. Lillie, B. L. Bishop, and R. L. Childs, "Neutronic Calculations in Support of the ORR-MFE-4A Spectral Tailoring Experiment," *ADIP Quart. Prog. Rep. Sept. 30, 1980,* DOE/ER-0045/4, pp. *14–19.*

5. R. A. Lillie, R. L. Childs, and T. A. Gabriel, "Neutronic Calculations in Support of the ORR-MFE-4A Spectral Tailoring Experiment," *ADIP Quart. Prog. Rep. Dec. 31, 1980,* DOE/ER-0045/5, pp. 15–18.

6. K. R. Thoms, personal communication, February 1980.

2.4 OPERATION OF THE ORR SPECTRAL TAILORING EXPERIMENT ORR-MFE-4A — K. R. Thoms (Oak Ridge National Laboratory)

2.4.1 ADIP Task

ADIP Task I.A.2, Define Test Matrices and Test Procedures.

2.4.2 Objective

This experiment will irradiate austenitic stainless steels, using neutron spectrum tailoring to achieve the same helium-to-displacement-per-atom (He/dpa) ratio as predicted for fusion reactor first-wall service. The experiment contains mainly type 316 stainless steel and Path A Prime Candidate Alloy (PCA) at irradiation temperatures near 300 and 400°C.

2.4.3 Summary

The ORR-MFE-4A experiment consists of two test regions designed to irradiate type 316 stainless steel and Path A PCA at temperatures of 330 and 400°C. The experiment was installed in the Oak Ridge Research Reactor (ORR) on June 10, 1980, and as of March 31, 1981, has operated for an equivalent 195 d at 30 MW reactor power, with maximum specimen temperatures in each region of 330 and 400°C, respectively.

The failure of test region thermocouples required the removal of the capsule from the reactor, but the successful removal of the broken flux monitor tube and its replacement with a multiple junction central thermocouple permitted reinstallation of the capsule two months after removal. Satisfactory operation is once more under way.

2.4.4 Progress and Status

The details of the ORR spectral tailoring experiments have been described previously.[1,2] The ORR-MFE-4A irradiation capsule was installed in the ORR on June 10, 1980, and as of March 31, 1981, has operated for an equivalent 195 d at 30 MW reactor power with the maximum specimen temperatures in the upper and lower test regions being controlled at 400 and 330°C, respectively.

During this report period, the capsule was removed from the reactor for a period of two months (January 20 through March 19, 1981) due to the

failure of five of the six test region thermocouples. After removal from the reactor, it was decided to install a multiple junction thermocouple in the flux monitor well, which runs down the centerline of the capsule. A major obstacle that had to be overcome was the removal of the flux monitor tube itself, which broke off of its lead tube during attempted removal in November 1980.

The broken flux monitor tube consisted of a 3.00-mm (0.118-in.)-OD by 0.28-m (0.011-in.) wall stainless steel tube approximately 0.3 m long. The lower 0.15 m of the tube was filled with 19 nickel wires and a package of thermal flux monitors. The removal of this broken tube required development of special techniques. A piece of "Nitinol" (memory metal) was fabricated that when heated above 49°C would swell about 7%. The piece made for this job was drawn to a diameter that would barely fit into the broken tube. After welding the piece to a length of stainless steel wire, it was pushed down the flux monitor guide tube into the flux monitor tube. A furnace was fabricated to slip over the capsule, and the lower 1 m of the capsule was heated to about 55°C. The flux monitor tube was then pulled out of the capsule into a shielded transfer cask and placed in the ORR hot cell where the nickel wires were recovered.

A multiple-junction thermocouple was fabricated by placing seven 0.51-m (0.020-in.)-OD sheathed Chromel/Alumel thermocouples in a 3-m (1/8-in.)-OD by 0.71-m (0.028-in.) wall stainless steel tube and then swaging the entire assembly. Although one of the seven thermocouples failed during the fabrication process, the assembly with six good thermocouples was then inserted in the flux monitor guide tube of capsule ORR-MFE-4A. The junctions of this central thermocouple lined up axially with the failed thermocouples 1 through 5 in the test region, while the sixth junction was located to measure the temperature of the central spline in the region between the capsule bulkhead and the NaK level.

With the multiple junction central thermocouple in place, the capsule was reinstalled in the ORR, and the reactor was started up on March 19, 1981. While the capsule was out of the reactor, the past operating data were thoroughly analyzed to obtain relationships between the one remaining test region thermocouple, TE-6, and the five failed

thermocouples. A complete history of control gas mixtures versus time in the fuel cycle was detailed, and a parametric one-dimensional heat transfer study was made. This gave confidence in the new mode of operation, where the test specimen temperature is controlled from the temperatures indicated by the central thermocouple. During the reactor startup, TE-6 failed, leaving no operating test region thermocouples. However, after the reactor was stabilized at 30 MW, a reading was obtained for TE-6 after pulse heating (discharging a series of capacitors across the open thermocouple, temporarily welding the broken Alumel wire together). This data point (247°C) was in the low range of previously observed readings for TE-6 at startup and gave us the necessary starting point to successfully determine the test specimen temperature. At present, the capsule is being controlled in a temperature range of about 375 to 400°C in the upper region and about 310 to 330°C in the lower region. Before the thermocouple failures, the capsule operated at a constant *400* and 330°C in the upper and lower regions, respectively. As more operating experience is gained, the range of control can be reduced, to operate very close to the conditions prior to the thermocouple failures.

A preliminary analysis of the cause of failure of the test region thermocouples indicates that there were probably two contributing factors. First, the use of grounded junction thermocouples probably put excessive stress on the thermocouple wires, due to the differential thermal expansion between the stainless steel sheath and the Alumel wire. Second, metallography performed on archive samples of the thermocouple material indicates excessively large grain size in the wire, causing a significant loss in wire ductility and strength. The combination of these two factors probably caused the early failure of the test region thermocouples. An effort will be made after irradiation to look at the failed thermocouples to support this explanation or determine other possible causes of failure.

The assembly of capsule ORR-MFE-4B was delayed while the thermocouple failure problem in ORR-MFE-4A was analyzed. The MFE-4B capsule is identical to -4A, except that it is designed to irradiate the test specimens at 500 and 600°C. The assembly of -4B was about 90% complete when the

failure of thermocouples occurred, and was well beyond the point of replacing the test region thermocouples. To avoid rebuilding the capsule, it was decided to complete the capsule and install a central multiple thermocouple similar to the one installed in -4A. Therefore, if the test region thermocouples fail (which is likely since they were made identical to those in -4A), we will have had much operating experience and also obtained good correlations between them and the central thermocouple. Present plans call for installing ORR-MFE-4B in the E-7 core position of the ORR during the quarterly shutdown scheduled for the week of April 19-24, 1981.

2.4.5 Conclusions

The first ORR spectral tailoring capsule, ORR-MFE-4A, has operated for an equivalent 195 d at 30 MW reactor power with maximum specimen temperatures in the two test regions controlled at 310 to 330°C and 375 to 400°C, respectively. The failure of test region thermocouples required the removal of the capsule from the reactor, but the successful removal of the broken flux monitor tube and its replacement with a multiple junction central thermocouple permitted reinstallation of the capsule two months after removal. Satisfactory operation is once more under way, with more precise control expected with more operating experience. The second capsule, ORR-MFE-4B, will be installed in the ORR during the week of April 19-24, 1981.

2.4.6 References

1. T. A. Gabriel, K. R. Thoms, and M. L. Grossbeck, "Design of Materials Irradiation Experiments in the ORR Utilizing Spectral Tailoring and Reencapsulation," *ADIP Quart. Prog. Rep. Mar. 31, 1978,* DOE/ET-0058/5, pp. 20-22.
2. T. A. Gabriel, K. R. Thoms, and J. W. Woods, "Design of Materials Irradiation Experiments Utilizing Spectral Tailoring," *ADIP Quart. Prog. Rep. Dec. 31, 1978,* DOE/ET-0058/4, pp. 10-17.

3. PATH A ALLOY DEVELOPMENT — AUSTENITIC STAINLESS STEEL

3.1 FATIGUE OF HFIK-IRRADIATED 20%-COLD-WORKED TYPE 316 STAINLESS STEEL AT 550°C — M. L. Grossberk and K. C. Liu (Oak Ridge National Laboratory)

3.1.1 ADIP Task

ADIP Task I.B.5, Stress-Strain Controlled Fatigue of Austenitic Alloys.

3.1.2 Objective

This study evaluates the efferts of simultaneous displacement damage and helium production during irradiation on the low-cyrle fatigue life of 20%-cold-worked type 316 stainless steel.

3.1.3 Summary

Specimens of 20%-cold-worked type 316 stainless steel were irradiated at 550°C in the High Flux Isotope Reactor (HFIR). Low-cycle, 550°C vacuum fatigue tests were performed on specimens with a damage level of approximately 9 dpa and containing approximately 400 at. ppm He. The preliminary results show essentially no effert of irradiation at these temperatures. Furthermore, the fatigue life of the unirradiated material tested at 550°C was very similar to the unirradiated life of the same heat of material tested at 430°C.

3.1.4 Progress and Status

3.1.4.1 Introduction

Since most tokamak fusion reactors are projerted to operate in a cyclic mode, fatigue life of irradiated structural romponents is of conrern. In order to address this question for fusion reactor first-wall materials, a study was initiated for the cyclic testing of irradiated stainless steel. Irradiation tests were performed in HFIK, so that the simultaneous production of displacement damage and helium would approximate these processes during service in a fusion reactor.

A total of 50 miniature hourglass fatigue specimens of 20%-cold-worked type 316 stainless steel were irradiated in the HFIR. Details of

the specimens and the irradiation vehicle have been reported previously.[1] Postirradiation tests are performed to determine the effects of neutron irradiation that produces transmutation helium as well as atomic displacements on the fatigue properties. Thirty specimens were irradiated at 430°C and twenty at 550°C. The 430°C fatigue data have been reported previously.[2-4] Tests are now being conducted on the material irradiated at 550°C, and four tests have been completed. Certainly no firm conclusions can be drawn from such a limited amount of data. However, these data are reported to give a first indication of the results.

3.1.4.2 Results

Fatigue tests were performed with a remotely controlled servo-hydraulic testing system equipped with an ultra-high vacuum chamber. All tests were conducted in a vacuum environment with the total pressure in the range 10^{-7} to 10^{-4} Pa. Tests temperatures were maintained by an induction heating system controlled by a thermocouple. The stress was applied as a ramp function to produce a strain rate of 4×10^{-3}/s in the low-cycle regime. Tests were strain controlled for total strain ranges above 0.42%. At 0.42% and below, strain control was employed until a stable hysteresis loop was established, after which control was shifted to load and the strain rate increased by a factor of 10. The details of the experimental procedure have been explained in previous reports.[2-4]

The irradiation parameters and fatigue test results are given in Table 3.1.1. The data are also plotted in Fig. 3.1.1, along with the previously reported results of the 430°C tests. As can be seen from the data, there appears to be no significant effect of irradiation at 550°C. This finding is in contrast to the results at 430°C where irradiation resulted in a reduction in fatigue life by a factor of 3 to 10, The effect of irradiation on the fatigue endurance limit remains to be investigated.

3.1.5 Conclusions

1. Irradiation in HFIR at 550°C, to fluences producing 9 dpa and 400 at. ppm He, had little effect on 550°C fatigue life of 20%-cold-worked type 316 stainless steel.

Table 3.1.1. Irradiation and Fatigue Test Parameters for 20%-Cold-Worked Type 316 Stainless Steel Irradiated and Tested at 550°C

Specimen[a]	Neutron Fluence, >0.1 MeV (neutrons/m^2)	Helium Content (at. ppm)	Displacement Damage Level (dpa)	Total Strain Range (%)	Maximum Stress at Half Life, $\Delta\sigma/2$ (MPa)	Cycles to Failure
G39	0			0.30	227	>11,359,000
G42	0			0.30	234	>10,046,900
G43	0			0.42	317	3,125,650
G51	0			0.70	455	56,692
G50	0			1.2	496	9,456
G41	0			1.5	351	3,043
A75	1.2×10^{26}	410	9.2	0.30	227	>10,437,200
A95	1.1	400	9.1	0.42	317	288,410
A76	1.2	390	9.0	0.87	337	31,595
A74	1.2	390	9.0	1.8	400	2,142

[a]Specimens machined from 6.48-mm (0.255-in.) -diam rod of 20%-cold-worked type 316 stainless steel, heat X15893.

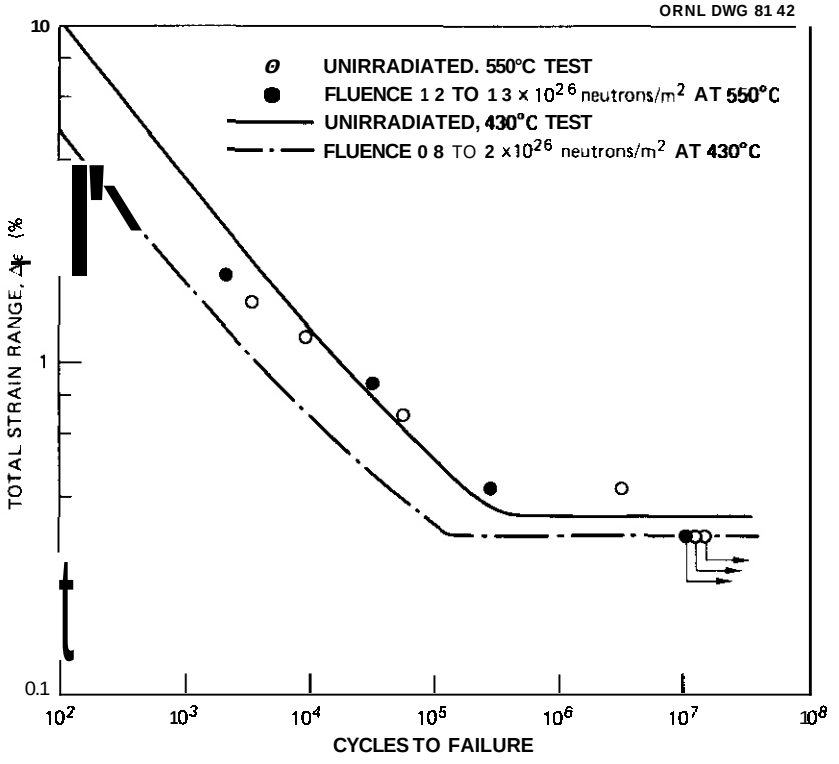

Fig. 3.1.1. Fatigue Life of 20%-Cold-Worked Type 316 Stainless Steel (Heat X15893) Irradiated in HFIR at 430 or 550°C and Tested at Irradiation Temperature. Data at 550°C are for irradiation producing 420–450 at. ppm He, 9–10 dpa.

2. The vacuum fatigue life of unirradiated 20%-cold-worked type 316 stainless steel was similar at 430 and 550°C.

3.1.6 References

1. M. L. Grossbeck and M. J. Kania, "HFIR Irradiation of Hourglass Fatigue Specimens," *ADIP Quart. Prog. Rep. January–March, 1978,* DOE/ET-0058/2, pp. 2C–35.
2. M. L. Grossbeck and K. C. Liu, "High-Cycle Fatigue Testing of HFIR–Irradiated 20%-Cold-Worked Type 316 Stainless Steel," *ADIP Quart. Prog. Rep. Mar. 31, 1980,* DOE/ER-0045/2, pp. 33–34.
3. M. L. Grossbeck and K. C. Liu, "Low-Cycle Fatigue Behavior of 20%-Cold-Worked Type 316 Stainless Steel After Irradiation in the HFIR," *ADIP Quart. Prog. Rep. June 30, 1979,* DOE/ET-0058/6, pp. 42–47.
4. M. L. Grossbeck and K. C. Liu, "Fatigue Behavior of Type 316 Stainless Steel Following Neutron-Irradiation-Inducing Helium," (Summary) *Tmns. Am. Nucl. Soc.* 34(TANSAO 34): 186–88 (June 1980).

3.2 MICROSTRUCTURAL DEVELOPMENT IN 20%-COLD-WORKED TYPE 316 STAINLESS STEEL AND TITANIUM-MODIFIED TYPE 316 STAINLESS STEEL IRRADIATED IN THE HFIR: FLUENCE DEPENDENCE OF THE CAVITY COMPONENT — P. J. Maziasz and M. L. Grossbeck (Oak Ridge National Laboratory)

3.2.1 ADIP Tasks

ADIP Tasks I.C.1, Microstructural Stability, and I.C.2, Microstructure and Swelling in Austenitic Alloys.

3.2.2 Objective

The objective of this work is to characterize and compare microstructural development of standard and titanium-modified type 316 stainless steel after High Flux Isotope Reactor (HFIR) irradiation. The total microstructure is then used for swelling determination, mechanical properties corrrelation, and input to alloy development. Extensive analysis of the data is aimed at defining the role of helium in microstructural evolution during irradiation.

3.2.3 Summary

Irradiation of 20%-cold-worked type 316 stainless steel (CW 316) and titanium-modified type 316 stainless steel (CW 316 + Ti) in HFIR results in ronsiderable microstructural development at 285°C and above at fluences as low as 7.7 dpa (380 at. ppm He). The microstrurtural development is significantly different in the two alloys; however, the cavity behavior is intimately related to the complex precipitation and dislocation behavior in both alloys. Total cavity swelling in CW 316 at 375 and 475°C is first first observed to increase and then decrease before increasing monotonically with increasing fluence. Swelling increases steadily with fluenre for CW 316 at 565°C and above. The steady-state swelling rate of CW 316 appears nearly temperature independent at a value of about 0.1%/dpa, with a minimum swelling rate of about 0.07%/dpa at 475°C. By comparison, steady-state swelling rates for the same material irradiated in the Experimental Breeder Reactor-I1 (EBR-II) are quite sensitive to temperature and have a maximum rate of about 0.5%/dpa at 500–550°C. At fluences up to 16 dpa, the swelling of CW 316 + Ti appears to inrrease with increasing fluence at rates that vary from about 0.008%/dpa at 375°C

to about 0.002%/dpa at 565°C, 10 to 40 times lower than CW 316 irradiated at the same conditions. Cavities are the dominant grain-boundary feature for both alloys at temperatures above 550°C and fluences of about 8 dpa or greater. The grain-boundary cavities are about a factor of 2 smaller in CW 316 + Ti than in CW 316. In CW 316 irradiated to higher fluenres at temperatures above 600°C, the grain-boundary cavities contribute significantly to the total swelling.

3.2.4 Progress and Status

3.2.4.1 Introduction

This continues a series of reports on the temperature and fluenre dependence of the microstructure of 20%-cold-workedtype 316 stainless steel (CW 316) and titanium-modified type 316 stainless steel (CW 316 + Ti) irradiated in HFIR. The various microstructural components will be correlated to establish the phenomenological interrelationships between cavity, dislocation, and precipitation components of the microstructure in order to understand the mechanisms of microstructural evolution during HFIR irradiation. The microstrurtural information will also be correlated with the tensile properties obtained from these same samples.[1,2] Swelling from immersion density and from cavity volume fraction and preliminary correlation of mechanical properties and microstructure (below 375°C) have been reported previously.[3-5]

3.2.4.2 Experimental

The compositions of the CW 316 and CW 316 + Ti stainlesss steel are given in Table 3.2.1. The details of specimen preparation and the HFIR irradiation experiments have been presented previously.[4-6] The irradiation temperatures reported here are calculated, based on a known heat transfer geometry and previous measurements and assumptions of nurlear heating values. Recent, inromplete analysis of temperature measurement indicates that the actual irradiation temperatures may be as much as 50 to 75°C higher than calculated. The presented fluence comparisons and comparisons between the two heats of steel involve relative temperature differences, and hence trends are valid but may need to be "shifted" when final temperature calibration is completed.

Table 3.2.1. Composition of Two Cold-Worked Austenitic Stainless Steels

Alloy	Content,[a] wt %										
	Cr	Ni	Mo	Mn	C	Ti	Si	P	S	N	B
316	18.0	13.0	2.58	1.90	0.05	0.05	0.80	0.013	0.016	0.05	0.0005
316 + Ti	17.0	12.0	2.50	0.5	0.06	0.23	0.40	0.01	0.013	0.0055	0.0007

[a]Balance iron.

Since the HFIK operates with little variation from cycle-to-cycle, comparison between experiments performed at different times does not introduce significant fluence or temperature uncertainties, for experiments designed on the same assumed nuclear heating rates. This allows comparison of results from the two experiment series, HFIR-SS-2 through -8 and HFIR-CTR-9 through -13, to develop fluence dependence for the displacement damage range 8 to 60 dpa for temperatures between 370 and 620°C.

Transmission electron microscopy sample preparation and examination techniques were reported previously.[4]

3.2.4.3 Results

Fluence Dependence of the Cavity Microstructure and Swelling for CW 316. The immersion density changes, cavity statistics, and cavity volume fraction (cvf) swellings for CW 316 at the various irradiation temperatures and fluenres are given in Table 3.2.2. The total cvf and immersion density values are plotted as a function of irradiation temperature in Fig. 3.2.1. Micrographs showing the intragranular cavity microstructure as a function of fluence at irradiation temperatures of 375 to 380°C, 460 to 475°C, 550 to 565°C, and 600 to 620°C are shown in Figs. 3.2.2 through 3.2.5, respectively. The fluenre dependence of the average cavity concentration and average cavity diameter are obtained from these microstructures and expressed graphically in Figs. 3.2.6 and 3.2.7, respectively.

It is obvious from Fig. 3.2.1 and micrographs shown previously[4,5] that there is considerable microstructural development at irradiation temperatures of 285°C and above and fluences as low as 7.7 dpa in HFIR. The micrographs in Figs. 3.2.2 through 3.2.5 indicate significant fluence dependence between 8 and 16 dpa, particularly at irradiation temperatures

Table 3.2.2 Swelling and Cavity Statistics for Cold-Worked Type 316 Stainless Steel Irradiated in HFIR

Irradiation Conditions				Swelling from Immersion Density (%)	Cavity Parameters					
					Matrix Cavities			Grain-Boundary Cavities		Total Cavity Volume Fraction (%)
Temperature (°C)	Neutron Fluence, >0.1 MeV (neutrons/m^2)	Displacement Damage (dpa)	Helium (at. ppm)		Average Diameter (nm)	Concentration (cavities/m^3)	Volume Fraction (%)	Average Diameter (nm)	Volume Fraction (%)	
55	1.4×10^{26}	10.8	80	-0.03	[a]		0	[a]		0
≥85	1.0	7.7	90	0.04	2	4×10^{21}	0.6	[a]		0.4
375	1.1	8.5	380	0	2.7 7.6[b]	2×10^{22} 2×10^{21}	0.2	[c]		0.12
385	1.7	13.0	140	0.8	2.6	$\geq \times 10^{22}$	0.03	[c]		0.03
430	7.45	69	320	1.6	9.5 11[e]	1.8×10^{22} 4.5×10^{18}	2.2 ± 0.4	[c]		2.2
475	1.4	10.0	500	-0.1	7	2.6×10^{21}	0.06 ± 0.01[d]	[c]		0.06
475	2.1	16.0	1020	0.03	2.2	2×10^{22}	0.02	3–5	>0.005	0.02
460	7.69	54	3660	0.8	17	6.6×10^{21}	2.0 ± 0.4			2.0
565	1.2	9.2	440	0.1	11	5.6×10^{20}	0.04	~35	0.02	0.06
565	2.0	15.0	880	0.37	21.5	2.7×10^{20}	0.13	~35	0.02	0.15
550	6.18	42	2990	0.0	21	2.4×10^{21}	1.4 ± 0.1	40	0.03	1.4
620	2.1	16.0	1020	0.37	21.5	2.0×10^{20}	0.12	~37	0.02	0.14
600[f]	8.71	60	4070	3.3	65	3.3×10^{20}	3.0 ± 0.5	350	0.4	3.4
680[g]	8.74	61	4140		110	6.5×10^{19}	6.0 ± 2.5	710	2.0	8.0

[a] None detected.

[b] Bimodal size distribution.

[c] Grain boundary precipitation of eta (M_6C) phase.

[d] Two separate disks with three areas analyzed in one disk and two areas analyzed in the other to show the area-to-area variation in swelling.

[e] Bimodal size distribution, large cavities exclusively associated with eta (M_6C) phase particles.

[f] Completely recrystallized fine grains.

[g] Completely recrystallized coarse grains.

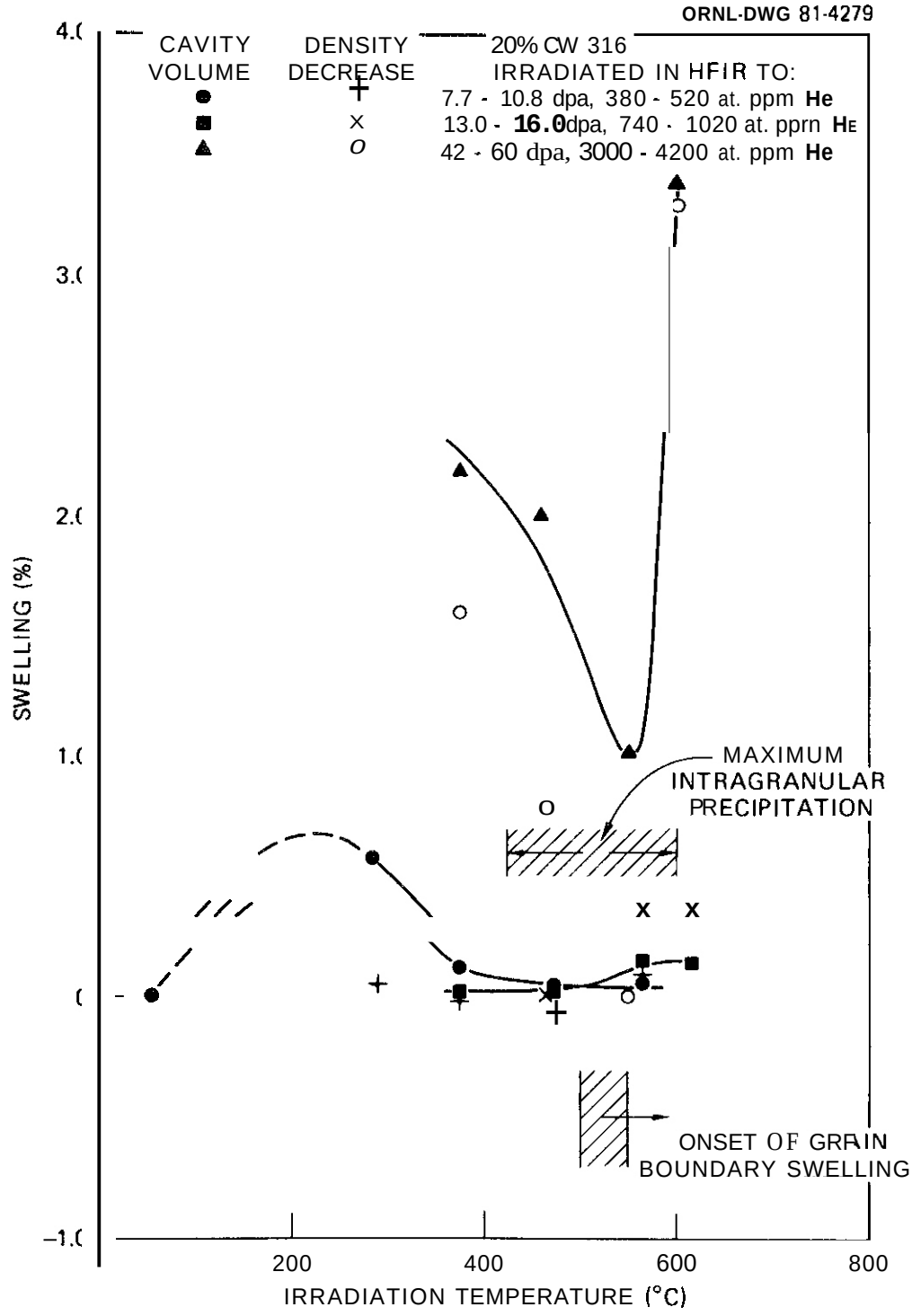

Fig. 3.2.1. Swelling as a Funrtion of Irradiation Temperature at Several Fluences for 20% CW 316 Irradiated in HFIK.

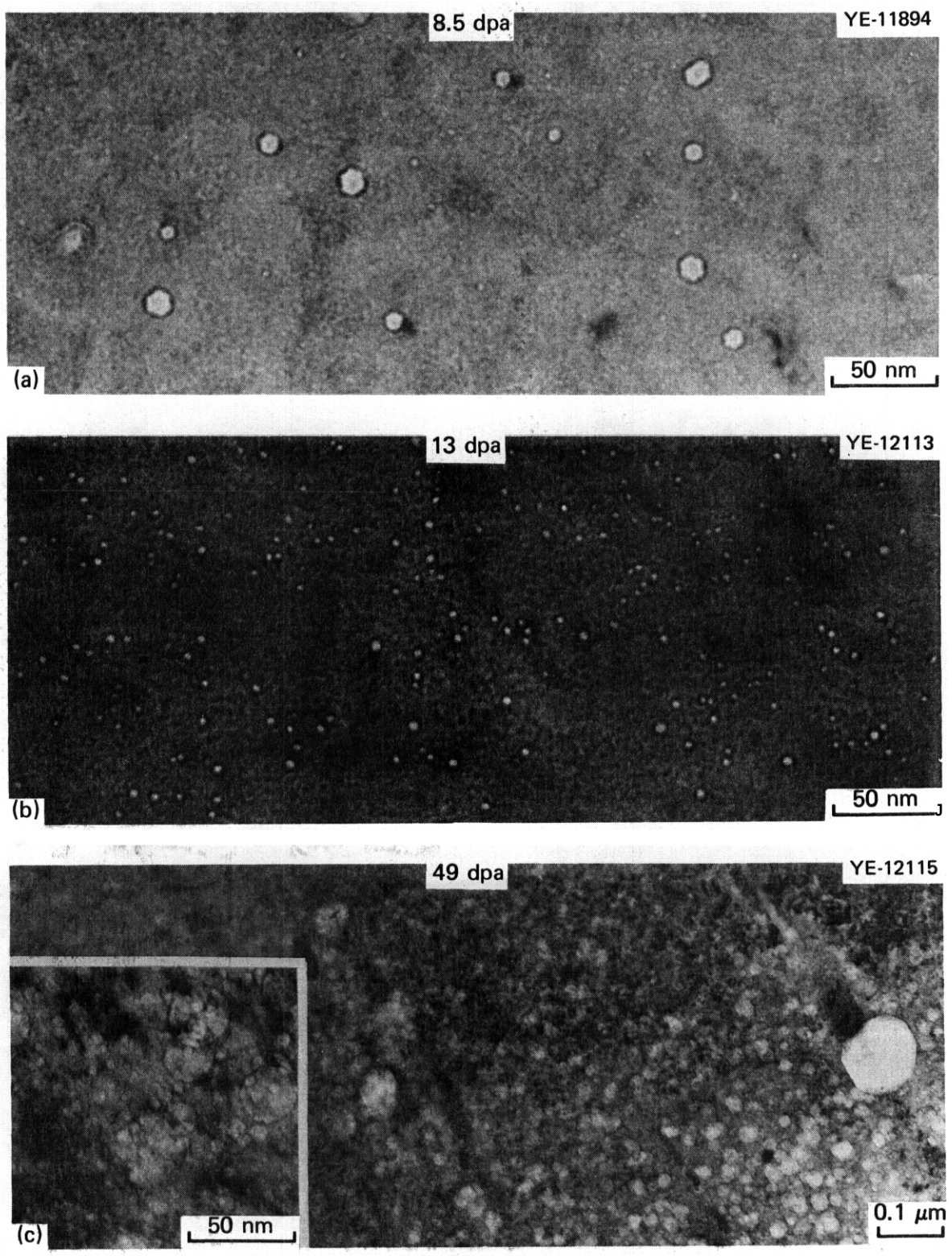

Fig. 3.2.2. Fluence Dependence of 20%CW 316 Irradiated in HFIR at 375 to 380°C to Fluences of (a) 8.5 dpa, (b) 13 dpa, and (c) *49* dpa.

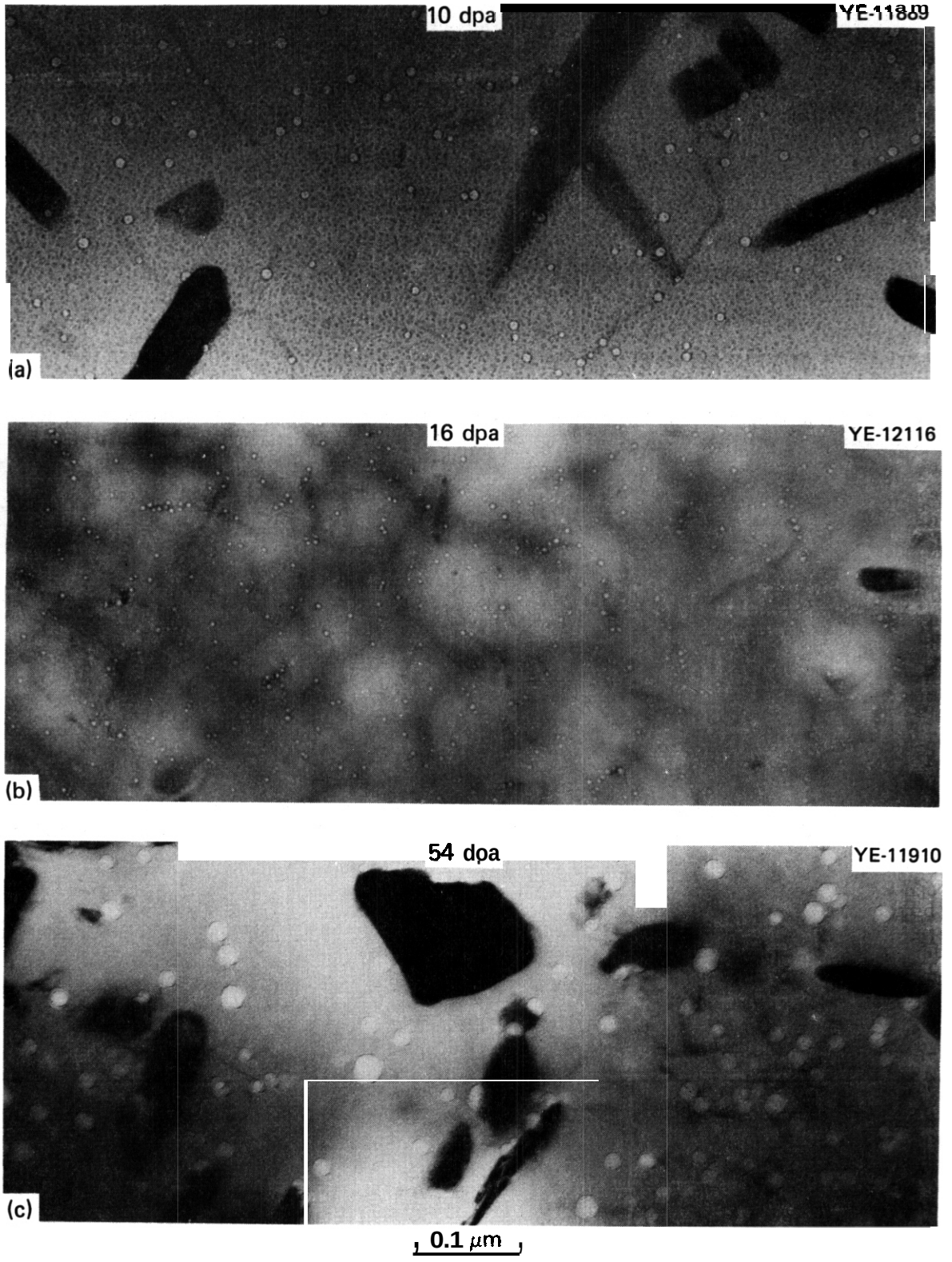

Fig. 3.2.3. Fluence Dependence of 20%CW 316 Irradiated in HFIR at *460* to *475°C* to Fluences of (a) 10 dpa, (b) 16 dpa, and (c) *54* dpa.

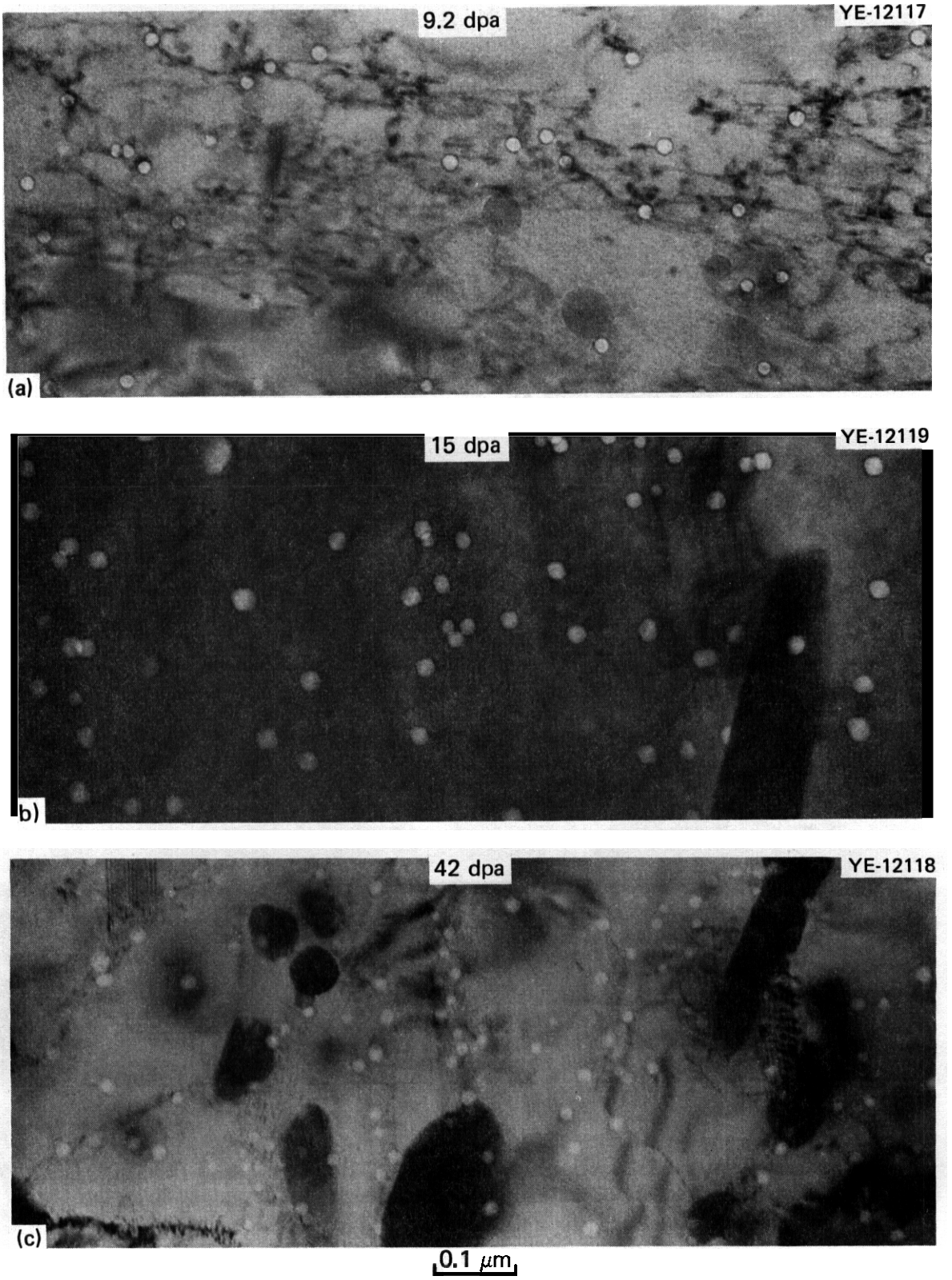

Fig. *3.2.4.* **Fluence Dependence of 20%CW 316 Irradiated in HFIR at 550 to 565°C to Fluences of (a) 9.2 dpa, (b) 15 dpa, and (c) *42* dpa.**

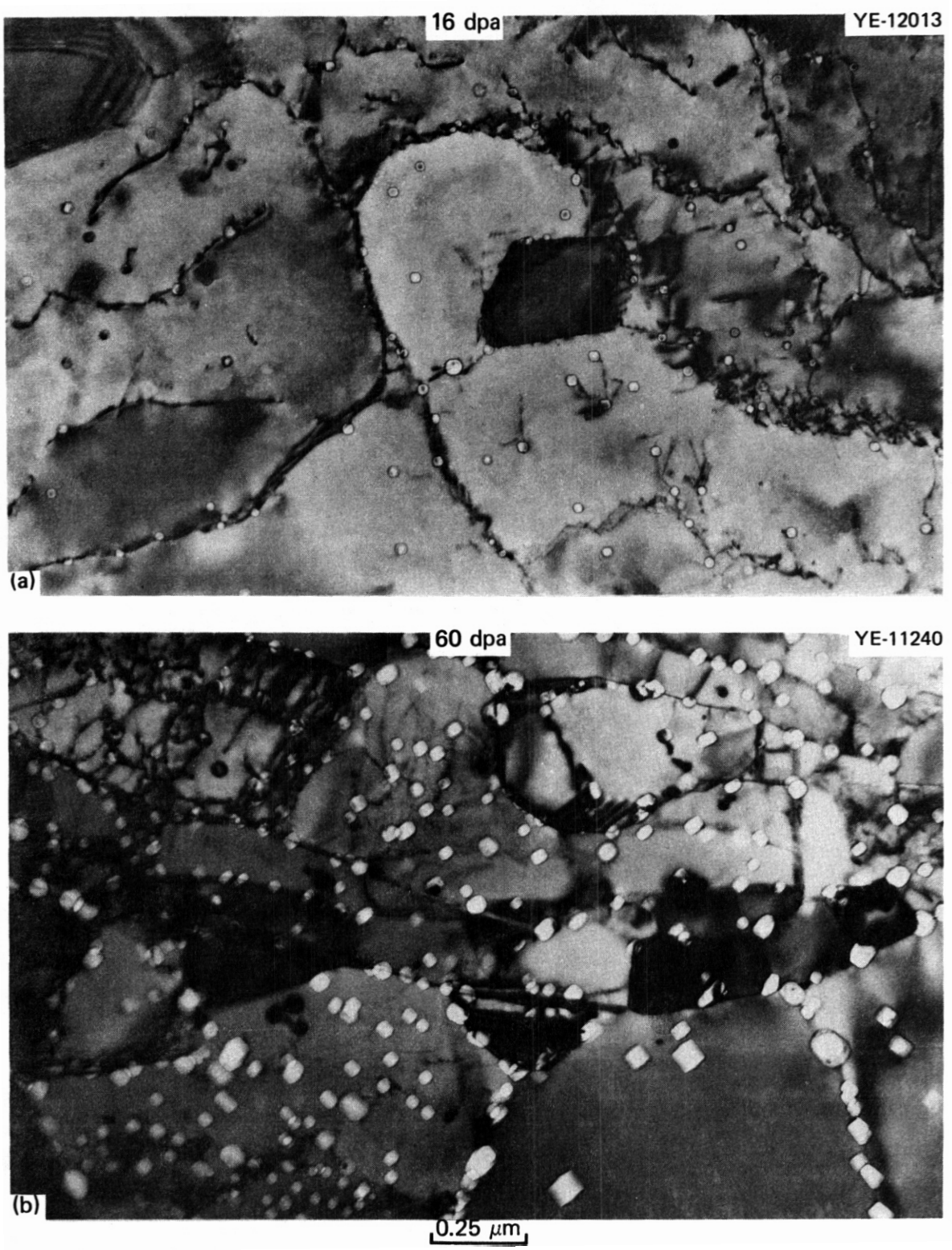

Fig. 3.2.5. Fluence Dependence of 20%CW 316 Irradiated in HFIR at 600 to 620°C to Fluences of (a) 16 dpa and (b) 60 dpa.

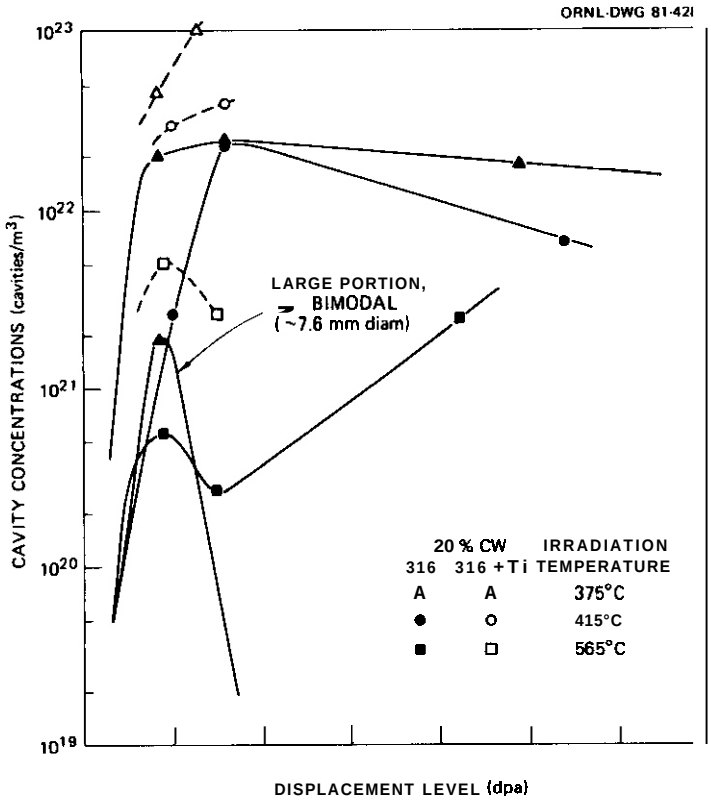

Fig. 3.2.6. Average Cavity concentration in Two Stainless Steels as a Function of Fluence in HFIR.

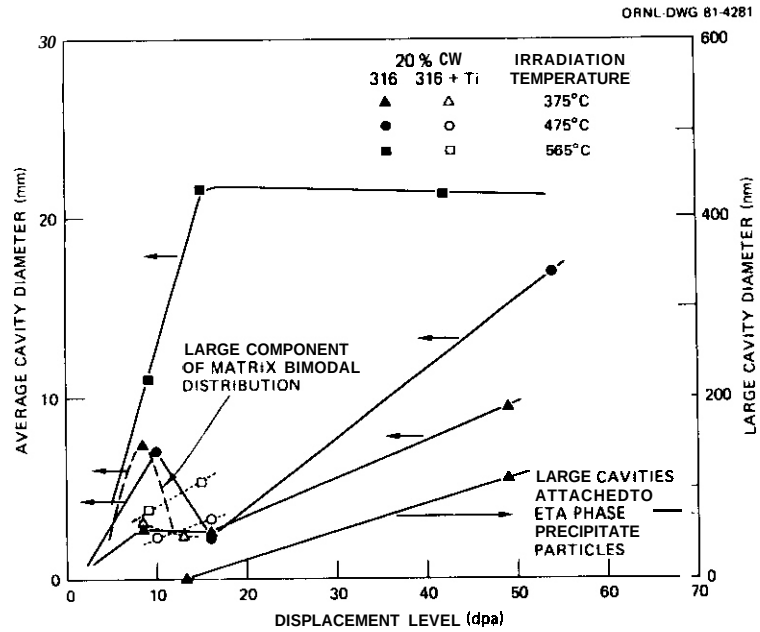

Fig. 3.2.7. Average Cavity Diameter as a Function of Fluence for Steels Irradiated in HFIR.

below 500°C. Figure 3.2.2(c) shows very large cavities (probably voids) attached to coarse eta phase precipitate particles. This is the only significant cavity–precipitate interaction for CW 316 irradiated in HFIR. (This same phase often has voids attached for samples irradiated in EBR-II). At 460 to 475°C and above, no large cavities form on precipitates and the cavity size distribution is quite narrow about the average size. At 600 to 620°C, Fig. 3.2.5(a) and (b) show appreciable cavity association with dislocation cell boundaries that form as the network recovers prior to recrystallization. [At higher fluenre, cells that remain stable apparently fill in with cavities and those that grow collect helium and cavities at the moving boundary [Fig. 3.2.5(b)].

The cavity diameter and concentration, presented as functions of fluenre in Figs. 3.2.6 and 3.2.7, show some rather unusual trends that can also be seen in Figs. 3.2.2 to 3.2.4. At 375°C the cavity behavior appears closely related to dramatic changes that occur in the precipitate and dislocation components of the microstructure.[7] These correlations are shown schematically in Fig. 3.2.8. For CW 316 at 375 to 380°C, Fig. 3.2.7

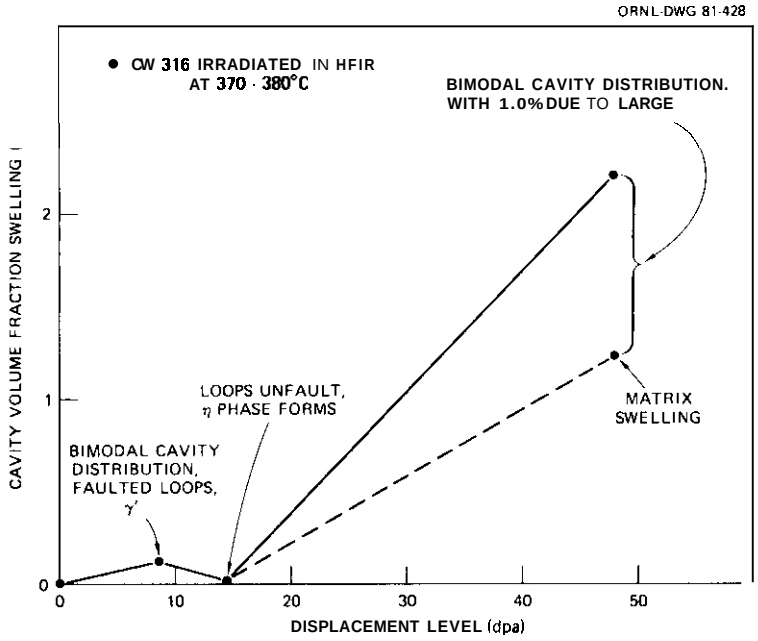

Fig. 3.2.8. Schematic Representation of Swelling as a Function of Fluence for 20% CW 316 Irradiated in HFIR at 375 to 380°C to Illustrate How Changes in Other Components of the Microstructure Correlate with the Cavity Swelling Behavior.

shows that matrix cavity size (smaller mode of the bimodal size distribution) is approximately constant (~2.5–2.75-nm diam) between 8.5 and 13 dpa while the large size mode (–7—7.5–nm diam) initially grow [Fig. 3.2.2(a)] and then shrink back to the average matrix size [Fig. 3.2.2(b)]. The total cavity concentration, Fig. 3.2.6, also remains about constant at these fluences. This disappearance of the bimodal size distribution is responsible for the reduced cavity volume fraction with increasing fluence. The larger cavities seen at 8.5 dpa may be voidlike. Their shrinkage apparently concides with a change in the interstitial sink structure, as network dislocations recover, Frank loops unfault, and fine gamma–prime (Ni_3Si type) precipitate dissolves and is replaced by much coarser eta phase (M_6C type). These changes could allow absorption of excess interstitials in the larger cavities. As fluence increases from 13 dpa to about 50 dpa, the cavity distribution is again bimodal, with large cavities (-100-nm diam) on the eta phase particles that formed at about 13 dpa. These large cavities contribute significantly to the total cavity swelling (Fig. 3.2.8).

At 475°C, cavity size decreases with increasing fluence from 10 to 16 dpa. At this temperature, however, Fig. 3.2.3(a) and (b) show that the cavity size distribution is quite uniform and narrow about the average size and that the size reduction with increasing fluence is also quite uniform. However, Fig. 3.2.6 shows that the cavity concentration continues to increase at these same fluences. Comparison of Fig. 3.2.3(b) and (c) indicates that the cavity size increases uniformly with increasing fluence above 16 dpa. The low fluence cavity shrinkage at 460 to 475°C appears to again correlate with changes in the precipitate component of the microstructure. In this case, some precipitate dissolution occurs between 10 and 16 dpa and readjustment to more Laves and less eta phase occurs at higher fluence.[7]

At 550 to 565°C, the cavity size distribution is narrow and the average diameter increases steadily with increasing fluence, before saturating at a diameter of about 21.5 nm above 15 dpa. The cavity concentration increases with fluence, with a small oscillation between 9 and 15 dpa. These trends can also be seen in Fig. 3.2.4.

Figures 3.2.6 and 3.2.7 give the fluence dependence of portions of the cavity microstructure. The microstructures are homogeneous and spacially uniform. The cavity size distributions are narrow, therefore the average diameter and diameter of the cavity of average volume are nearly equal. We can, therefore, construct total cvf swellings from interpolation of the microstructural components to give the fluence dependence of cvf swelling between 16 dpa and the highest fluence. This is analogous to the procedure whereby theoretical models evolve swelling results from cavity growth and nucleation considerations. The resulting total cvf swelling for CW 316 as a function of fluence is plotted for the various irradiation temperatures in Fig. 3.2.9.

The grain boundary cvf as a function of temperature at several fluences is shown in Fig. 3.2.10. This shows that total swelling is primarily due to matrix cavities below about 575°C. At higher fluence, for temperatures above 600°C, the grain-boundary cvf begins to contribute significantly. Figure 3.2.11 shows the grain-boundary microstructure as a function of fluence at 550 to 565°C.

An important feature of Fig. 3.2.9 is that despite initial transients and low fluence oscillations in the swelling at 375 to 380°C and 460 to 475°C, the swelling rate at all temperatures eventually approaches a steady state. At 550 to 575°C and 600 to 620°C the cvf swelling appears to increase monotonically over the entire fluence range. Another important feature seen in Fig. 3.2.9 is that the steady-state swelling rate is nearly temperature independent, being about 0.1%/dpa at 375 to 620°C with a minimum of about 0.07%/dpa at about 460 to 475°C. Several of the lower fluence swelling fluctuations and approach to steady-state swelling behavior were also observed in the earlier immersion density measurements of Grossbeck and Maziasz[3] on the same samples. The fluence plots in Fig. 3.2.9 are consistent with a minimum in the temperature dependence of the swelling at a given fluence, as shown in Fig. 3.2.1 and pointed out last quarter.[4]

Fluence Dependence of the Cavity Microstructure and Swelling for CW 316 + Ti. The immersion density changes, cavity statistics, and cvf swellings for CW 316 + Ti are given in Table 3.2.3. Total cvf swelling

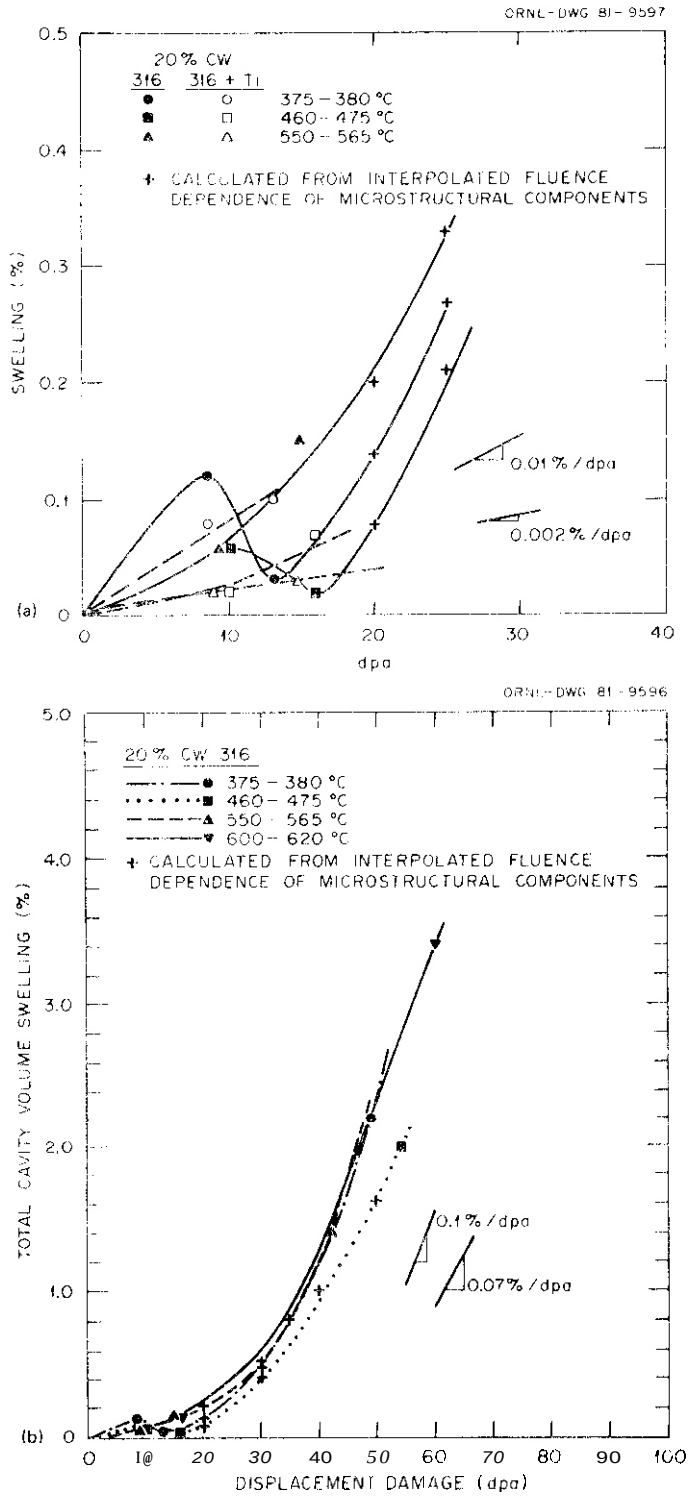

Fig. 3.2.9. Total Cavity Swelling as a Function of Fluence for Steels Irradiated in HFIR.

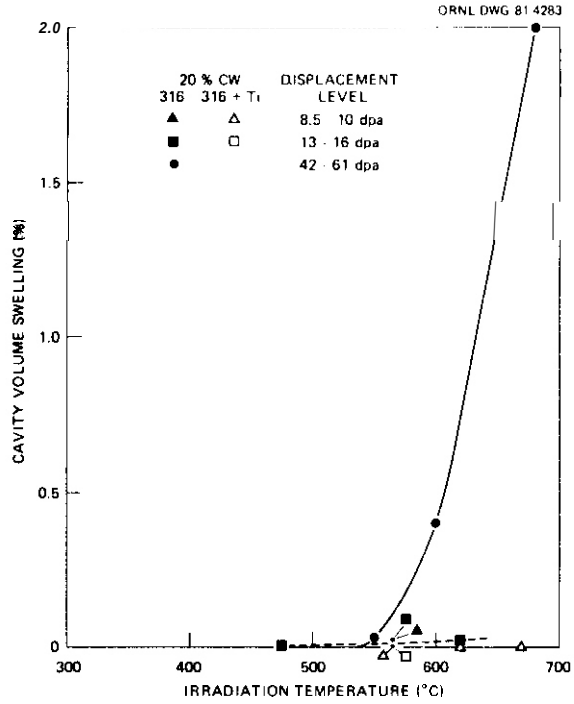

Fig. 3.2.10. Grain Boundary Component of Swelling as a Function of Temperature in HFIR.

and immersion density change as a function of temperature at the two general fluence levels examined are plotted in Fig. 3.2.12, with CW 316 irradiated to 7.7 to 10.8 dpa replotted for reference. Unlike the data on CW 316 shown in Fig. 3.2.1, the swelling curves for CW 316 + Ti are parallel for the two fluence ranges. The immersion density results also parallel the cvfs, and the offsets could reflect densification (and/or swelling) due to precipitation.

Micrographs in Figs. 3.2.13 to 3.2.15 show the evolution of the cavity microstructure with increasing fluence for HFIR irradiation at 375, 475, and 565°C, respectively. The average cavity diameter and cavity concentration from these micrographs are also given as functions of fluence in Figs. 3.2.7 and 3.2.6, respectively. Compared to CW 316, the cavities in CW 316 + Ti are quite fine (small size, high concentration) at all the temperatures observed. The differences in scale and uniformity of the cavity microstructures can be seen by comparing Figs. 3.2.13 to 3.2.15 for CW 316 + Ti with Figs. 3.2.2 to 3.2.4 for CW 316 and comparing the curves in Figs. 3.2.6 and 3.2.7. The cavity densities in CW 316 + Ti are a factor of 2 to 10 higher than in CW 316 irradiated at the same conditions.

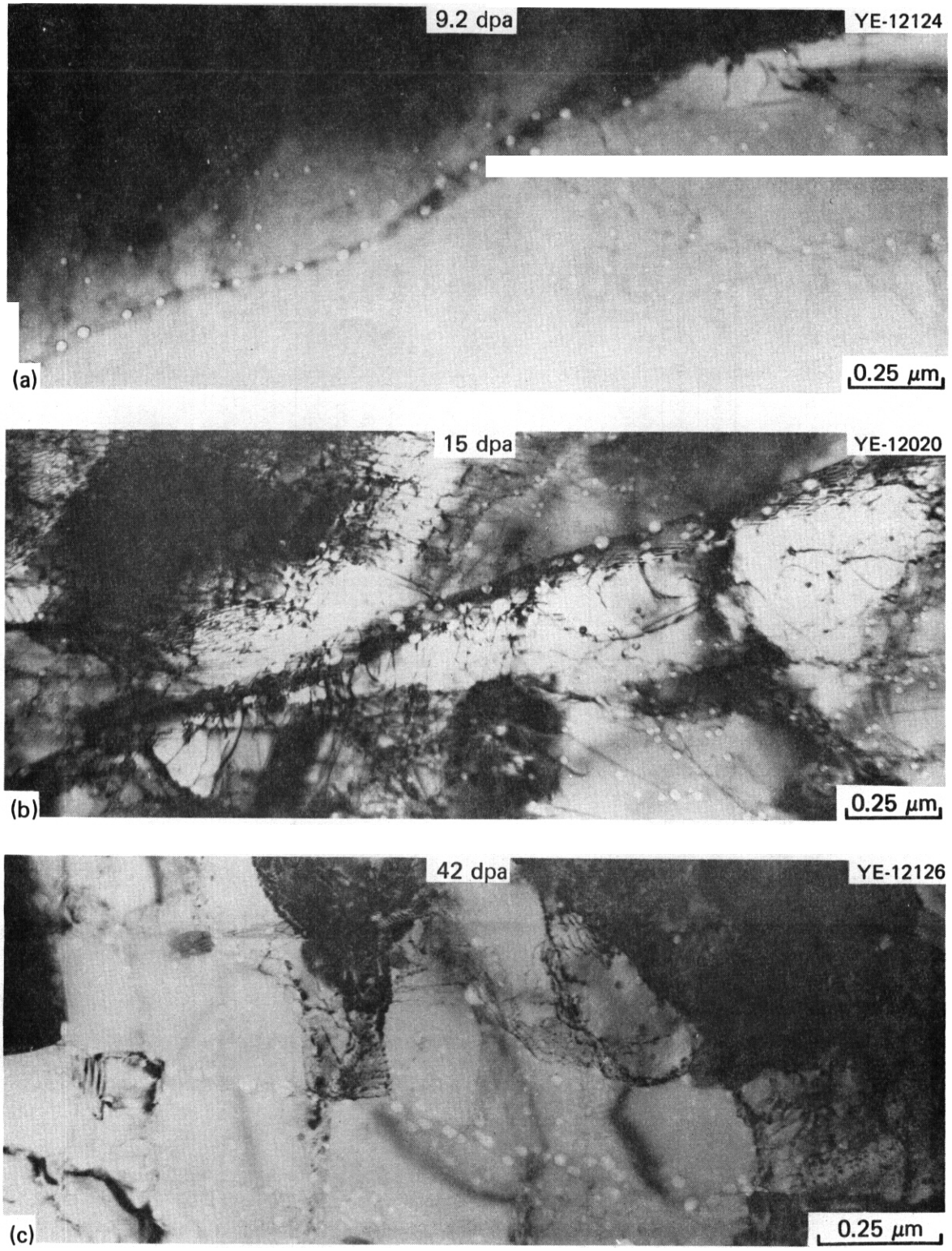

Fig. 3.2.11. Fluence Dependence of the Grain Boundary Microstructure of 20%CW 316 Irradiated in HFIR at 550 to 565°C to Fluences of (a) 9.2 dpa, (b) 15 dpa, and (c) 42 dpa.

Table 3.2.3. Swelling and Cavity Statistics for Cold-Worked Titanium Modified Type 316 Stainless Steel Irradiated in HFIR

Irradiation Conditions				Swelling from Immersion Density (%)	Cavity Parameters					
					Matrix Cavities			Grain-Boundary Cavities		Total Cavity Volume Fraction (%)
Temperature (°C)	Neutron Fluence, >0.1 MeV (neutrons/m^2)	Displacement Damage (dpa)	Helium (at. ppm)		Average Diameter (nm)	Concentration (cavities/m^3)	Volume Fraction (%)	Average Diameter (nm)	Volume Fraction (%)	
55	1.3	10.5	490			[a]	0		[a]	0
285	1.0	7.7	390	0.17	2.9	$\geq 7 \times 10^{23}$	0.36		[a]	0.36
375	1.1	8.5	380	−0.13	3.1	5.6×10^{22}	0.08		[c]	0.08
375	1.7	13.0	740	−0.06	2.2 13.0[b]	1×10^{23} 4×10^{20}	0.1		[a]	0.1
475	1.3	10.0	500	−0.14	2.2	3.0×10^{22}	0.02		[c]	0.02
475	2.1	16.0	1020	0.05	3.2	4×10^{22}	0.07		[c]	0.07
565	1.2	9.2	440	−0.14	3.7	5.0×10^{21}	0.02	16–18	>0.005	0.02
565	2.0	15.0	880	−0.04	5.4	2.7×10^{21}	0.03	16–18	>0.005	0.03
620	1.3	10.0	500	0.02	5.5	2.0×10^{21}	0.03	18–20	>0.005	0.03
670	1.3	10.0	500	0.18	22.5	1.7×10^{20}	0.09	~24	>0.005	0.09

[a] None detected.

[b] Bimodal size distribution.

[c] Grain boundary precipitation of eta (M_6C) phase.

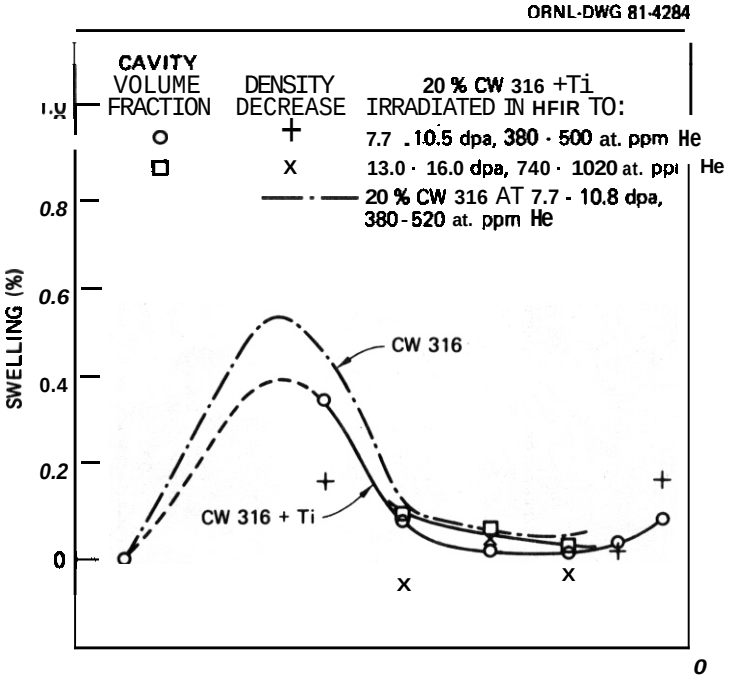

Temperature at

The cavity sizes for the two alloys are quite similar at 375 and 475°C, but at 565°C, the cavity diameter in CW 316 + Ti is a factor of 4 to 5 smaller than in CW 316. The cavity size in CW 316 + Ti does not show the sharp fluctuations with fluence that CW 316 shows at the same conditions. Unlike CW 316, there is nearly 100% association between the cavities observed and fine MC precipitate particles in CW 316 + Ti irradiated in HFIR at temperatures below 650°C. This is not apparent in the micrographs because imaging conditions were set for maximum cavity visibility and the fine precipitates are not visible. The MC-cavity association was shown clearly in micrographs from these same samples included in refs. 7 and 8. The cavities in the CW 316 + Ti appear to be strung along dislocations, but this is only because all fine MC particles in the CW 316 + Ti are also dispersed along the dislocations. These observations show that the basic mechanisms controlling swelling in WIR are different in each of these alloys. The decreased sensitivity of cavity size to irradiation temperature in the CW 316 + Ti is a direct consequence of the MC-helium trapping mechanism.[8]

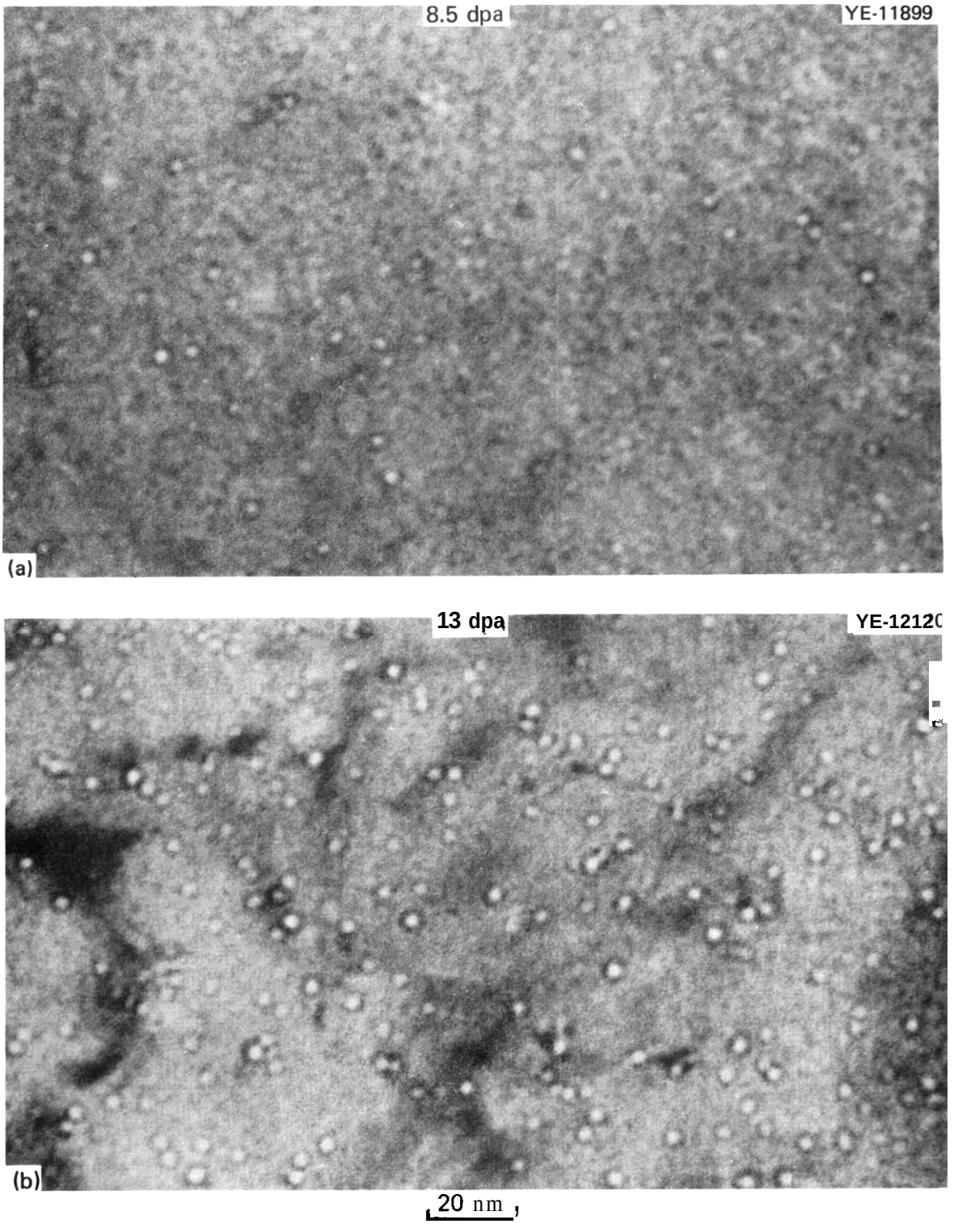

Fig. 3.2.13. Fluence Dependence of *20%* CW 316 + Ti Irradiated in HFIR at 375°C *to* Fluences of (a) 8.5 dpa and (b) 13 dpa.

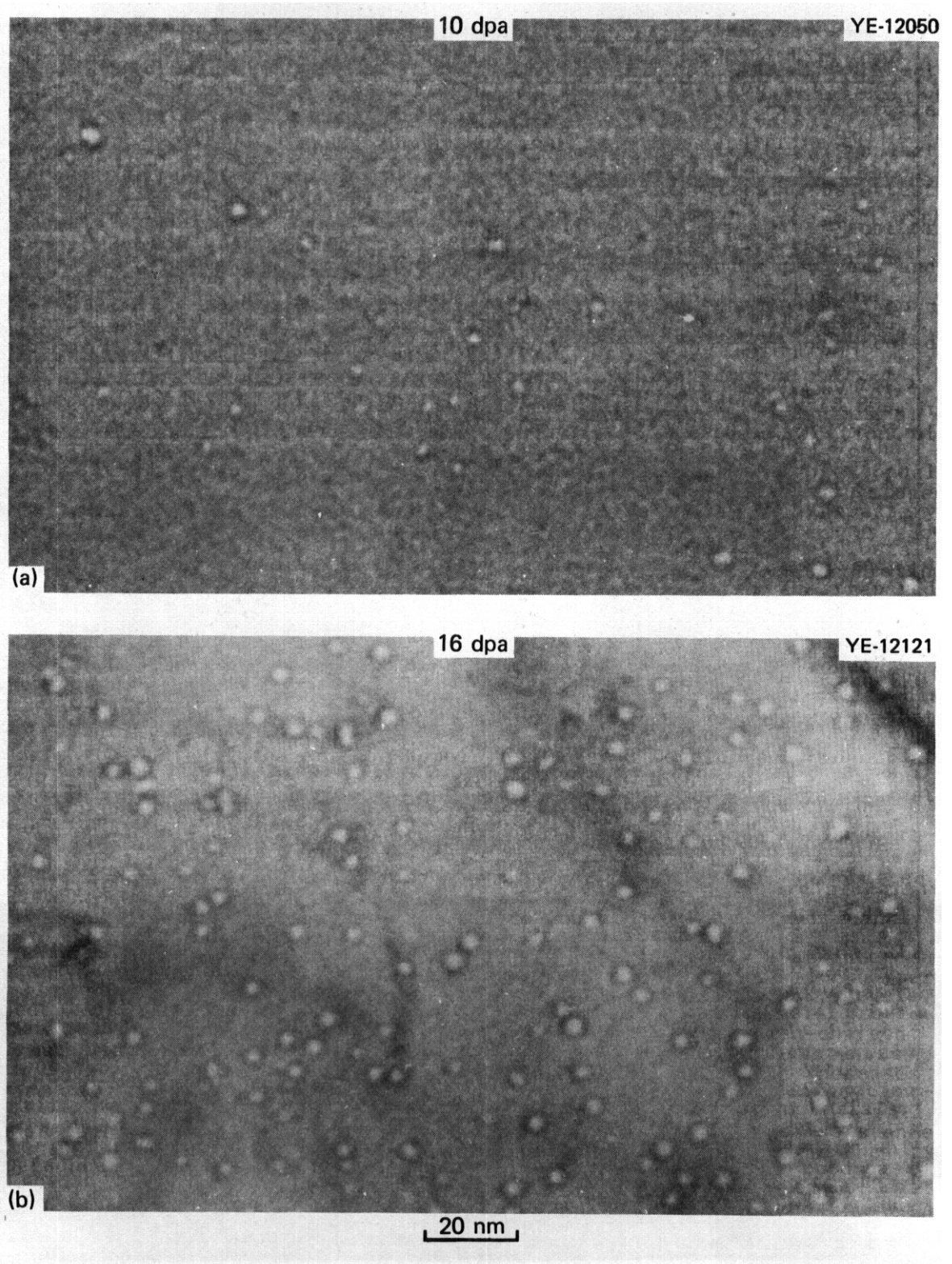

Fig. 3.2.14. Fluence Dependence of 20% CW 316 + Ti Irradiated in HFIR at 475°C to Fluences of (a) 10 dpa and (b) 16 dpa.

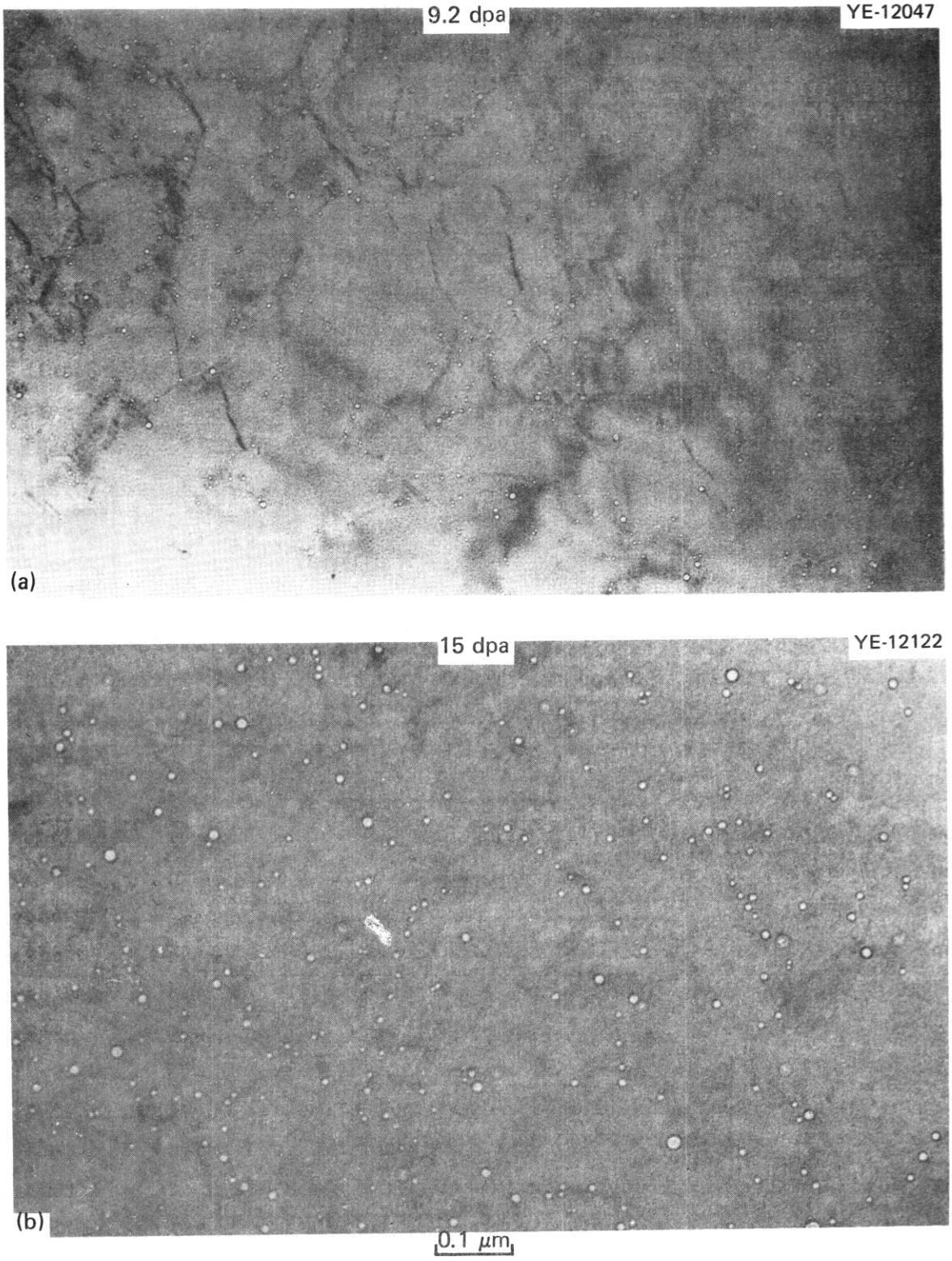

Fig. 3.2.15. Fluence Dependence of 20% CW 316 + Ti **Irradiated in HFIR at 565°C to Fluences** of **(a) 9.2 dpa and (b) 15 dpa.**

The total cvf swelling for the CW 316 + Ti is shown as a function of fluence in Fig. 3.2.9 for comparison with CW 316 at the same low fluences. Whereas the swelling in CW 316 shows considerable fluctuation at these fluences, the CW 316 + Ti swelling is much more regular. Even though these are moderate fluence levels, this behavior is consistent with both the fine-scale microstructures observed in Figs. 3.2.13 through 3.2.15 and the understanding of MC-helium trapping. The swelling curves for CW 316 + Ti show an inverse temperature dependence, with the lowest swelling observed at the highest temperature of 565°C. The slopes for these portions of the swelling curves for CW 316 + Ti indicate low swelling rates, ranging from 0.002%/dpa at 565°C to 0.008%/dpa at 375°C, as clearly shown in Fig. 3.2.9. These are between a factor of 10 to 40 less than the steady swelling rates for CW 316.

Finally, consider the grain-boundary behavior of the CW 316 + Ti during HFIR irradiation. Figure 3.2.16 shows the grain-boundary cavity structure as a function of fluence for CW 316 + Ti irradiated at 565°C. The grain-boundary cavities are considerably smaller in Fig. 3.2.16 than for CW 316 irradiated at the same conditions and shown in Fig. 3.2.11. Comparison of Tables 3.2.2 and 3.2.3 gives the comparative data. The cavity size is about a factor of 2 smaller in the CW 316 + Ti than in CW 316 and hence the grain-boundary cvf contributions to total cavity swelling is very small, less than 0.005%, at all conditions observed. (See also Fig. 3.2.10.) Just as with the complex precipitation-swelling behavior shown in Fig. 3.2.8 for CW 316, the grain-boundary behavior of CW 316 + Ti and its comparison with CW 316 cannot be completely divorced from precipitation phenomenon, particularly at 475°C. Figure 3.2.17 compares the fluence dependence of grain-boundary microstructure in both alloys irradiated in HFIR at 475°C. In CW 316, the partial eta-phase dissolution coincides with covering more of the grain-boundary area with a fine dispersion of helium bubbles. By comparison, the grain-boundary eta-phase in the CW 316 + Ti persists at the same irradiation conditions.

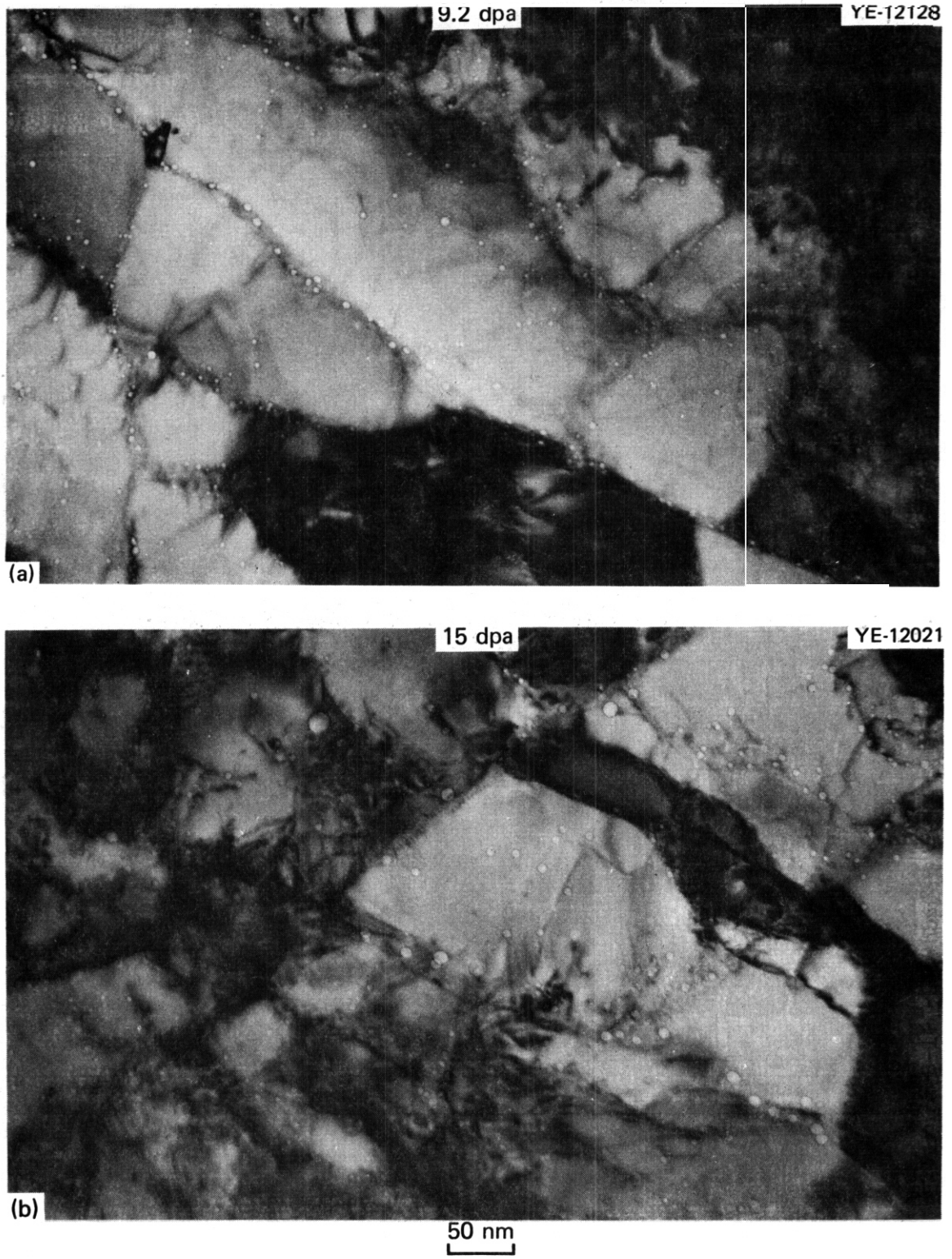

Fig. 3.2.16. Fluence Dependence *of* the Grain Boundary Microstructure of 20% CW 316 + Ti Irradiated in HFIR at 565°C to Fluences of (a) 9.2 dpa and (b) 15 dpa.

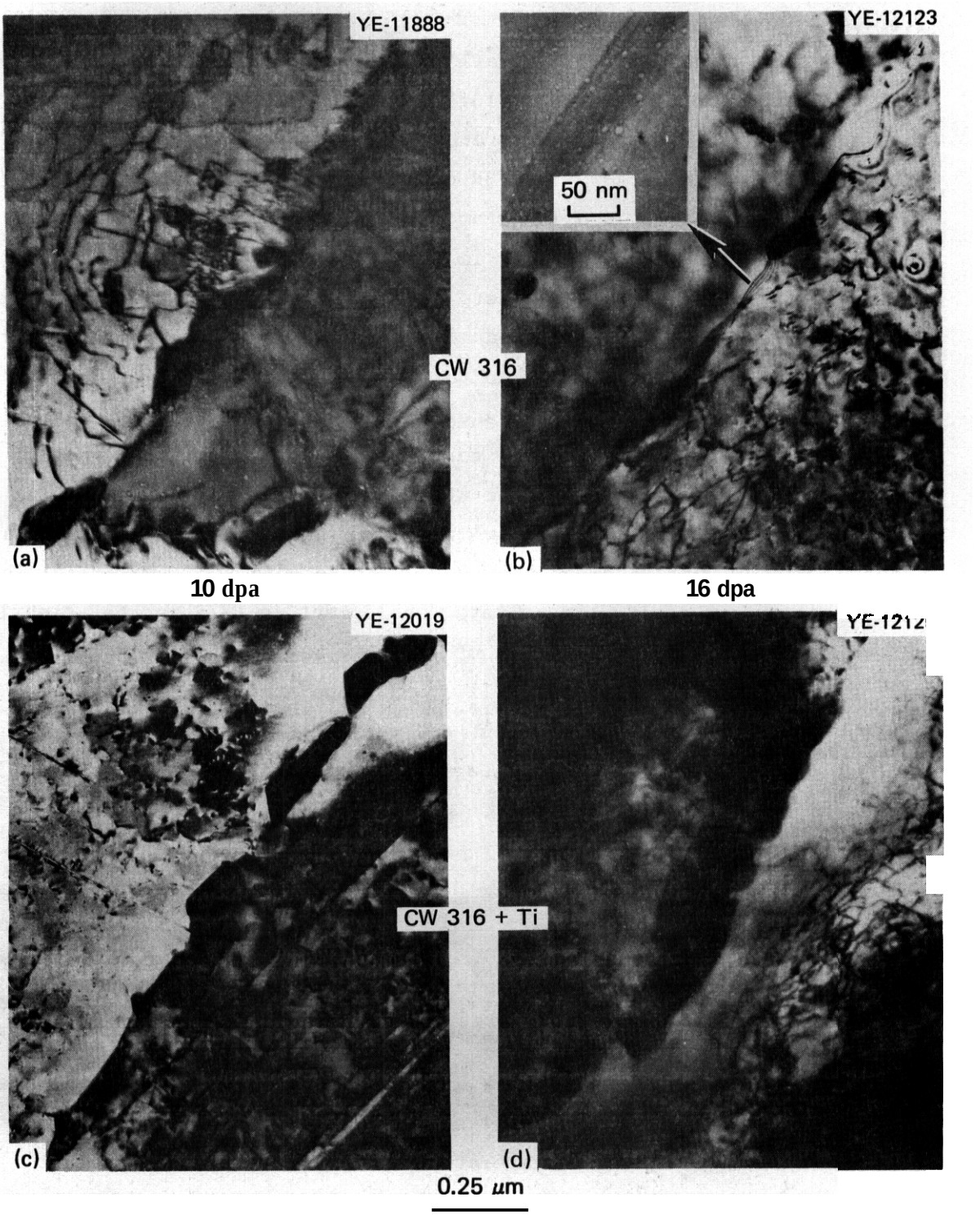

Fig. 3.2.17. Fluence Dependence of Grain Boundary Microstructure in 20%CW 316 and 316 + Ti after HFIR Irradiation at 475°C. (a) CW 316, 10 dpa, (b) CW 316, 16 dpa, (c) CW 316 + Ti, 10 dpa, and (d) CW 316 + Ti, 16 dpa.

3.2.4.4 Discussion

The data presented show an early development of cavity and precipitate microstructures in both CW 316 and CW 316 + Ti during HFIR irradiation as compared to the fast breeder reactor (FBR) irradiation, where little helium is produced. The FBR data[9-11] are quite sparse for CW 316 + Ti, but there is a large amount of FBR data on the particular heat of CW 316 (DO heat) examined in this work and other heats of type 316 stainless steel as well.[10,11] There are, of course, heat-to-heat variations in the fast breeder reactor swelling behavior of CW 316, and silicon is an important element in this variation. The DO heat of type 316 stainless steel has a higher than average initial silicon concentration (0.8 wt % compared to the normal 0.4-0.5 wt %). The DO heat, however, appears typical of higher silicon heats of type 316 stainless steel. As a result it has a somewhat longer incubation fluence in a fast breeder reactor until the onset of steady-state void swelling.[10,11] The early, concurrent cavity-precipitate development in HFIR is thus clearly an effect of helium. Irradiation of the same material in the same microstructural condition in EBR-II, to 8.4 dpa at 500°C, produced no cavity or helium bubble development and very little precipitation.[7,12] Incubation periods for steady-state void swelling in EBR-II are about 30 to 40 dpa in a variety of heats of CW 316 irradiated at 350 to 650°C (ref. 11). It appears that cavity and precipitate formation do not require long incubation periods in HFIR and that a transition to a steady-state rate of swelling in HFIR occurs at fluences that correspond to incubation doses in EBR-II. The steady-state swelling rate in HFIR is quite unusual in both its low-temperature sensitivity and low value of 0.1%/dpa in the temperature range 376 to 620°C. However, high swelling rates have been measured for isolated data points at irradiation temperatures above and below this temperature range. In contrast, the steady-state swelling rate is a strongly temperature-sensitive parameter for fast breeder reactor irradiation and normally reaches a maximum at about 0.5%/dpa at the peak swelling temperature of 525 to 575°C. Brager and Garner[13,14] show that the void swelling peak in EBR-II, between 500 and 600°C, is intimately connected with precipitation of eta, tau, and Laves

phases. Clearly, the nature of the swelling (bubbles in HFIR rather than voids, this work and particularly ref. 4) and the precipitation phenomena that correlate with and affect or control swelling in HFIR are different than in EBR-II. The differences reflect the helium effect on microstructural development in HFIR. Some mechanistic interpretations of this role of helium have been suggested by Maziasz et al.[6] The grain-boundary cavity and swelling behavior in HFIR is another helium effect that does not occur during fast breeder reactor irradiation.

The swelling behavior of the CW 316 + Ti differs from CW 316, with less fluctuations in swelling with fluence and generally lower swelling rates. There is also less phase instability in the CW 316 + Ti than in the CW 316 irradiated in HFIR (ref. 7). Although the data do not extend beyond 16 dpa, the microstructure of CW 316 + Ti irradiated at 565°C is a good indication of the beneficial behavior of cavity refinement and interfacial helium trapping achieved by the finely dispersed MC particles distributed along the dislocation network. The grain boundaries of CW 316 + Ti are also more resistant to cavity growth than the boundaries of CW 316.

The same beneficial effects of helium trapping at titanium-rich MC precipitates are expected to prevail in the Path A Prime Candidate Alloy (PCA). Microstructures have been designed to test this alloy during HFIR irradiation.[15]

3.2.5 Conclusions

1. Cold-worked type 316 stainless steel irradiated in HFIR shows considerable fluence dependence in total cavity volume fraction swelling at 375 to 380°C and 460 to 475°C at fluences as low as 8.5 dpa. At both these temperatures, swelling initially increases, then decreases, and finally increases monotonically with increasing fluence. The fluctuations are related to changes in the dislocation and precipitation components of the microstructure. At 550 to 565°C and 600 to 620°C the swelling increases monotonically over the fluence range.

2. Cavity concentration appears to saturate with increasing fluence in CW 316 at 375 to 380°C, and cavity size appears to saturate with

fluenre at 550 to 565°C. Grain-boundary-cavity size increases with inrreasing temperature above 475°C, but does not contribute significantly to total cvf swelling until higher fluenres at irradiation temperatures above 600°C.

3. After initial flurtuations in total cvf swelling as a function of fluence, the swelling rate reaches a steady state at fluences above about 25 to 30 dpa and temperatures in the range 375 to 620°C. Within this range the swelling rate is fairly temperature insensitive at a value of about 0.1%/dpa, with a minimum of about 0.07%/dpa at around 475°C.

4. For irradiation temperatures of 375 to 565°C, and fluences producing less than 16 dpa, CW 316 + Ti shows much steadier fluence dependence for the total cvf swelling than does CW 316. The cavity conrentrations in CW 316 + Ti are between 2 and 10 times greater than in CW 316. At 375 and 475°C the cavity sizes are similar in the two alloys, but at 565°C are 4 to 5 times smaller in CW 316 + Ti than in CW 316. The grain-boundary cavity size is about a factor of 2 smaller in CW 316 + Ti than in CW 316 at 565°C and above.

5. The microstructural differences between CW 316 + Ti and CW 316 result in earlier attainment of steady-state swelling and significantly lower swelling rates in CW 316 + Ti. The swelling rates in CW 316 + Ti range from 0.008%/dpa at 375°C to 0.002%/dpa at 565°C. a factor of 10 to 40 less than CW 316 at fluences below about 20 dpa. Probably the largest single reason for the differences in microstructural development in the two alloys is the influence of MC-helium trapping and dislocation pinning in the CW 316 + Ti.

3.2.6 Future Work

The dislocation and precipitate components of the microstructure for these same samples will be presented in future reports. The various microstructural components will be correlated to begin to understand the mechanisms responsible for microstructural development. These microstructures will then be correlated with mechanical properties data generated from these same samples.

3.2.7 References

1. M. L. Grossbeck and P. J. Maziasz, "Tensile Properties of HFIR-Irradiated Types 316 and TiM 316 Stainless Steel at 200 to 1000 at. ppm He," *ADIP Quart. Prog. Rep. Sept. 30, 1978,* DOE/ET-0058/3, pp. 32–49.
2. M, L. Grossbeck and P. J. Maziasz, "Tensile Properties of Type 316 Stainless Steel Irradiated in a Simulated Fusion Reactor Environment," *J. Nucl. Mater.* 85&86: 883–87 (1979).
3. M. L. Grossbeck and P. J. Maziasz, "The Swelling of 20%–Cold–Worked Type 316 Stainless Steel Irradiated in HFIR to Helium Levels of 200–3700 at. ppm," *ADIP Quart. Prog. Rep. January–March, 1978,* DOE/ET-0058/1, pp. 82-85.
4. P. J. Maziasz and M. L. Grossbeck, "Swelling and Microstructure of HFIR–Irradiated 20%–Cold–Worked Types 316 Stainless Steel and 316 + 0.23 wt % Ti," *ADIP Quart. Prog. Rep. Dec. 31, 1980,* DOE/ER-0045/5, pp. 43-69.
5. P. J. Maziasz, M. L. Grossbeck, and F. W. Wiffen, "The Microstructure and Mechanical Properties of 20%-Cold-Worked Types 316 Stainless Steel and 316 + 0.23 wt % Ti After HFIR Irradiation at 55 to 375°C," *ADIP Quart. Prog. Rep. June 30, 1980,* DOE/ER-0045/3, pp. 48-74.
6. P. J. Maziasz, F. W. Wiffen, and E. E. Bloom, "Swelling and Micro–structural Changes in Type 316 Stainless Steel Irradiated Under Simulated CTR Conditions," pp. 259–88 in *Radiation Effects and Tritium Technology for Fusion Reactors*, CONF–750989, vol. I (March 1976).
7. P. J. Maziasz, J. A. Horak, and B. L. Cox, "The Influence of Both Helium and Neutron Irradiation on Precipitation in 20%-Cold-Worked Austenitic Stainless Steels," to be published in *Proceedings of Symposium on Irmdiation Effects on Phase Stability,* eds. J. R. Holland, L. K. Mansur, and D. I. Potter, IMS–AIME, 1981.
8. P. J. Maziasz, "Helium Trapping at Ti–Rich MC Particles in Ti–Modified Austenitic Stainless Steels," to be published in *Proceedings of Symposium on Irmdiation Effects on Phase Stability,* eds., J. R. Holland, L. K. Mansur, and D. I. Potter, TMS–AIME, 1981.

9. E. E. Bloom, J. M. Leitnaker, and J. O. Stiegler, "Effect of Neutron Irradiation on the Microstructure and Properties of Titanium-Stabilized Type 316 Stainless Steels," *Nucl. Technol.* 31: 232–43 (1976).

10. W. K. Appleby, E. E. Bloom, J. E. Flinn, and F. A. Garner, "Swelling in Neutron Irradiated 300-Series Stainless Steels," pp. 509-28 in *Radiation Effects a Breeder Reactor Structuml Materials,* eds., M. L. Bleiburg and J. W. Bennett, TMS-AIME, Metallurgical Soriety of AIME, New York (1977).

11. G. R. Odette, "Modeling of Mirrostrurtural Evolution Under Irradiation," *J. Nucl. Mater.* 85&86: 533–45 (1979).

12. P. J. Maziasz, B. L. Cox, and J. A. Horak, "The Effert of Preinjected Helium on the Mirrostrurture and Tensile Properties of EBR-II-Irradiated 20%-Cold-Worked Type 316 Stainless Steel," *ADIP Quart. Prog. Rep. Mar. 31, 1980.* DOE/ER-0045/2, pp. 35–57.

13. H. R. Brager and F. A. Garner, "Swelling as a Consequenre of Gamma Prime (γ') and $M_{23}(C,Si)_6$ Formation in Neutron Irradiated 316 Stainless Steel," *J. NucZ. Mater.* 73: 9–19 (1979).

14. H. R. Brager and F. A. Garner, "Dependence of Void Formation on Phase Stability in Neutron-Irradiated Type 316 Stainless Steel," pp. 207–32 in *Effects of Radiation a Structural Materials, ASTM Spec. Tech. Pubt.* 683, eds., J. A. Sprague and D. Kramer, American Society for Testing Materials, Philadelphia, 1979.

15. P. J. Maziasz and T. K. Roche, "Design and Fabrication of Preirradiation Microstrurtures in Path A Prime Candidate Alloy," *ADIP Quart. Prog. Rep. Dec. 31, 1980,* DOE/ER-0045/5, pp. 25–42.

3.3 MICROSTRUCTURAL DEVELOPMENT IN 20%-COLD-WORKED TYPES **316** AND **316 + Ti** STAINLESS STEELS IRRADIATED IN HFIR: TEMPERATURE AND FLUENCE DEPENDENCE OF THE DISLOCATION COMPONENT — P. J. Maziasz (Oak Ridge National Laboratory)

To be reported in the next quarterly report.

3.4 TENSILE PROPERTIES AND SWELLING OF 20%-COLD-WORKED TYPE 316 STAINLESS STEEL IRRADIATED IN HFIR – R. L. Klueh and M. L. Grossberk (Oak Ridge National Laboratory)

3.4.1 ADIP Tasks

ADIP Task I.B.13, Tensile Properties of Austenitir Alloys, and I.C.2, Mirrostrurture and Swelling in Austenitic Alloys.

3.4.2 Objective

The primary goal of this series of experiments (HFIR-CTR-26 through -29) is to expand the mechanical property, microstructure, and swelling data base on irradiated 20%-cold-worked type 316 stainless steel. Previous irradiation experiments (HFIR-CTR-9 through -13) provided an initial, lower fluence data base for an understanding of the behavior of the material. Earlier experiments HFIR-SS-2 through -8 had also provided high-fluence data. However, the previous work was on specimens from an experimental heat of steel. In the present experiment series, the MFE reference heat of type 316 stainless steel (heat X15893) was used. Sufficient overlap with previous irradiation conditions should enable a correlation to be made between the irradiation response of the two heats of steel.

3.4.3 Summary

Immersion density and elevated-temperature tensile properties were determined on 20%-cold-worked type 316 stainless steel irradiated at approximately 285, 370, 470, 560, and 620°C. Irradiation was to fluences up to 3.9×10^{26} neutrons/m^2 (>0.1 MeV); this fluenre resulted in displacement damage levels up to 29 dpa and helium concentrations up to 1900 at. ppm. Tensile tests were at temperatures near the irradiation temperatures (300, 350, 450, 575, and 600°C).

Immersion density results indicated that swelling increased with inrreasing irradiation temperature. A maximum swelling of 1.2% was observed after the 620°C irradiation. Irradiation at the lowest temperature (284°C) increased the strength. At 370°C the strength went through a maximum with increasing neutron fluenre. At the higher

irradiation temperatures (470, 575, and 620°C) the strength decreased with increasing fluence. Ductility (both total and uniform elongation) generally reflected the strength behavior: an increase in strength resulted in a decrease in ductility. The large decrease in ductility at 575°C that was noted in a previous experiment was not found in the present work.

3.4.4 Progress and Status

3.4.4.1 Introduction

The first wall of a fusion reactor will be subjected to high-energy neutron irradiation, which will result in atom displacement damage and the production of helium in transmutation reactions. Because of this high helium production rate, the properties determined on materials irradiated in fission reactors may not be directly applicable to fusion reactors. However, for nickel-containing alloys irradiated in a mixed-spectrum fission reactor such as HFIR, transmutation of ^{58}Ni by thermal neutrons can give helium generation rates approximating those projected for fusion reactor service. At the same time, the fast neutrons produce displacement damage at relevant rates. Previous studies conducted on an experimental heat of type 316 stainless steel have shown that the helium generated during HFIR irradiation has a significant effect on the swelling, microstructural response, strength and ductility of 20%-cold-worked type 316 stainless steel.[1,2] Irradiations achieved damage levels of 2 to 6 dpa with helium concentrations of 16 to 50 at. ppm (ref. 2), up to 60 dpa with helium concentrations up to 4200 at. ppm (ref. 2), and 5 to 16 dpa and 200 to 1000 at. ppm He (ref. 1).

In the results presented in this report, the MFE reference heat (X15893) was irradiated in experiment HFIR-CTR-26 to a maximum fluence of 3.9 x 10^{26} neutrons/m^2 (>0.1 MeV). This exposure resulted in a maximum displacement damage level of 29 dpa and about 1900 at. ppm He. Irradiation temperatures ranged from 284 to 620°C. This experiment is one of a series of four irradiation experiments, HFIR-CTR-26 through -29. HFIR-CTR-28 is a duplicate of -26. Experiments HFIR-CTR-27 and -29 will be irradiated to 6.5 x 10^{26} neutrons/m^2 (>0.1 MeV) to give a maximum of

49 dpa and 3200 at. ppm He. The results from these experiments will be combined with results from previous irradiation experiments[1,2] to assess the effect of irradiation over the range 0 to 60 dpa and 0 to 4200 at. ppm He on the microstructural response, swelling, tensile properties, and fracture characteristics of 20%-cold-worked type 316 stainless steel.

3.4.4.2 Experimental Procedure

Tensile specimens with a 2.03-mm-diam by 18.3-mm-long reduced section (Fig. 3.4.1) were fabricated from 20%-cold-worked type 316 stainless steel. The chemical composition of the MFE reference heat (X15893), which was supplied by the vendor, is

Element	Wt %	Element	Wt %	wt ppm
Cr	17.28	Nb	<0.05	
Mn	1.70	Ta	<0.05	
Ni	12.44	Ti	<0.05	
Mo	2.10	B		4
co	0.3	C		613
cu	0.3	S		179
Si	0.67	P	0.037	

Before specimen fabrication the stainless steel rod was annealed 1 h at 1150°C, then swaged to obtain the proper diameter prior to the final cold work. The rod was annealed 1 h at 1050°C and swaged to a 20% reduction of area to obtain the cold-worked material from which the specimens were machined.

The specimens in the HFIR-CTR irradiation experiments are contained in a 0.62-m-long aluminum tube that is surrounded by a shroud to provide a high coolant velocity. Eleven specimens were arranged along the capsule axis with each specimen surrounded by an aluminum holder. Each holder was sized to maintain the specimen gage section at the specified temperature. The temperature is determined by the thickness of a helium-filled gap between the specimen and holder, which provides resistance to the radial flow of heat produced in the specimen by nuclear heating. The details on the design of this holder have been published.[3]

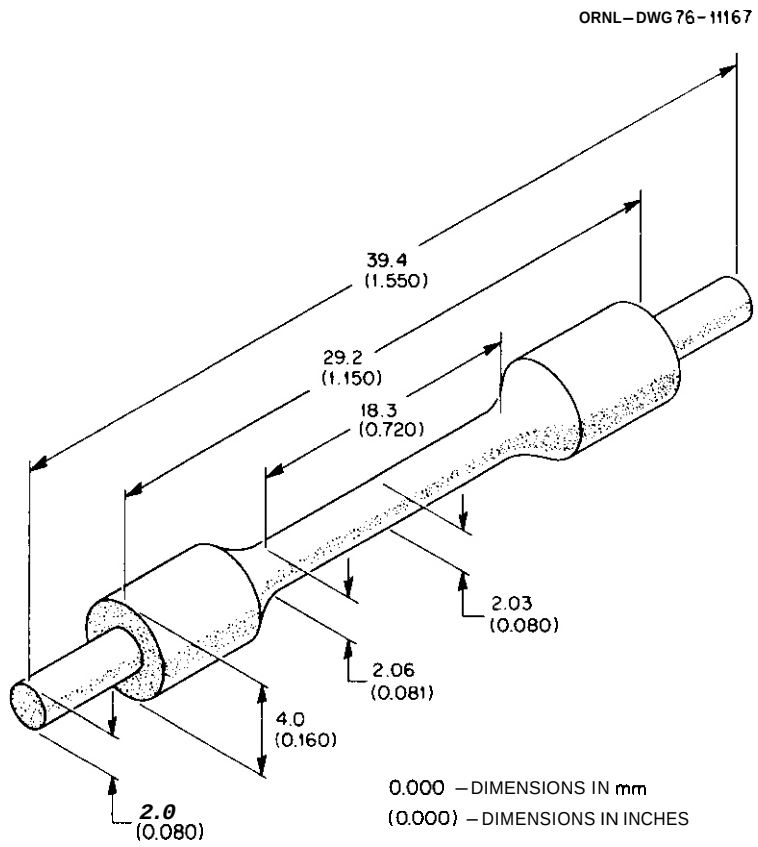

Fig. 3.4.1. Tensile Specimen Used for HFIR-CTR Irradiation Experiments.

The experiment was irradiated in a HFIR peripheral target position with a peak thermal neutron flux of 2.5 x 10^{19} neutrons/(m^2·s) and fast flux of 1.3 x 10^{19} neutrons/(m^2·s) 00.1 MeV). Irradiation temperatures were approximately 284, 370, 470, 560, and 620°C. The displacement damage and helium production were calculated by the procedures described by Gabriel, Bishop, and Wiffen.' Fluences ranged from 2.1 to 3.9 x 10^{26} neutrons/m^2 (>0.1 MeV), displacement damage levels from 16 to 29 dpa, and helium concentrations from 900 to 1900 at. ppm.

Immersion density measurements in Fluorinert-43 were made to determine any swelling produced by the irradiation. Tensile tests were conducted in a vacuum chamber on a 44-kN capacity Instron universal testing machine using a nominal strain rate of 4.6 x 10^{-5}/s (0.85 μm/s crosshead speed). Test temperatures were selected to be close to the calculated irradiation temperatures; tests were at 300, 350, 450, 575, and 600°C.

3.4.4.3 Results and Discussion

The immersion density results showed measurable swelling at all but the lowest irradiation temperature (Table *3.4.1).* The swelling increased with temperature, with a maximum measured swelling of *1.2%* for irradiation at 620°C. It was not possible to separate any fluence dependence within this limited fluence range. When the results are compared with previously obtained results,[5,6] the agreement is as expected (Fig. *3.4.2).* The results from this study fall below swelling for 20%-cold-worked type *316* stainless steel irradiated in HFIR to higher fluences[5] (42–61 dpa, 3000–4200 at. ppm He vs *16–29* dpa, *900–1900* at. ppm He for the present study), but the swelling is above the immersion density data[6] from material irradiated in EBR-II, where the irradiation produced approximately *15* at. ppm He and displacement damage of *31* to *37* dpa. Note, however, that the previous results were determined by different techniques than those of the present study, where only immersion density measurements are available at this time.

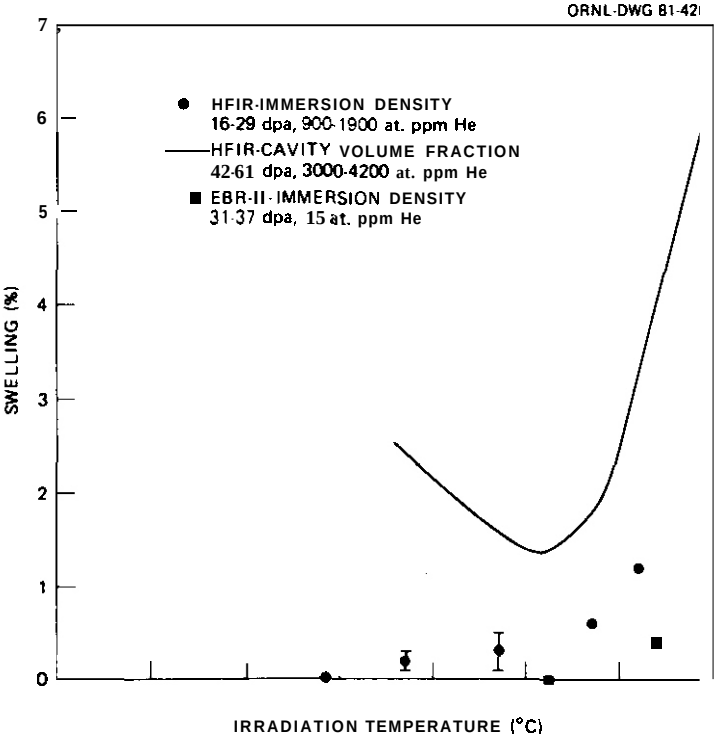

Fig. *3.4.2.* Swelling as a Function of Irradiation Temperature for 20%-Cold-Worked Type *316* Stainless Steel.

Table 3.4.1 Swelling Behavior and Tensile Properties of HFIR-Irradiated 20%-Cold-Worked Type 316 Stainless Steel

Temperature, °C		Fluence[b] >0.1 MeV (neutrons/m^2)	Displacement Damage (dpa)	Helium Content[c] (at. ppm)	Strength, MPa		Elongation,[e] %		Swelling[f] (%)
Test	Irradiation[a]				Yield[d]	Ultimate	Uniform	Total	
300		0			722	746	1.2	7.9	
300	284	2.1×10^{26}	16	887	1032	1093	0.7	6.0	0.0
350		0			689	713	1.7	7.6	
350		0			682	710	1.2	6.7	
350	370	2.1	16	903	901	951	2.1	6.3	0.1
350	370	3.1	24	1483	790	888	4.8	7.8	0.3
350	370	3.1	23	1464	794	894	6.6	9.9	0.2
450		0			672	726	5.1	10.4	
450		0			679	725	4.2	8.5	
450	470	2.6	20	1200	482	625	5.9	7.4	0.3
450	470	2.6	20	1204	519	682	8.6	10.7	0.2
450	470	3.8	29	1845	453	626	10.3	12.2	0.5
450	470	3.8	29	1841	444	620	9.9	11.9	0.4
575		0			628	708	6.7	11.8	
575	560	3.5	27	1700	323	524	7.4	9.7	0.6
575	560	3.5	27	1690	331	542	7.9	9.5	0.6
600		0			620	693	6.4	11.7	
600	620	3.9	29	1895	303	491	8.8	10.0	1.2

[a]Irradiation temperatures are calculated, ±50°C.

[b]Calculated from dosimetry of previous experiments.

[c]Calculated from empirical relationship.

[d]0.2% offset.

[e]Based on an 18.3-mm gage length.

[f]Immersion density values.

Tensile test results are tabulated in Table 3.4.1. In Fig. 3.4.3 the 0.2%-offset yield strength is plotted as a function of fluence (and displacement damage) at the test temperatures of 350, 450, and 575°C. Because of the relatively few data, straight lines or simple smoothed curves were drawn through the points to show trends. Also shown in Fig. 3.4.3 are the data of Grossbeck and Maziasz[1] for tests at comparable fluences. At 350°C the yield strength first increases, then decreases with fluence, while at the two higher temperatures there is a continuous

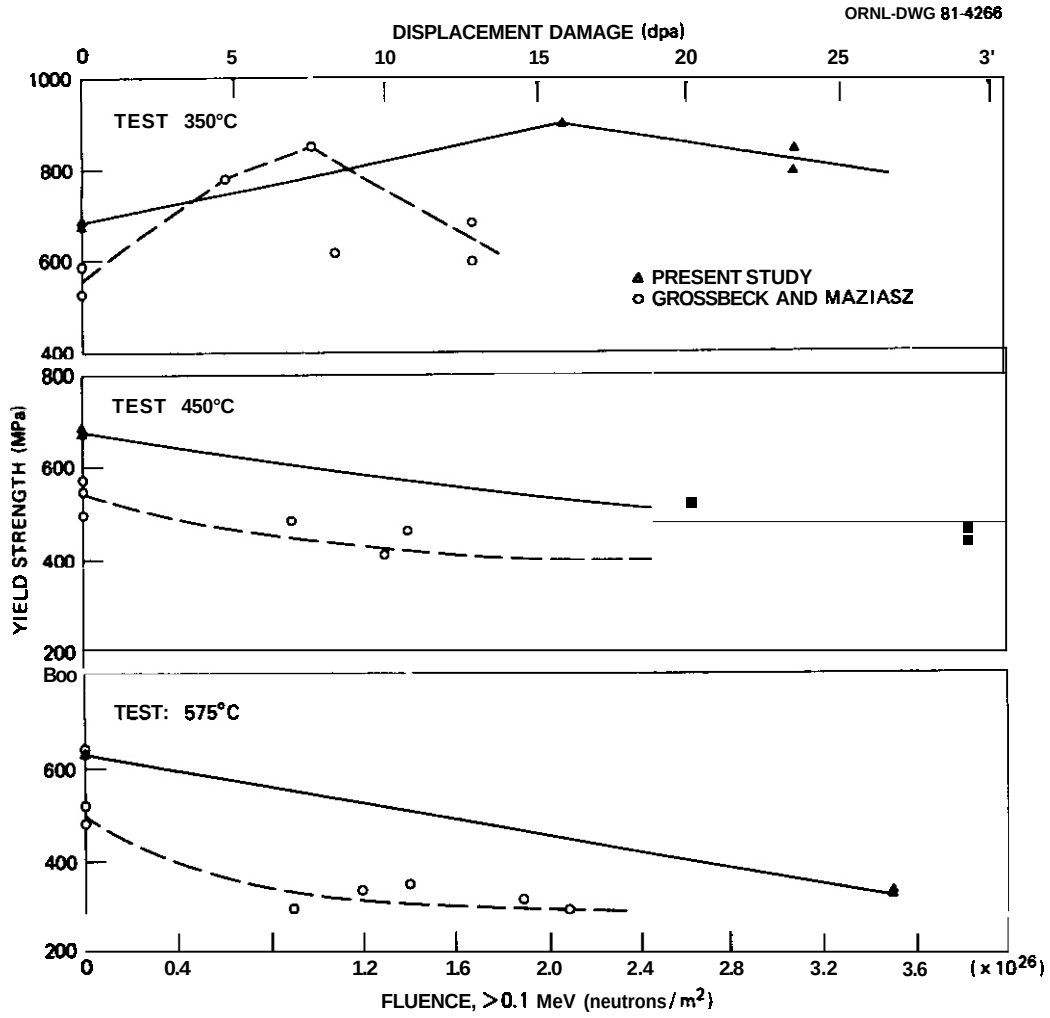

Fig. 3.4.3. The 0.2%-Offset Yield Strength as a Function of Fluence (>0.1 MeV) for Irradiated 20%-Cold-Worked Type 316 Stainless Steel for Test Temperatures of 350, 450, and 575°C. Values of displacement damage are also given. Irradiation temperatures were near tensile test temperatures, and are given in Table 3.4.1.

decrease in strength with increasing fluence. Although not shown, the ultimate tensile strength data show trends similar to the yield strength (Table *3.4.1).* The data trends for the strengths are in agreement with those of Grossbeck and Maziasz on another heat of steel.]

The total elongation as a function of fluence OK displacement damage (Fig. *3.4.4)* is generally the inverse of the strength results (i.e., an increase in strength results in a decrease in ductility and vice versa).

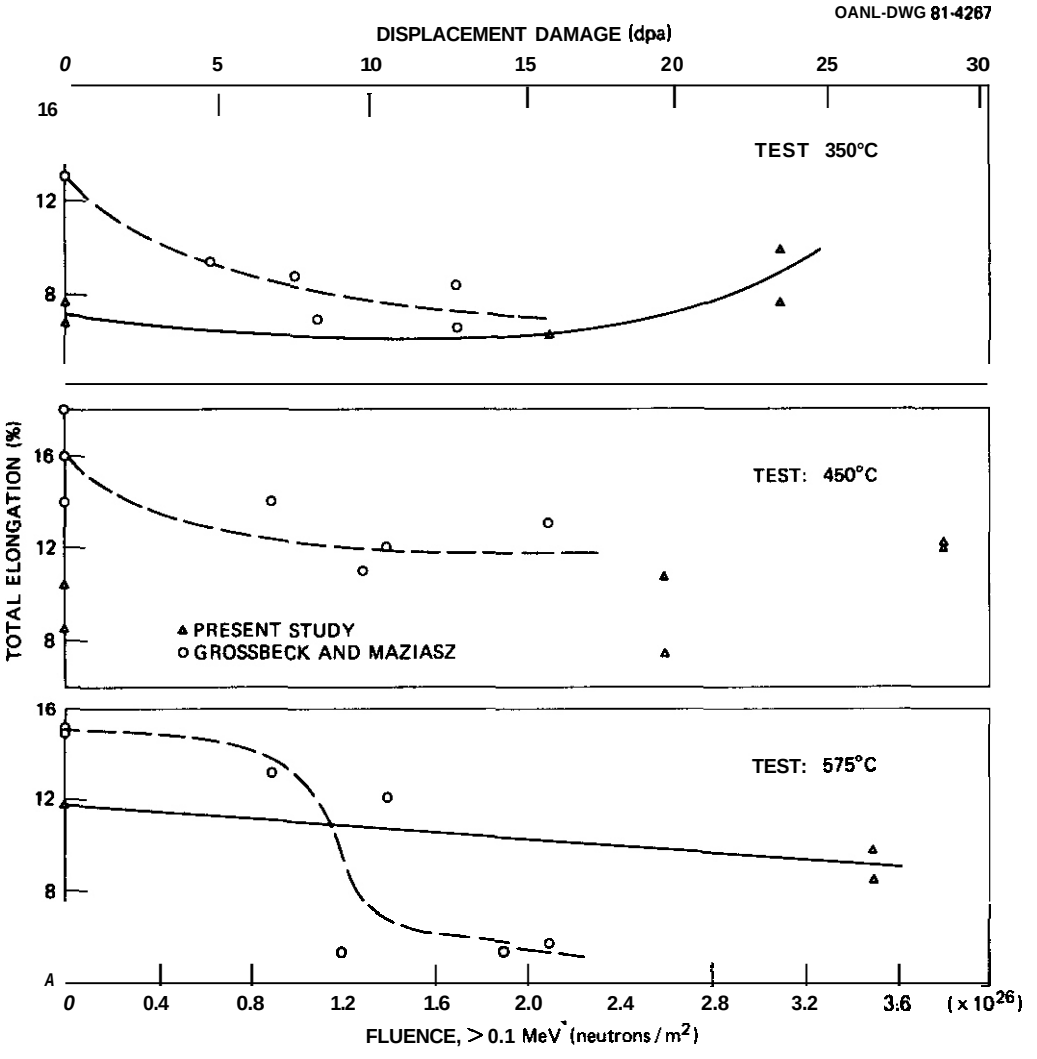

Fig. *3.4.4.* Total Elongation as a Function of Fluence (>0.1 MeV) and Displacement Damage for 20%–Cold–Worked Type *316* Stainless Steel for Test Temperatures of 350, 450, and 575°C. See Table *3.4.1* for irradiation parameters. Data source: M. L. Grossbeck and P. J. Maziasz, "Tensile Properties of Type *316* Stainless Steel Irradiated in a Simulated Fusion Reactor Environment," *J. Nucl. Muter.* 85&86 (II,B): 883-87 (1979).

However, at 575°C the yield strength and ductility bath decrease with increasing fluence. The uniform elongation values generally follow those for the total elongation (Table *3.4.1).*

The tensile data at *300* and 600°C (not shown in the figures) show the extremes of the irradiation effects (Table *3.4.1).* Irradiation has increased the strength at 300°C by over 40%, while the ductility showed a relatively small change. At 600°C the strength after irradiation is only about one-half of that before irradiation, while there appears to be relatively little change in ductility. It should again be emphasized, however, there was but one irradiated specimen tested at each of the temperature extremes.

In Figs. *3.4.5* and *3.4.6* we have compared our 350 and 575°C results with those of Grossbeck and Maziasz[1] and Bloom and Wiffen.[2] The latter

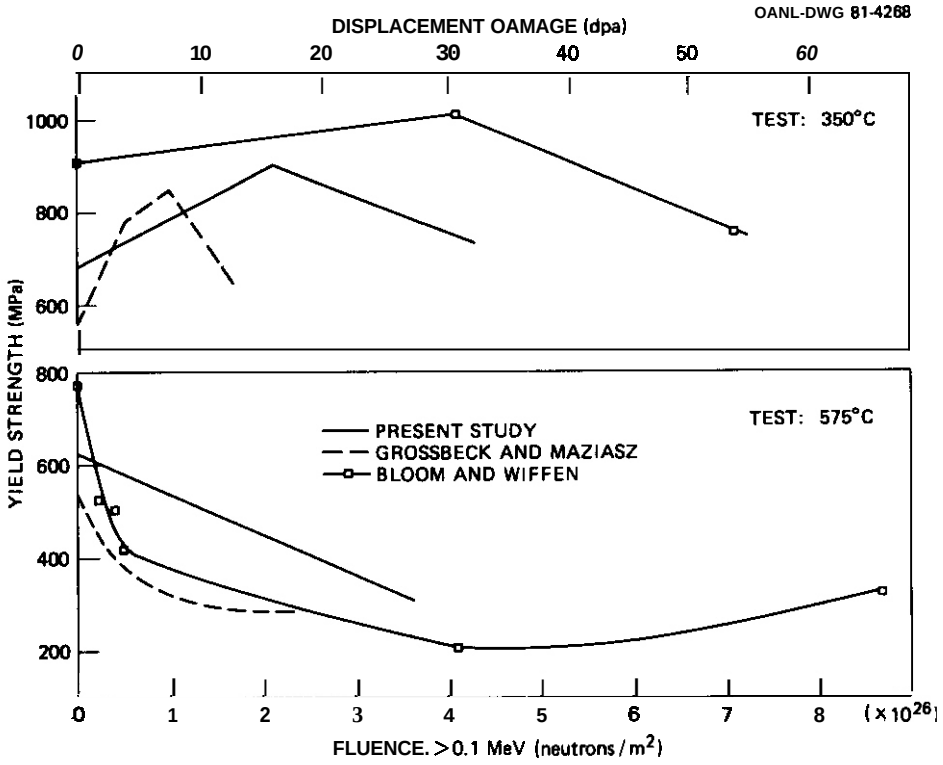

Fig. *3.4.5.* Comparison of Yield Strength as a Function of Fluence (>0.1 MeV) for Irradiated 20%-Cold-Worked Type *316* Stainless Steel at *350* and 575°C for Three Experiments. The two curves without data points are taken from Fig. *3.4.3,* and the third curve was drawn through data taken from E. E. Bloom and F. W. Wiffen, "The Effects of Large Concentrations of Helium on the Mechanical Properties of Neutron-Irradiated Stainless Steel," *J. Nucl.* Muter. 58(2): 171-84 (1975).

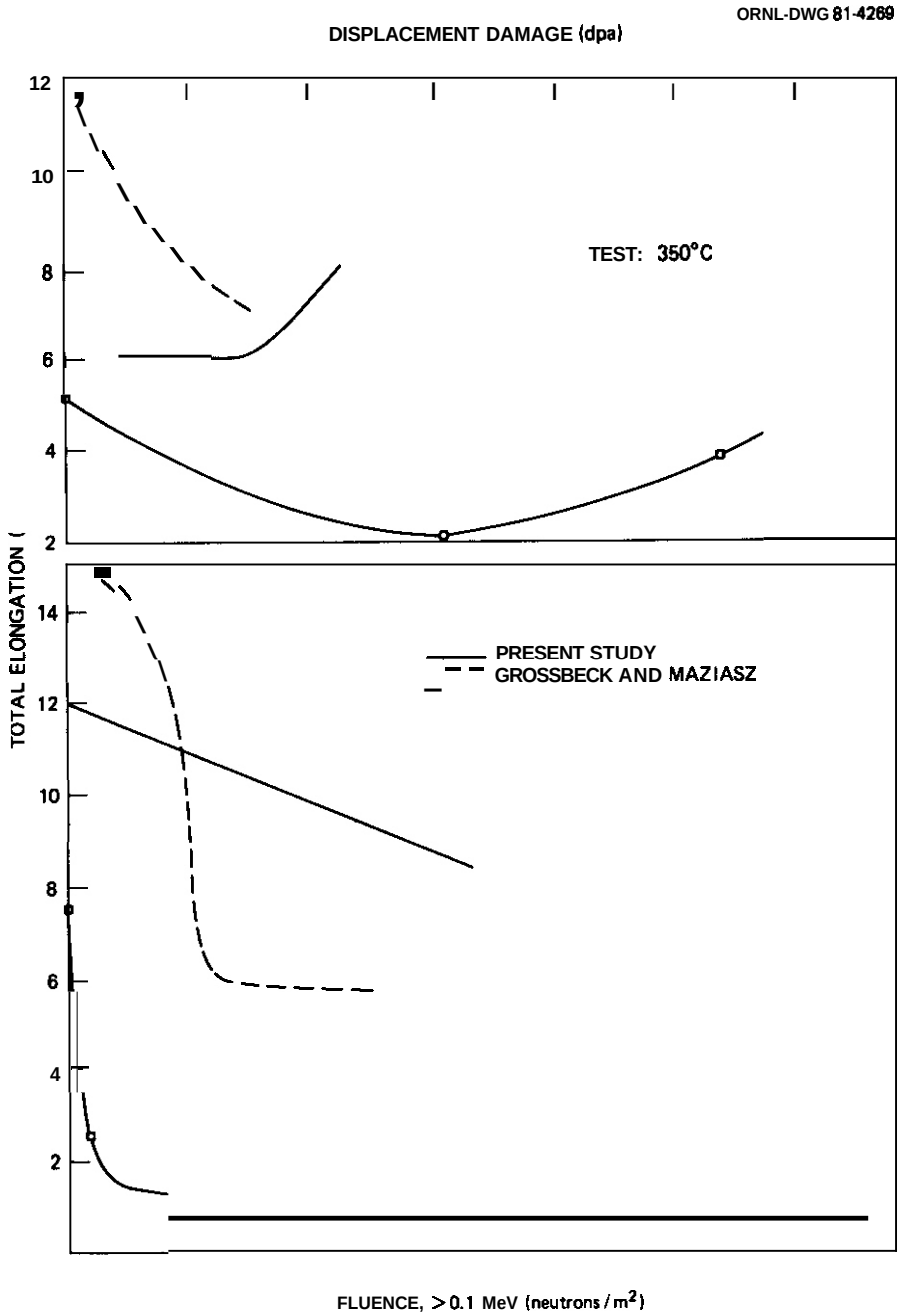

Fig. 3.4.6. Comparison of Total Elongation as a Function of Fluence (>0.1 MeV) for Irradiated 20%–Cold–Worked Type 316 Stainless Steel at 350 and 575°C for Three Experiments. The two curves without data points are taken from Fig. 3.4.4 and the third curve was drawn through data taken from E. E. Bloom and F. W. Wiffen, "The Effects of Large Concentrations of Helium on the Mechanical Properties of Neutron–Irradiated Stainless Steel," *J. Nucl. Mater.* 58(2): 171–84 (1975).

results were for fluences over twice those of the present studies. Bloom and Wiffen used the same experimental heat of steel used by Grossbeck and Maziasz.

The effects of irradiation on the yield strengths show similar trends for all three experiments. The major difference between the Bloom and Wiffen[2] results and the other two experiments involves the ductility, especially at 575°C. Bloom and Wiffen reported that at 575°C the total elongation approaches quite low values at the highest fluences. No such rapid decrease in ductility is indicated in the other two studies. Grossbeck and Maziasz[1] concluded that this difference may have arisen from differences in the fabrication procedures used when the specimen material was cold worked. Such a possibility agrees with the observation that the as-received specimens used by Bloom and Wiffen[2] were stronger and less ductile than those used in the present work or the work of Grossbeck and Maziasz[1] (Figs. 3.4.5 and 3.4.6).

3.4.5 Future Work

One of the higher fluenre companion experiments (HFIR-CTR-27) has been removed from the reactor after 25 cycles (compared to 15 cycles for HFIR-CTR-26). Temperatures were the same as those in the present experiment, but total fluenres range to 6.5 x 10^{26} neutrons/m^2 (>0.1 MeV) with 49 dpa and 3165 at. ppm He. Immersion density measurements and tensile tests are planned.

3.4.6 References

1. M. L. Grossbeck and P. J. Maziasz, "Tensile Properties of Type 316 Stainless Steel Irradiated in a Simulated Fusion Reactor Environment," *J. Nucl. Mater.* 85&86 (II,B): 883-87 (1979).
2. E. E. Bloom and F. W. Wiffen, "The Effects of Large Concentrations of Helium on the Mechanical Properties of Neutron-Irradiated Stainless Steel," *J.* Nucl. *Mater.* 58(2): 171-84 (1975).
3. F. W. Wiffen, *The Effects of CTR Irradiation on the Mechanical Properties of Structural Materials,* ORNL/TM-5624 (November 1976).

4. T. A. Gabriel, B. L. Bishop, and F. W. Wiffen, *Catcutated Irmdiation Response of Materials Using Fission Reactor (HFIR, ORR, and EBR-II) Neutron Spectra,* ORNL/TM-6361 (August 1979).

5. P. J. Maziasz and M. L. Grossbeck, "Swelling and Microstructure of HFIR-Irradiated 20%-Cold-Worked Types 316 Stainless Steel and 316 + 0.23 wt % Ti," *ADIP Quart. Prog. Rep. Dec. 31, 1980,* DOE/ER-0045/5, pp. 43-69.

6. P. J. Maziasz, F. W. Wiffen, and E. E. Bloom, "Swelling and Microstructural Changes in Type 316 Stainless Steel Irradiated Under Simulated CTR Conditions," *Radiation Effects and Tritium Technology for Fusion Reactors,* CONF-750989, vol. *I*, pp. 259-88 (March 1976).

3.5 MICROSTRUCTURAL DEVELOPMENT AND THE EFFECTS OF HELIUM IN TYPE 316 STAINLESS STEEL IRRADIATED IN HFIR AND IN EBR-II — P. J. Maziasz (Oak Ridge National Laboratory)

3.5.1 ADIP Tasks

ADIP Tasks I.C.1, Mirrostructural Stability, and I.C.2, Microstructures and Swelling in Austenitic Alloys.

3.5.2 Objertive

The objective is to review mirrostructural data for type 316 stainless steel irradiated in fast- and mixed-spectrum fission reactors. Correlation of the results will identify the effects of helium on microstructure and properties. Extension of the results, with the aid of modeling tasks, can lead to a fission-fusion damage correlation that will guide fusion reactor design efforts and alloy development programs.

3.5.3 Summary

The effects of different continuous helium generation rates on microstructural evolution of type 316 stainless steel is examined by comparing samples of a single heat, irradiated in HFIR and in EBR-II at similar temperatures and displarement damage levels. The effert of different initial helium concentrations is examined by comparing samples with 0 and 110 at. ppm preinjected helium irradiated in EBR-II. Both comparisons show important effects of helium on the microstructure developed during irradiation. In solution-annealed type 316 stainless steel, increased helium favors fine bubble formation, instead of coarse void formation and inrreased preripitation. In the 20%-cold-workedtype 316 stainless steel (CW 316) the helium results in similar effects and also considerable dislocation recovery. High-magnification examination of samples irradiated in EBR-II shows that helium bubbles at dislocations or precipitate interfaces precede void formation at these same sites. Helium preinjection amplifies the bubble nurleation effert during EBR-II irradiation, reduces void swelling, and increases precipitation, analogous to the effect observed during continuous, high-rate helium generation. The increased helium generation rate also causes more grain-boundary cavity formation.

3.5.4 Progress and Status

3.5.4.1 Introduction

Extensive data support the contention that helium aids the nucleation of both bubbles and voids during irradiation.[1-6] Theoretical study also supports this position.[7]

More recently, however, study of precipitation and matrix composition has raised doubts about the importance of helium on void nucleation in type 316 stainless steel.[8,9] These studies emphasize the role of matrix chemistry instead. A recent high-fluence comparison of (CW 316) irradiated in EBR-II and in HFIR has concluded that helium plays a minor role in swelling.[10]

The data base for the evaluation of helium effects in type 316 stainless steel is expanding as material irradiated in HFIR is examined. Sufficient data are now available for re-examination of the effects of helium on swelling.

3.5.4.2 Sources of Experimental Data

Specimens of type 316 stainless steel from the DO heat have been included in a number of irradiation experiments in both the EBR-II and HFIR. Material in both the solution annealed (SA) and 20%-cold-worked (CW) condition have been included.

The EBR-II experiments X-034 and X-100 (ref. 11) contained these materials irradiated at 450 to 715°C to fluences producing up to about 36 dpa. The microstructures were examined and described.[12-15] Specimens of this heat of steel were also included in EBR-II experiment X-264, with uninjected and helium preinjected material irradiated in the same sodium-filled subcapsules, at 500 and 625°C to 8.4 dpa. The experimental details are reported elsewhere.[16,17] The HFIR experiments (HFIR-SS-2 to -8 and HFIR-CTR-9 to -13) give the first fluence dependence information on HFIR irradiated DO-heat type 316 stainless steel. Some data on the cavity and precipitate components of these microstructures have been reported.[17-19]

3.5.4.3 Results

The data included in this report are only a subset of the available data and were chosen to best illustrate the effects of helium on microstructural evolution. Figure 3.5.1(a) and (b) shows SA DO-heat type 316 stainless steel irradiated in EBR-II at 500 to 525°C. Both voids and precipitation continue to form and develop as fluenre increases from 8.4 to 31 dpa at the low, continuous helium generation rate of about 0.5 appm/dpa. Figure 3.5.1(c) shows the same material irradiated in HFIR at 465°C to 11 dpa, but now with a helium generation rate that is 100 times greater than in EBR-II. Considerably more Precipitation (primarily of eta phase) develops in HFIR at a lower fluence, so that at least the kinetics of eta phase formation are accelerated. Rather than a few coarse voids attached to precipitates, as developed in EBR-II, HFIR irradiation produced a fine, uniform dispersion of cavities in the matrix and at the precipitate interfaces. The apparent void and precipitate coformation observed in EBR-II is not observed for HFIR irradiation.

A similar comparison of CW DO-heat type 316 stainless steel irradiated in EBR-II and HFIK is shown in Fig. 3.5.2. At 500°C and *8.4* dpa in EBR-II [Fig. 3.5.2(a)], there are no observable voids or bubbles, a small amount of precipitation (sparsely distributed), and recovery of the cold-worked dislocation concentration by about an order of magnitude. Figure 3.5.2(b) shows obvious differences in microstructural development for HFIR irradiation of the same material at 475°C and 10 dpa, but with 100 times more continuously generated helium. There is copious precipitation of eta and Laves phases, considerably more dislocation recovery, and fine, uniform cavity formation compared to the EBR-II irradiated specimen. The cavities are difficult to see in Fig. 3.5.2(b), but can clearly be seen in a previous report.[18] Together, Figs. 3.5.1 and 3.5.2 show that a change in the continuous helium generation rate significantly affects evolution of all components of the microstructure during neutron irradiation of type 316 stainless steel.

Comparison of microstructural evolution in the two reactor environments should include the fluence dependence of the microstructure. Figure 3.5.3 shows the microstructural development of CW 316 during EBR-II irradiation at 500 to 525°C from 8.4 to 36 dpa. At the higher fluence,

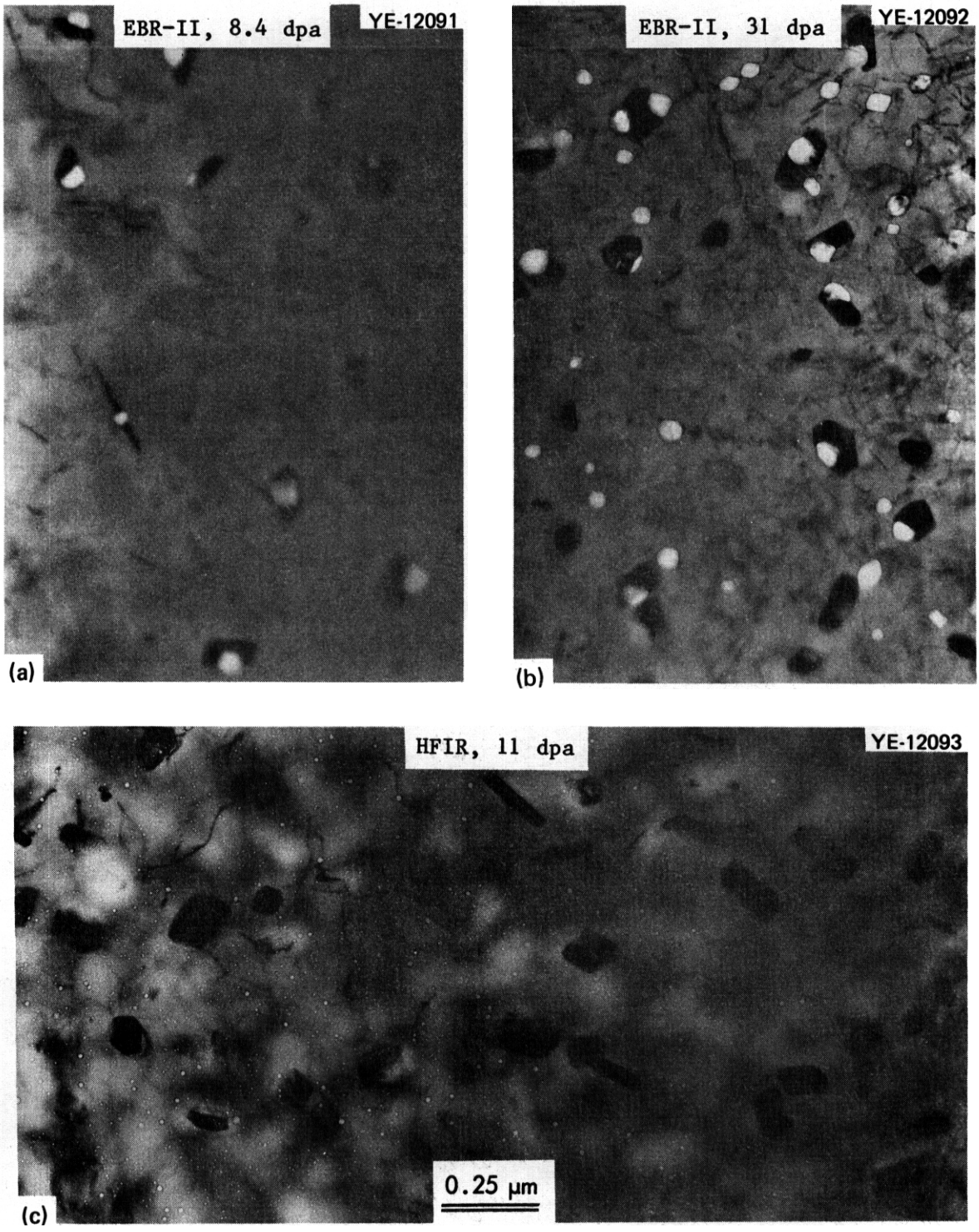

Fig. 3.5.1. Comparison of Microstructures Developed in SA DO-Heat 316 Developed During EBR-II and HFIR Irradiation. EBR-II irradiation at 500 to 525°C to (a) 8.4 dpa, ~5 at. ppm He, (b) 31 dpa, ~18 at. ppm He, and (c) HFIR irradiation at 465°C to 11 dpa, 600 at. ppm He.

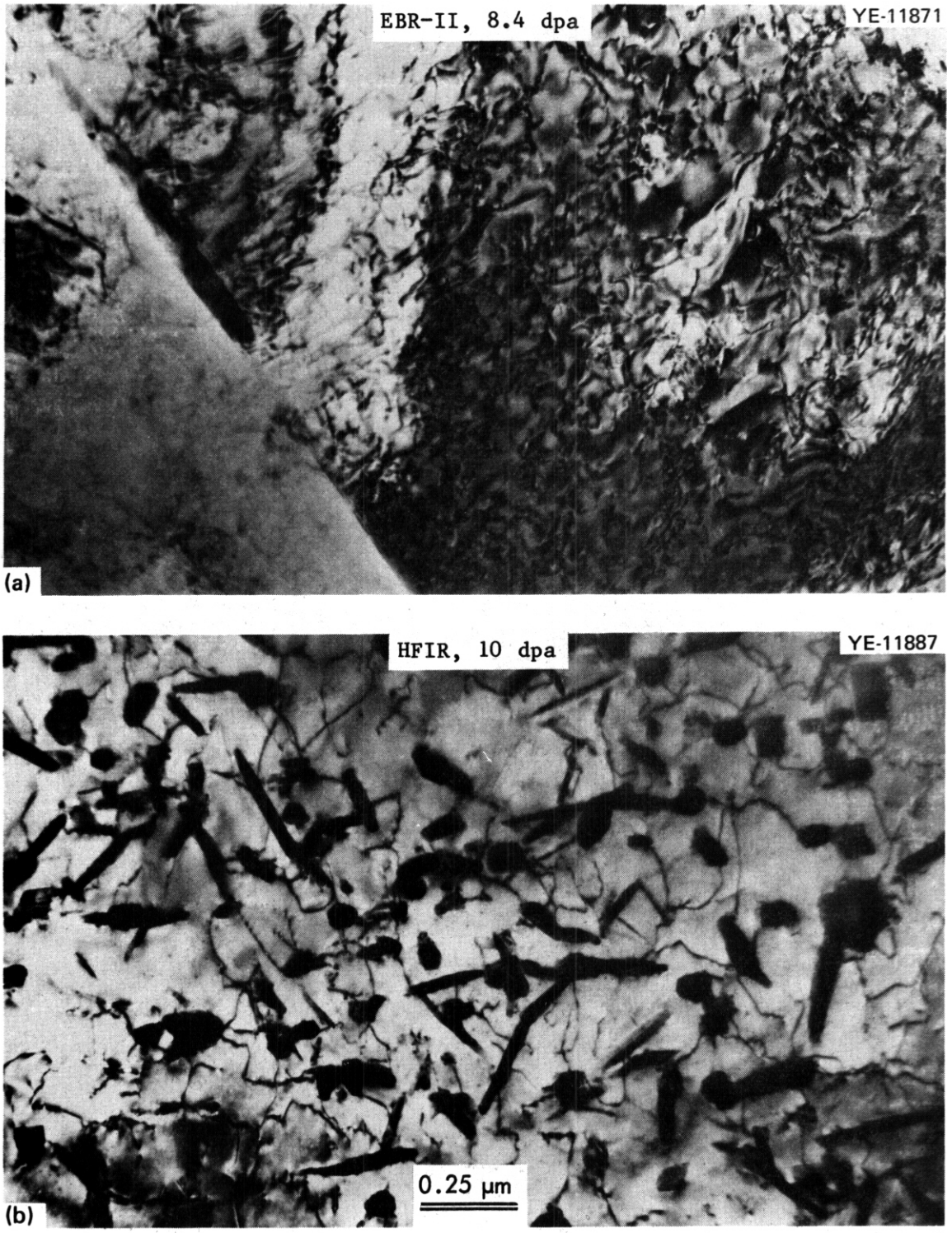

Fig. 3.5.2. Comparison of Microstructures in 20% CW DO-Heat 316 after Low Fluence Irradiation in EBR-II and HFIR. (a) EBR-II irradiation at 500°C to 8.4 dpa and ~5 at. ppm He and (b) HFIR irradiation at 475°C to 10 dpa and 500 at. ppm He.

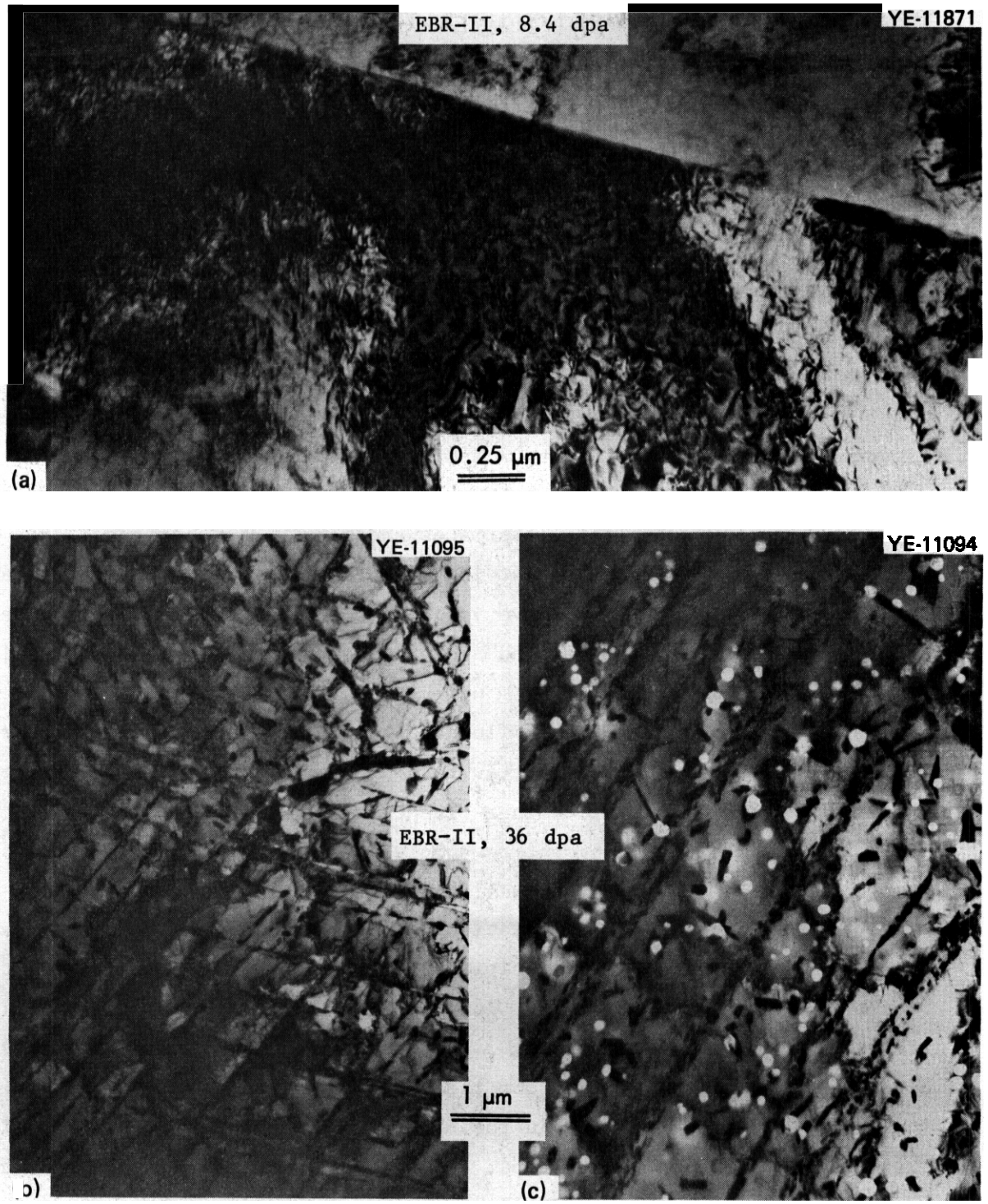

Fig. 3.5.3. Microstructural Development at Several Fluences for 20% CW W-Heat 316 Irradiated in EBR-II at 500 to 525°C. (a) Uniform microstructure after 8.4 dpa and ~5 at. ppm He. (b) and (c) Two typical areas of the heterogeneous microstructure developed at 36 dpa and ~22 at. ppm He.

there is now considerable precipitation, primarily eta with some Laves, and area-to-area heterogeneity of the void population. Voids tend to form in the areas with the coarser banded structure that results from precipitation on deformation bands and faulted bands that form as the dislocation structure recovers. Exactly the same effect is observed when this material is thermally aged at higher temperatures.[16] Figure 3.5.3(c) shows both matrix voids and voids attached to precipitate. The precipitatevoids are the largest of the two. About three-quarters of the sample appears without voids, like Fig. 3.5.3(b) and one-quarter of the samples with voids, like Fig. 3.5.3(c). Figure 3.5.4 shows higher magnification of representative areas from both general types of regions. Figure 3.5.4(a) shows both matrix and precipitate voids. However, the void-free area of Fig. 3.5.4(b) shows that helium apparently nucleates small bubbles at precipitate interfaces and matrix dislocations. This effect is usually not detected at low magnifications or in thicker areas of the foil often used to observe voids. These bubbles apparently develop into voids at higher fluence, and are clearly consistent with voids being attached to precipitates.

Microstructures for higher fluence irradiation in both reactors are shown in Fig. 3.5.5. (It is better to compare a typical voided region of the EBR-II material because higher fluence irradiation of this same material indicates that the entire samples will fill in more uniformly with voids as it continues to swell.[10,20]) Figure 3.5.5 shows similar precipitation for the two irradiations, but important differences in the cavity microstructure. The precipitate compositions are similar in both reactors at these conditions and eta and Laves phases are enriched in nickel and silicon.[21,22] Figure 3.5.6 shows the differences in fluence dependence of cavity swelling for these two materials, with Fig. 3.5.6(b) indicating that the swelling in the EBR-II material will be about double that of the HFIR sample at 54 dpa. The microstructural statistics have been reported for both the EBR-II irradiated material at about 70 dpa (ref. 20) and the HFIR irradiated material at about 54 dpa,[3,18,19] and these are compared using the rate theory formulations of Mansur.[23] If approximately equivalent saturation dislocation structures are assumed,

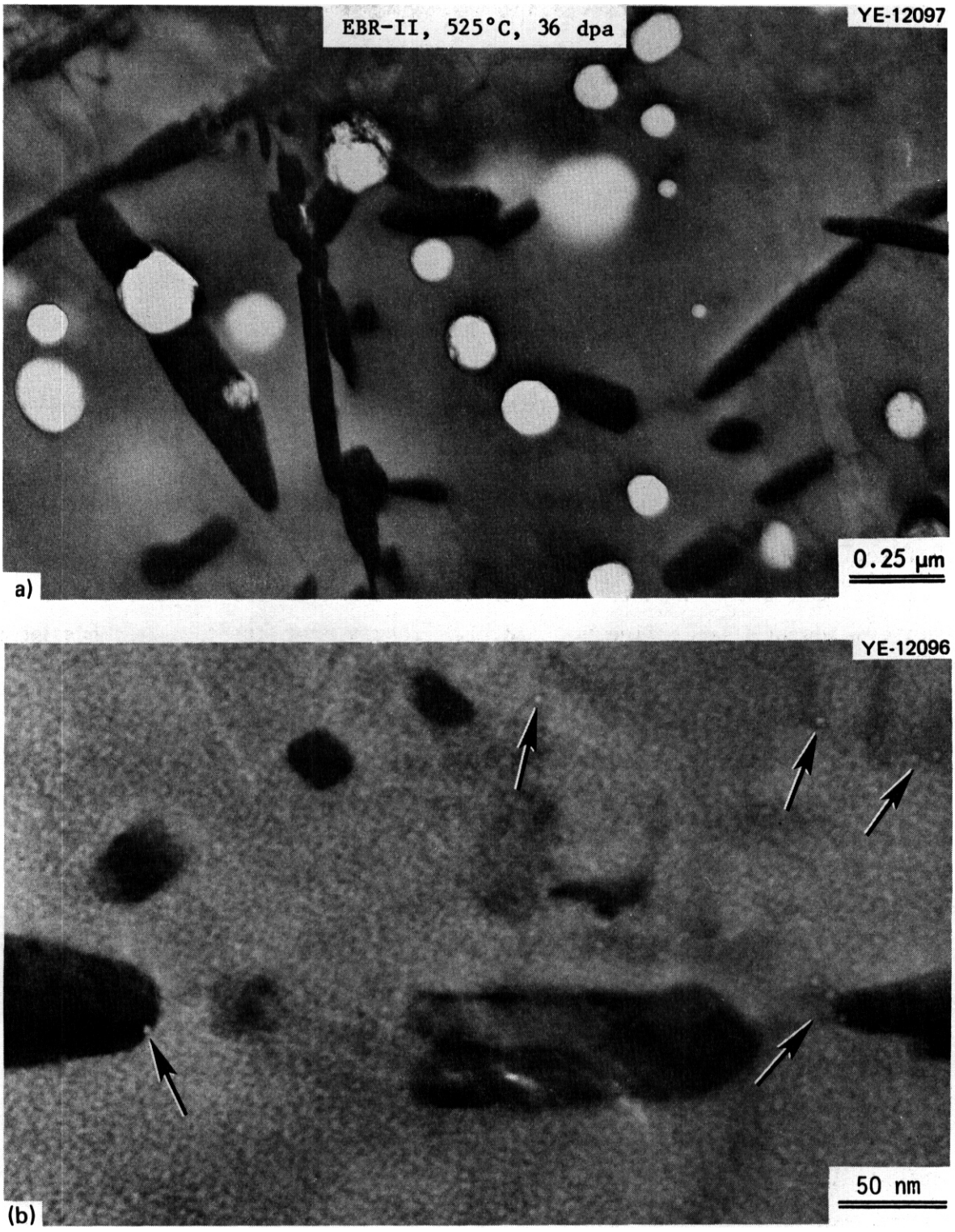

Fig. 3.54. Higher Magnification Examination of the Typical (a) Void and (b) Void-Free Areas of the Heterogeneous Microstructure Developed in 20% CW DO-Heat 316 Irradiated in EBR-II at 525°C to 36 dpa and ~22 at. ppm He. Tiny bubbles (arrows) on dislocations and at precipitate interfaces are shown in (b).

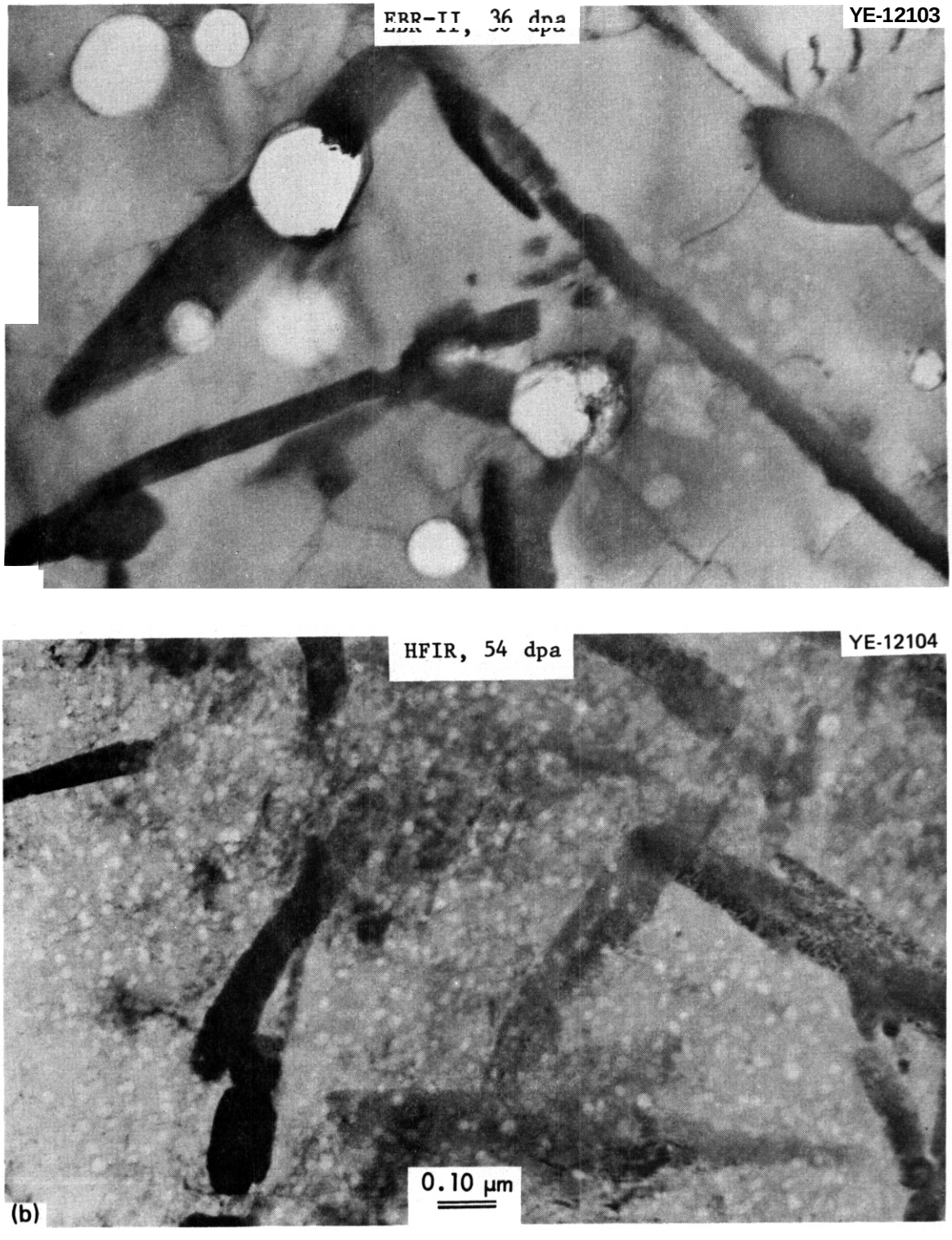

Fig. 3.5.5. Comparison of Microstructures in 20% CW DO-Heat 316 Irradiated in EBR-II and HFIR. (a) EBR-II at 525°C to 36 dpa and ~22 at. ppm He. (b) HFIR at 460°C to 54 dpa and 3600 at. ppm He. Both samples have eta and Laves precipitates of similar composition.

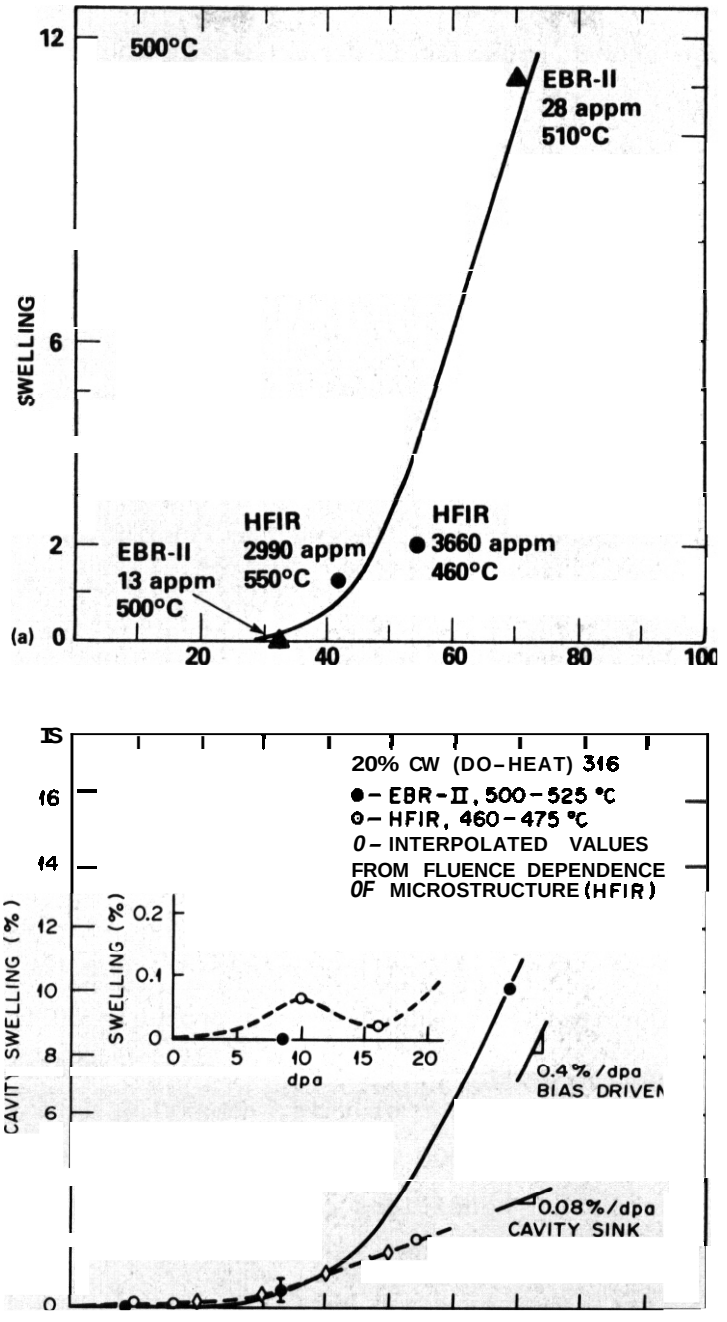

Fig. 3.5.6. Swelling as a Function of Fluence for 20% CW DO-Heat 316 Irradiated in EBR and HFIR at ~500°C. (a) Earlier correlation taken from F. A. Garner, P. J. Maziasz, and W. G. Wolfer, "Development of a Swelling Equation for 20%-CW 316 in a Fusion Device," *DAPS Quart. Prog. Rep. Sept.* 30, 1980, DOE/ER-0046/3, pp. 159—11. (b) Replotted data including lower fluence HFIR and EBR-II points and a better comparison of equivalent irradiation temperature.

theory indicates that the large voids at a lower number density should be in a bias-driven growth mode, swelling at nearly their maximum rate, as indicated in Fig. 3.5.6(b). This same treatment shows that the HFIR material with a high-number density of much smaller cavities is in a sink-dominated swelling region with cavities as the dominant sinks. The theory predicts that the HFIR material should not be swelling at all. It swells at a low rate, however, because the gas generation continues to drive bubble growth. The swelling curves in Fig. 3.5.6(b) are consistent, then, with the pronounced microstructural differences between the material irradiated in the two reactors. This new data also justify the redrawing of the comparison curve drawn by Garner et al.[10] [shown in Fig. 3.5.6(a)] to the curves of Fig. 3.5.6(b) and changing the conclusions drawn on the basis of this comparison. The swelling behavior is not the same in the two reactors at these conditions, and the controlling mechanisms reflect the effects of helium.

Several other points about Fig. 3.5.6 need clarification. The points connecting high- and low-fluence HFIR data are based upon reasonable interpolation of the fluence-dependent microstructural data discussed elsewhere in this report.[19] Secondly, somewhat different irradiation temperatures are compared in Fig. 3.5.6(a) and (b) between EBR-II and HFIR. It is pointed out in several reports[16,19] that the HFIR temperatures are calculated, and that they are probably 50 to 75°C lower than the actual irradiation temperatures based on more recent but as yet incompletely analyzed data. In light of this, comparing data in HFIR at 460 to 475°C with data in EBR-II at 500 to 525°C is probably a better comparison of equivalent irradiation conditions than 550°C in HFIR with 500°C in EBR-II, as was done in Fig. 3.5.6(a).

High-magnification examination of CW 316 irradiated in EBR-II reveals a previously unobserved role of helium bubble formation at higher irradiation temperatures. Figure 3.5.7 shows CW 316 (D0 heat) irradiated in EBR-II at about 630°C to about 31 dpa and about 19 at. ppm He. Many tiny helium bubbles are nested on matrix dislocations and precipitate interfares. These will develop into voids at higher fluences.[20] Swelling

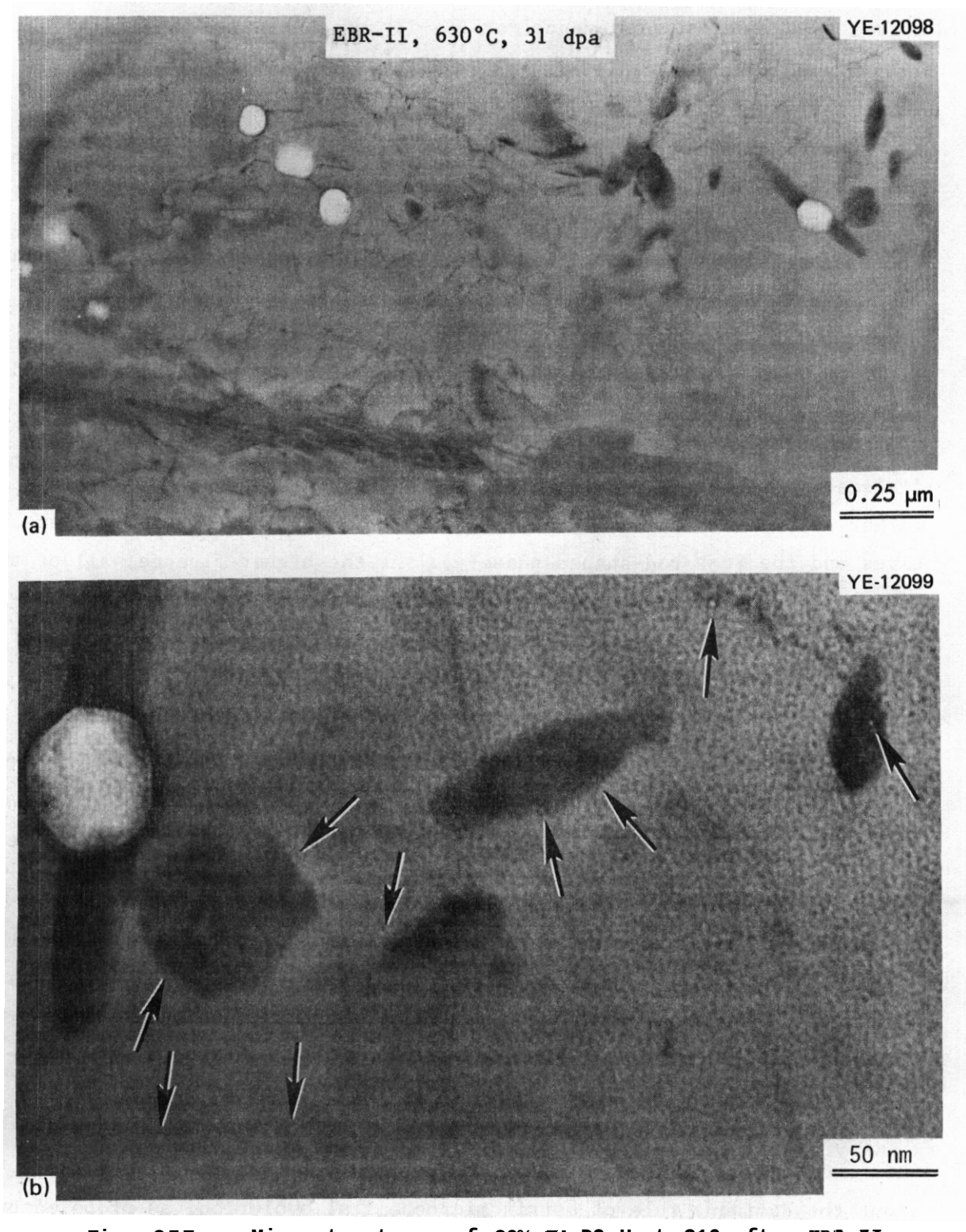

Fig. 3.5.7. Microstructures of 20% CW DO-Heat 316 after EBR-II Irradiation at 630°C to 31 dpa and ~18 dpa. (a) Low magnification of a typical void-containing region. (b) High magnification of the upper right corner of (a) to show tiny helium bubbles in the matrix and at precipitate interfaces.

curves as a function of fluence for EBR-II and comparable HFIR data[19] at this temperature are shown in Fig. 3.5.8. The curves in Fig. 3.5.8(b) fall quite close to each other, but both Figs. 3.5.6(b) and 3.5.8(b) illustrate the fundamental point that the HFIR swelling curve lies above the EBR-II curve at low fluences because microstructure develops much earlier in HFIR. The curves cross at higher fluences because void swelling in EBR-II overtakes the bubble swelling occurring in HFIR, emphasizing that the microstructural evolution is different in both reactors due to the difference in helium generation rate.

The microstructural development in solution-annealed type 316 stainless steel (D0 heat) irradiated in EBR-II at 625 to 630°C is shown in Fig. 3.5.9. This figure shows differences in void, precipitate, and dislocation structure development between 8.4 and 36 dpa. Voids become larger and more numerous, as do precipitate particles (primarily of eta, Laves and the Fe_2P rod-shaped phase[22]). At the higher fluence, all of the largest voids are again attached to precipitates, but some smaller cavities are now visible in the matrix. Higher magnification examination of the lower fluence sample (Fig. 3.5.10) shows tiny cavities, presumably helium bubbles, located at matrix dislocations (one of their natural nucleating sites). These cavities later develop into voids. Similar micrographs show cavities at the interfaces of precipitates that do not yet have associated voids (similar to Figs. 3.5.4 and 3.5.7).

The effect of helium preinjection has also been evaluated in the same material irradiated in EBR-II. The bubble nucleating role of helium, amplified by the helium preinjection, is shown in Figs. 3.5.11 and 3.5.12. A high concentration of tiny cavities are distributed quite uniformly in the matrix and at interphase boundaries in the helium injected sample (Fig. 3.5.12). The amount of precipitation also increased in the preinjected sample (Fig. 3.5.11).

These observations demonstrate that helium preinjection uncouples void swelling from the precipitation phenomenon. This raises questions about the dominant role of matrix microchemical evolution, as proposed by Brager and Garner,[8,9] but it supports the suggestions[1,4,24] and theory[25,26] of point defect and helium collection at precipitates. This process then

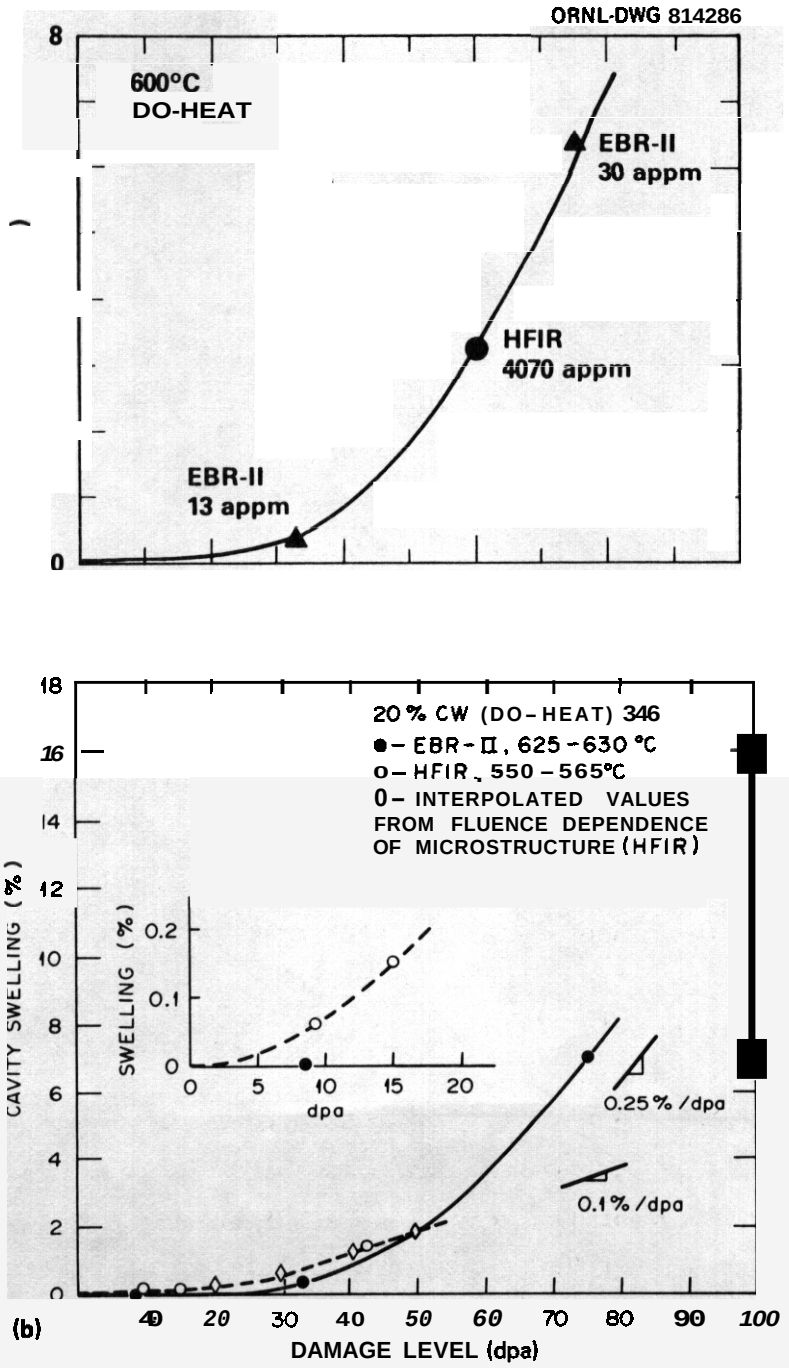

Fig. 3.5.8. Swelling as a Function of Fluence for 20% CW DO-Heat 316 Irradiated in EBR-II and HFIR Near 625°C. (a) Earlier correlation taken from F. A. Garner, P. J. Maziasz, and W. G. Wolfer, "Development of a Swelling Equation for 20%-CW 316 in a Fusion Device," *DAFS Quart. Prog. Rep. Sept. 30, 1980,* DOE/ER-0046/3, pp. 159–77. (b) Replotted data including lower fluence HFIR and EBR-II points and a better comparison of equivalent irradiation temperature.

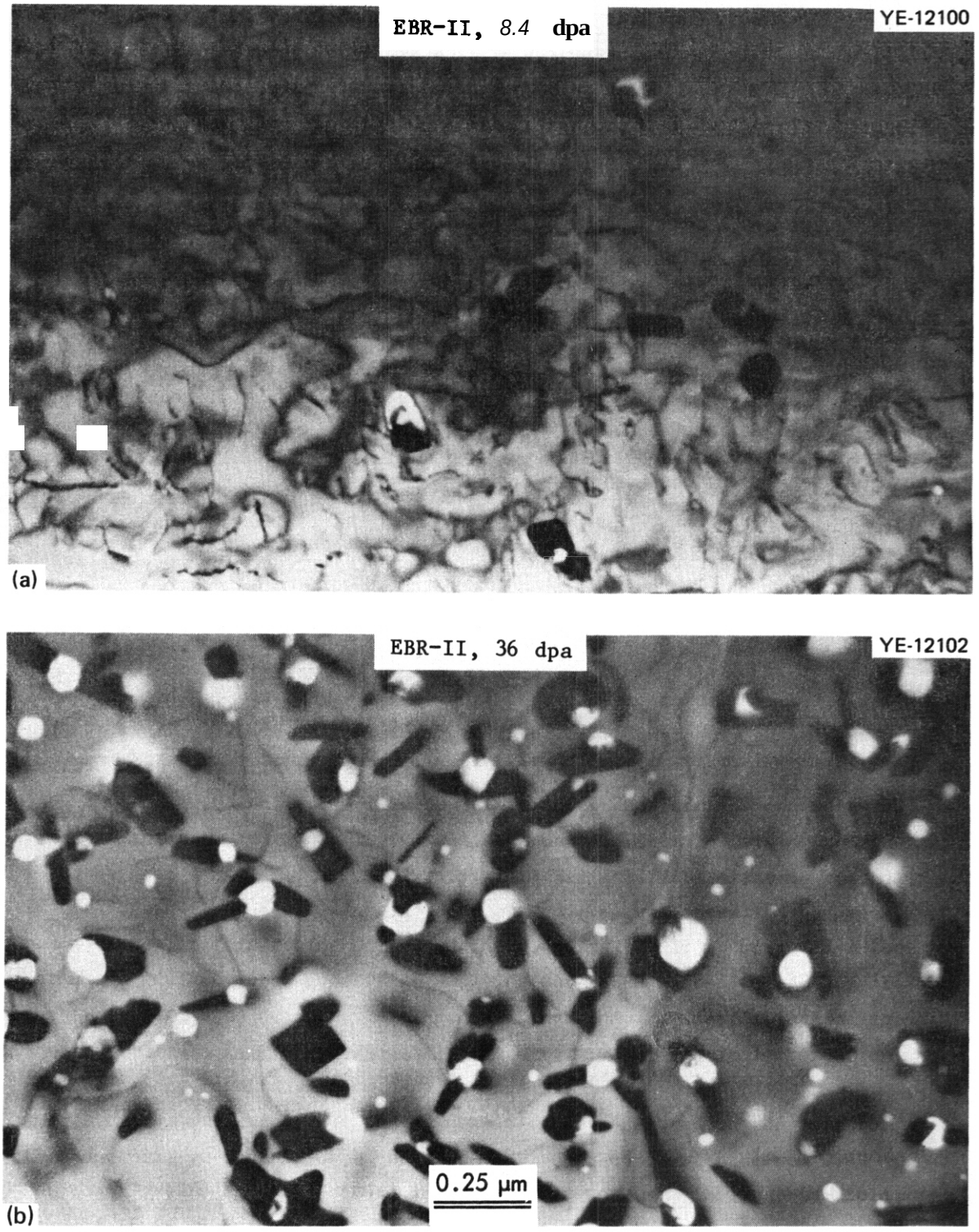

Fig. 3.5.9. Microstructural Evolution in SA W–Heat 316 Irradiated in EBR-II at 625 to 630°C to Fluences of (a) 8.4 dpa and ~5 at. ppm He and (b) 36 dpa and ~22 at. ppm He. In (a) there are only visible voids on precipitates, but in (b) they are also present in the matrix.

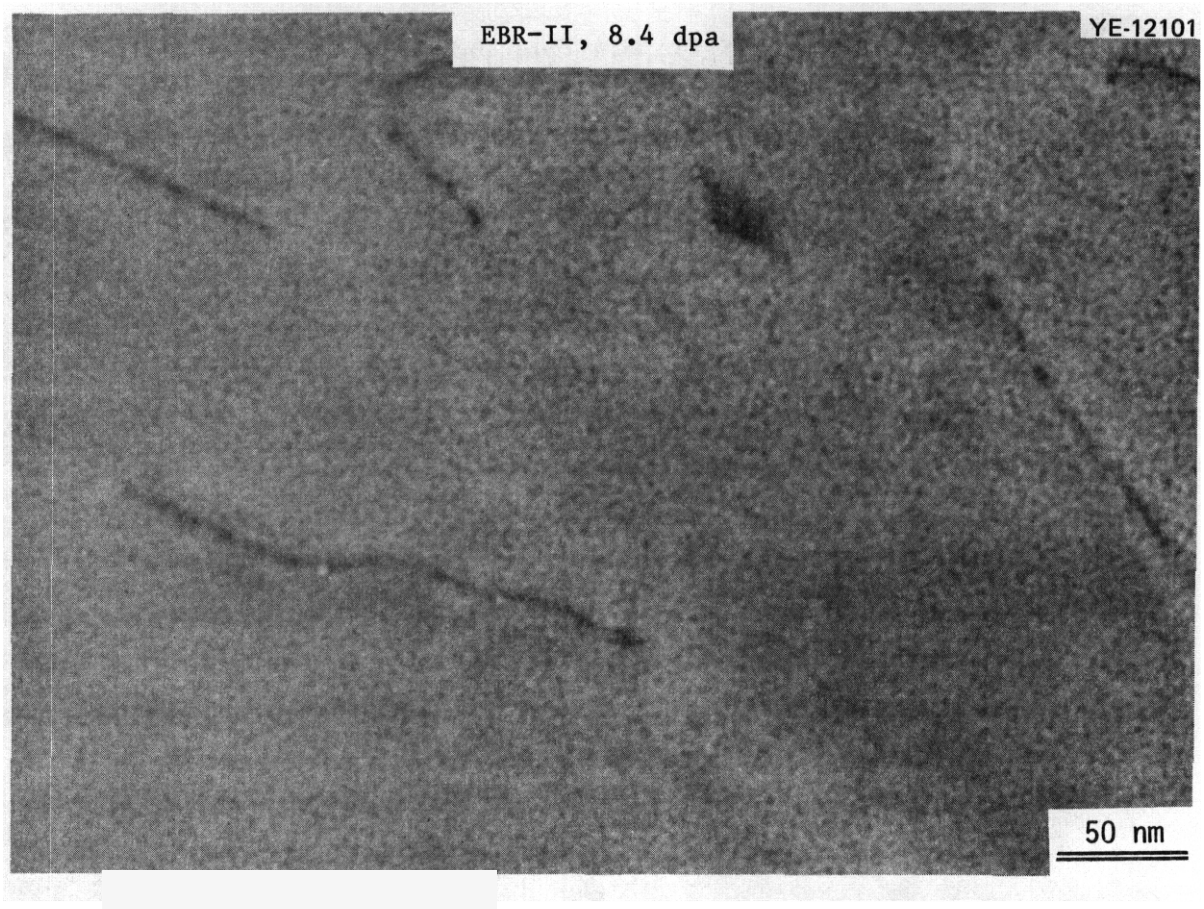

Fig. 3.5.10. High Magnification of SA 316 Irradiated in EBR-II at 625°C to 8.4 dpa and ~5 at. ppm He. Some of the dislocations, when imaged in kinematical diffracting conditions, show tiny helium bubbles that will develop into matrix voids at higher fluence, as shown in Fig. 3.5.9.

determines void location. Cavity populations are much finer after helium preinjection than after comparable HFIR irradiation, where the helium builds up gradually during irradiation [cf. Fig. 3.5.12 with Fig. 3.5.1(c)]. It is, therefore, important, as pointed out previously,[24,27,28] that helium effects be fully understood for extrapolation and/or interpolation of results from available irradiation facilities to the predictions of service in fusion reactors.

The effects of helium at grain boundaries is of special importance, particularly to properties other than swelling. Grain-boundary microsturctural development for HFIR and EBR-II irradiated CW 316 (DO heat) at several temperatures is compared in Fig. 3.5.13. These micrographs show

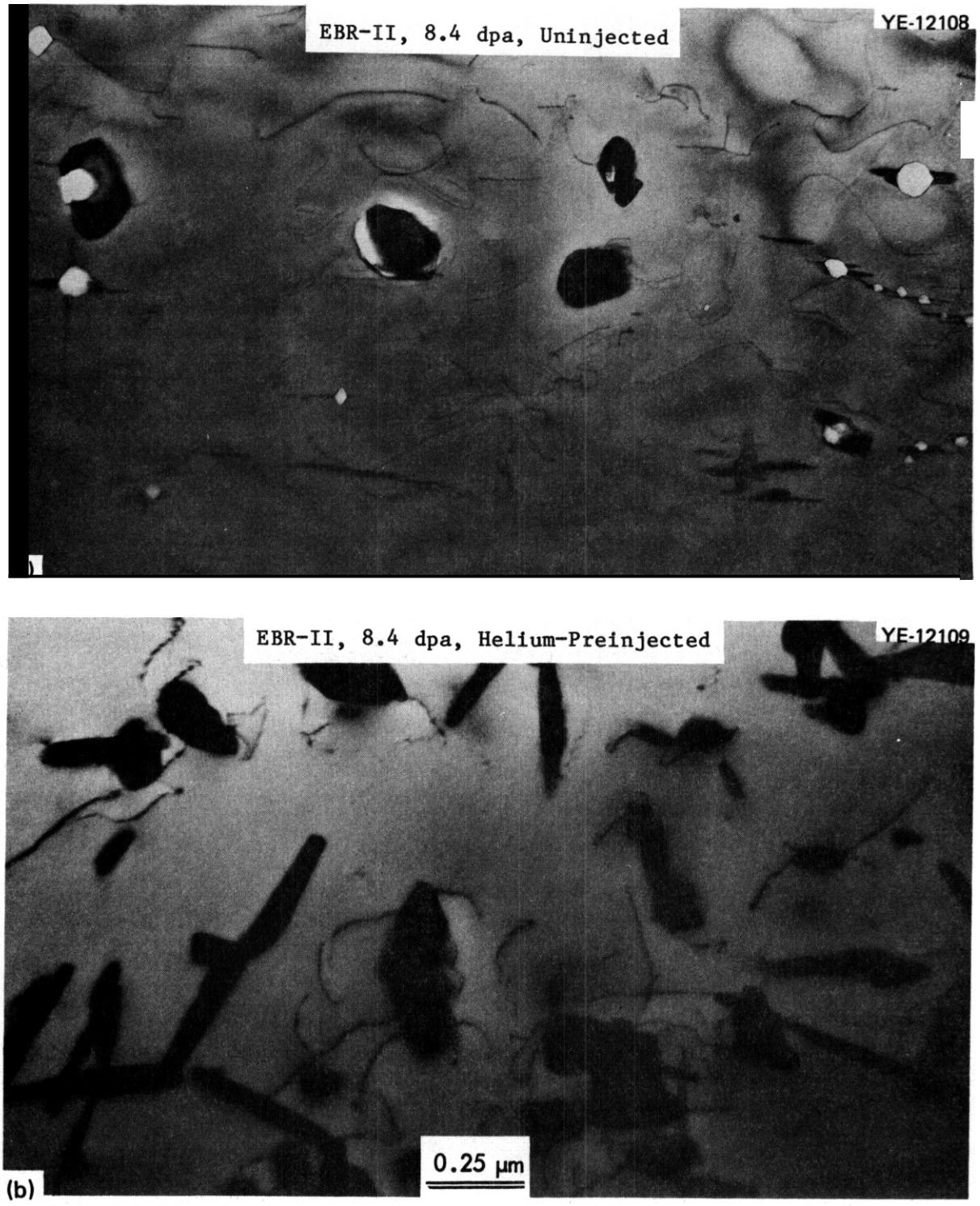

Fig. 3.5.11. The Effect of Helium Preinjection in Microstructural Evolution in SA DO-Heat 316 Irradiated in EBR-II at 625°C to 8.4 dpa. (a) Uninjected and (b) helium preinjected (110 at. ppm).

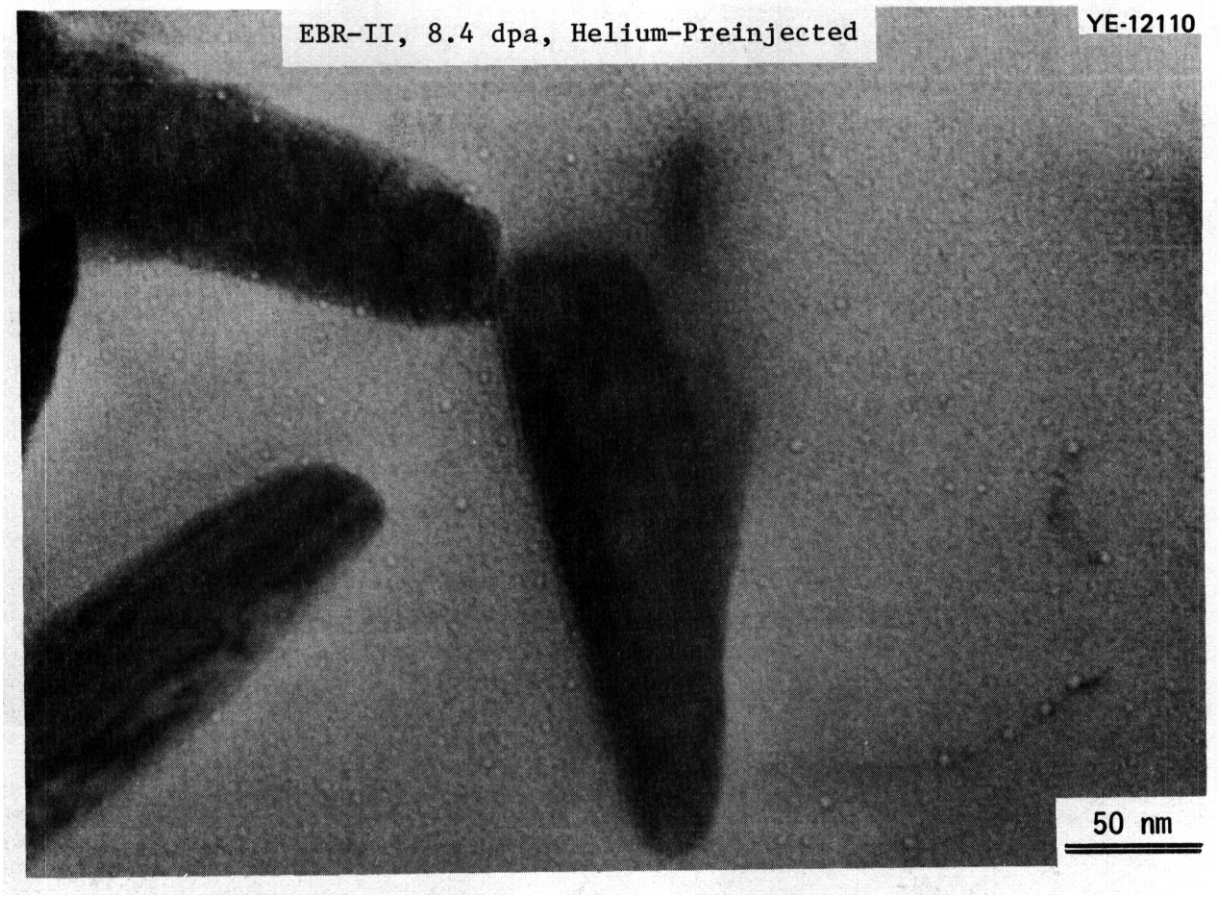

Fig. 3.5.12. Higher Magnification of SA W-Heat 316 Preinjected with 110 at. ppm He and Irradiated in EBR-II at 625°C to 8.4 dpa (shown also in Fig. 3.5.11). Together with the increased precipitation of Laves and eta phases, the preinjected helium induces nucleation of tiny cavities, uniformly distributed in the matrix as well as at their normal sites of dislocations and interphase boundaries.

that visible grain-boundary bubbles will develop after high-fluence irradiation in EBR-II, but that they are quite small, sparsely distributed, and rather temperature insensitive. At the higher, continuous helium generation rate in HFIR there is both profuse cavitation and considerable temperature dependence to the grain-boundary microstructure.

3.5.5 Conclusions

1. Helium plays a significant role in microstructural development during irradiation in either EBR-II or HFIR.

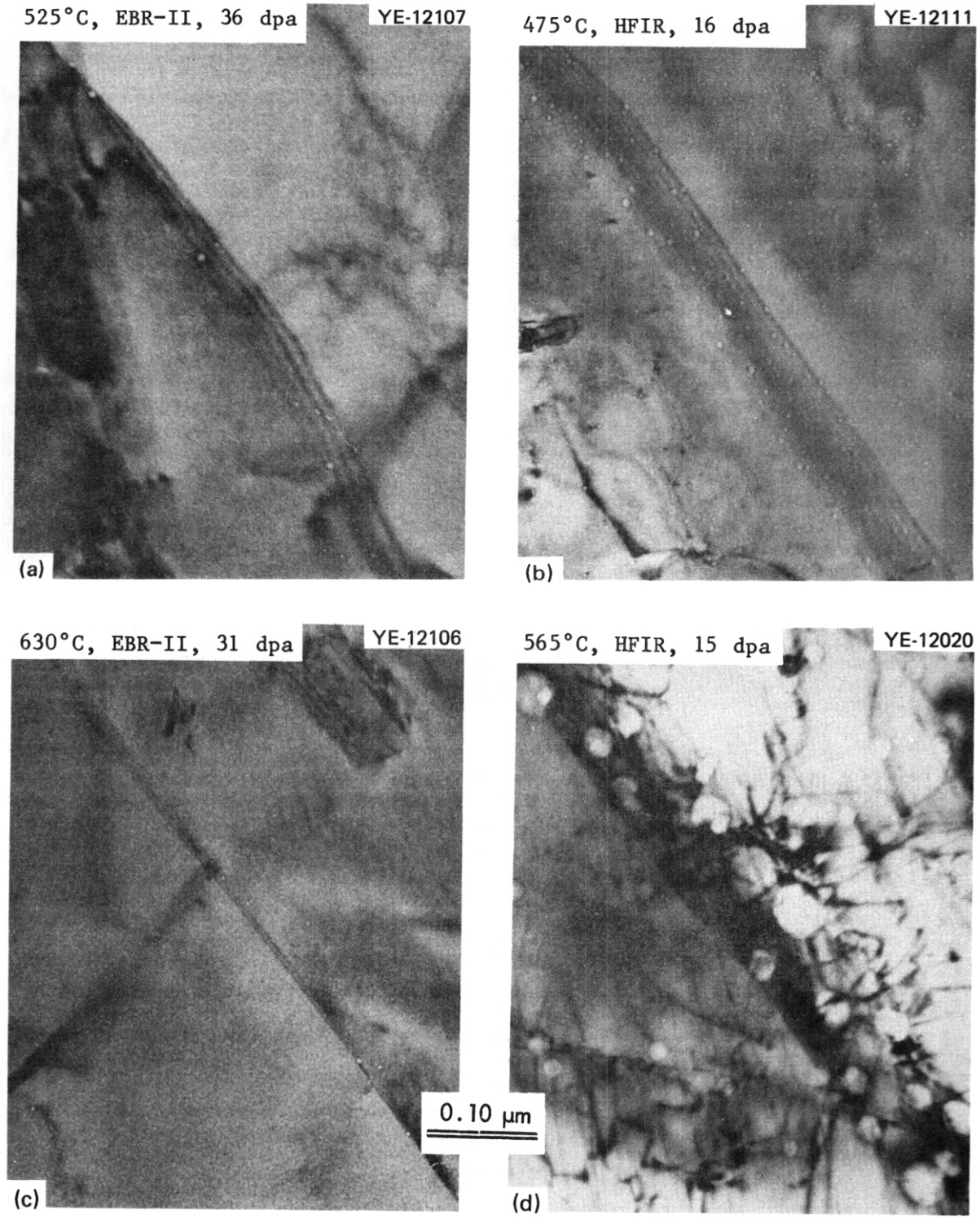

Fig. 3.5.13. A Comparison of Grain Boundary Microstructures Developed in 20% CW DO-Heat 316 Irradiated in EBR-II (a) and *(c)* and in HFIR (b) and (d). The helium level in EBR-II is ~20 at. ppm and in HFIR it is ~900 to 1000 at. ppm.

2. At the low, continuous helium generation rate in EBR-II, helium accumulation appears to be responsible for cavity or bubble nucleation at dislocations and precipitate interfaces. This determines the location and distribution of voids that will develop at higher fluences.

3. At the high, continuous helium generation rate in HFIR, helium appears to affect all components of the microstrurture. Two obvious effects are enhanred and often increased precipitation coincident with a fine and uniform cavity population that develops very early in the irradiation. In cold-worked material dislocation recovery is more rapid in HFIR than in EBR-II.

4. Helium preinjection uncouples the void formation and precipitation phenomena during EBR-II irradition. Void swelling is suppressed in solution-annealed material and precipitation is enhanced. These efferts coincide with nucleation of very fine helium bubbles in the matrix, at dislocations, and at interphase boundaries.

5. Grain boundary microstructural development is considerably different for the two different helium generation rates of HFIR and EBR-II. In EBR-II a few very small bubbles are sparsely dispersed on grain boundaries. In HFIR, at high helium concentrations, there is copious cavity formation that coarsens rapidly with increasing irradiation temperature.

3.5.6 Future Work

Future efforts will extend the data comparisons and begin to correlate the microstructure with models.

3.5.7 References

1. C. Cawthorne and J. E. Fulton, "The Influence of Irradiation Temperature on the Defect Structure in Stainless Steel," *The Nature of Small Defect Clusters,* ed. by M. J. Makin, AERE Harwell Report, AERE-R **5269,** vol. **2,** pp. **446-60 (1966).**

2. E. E. Bloom and J. O. Stiegler, "The Effect of Helium on Void Formation in Irradiated Stainless Steel," ***J. Nucl. Mater.* 36: 331-34 (1970).**

3. P. J. Maziasz, F. W. Wiffen, and E. E. Bloom, "Swelling and Microstructural Changes in Type 316 Stainless Steel Irradiated Under Simulated CTR Conditions," *Radiation Effects and Tritium Technology for Fusion Reactors,* CONF 750989, vol. 1, pp. 259-88 (March 1976).

4. H. R. Brager and J. L. Straalsund, "Defect Development in Neutron Irradiated Type 316 Stainless Steel," *J. Nucl. Muter.* 46: 134-58 (1973).

5. H. R. Brager and R. E. Robbins, "Stabilized Cavities in Irradiated Austenitic Stainless Steel," *Tmns. Metall. Soc. AIME* 242: 2010-11 (1968).

6. K. Farrell, "Experimental Effects of Helium on Cavity Formation During Irradiation — A Review," *Radia. Eff.* 53: 175—94 (1980).

7. D. J. Reed, "A Review of Recent Theoretical Developments in the Understanding of the Migration of Helium in Metals and Its Interaction with Lattice Defects," *Radia. Eff.* 31: 129—47 (1977).

8. H. R. Brager and F. A. Garner, "Dependence of Void Formation on Phase Stability in Neutron-Irradiated Type 316 Stainless Steel," pp. 207-32 in *Effects of Radiation on Structural Materials, ASTM Spec. Tech. Publ.* STP 683, ed. by J. A. Sprague and D. Kramer, American Society for Testing Materials, Philadelphia, 1979.

9. H. R. Brager and F. A. Garner, "Microstructural Evolution of Neutron-Irradiated Stainless Steel," paper presented at the *Tenth International Symposium on Effects of Radiation* on *Materials,* held in Savannah, GA, June 3—5, 1980, to be published in the proceedings; also HEDL-SA-2001.

10. F. A. Garner, P. J. Maziasz, and W. G. Wolfer, "Development of a Swelling Equation for 20%-CW 316 in a Fusion Device," *DAFS Quart. Prog. Rep. Sept.* 30, *1980,* DOE/ER-0046/3, pp. 159-77.

11. E. E. Bloom, "Status of Irradiation Experiments," *Fuels and Materials Development Program Quart. Prog. Rep. Dec. 31, 1970,* ORNL-TM-3300, pp. 97-99.

12. J. O. Stiegler and E. E. Bloom, "Some Effects of Composition and Microstructure on Radiation Damage in Stainless Steel," *Fuels and Materials Development Progmm Quart. Prog. Rep. Sept. 30, 1971,* ORNL-TM-3550, pp. 90—109.

13. E. E. Bloom and J. O. Stiegler, "Effect of Irradiation on the Microstructure and Creep-Rupture Properties of Type 316 Stainless Steel," pp. 360–82 in *Effects of Radiation on Substructure and Mechanical Properties of Metals and Alloys,* *ASTM Spec. Tech. Publ.* STP 529, American Society for Testing Materials, Philadelphia (1973).

14. J. M. Leitnaker, E. E. Bloom, and J. O. Stiegler, "Transmission Electron Microscopy Examination of Irradiated Austenitic Stainless Steel," *Fuels and Materials Development Progmm Quart. Prog. Rep. Dec. 31,* 1972, ORNL-TM-4105, pp. 3.19–3.39.

15. P. S. Sklad and E. E. Bloom, "Effects of Preirradiation Microstructure on Swelling and Mechanical Properties," *HEDL Semiannual Progress Report on Irmdiation Effects on Reactor Structuml Materials, August,* 1974 *to February,* 1975, HEDL-TME 75-23, pp. ORNL-1–ORNL-10.

16. P. J. Maziasz, J. A. Horak, and B. L. Cox, "The Influence of Both Helium and Neutron Irradiation on Precipitation in 20%-Cold-Worked Austenitic Stainless Steel," paper presented at the IMS-AIME Fall Meeting, Pittsburg, Oct. 5–9, 1980, to be published in *Irradiation Effects on Phase Stability,* ed. by J. R. Hall, L. K. Mansur, and D. I. Potter.

17. P. J. Maziasz, B. L. Cox. and J. A. Horak. "The Effect of Preinjected Helium on the Microstructure and Tensile Properties of EBR-II Irradiated 20%-Cold-Worked Type 316 Stainless Steel," *ADIP Quart. Prog. Rep. Mar. 31, 1980,* DOE/ER-0045/2, pp. 35–57.

18. P. J. Maziasz and M. L. Grossbeck, "Swelling and Microstructure of HFIR-Irradiated 20%-Cold-Worked Types 316 and 316 + 0.23 wt % Ti," *ADIP Quart. Prog. Rep. Dec. 31, 1980,* DOE/ER-0045/5, pp. 43–69.

19. P. J. Maziasz and M. L. Grossbeck, "Microstructural Development in 20%-Cold-Worked Types 316 and 316 + Ti Stainless Steels Irradiated in HFIR: Fluence Dependence of the Cavity Components," Sect. 3.3 of this report, pp.

20. H. R. Brager and F. A. Garner, private communication of data to be published in future *Damage Analysis Fundamental Studies.*

21. P. J. Maziasz, "Composition and Microstructure of Precipitate Phases in Austenitic Stainless Steels," *ADIP Quart. Prog. Rep. June 30, 1980,* DOE/ER-0045/3, pp. 75–129.

22. E. H. Lee, P. J. Maziasz, and A. F. Rowcliffe, "The Structure and Composition of Phases Occurring in Austenitic Stainless Steels in Thermal and Irradiation Environments," paper presented at the TMS-AIME Fall Meeting, Pittsburg, Oct. 5–9, 1980, to be published in *Irradiation Effects on Phase Stability*, ed. by J. R. Hall, L. K. Mansur, and D. I. Potter.

23. L. K. Mansur, "Void Swelling in Metals and Alloys Under Irradiation: An Assessment of the Theory," *Nucl. Technol.* 40: 5–34 (1978).

24. G. R. Odette, "Modeling of Microstructural Evolution Under Irradiation," *J. Nucl. Mater.* 85686: 53-45 (1979).

25. L. K. Mansur, M. R. Hayns, and E. H. Lee, "Mechanisms Affecting Swelling in Alloys with Precipitate," paper presented at the IMS-AIME Fall Meeting, Pittsburg, Oct. 5–9, 1980, to be published in *Irradiation Effects on Phase Stability*, ed. by J. R. Hall, L. K. Mansur, and D. I. Potter.

26. L. K. Mansur, "Theoretical Evaluation of a Mechanism of Precipitate-Enhanced Cavity Swelling During Irradiation," to be published in *Journal of Nuclear Materials* (1981); also ORNL/TM-7645 (March 1981).

27. G. R. Odette and S. C. Langley, "Modeling of Synergistic Effects of Displaced Atom and Transmutant Damage in Fusion and Fusion Environments," *Radiation Effects and Tritium Technology*, CONF 750989, vol. 1, p. 39–16 (March 1976).

28. J. A. Spitznagel, F. W. Wiffen, and F. V. Nolfi, "Microstructure Developed in 'Simulated' Fusion Irradiations," *Radiation Effects and Tritium Technology*, CONF 750989, vol. 1, pp. 629–46 (March 1976).

4. PATH B ALLOY DEVELOPMENT — HIGHER STRENGTH Fe-Ni-Cr ALLOYS

No contribution.

5. PATH C ALLOY DEVELOPMENT — REACTIVE AND REFRACTORY ALLOYS

5.1 MECHANICAL PROPERTY EVALUATIONS OF PATH C VANADIUM SCOPING ALLOYS - R. E. Gold and R. L. Ammon (Westinghouse Electric Corporation)

5.1.1 ADIP Tasks

I.B.ll. Stress-Rupture Properties of Reactive/Refractory Metal Alloys (Path C)

I.B.15. Tensile Properties of Reactive/Refractory Metal Alloys (Path C)

5.1.2 Objective

The objective of this program is to develop tensile and creep/stress-rupture data for the unirradiated Path C vanadium Scoping Alloys. In addition, methods will be explored for introducing controlled levels of nonmetallic impurities into test specimens in order to examine their effects on mechanical properties.

5.1.3 Summary

Tensile testing of sheet specimens of the three Path C vanadium Scoping Alloys has been completed at room temperature, 450, 500, 550, 600, 650, 700, and 750°C. The results of these tensile tests are in good agreement with values reported previously in the literature for other heats of these alloys. A series of creep/stress-rupture tests has been initiated. To date, a single specimen of each alloy is undergoing testing at 650°C in ultrahigh vacuum (pressure < 10^{-8} torr). Stresses were selected to produce rupture in approximately 1000 hours; these stresses sre 148, 276, and 414 MPa for the alloys V-20Ti, VANSTAR-7, and V-15Cr-5Ti, respectively. At the time of this report total test times of 880, 1170, and 550 hours, respectively, have been accumulated for these initial tests.

5.1.4 Progress and Status

The Path C vanadium-base Scoping Alloys which were prepared for the ETM Research Materials Inventory, sited at the Oak Ridge National Laboratory, are the subject of this evaluation. These include: (compositions in vt. percent)

V-20Ti

V-15Cr-5Ti

VANSTAR-7 (V-9Cr-3.3Fe-1.2Zr-0.054C)

This program was initiated to develop the tensile and stress-rupture data base for the unirradiated alloys. In this respect, it is complementary to the fatigue and crack growth investigations being conducted by K. Liu at the Oak Ridge National Laboratory; the results of these latter investigations have been reported in recent ADIP Quarterly Reports.[1-3] Because nonmetallic impurities are known to have significant effects on the mechanical behavior of refractory metal alloys, an additional objective of this program is to begin the development of means to introduce controlled levels of impurities such as oxygen and nitrogen into mechanical property specimens.

Specific tasks associated with FY'81 efforts are:

Task 1. Material Procurement

Task 2. Initial Specimen Preparation and Heat Treatments

Task 3. Tensile Evaluations

Task 4. Creep/Stress Rupture Testing

Task 5. Evaluation of the Effects of Nonmetallic Contamination on Mechanical Properties

Task 6. Microstructural Characterizations

Efforts to date have concentrated on Tasks 1 through 4 with some preliminary, supporting efforts on Task 6. These are summarized in the following subsections.

5.1.4.1 Material Identification and Condition

The analyzed chemical compositions for the three Path C vanadium Scoping Alloys are presented in Table 5.1.1.[4]

Table 5.1.1
Chemical Analysis of Path C Vanadium Alloy Sheet

	ELEMENTAL ANALYSIS (w/o)						
ALLOY	Ti	Cr	Fe	Zr	C	O	N
V-20Ti	19.7				0.029	0.045	0.056
V-15Cr-5Ti	15.3	5.0			0.017	0.023	0.052
VANSTAR-7		9.7	3.4	1.3	0.064	0.028	0.052

Prior to machining mechanical property specimens, all slloys were given a one hour heat treatment at temperatures determined experimentally to produce a fully recrystallized, equiaxed (grain size $\sim$30 μm) microstructure. These temperatures are 1100, 1200, and 1350°C for the V-20Ti, V-15Cr-5Ti, and VANSTAR-7 alloys, respectively.

An identical specimen design was utilized for both tensile and creep-rupture testing for this program. A sketch of this specimen is shown in Figure 5.1.1.

5.1.4.2 Tensile Tests

Tensile tests were conducted on sheet specimens of each of the three vanadium alloys at room temperature, 450, 500, 550, 600, 650, 700, and 750°C. Duplicate specimens were tested at each temperature. A constant strain rate of 3.3×10^{-4} s^{-1} was used throughout all tests; testing vas performed in a vacuum environment, maintained below

about 5 x 10^{-6} torr throughout the tests.

The test results are presented on Figures 5.1.2 through 5.1.4, and in Tables 5.1.2 through 5.1.4, for the alloys V-20Ti, V-15Cr-5Ti, and VANSTAR-7, respectively. On Figures 5.1.2 through 5.1.4 the average values of the duplicate test results reported in the corresponding table are plotted. Also shown on Figures 5.1.2 and 5.1.4 are the results of previous tensile tests reported by Whitlow, et al.[5] for other heats of the V-20Ti and VANSTAR-7 alloys. Fairly good agreement is observed between these two sets of data.

5.1.4.3 Creep-Rupture Tests

Creep-rupture testing has been started during this reporting period. A single sheet specimen is under test at 650°C in ultrahigh vacuum (pressure < 10^{-8} torr). An estimate was made of the stress which would produce rupture in approximately 1000 hours. This estimate was based on data available in the literature. Accumulated test times to date and testing conditions sre:

Alloy	Applied Stress (MPa)	Time (as of 5-8-81) (hrs.)	Measured Strain (%)
V-20Ti	148	880	0.15
V-15Cr-5Ti	414	550	0.50
VANSTAR-7	276	1170	0.15

It is apparent from these data that the stresses vhich were selected are too low. Consideration is being given to changing the applied stress to accelerate the creep process, or to terminate these tests and initiate a second series at different temperatures and/or stress conditions.

5.1.5 References

1. K. C. Liu, "Fatigue Behavior of Unirradiated Path C Alloys," Alloy Development for Irradiation Performance, Qtrly. Progress Report for

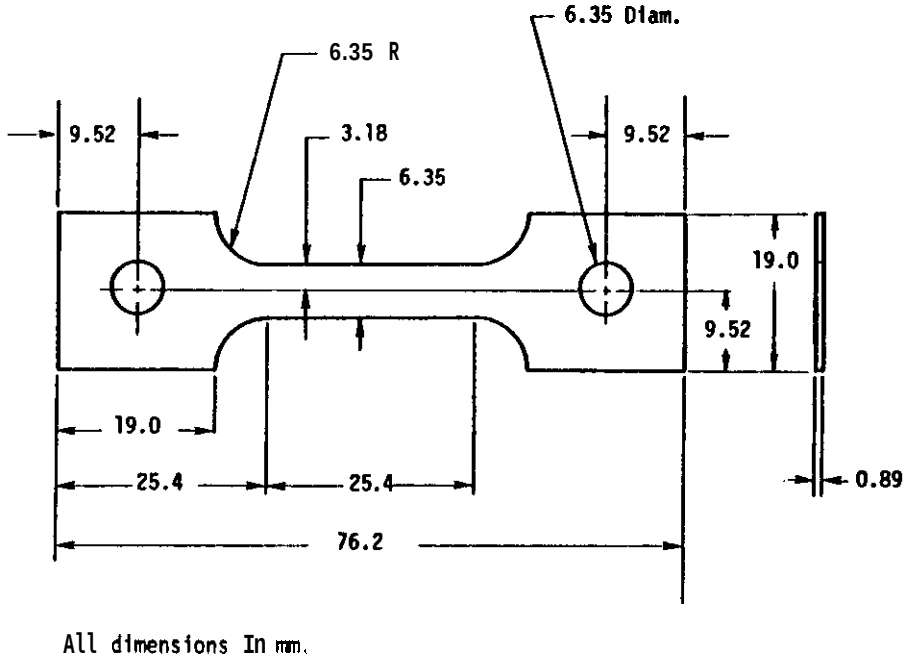

Figure 5.1.1. Specimen design used for tensile and creep-rupture testing of the vanadium scoping alloys.

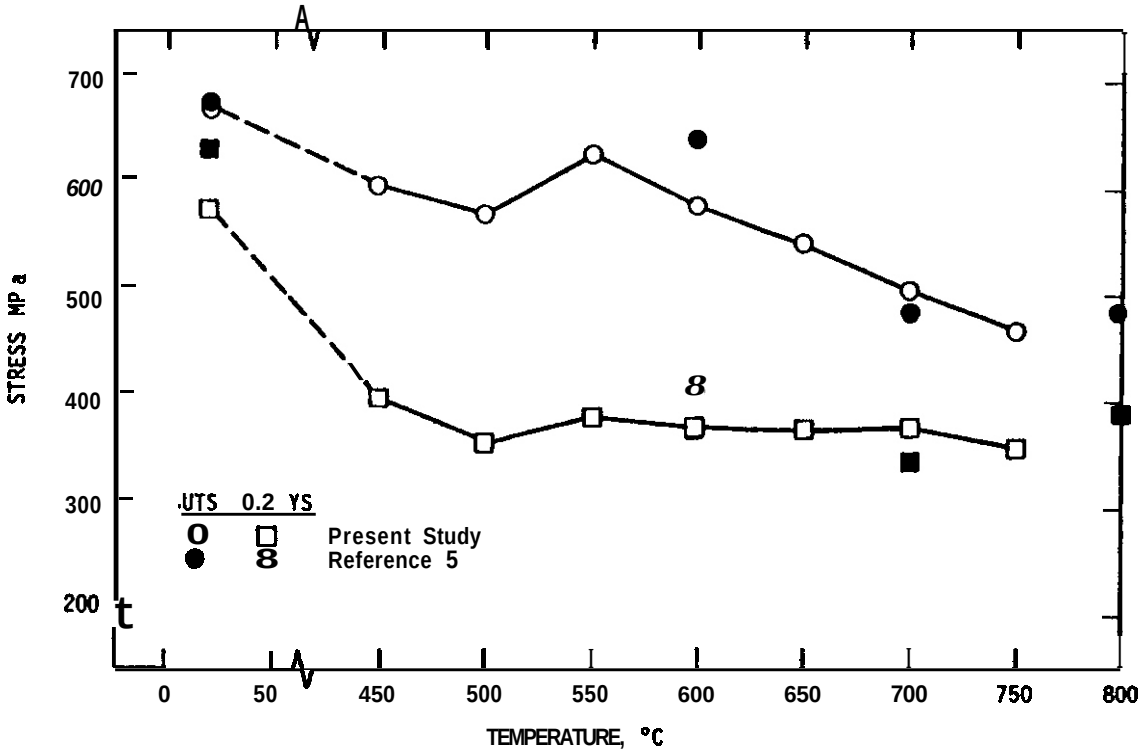

Figure 5.1.2. The tensile strength of V-20Ti as a function of test temperature.

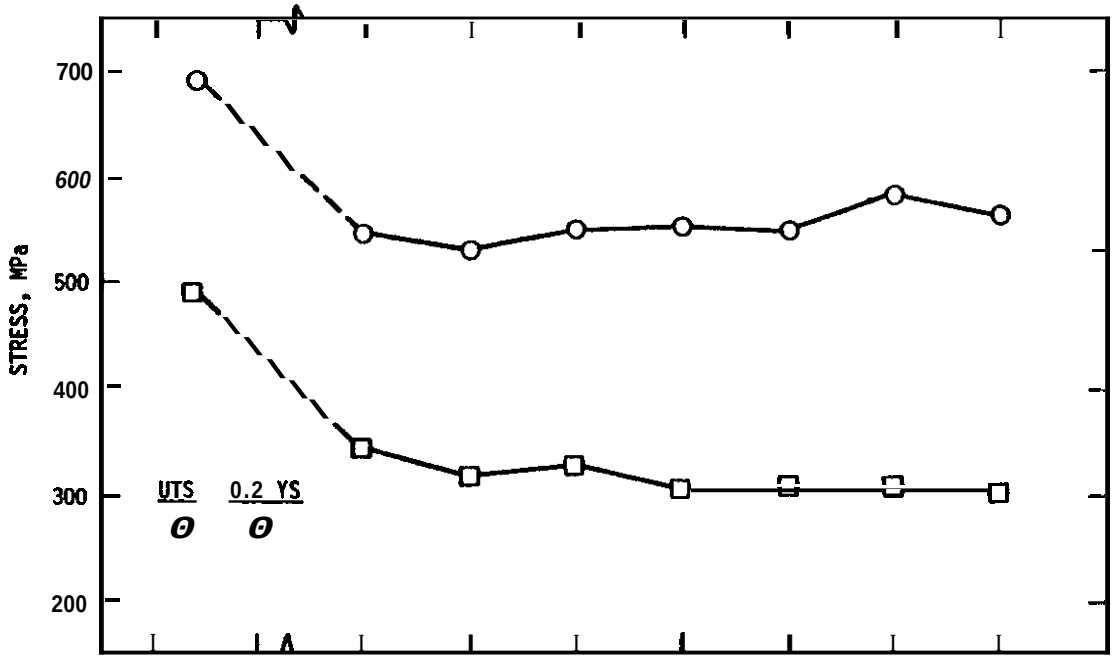

Figure 5.1.3. The tensile strength of V-15Cr-5Ti as a function of test temperature.

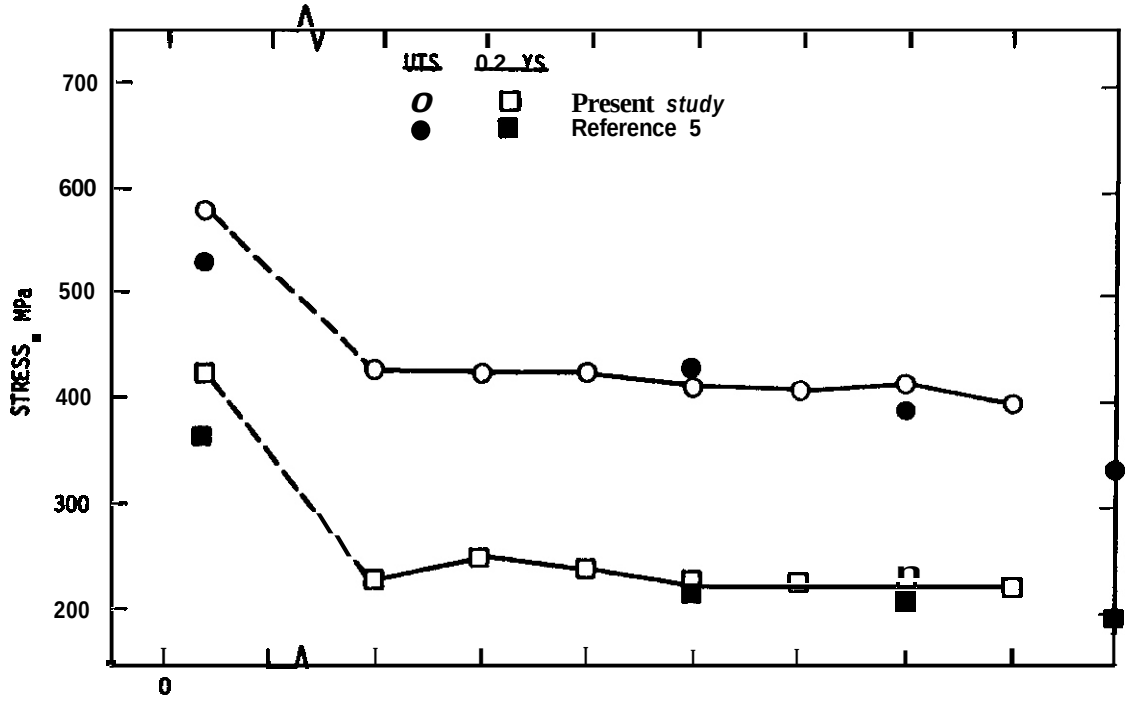

Figure 5.1.4. The tensile strength of VANSTAR-7 as a function of test temperature.

Table 5.1.2
Tensile Test Results for the V–20Ti Alloy

Specimen Identific.	Test Temp. (°C)	0.2% Y.S. (MPa)	UTS (MPa)	Elongation	
				Uniform (%)	Total (%)
VT-1	RT	576	676	19.1	21.4
–2	RT	579	674	19.0	23.3
-29	450	414	601	12.7	15.2
–30	450	383	607	13.8	15.4
–3	500	390	605	14.5	17.4
–4	500	323	544	14.6	18.0
–5	550	377	625	17.6	19.4
–6	550	389	643	21.4	23.0
–7	600	376	584	14.2	17.9
–8	600	374	584	14.1	18.9
–9	650	373	545	13.4	19.3
–10	650	370	550	12.7	19.4
–11	700	373	500	10.3	19.2
–12	700	373	510	10.5	16.8
–13	750	361	467	4.6	16.0
–14	750	349	463	9.5	16.7

All tests at a strain rate of $3.3 \times 10^{-4}\ s^{-1}$ throughout.

Table 5.1.3
Tensile Test Results for the V-15Cr-5Ti Alloy

Specimen Identific.	Test Temp. (°C)	0.2% Y.S. (MPa)	UTS (MPa)	Elongation	
				Uniform (%)	Total (%)
VCT-1	RT	457	690	23.3	27.8
-2	RT	521	684	22.4	27.7
-28	450	358	550	13.4	16.5
-29	450	330	537	12.5	16.8
-3	500	316	528	14.3	18.4
-4	500	320	536	13.7	15.9
-5	550	323	561	16.2	19.7
-6	550	332	544	14.0	18.7
-7	600	321	565	13.5	16.6
-8	600	291	547	12.2	15.8
-9	650	323	561	13.3	17.3
-10	650	299	542	13.9	16.9
-11	700	310	590	15.7	19.3
-12	700	307	583	15.9	18.9
-14	750	302	556	11.6	15.4
-30	750	305	572	11.8	16.1

All tests at a strain rate of 3.3×10^{-4} s^{-1} throughout.

Table 5.1.4
Tensile Test Results for the VANSTAR-7 Alloy

Specimen Identific.	Test Temp. (°C)	0.2% Y.S. (MPa)	UTS (MPa)	Elongation	
				Uniform (%)	Total (%)
VS-1	RT	408	572	20.0	25.1
-2	RT	438	583	19.9	23.5
-26	450	226	427	14.6	17.3
-27	450	250	427	13.5	17.8
-3	500	250	430	19.1	20.0
-4	500	246	423	13.8	17.0
-28	550	231	421	16.3	18.9
-29	550	248	432	13.9	17.9
-7	600	217	406	14.4	18.4
-8	600	228	418	14.2	17.2
-9	650	231	410	11.2	15.0
-10	650	224	405	11.2	15.6
-11	700	238	425	14.3	17.1
-30	700	230	407	12.4	16.7
-13	750	(a)	396	(a)	15.1
-14	750	225	396	10.3	15.5

All tests at a strain rate of 3.3 $\times 10^{-4}$ s^{-1} throughout.

(a) No reading of load at yield; chart recorder malfunctioned.

Period Ending June 30, 1980, DOE/ER-0045/3, p. 146 (October 1980).

2. K. C. Liu, "Fatigue Behavior of Unirradiated V-15%Cr-5%Ti," Alloy Development for Irradiation Performance, Qtrly. Progress Report for Period Ending September 30, 1980, DOE/ER-0045/4, p. 100 (December 1980).

3. K. C. Liu, "Fatigue Behavior of Path C Vanadium Scoping Alloys," Alloy Development for Irradiation Performance, Qtrly. Progress Report for Period Ending December 31, 1980, DOE/ER-0045/5, p. 98 (April 1981).

4. R. L. Ammon, "Melting and Processing of Niobium and Vanadium Alloy Sheet and Rod," Report AESD-M-FR-79-004, Westinghouse Advanced Energy Systems Division, Pittsburgh, PA (October 1979).

5. G. A. Whitlow, R. A. Nadler, and R. C. Svedberg, "Vanadium Alloy Cladding Development: Final Report," WARD-3791-47, Westinghouse Advanced Reactors Divison, Madison, PA (November 1970).

5.2 CORROSION OF TITANIUM ALLOY SPECIMENS FROM AD-1 EXPERIMENT - R. J. Puigh (Hanford Engineering Development Laboratory)

5.2.1 ADIP Task

The Department of Energy (DOE)/Office of Fusion Energy (OFE) has cited the need for these data under the following ADIP Program Plan Tasks:") I.B.3, Fatigue Crack Growth in Reactive/Refractory Alloys (Path C); I.B.7, Stress/Strain Controlled Fatigue of Reactive/Refractory Alloys (Path C); I.B.15, Tensile Properties of Reactive/Refractory Alloys (Path C); and I.C.8, Irradiation Creep of Reactive/Refractory Alloys (Path C).

5.2.3 Objectives

The objective of the AD-1 irradiation experiment is to provide baseline, high-fluence data at several elevated temperatures on materials which have been suggested for the first wall of a fusion power reactor. Specifically, the experiment is designed to provide data concerning temperature and radiation effects upon mechanical properties such as fatigue, crack growth, tensile strength and creep. Characterization of the radiation effects upon microstructure and swelling will also be performed.

5.2.4 Summary

The three capsules comprising the AD-1 experiment were designed for irradiation temperatures of 394°C, 450°C and 550°C and have been irradiated in EBR-II until fluences greater than 4×10^{22} n/cm^2 (E>0.11 MeV) were attained. Corrosion was observed on several titanium alloy specimens contained in the subcapsule designed for an irradiation temperature of 550°C, and evidence has been obtained indicating this corrosion is due to the NaK and water reaction which occurred during the cleaning of the specimens. The other two capsules have been opened using a new cleaning technique and no evidence for corrosion has been observed.

5.2.5 Progress and Status

In the last report on the AD-1 experiment[2] the details of the experiment were given. Also reported was the evidence for corrosion found on the titanium alloys. Examples of this corrosion can be seen in Figure 5.2.1. In general this corrosion attack was found to be very localized. All the titanium alloys were equally affected. From independent chemical testing it was concluded that the corrosion was not the result of the hydroxide solution formed after the cleaning of the NaK from the specimens.

The remaining two pins have been opened using a process which minimizes the NaK on the specimens and avoids the possibility of introducing liquid water on the NaK covered specimens. Upon opening the subcapsule the specimens are dropped onto a large mesh screen and are then moved to a separate tray for the removal of the residual NaK remaining on the specimens. An argon plus water vapor gas is then passed over the specimens to remove the residual NaK. A condensation trap is located in the gas line just before the covered tray containing the specimens. The reaction lasts from 3 to 4 hours. The specimens are then rinsed with water and decontaminated in a water solution containing TURCO 4306 D.

To ascertain whether the water reaction with the NaK was the source of the corrosion, a piece of Ti-6Al-4V tubing was placed in the residual NaK from the subcapsule. The NaK was then removed using a process equivalent to the one used in cleaning the 550°C capsule's specimens. Again water droplets could be observed entering the tray containing the NaK and Ti-6Al-4V tube. The tube was then rinsed with water and visual evidence for corrosion was found. This observation plus the fact that no evidence of corrosion was found on the specimens from the other two capsules tends to give credence to our hypothesis that the NaK plus water reaction was responsible for the corrosion observed earlier.

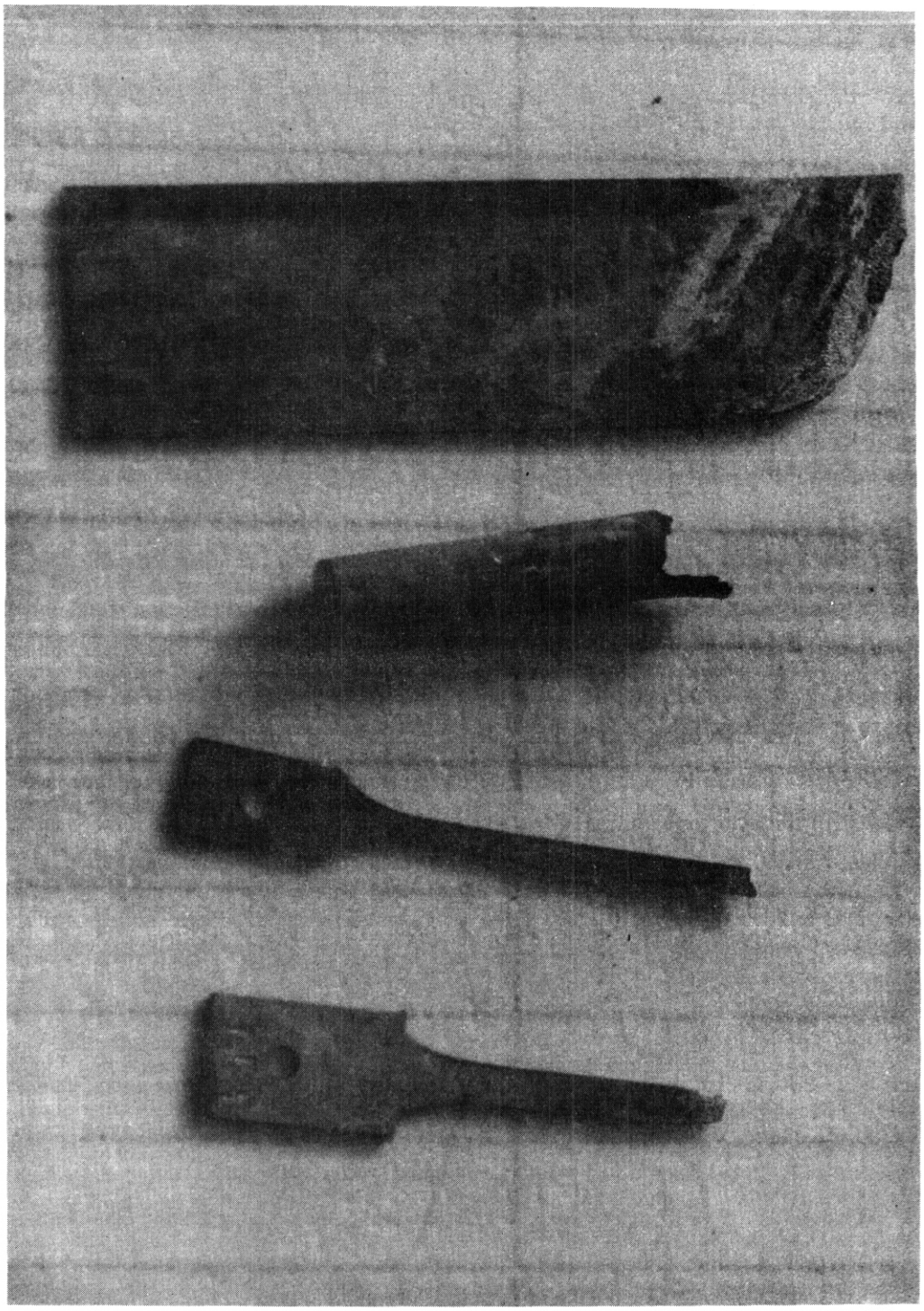

FIGURE 5.2.1 Corrosion observed in titanium specimens irradiated at 550°C.

5.2.6 Future Work

Upon the completion of the decontamination of these specimens the post irradiation testing of these specimens will begin.

Selected fragments from the corroded specimens have been sent to McDonnell-Douglas for examination.

5.2.7 References

1. J. O. Stiegler, et al, "Alloy Development for Irradiation Performance," The Fusion Reactor Materials Program Plan, July, 1978.

2. R. J. Puigh and E. K. Opperman, "Examination of Titanium Alloy Specimens Irradiated in EBR-II, *ADIP Quarterly Report, Dec. 31,* 1979, DOE/ER-0045/1, pp. 58-69.

5.3 THE EFFECT OF HYDROGEN ON FLAW GROWTH OF TITANIUM ALLOY Ti-6242s

G. W. Wille and P. S. Pao (McDonnell Douglas Corporation)

5.3.1 ADIP Task

Task 1.B.3, Fatigue Crack Growth in Reactive/Refractory Alloys (Path C).

5.3.2 Objective

The objective of this study is to develop quantitative data to determine the effects of both internal and external hydrogen on fatigue crack growth of Ti-6242s alloy at temperatures and hydrogen pressures of interest for fusion reactors.

5.3.3 Summary

Fatigue crack growth rate tests are being conducted at room and elevated temperatures with environment hydrogen pressures from 0 to 400 Pa on Ti-6242s samples containing 50 and 530 wppm internal hydrogen. Based on these tests the following conclusions have been made: External environment hydrogen at pressures less than 400 Pa has no effect on the fatigue crack growth rate in Ti-6242s with 50 or 530 wppm H; internal hydrogen at a concentration of 530 wppm increases the crack growth rate at intermediate and high stress intensity factor levels; the crack growth rate in Ti-6242s with 530 wppm H progressively diminishes as the temperature increases from room temperature; and the crack growth rate in hydrogen charged Ti-6242s increases with decreasing cyclic load frequency.

5.3.4 Progress and Status

The fatigue fracture-surfaces of failed test specimens have been examined. Representative fatigue fracture-surfaces of as-received (50 wppm H) and hydrogen charged (530 wppm H) Ti-6242s tested in argon at 25°C are shown in Figure 5.3.1 and 5.3.2. Fatigue striations are not defined in any of the fractographs. The fatigue fracture in the as-received material (Figure 5.3.1) is predominantly transgranular with

some ductile tearing; this is typical of other as-received samples tested in vacuum or hydrogen pressure less than 400 Pa and at room or elevated temperatures. The fracture surface of hydrogen charged material (Figure 5.3.2) shows a large amount of intergranular separation along alpha grain boundaries, although some transgranular fracture is visible. The fine protrusions and craters evident in Figure 5.3.2 agree well with the alpha grain size of the hydrogen charged microstructure shown in Figure 5.3.3. Ductile ridges associated with these protrusions and craters may result from tearing the continuous beta phase surrounding the alpha grains during the fatigue process. Other hydrogen charged specimens tested at 25°C in a hydrogen environment, rather than argon, exhibited fracture surfaces similar to that sham in Figure 5.3.2.

At 200°C, the fatigue crack growth in both as-received and hydrogen charged Ti-6242s exhibit the same transgranular fracture pattern as shown in Figure 5.3.4. This suggests that the internal hydrogen concentration is not influencial at higher temperatures.

5.3.5 Conclusions

The principle conclusions based on this study therefore are as follows:

- External hydrogen at pressures <400 Pa has no effect on the fatigue-crack-growth rate in either as-received or hydrogen-charged Ti-6Al-2Sn-4Zr-2Mo-0.1Si (Ti-6242s).
- Internal hydrogen at a concentration of 530 wppm significantly increases the fatigue-crack-growth rate in Ti-6242s at intermediate and high stress-intensity-factor amplitude, ΔK, levels.
- The increase in fatigue-crack-growth rate in hydrogen-charged Ti-6242s progressively diminishes as the temperature increases from room temperature to 423 K.
- Stress-assisted hydride formation is hypothesized to be the mechanism for hydrogen-enhanced fatigue crack-growth in Ti-6242s containing 530 wppm hydrogen based on the fatigue-crack-growth kinetics and fractographic observations.
- The fatigue-crack-growth rate in hydrogen-charged Ti-6242s increases with decreasing cyclic load frequency.

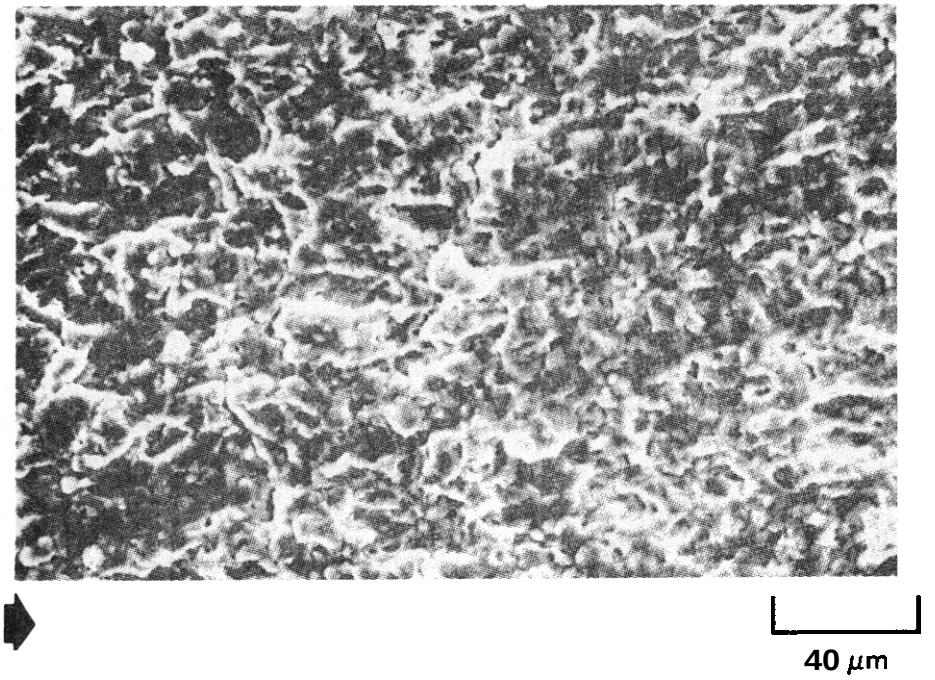

FIGURE 5.3.1. FRACTURE SURFACE OF AS-RECEIVED Ti-6242s TESTED AT ROOM TEMPERATURE IN ARGON. ARROW INDICATES CRACK PROPAGATION DIRECTION.

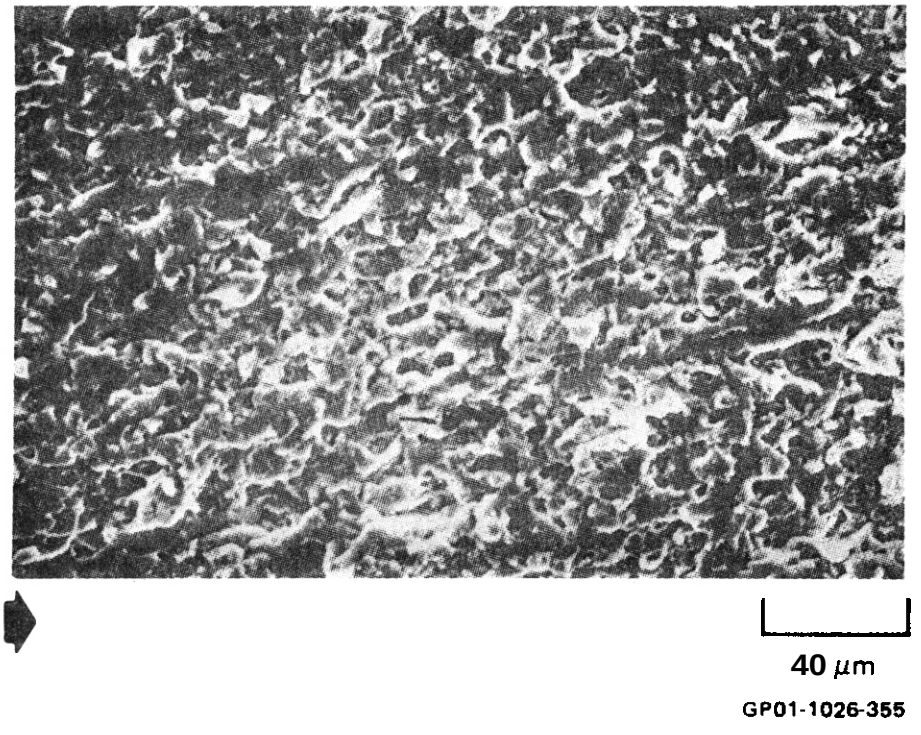

FIGURE 5.3.2. FRACTURE SURFACE OF HYDROGEN-CHARGED Ti-6242s TESTED AT ROOM TEMPERATURE IN ARGON. ARROW INDICATES CRACK PROPAGATION DIRECTION.

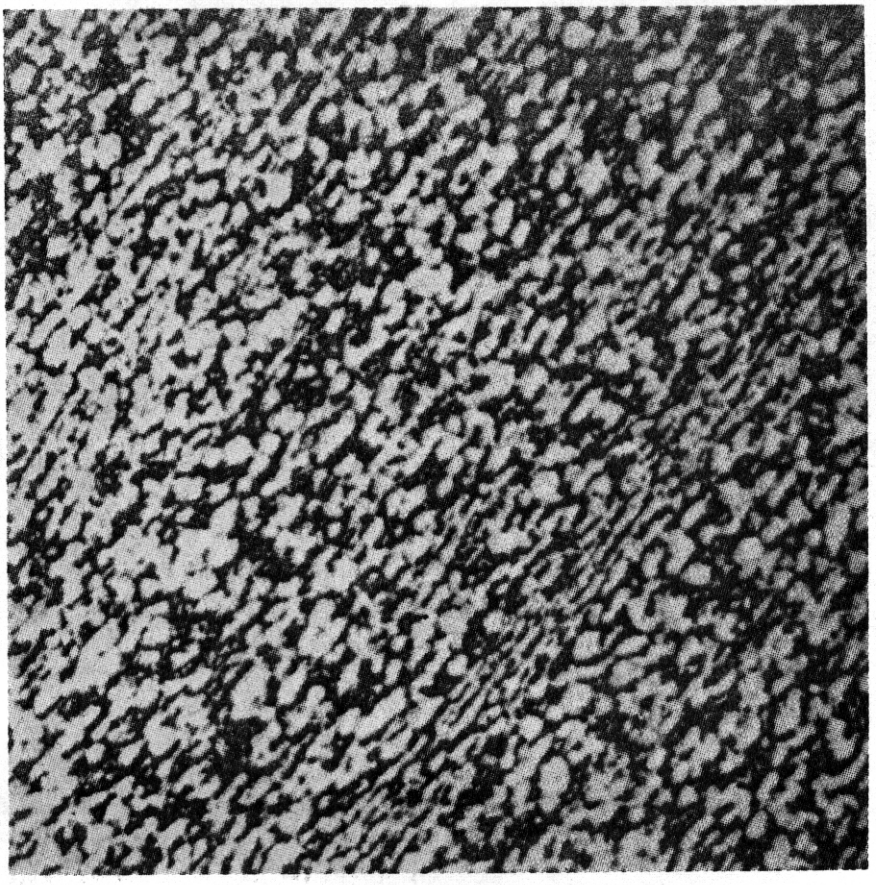

FIGURE 5.3.3. PHOTOMICROGRAPH OF Ti-6242s HYDROGEN CHARGED TO 24,000 appm (530 wppm) H.

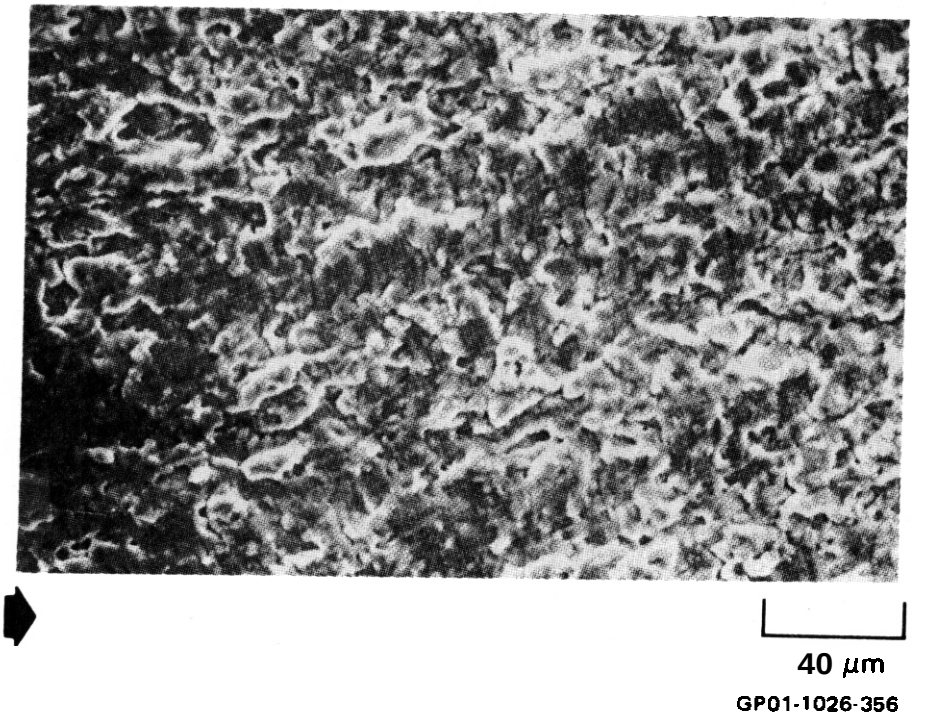

FIGURE 5.3.4. TYPICAL FRACTURE SURFACE OF AS-RECEIVED *AND* HYDROGEN CHARGED Ti-6242s TESTED AT 200°C, IN ARGON ENVIRONMENT. ARROW INDICATES CRACK PROPAGATION DIRECTION.

6. PATH D ALLOY DEVELOPMENT — INNOVATIVE MATERIAL CONCEPTS

6.1 THE EFFECT OF NEUTRON IKRADIATION ON THE TENSILE PROPERTIES OF LONG-RANGE-ORDERED ALLOYS — D. N. Braski (Oak Ridge National Laboratory)

6.1.1 ADIP Task

ADIP Task I.B.16, Tensile Properties of Special and Innovative Materials.

6.1.2 Objective

The objective of this research is to define the response of a new class of $(Fe,Ni)_3V$ long-range-ordered (LRO) alloys to both neutron and ion irradiation. The overall goal is to determine the potential use of this alloy class as a structural material for fusion energy systems.

6.1.3 Summary

Postirradiation tensile tests were conducted on specimens of two different long-range-ordered alloys that had been irradiated in the ORR at temperatures of 250, 350, and 550°C, to a fluenre produring 3.8 dpa and 19 to 29 at. ppm He. The irradiation increased the yield strength or "hardened" the material while the ultimate strength was derreased at all temperatures except 350°C. The ductility also decreased at all test temperatures, as evidenced by the reduction in uniform elongation and the appearance of areas of intergranular fracture in scanning electron microscopy (SEM) fractographs. The reason for the relatively high ductility of the specimens that were irradiated and tested at 350°C compared to those at either 250 or 550°C is not clear.

6.1.4 Progress and Status

6.1.4.1 Introduction

For the past year, a number of LRO alloys in the $(Fe,Ni)_3V$ system have been investigated to determine to their resistanre to irradiation using 4 MeV nickel ions and simultaneously injected $He^+ + D_2^+$ (refs. 1, 2, and 3). Under the experimental conditions used, the LRO alloys have demonstrated lower swelling than 20%-cold-worked type 316 stainless steel

that had been used as a standard of comparison. Small tensile specimens of two LRO alloys, LRO-15 and -16, were also inrluded in the ORR-MFE-2 irradiation experiment. The experiment ended in March 1980 after successfully completing 10,950 MWd of exposure. The irradiated samples were tensile tested in vacuum at the same temperature as the irradiation (i.e., 250, 350, OK 550°C). The fracture surfaces of representative specimens were subsequently examined in a shielded SEM. The results are presented in this report.

6.1.4.2 Experimental

Small ingots of LRO-15 and -16, with the compositions given in Table 6.1.1, were produced by arc melting, clad in molybdenum sheet, hot rolled at 1100°C. and finally cold rolled with intermediate anneals at 1100°C to produce a final sheet thickness of 0.76 mm (ref. 4). The alloys were heat treated into the fully ordered condition. This was achieved by annealing at 1050°C for 10 min, water-quenching, aging at 700°C for 7 h, aging at 650°C for 24 h, and finally aging at 600°C for 67 h. Sheet-tensile specimens (SS-1 type) having a gage width of 1.52 mm and a gage length of 20.32 mm were machined from the sheet. (See ref. 5 for specimen configuration.) Nine specimens of each alloy were included in the ORR-MFE-2 experiment[6] with three specimens of each at 250, 350, and 550°C. The arrumulated fluenre was 4.8 $\times 10^{25}$ neutrons/m^2 (>0.1 MeV), which resulted in a displacement damage level of 3.8 dpa. The amount of helium

Table 6.1.1. Nominal Composition of Two Long-Range-Ordered Alloys

Alloy	Composition, wt %			
	Fe[a]	Ni	CO	V
LRO-15	36	20	21	23
-16	46	31	0	23

[a]Content by difference.

generated in the LRO–15 and –16 sperimens was calculated to be approximately 19 and 29 at. ppm, respertively. The sperimens were tensile tested in an Instron machine in a shielded hot cell. The machine was fitted with a vacuum rhamber that operated in the 10^{-5} Pa range. The crosshead speed used was 0.05 mm/min. Fracture surfaces were examined in a shielded SEM at 25 kV.

6.1.4.3 Results

The irradiation conditions, tensile results on unirradiated control specimens, and results for the irradiated material are given in Table 6.1.2 and Fig. 6.1.1. Three irradiated specimens, but only one control specimen, of each LRO alloy were tensile tested at the three test temperatures (see Table 6.1.2). There was no control specimen for the LRO–15 alloy at 350°C. The three values of the respective tensile properties have been averaged and these values have been plotted in Fig. 6.1.1 as a function of irradiation temperature. The irradiation temperature was also used as the tensile test temperature. The ultimate and yield strengths of unirradiated and irradiated LRO–15 are shown in Fig. 6.1.1(a), while those for LRO–16 are given in Fig. 6.1.1(b). Unirradiated material of both alloys showed ultimate strengths that decreased and yield strengths that increased, with increasing test temperature. The increase in yield strength with temperature is an interesting feature of LRO alloys, and possible mechanisms causing it are discussed by Stoloff and Davis.[7] The LRO–15 alloy [Fig. 6.1.1(a)] demonstrated a higher ultimate strength than LRO–16 throughout this temperature range — perhaps due to its cobalt content.

Irradiation raised the yield strength of both LRO alloys; the "hardening" effect was greatest at 250°C and decreased with temperature until, at 550°C, the irradiation produced little change in the yield strength. The ultimate strength of both LRO alloys was decreased by the irradiation to values near the yield at 250 and 550°C, but was increased by irradiation at 350°C. The effect of the irradiation on the ductility of LRO–15 and –16 is shown in Fig. 6.1.1(c), with uniform elongation plotted as a function of the test temperature. Again, both alloys behaved

Table 6.1.2. Unirradiated and Postirradiated Tensile Properties of LRO-15 and -16[a]

Irradiation Temperature (°C)	Displacement Damage[b] (dpa)	Helium Level[b] (at. ppm)	Test Temperature (°C)	Strength, MPa		Elongation, %	
				0.2% Offset Yield	Ultimate	Uniform	Total
			Allay LRO-15				
c			250	331	1155	32.55	35.03
c			550	380	1012	35.49	36.75
250	3.8	-19	250	842	994	4.85	6.33
				989	1124	4.56	6.15
				1059	1156	5.03	6.63
				963 av[d]	1091 av	4.81 av	6.37 av
350	3.8	-19	350	649	1194	18.44	19.23
				655	1185	17.50	18.15
				652	1184	18.43	19.34
				652 av	1188 av	18.12 av	18.91 av
550	3.8	-19	550	499	574	2.05	2.28
				495	621	3.70	3.80
				526	549	0.68	0.91
				507 av	581 av	2.14 av	2.33 av
			Alloy LKO-16				
c			250	367	988	26.06	26.22
c			350	399	974	24.98	25.04
c			550	419	a99	30.75	31.31
250	3.8	-29	250	875	882	7.89	9.91
				866	878	9.33	11.63
				879	894	9.18	10.02
				873 av	885 av	8.80 av	10.52 av
350	3.8	-29	350	650	1072	13.04	13.64
				684	1083	12.87	13.45
				834	1123	11.20	11.75
				723 av	1093 av	12.37 av	12.95 av
550	3.8	-29	550	441	475	2.56	2.90
				431	526	4.12	4.42
				441	465	0.88	1.12
				438 av	489 av	2.52 av	2.81 av

[a]All specimens were fully ordered before irradiation.

[b] e fluenre on the specimens was 4.8 × 10^{25} neutrons/m^2 00.1 MeV).

[c]Unirradiated.

[d]Averages are for the three specimens with identical irradiation and test conditions.

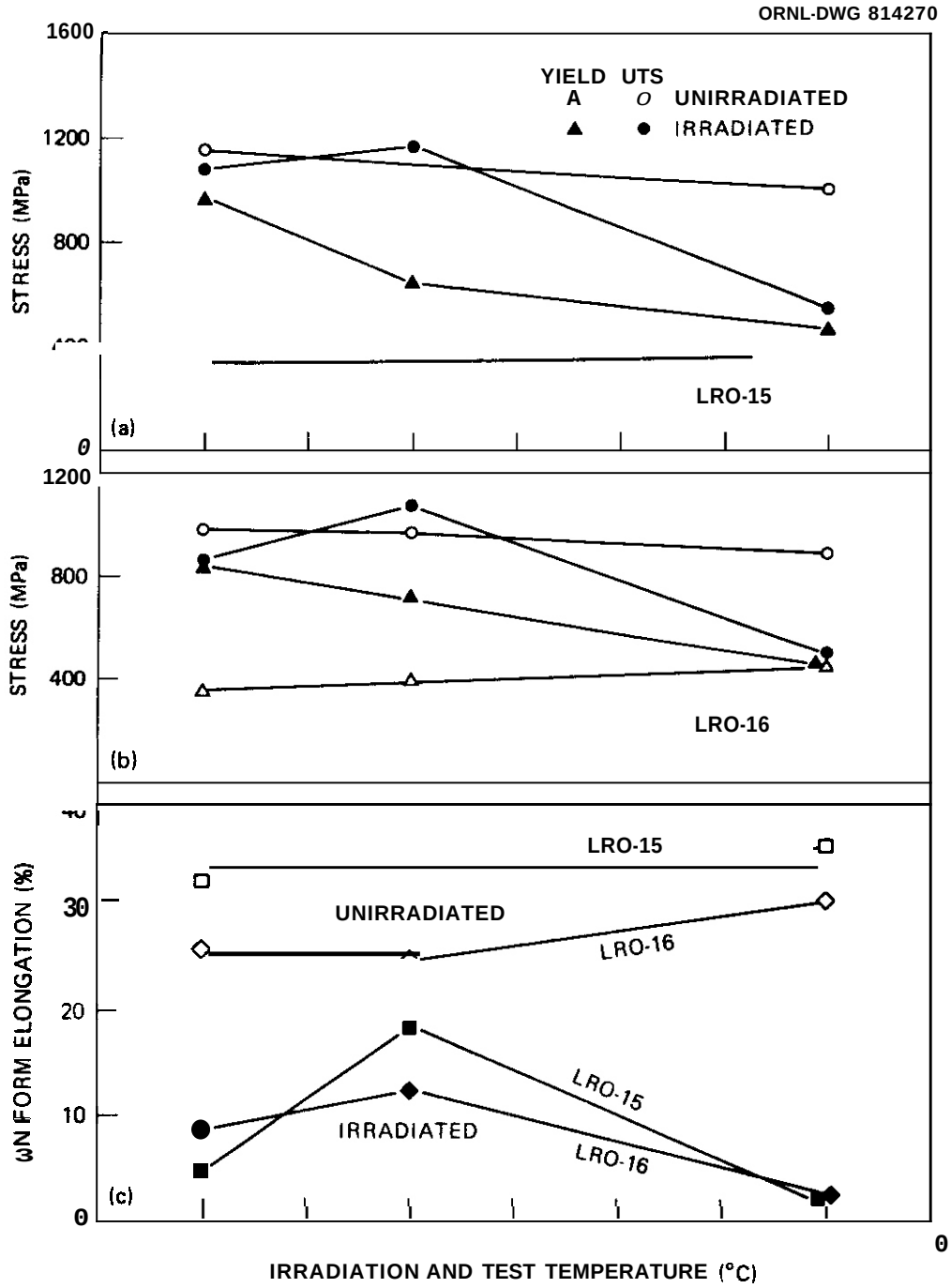

Fig. 6.1.1. Postirradiation Tensile Properties for LRO–15 and –16 after Irradiation in the ORR to Produce **3.8** dpa and 19 or 29 at. ppm He, Respectively. The tensile properties are given as a function of irradiation and test temperature. (a) Yield and ultimate strength (UTS) of LRO–15, (b) yield and ultimate strength of LRO–16, and (c) uniform elongation of LRO–15 and –16.

similarly. Irradiation has reduced the ductility for all three temperatures, with low ductilities at the lower and higher temperatures and relatively higher ductilities at 350°C. The reduced ductility was probably the result of the irradiation-produced increase in the yield strength and it followed the usually observed higher strength-lower ductility relationship. Helium embrittlement also may have contributed to the ductility losses at 550°C for both LRO alloys. The reason for the ductility maximum at 350°C is not clear. Future transmission electron microscopy may supply microstructural information that will help explain the observed property changes.

Scanning electron micrographs of typical fracture surfaces from both unirradiated and irradiated LRO-16 specimens are shown in Fig. 6.1.2. (The fracture surfaces of LXO-15 specimens were not examined because of their extremely high radioactivity levels, but on the basis of the mechanical properties they can be expected to be similar to those for LRO-16.) The unirradiated specimen tested at 250°C [Fig. 6.1.2(a)] had a dimpled fracture surface, which is characteristic of ductile fracture. However, the "bottoms" of the dimples were often flat instead of conical in shape. Sometimes the flat surface had "river" or flow patterns indicative of cleavage fracture, but often it was quite smooth, suggesting intergranular fracture. The unirradiated specimen tested at 350°C [Fig. 6.1.2(b)] had a similar fracture appearance to that at 250°C except that there were fewer flat areas. At 550°C [Fig. 6.1.2(c)], the unirradiated specimen had a totally dimpled appearance. Therefore, the unirradiated fracture surfaces were mostly ductile, with a few areas of possible brittle behavior at the lower temperatures, and completely ductile at 550°C. The irradiated specimens tested at 250°C [Fig. 6.1.2(d)] and 350°C [Fig. 6.1.2(e)] had fracture surfaces quite similar in appearance to those for unirradiated material, except that there were more areas that appeared to be intergranular. Several examples of such areas are marked in Fig. 6.1.2(d) and (e). The specimens tested at 550°C [Fig. 6.1.2(f)] had the greatest amount of intergranular fracture, with the exposed grain-boundary surfaces of several rather large grains shown. A good qualitative correlation can be seen between these fractographs and the

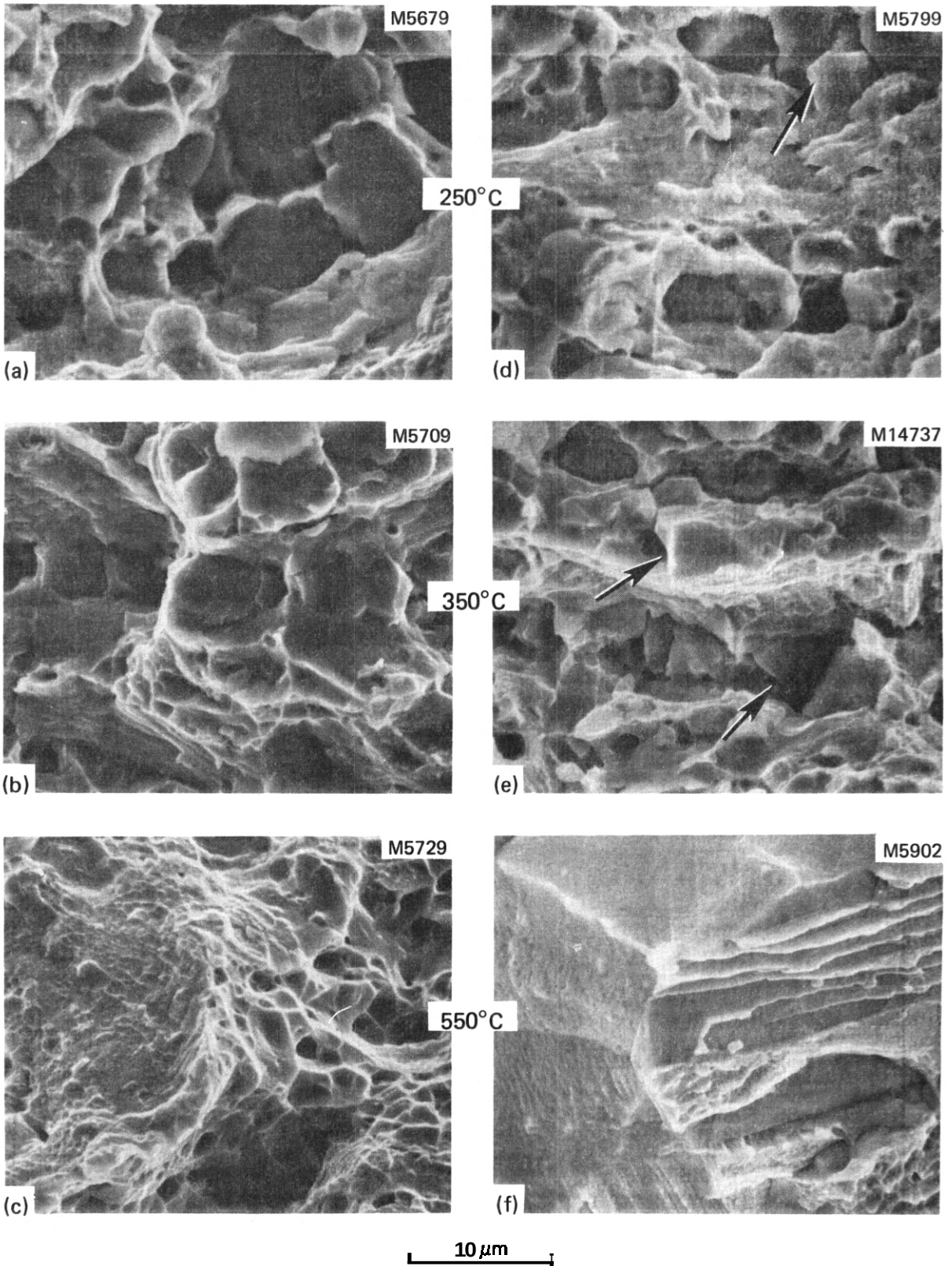

Fig. 6.1.2. Scanning Electron Mirroscopy Frartographs of LRO-16 Specimens, (a,b,c) Unirradiated and (d,e,f) Irradiated in ORR to Produce 3.8 dpa and 29 at. ppm He. Irradiation and test temperature are given. Arrows in (d) and (e) indicate areas of possible intergranular fracture.

measured postirradiation tensile properties. In general, the reduction in ductility can be related to the increase in fraction of intergranular fracture. At the highest temperature, it is likely that intergranular fracture was aided by the presence of helium in the grain boundaries. More work such as transmission electron microscopy needs to be done to fully understand the results. Transmission electron microscopy is also needed to assess the amount of swelling and other microstructural changes that occurred in LRO specimens due to the irradiation.

6.1.5 Conclusions and Future Work

Postirradiation tensile tests were conducted on LRO-15 and -16 specimens that been irradiated in the ORR to a fluence of 4.8 x 10^{25} neutrons/m^2 (>0.1 MeV), producing 3.8 dpa and 19 to 29 at. ppm He. Irradiation and test temperatures were 250, 350, and 550°C. From the results the following conclusions were made.

1. The irradiation of both LRO alloys raised the yield strength above that for the unirradiated material. The effect was especially noticeable at the lower irradiation temperatures, where the yield stress was more than doubled.

2. The irradiation reduced the ultimate strength slightly at 250°C and markedly at 550°C for both alloys. The ultimate strength was increased slightly by irradiation at 350°C.

3. The irradiation reduced the ductility of both LRO alloys as shown by their low uniform elongation values and the increase in fraction of intergranular fracture area observed by SEM. The ductility maximum observed near 350°C for both alloys should be investigated further.

Microstructural examinations, using mainly TEM, will be conducted to determine the effect of the neutron irradiation on the phase stability, degree of order, dislocation microstructure, and amount of swelling in LRO-16.

6.1.6 References

1. D. N. Braski, "The Effect of 4-MeV Nickel Ion Irradiation on the Microstructure of $(Fe,Ni)_3V$ Long-Range-Ordered Alloys," *ADIP Quart. Prog. Rep. June* 30, 1980, DOE/ER-0045/3, pp. 162–73.

2. D. N. Braski, "The Effect of 4-MeV Nickel Ion Irradiation on the Microstructure of $(Fe,Ni)_3V$ Long-Range-Ordered Alloys," *ADIP Quart. Prog. Rep. Sept. 30, 1980,* DOE/ER-0045/4, pp. 114-21.
3. D. N. Braski, "The Effect of 4-MeV Nickel Ion Irradiation on the Microstructure of $(Fe,Ni)_3V$ Long-Range-Ordered Alloys," *ADIP Quart. Prog. Rep. Dec. 31, 1980,* DOE/ER-0045/5, pp. 119-22.
4. C. T. Liu, "Development of Iron-Base Alloys with Long-Range-Ordered Crystal Structure," *ADIP Quart. Prog. Rep. Dec. 31, 1980,* DOE/ER-0045/5, pp. 72-79.
5. M. L. Grossbeck and K. R. Thoms, "ORR-MFE-4: A Spectral Tailoring Experiment to Simulate the He/dpa Ratio of a Fusion Reactor in Austenitic Stainless Steel," *ADIP Quart. Prog. Rep. June 30, 1980,* DOE/ER-0045/3, p. 18.
6. J. W. Woods, E. E. Bloom, A. F. Zulliger, "Status of ORR-WE-2," *ADIP Quart. Prog. Rep. June 30, 1978,* DOE/ER-0058/2, pp. 132-46.
7. N. S. Stoloff and R. G. Davis, *Acta Metall.* **12**: 473 (1964).

6.2 MECHANICAL PROPERTIES OF IRON-BASE LONG-RANGE-ORDERED ALLOYS - C. T. Liu (Oak Ridge National Laboratory) and N. S. Stoloff (Rensselaer Polytechnic Institute)

6.2.1 ADIP Task

ADIP Task I.B.12, Stress-Rupture Properties of Special and Innovative Materials, and Task I.B.8, Stress/Strain Controlled Fatigue of Special and Innovative Materials.

6.2.2 Objective

The objective of this study is to evaluate the mechanical properties of an unique class of high-temperature alloys — ductile long-range-ordered (LRO) alloys based on $(Fe,Ni)_3V$ — as potential structural materials for fusion energy systems.

6.2.3 Summary

Creep behavior and fatigue properties of several iron-base LRO alloys were characterized as functions of stress, temperature, and alloy composition. The LRO alloys showed a very rapid change in creep rate near their critical ordering temperature, T_c. Formation of long-range order lowers the steady-state creep rate by more than 3 orders of magnitude. The alloys exhibited a rupture ductility of 3.7 to 5.6% at temperatures below T_c. Preliminary examination of fracture surfaces revealed that the low ductility is associated with nucleation, growth, and coalescence of cavities along grain boundaries. Limited creep data indicate that preparation of LRO-37 (Fe–22% V–40% Ni–0.4% Ti) from commercial-grade ferrovanadium does not degrade the creep properties of the alloy, compared to material produced from high-purity melt stock. High-frequency fatigue tests of alloy LRO-37 showed a small decrease in fatigue resistanre with increasing temperature. Comparison of fatigue data among commercial alloys has demonstrated that LRO-37 is superior to type 316 stainless steel, Inconel 617, and Hastelloy X near 600°C, and superior to Inconel 617 near 400°C and at 25°C. Fractographic examination of fatigue failure surfaces in alloy LRO-37 revealed a very faceted appearance, whirh is partially due to cracking along annealing twin boundaries.

6.2.4 Progress and Status

6.2.4.1 Introduction

Long-range-ordered alloys generally offer significant advantages over conventional or disordered alloys for high-temperature structural applications.[1,2] This advantage is based largely on relatively slow solid-state diffusion processes and unique dislocation dynamics of ordered lattices. The main difficulty limiting the use of LRO alloys is their low ductility and brittle fracture in the ordered state. Recent work on the $(Fe,Ni)_3V$ alloy system has demonstrated[3,4] that the ductility of the ordered alloys can be controlled by adjusting alloy composition and ordered crystal structure. The alloys with $L1_2$-type cubic-ordered structure are ductile with tensile elongation exceeding *30%* at room temperature. These LRO alloys are fabricable and weldable by conventional techniques. Limited results have indicated that the LRO alloys possess high elevated-temperature strength, good structural stability, and resistance to radiation damage. Accordingly, they offer promise as structural materials for fusion reactor systems. The current efforts of the LRO alloy development are focussed on characterization of their mechanical properties, including creep behavior and fatigue properties. The nominal composition of alloys included in this report is given in Table *6.2.1.*

Table *6.2.1.* Nominal Composition of Long-Range-Ordered Alloys

Alloy	Composition, wt %			
	Fe[a]	Ni	V	Ti
LRO-35	*45.6*	*32*	*22*	*0.4*
-*31*	*31.6*	*40*	*22*	*0.4*
-*38*	*37.1*	*40*	*22*	*0.9*
-*39*	*45.1*	*32*	*22*	*0.9*

[a]Content by difference.

6.2.4.2 Creep Behavior

Creep behavior of LRO alloys was characterized as functions of stress, temperature, and alloy composition. Creep specimens, fabricated from 0.76-mm sheet, were solution treated for 20 min at 1150°C, followed by an ordering treatment involving step-cooling from 650 to 500°C over a period of five days. Creep tests were performed in vacuum (1×10^{-4} Pa) under a dead-load arrangement and strain was measured by use of a dial gage.

The creep data are summarized in Table 6.2.2. The steady-state creep rate of the LRO alloys appears insensitive to nickel and titanium concentration. Alloy LRO-35 tested at 276 MPa shows a very rapid change in creep rate near its critical ordering temperature, T_c, of 690°C. The creep rate decreases from 3.9×10^{-2} to 8.4×10^{-6}/h as the test temperature decreases from 710°C (20° above T_c) to 670°C (20°C below T_c). This demonstrates that formation of long-range order lowers the creep rate of the alloy by more than 3 orders of magnitude. The same change in creep rate near T_c also occurs in LRO-37. The LRO alloys are very resistant to creep deformation when in the ordered state. The creep rate of the LRO alloys is lower than the creep rate is annealed type 316 stainless steel by more than 3 orders of magnitude.

The LRO alloys exhibit a rupture ductility of 3.7 to 5.6% at temperatures below T_c. Preliminary examination of the fracture surfaces showed cavities formed on grain boundaries of the alloys in the ordered state. The low creep ductility is believed to be due to growth and coalescence of cavities along grain boundaries. On the other hand, the alloys showed ductile failure with creep elongation exceeding 50% at temperatures above T_c (Table 6.2.2).

Table 6.2.3 compares the creep properties of LRO-37 type alloy prepared from either high-purity materials or commercial grade materials. The original heat of LRO-37 was prepared from high-purity vanadium while LRO-37-5* and -37-6* were prepared from as-received ferrovanadium and ferrovanadium that had been electron-beam melted for purification. The limited creep data in Table 6.2.3 indirate that the creep properties of LRO-37 are not affected by the purity of the vanadium feed stocks used in

*Alloys LRO-37, heat 5 and LRO-37, heat 6.

Table 6.2.2. Creep Properties of Iron–Base LRO Alloys Tested in Vacuum

Test	Alloy	Creep Condition		Steady–State Creep Rate (h^{-1})	Rupture	
		Stress (MPa)	Temperature (°C)		Ductility (%)	Life (h)
1	LRO–35	276	650	2.6×10^{-6}	a	>1000
2	–35	276	670	8.4×10^{-6}	a	>1100
3	–35	276	690[b]	2.4×10^{-4}	5.6	51.
4	–35	276	710	3.9×10^{-2}	60.0	5.3
5	–35	413	650	2.0×10^{-5}	a	>1000
6	–39	413	650	1.6×10^{-5}	4.6	925
7	LRO–37	413	650	1.1×10^{-5}	a	>1100
8	–37	413	700	5.6×10^{-1}	52.	0.4
9	–38	551	650	4.9×10^{-3}	3.7	15.3

[a]Not ruptured.

[b]T_c of the alloy.

Table 6.2.3. Comparison of Creep Properties of LRO-37[a] Prepared from Pure Vanadium or Ferrovanadium

Alloy	Charge Material	Steady–State Creep Rate[b] (h^{-1})	Rupture	
			Ductility (%)	Life (h)
LRO–37	Pure vanadium	1.1×10^{-5}	c	>1100
–37–5	As–received ferrovanadium	1.3×10^{-5}	7.7	1721
–37–6	EB melted ferrovanadium	1.4×10^{-5}	c	>1000

[a]Fe–40% Ni–22% V–0.4% Ti.

[b]Creep tests at a stress of 413 MPa at 650°C.

[c]Not ruptured.

alloy preparation. Thus, based on consideration of creep properties, it appears to be feasible to lower the cost of alloy preparation by the use of commercial-grade ferrovanadium.

6.2.4.3 Fatigue Properties

Evaluation of the fatigue properties of iron-base LRO alloys at room and elevated temperatures has been initiated under subcontract by Rensselaer Polytechnic Institute (RPI). Rod fatigue samples, with a 3.2-mm minimum diameter gage section, were prepared from a single heat of LRO-37-8.* The samples were heat treated to a fully ordered condition. Tests were conducted in tension-tension cycling (with a minimum stress of 34.5 MPa) in vacuum of 0.1 mPa ($\sim 10^{-6}$ torr) at temperatures of 25, 400, and 600°C. The frequency was maintained constant at 20 Hz during all tests.

Figure 6.2.1 shows the fatigue data for the alloy LRO-37 at test temperatures of 25, 400, and 600°C. There is relatively little decrease in

* Alloy LRO-37, heat 8.

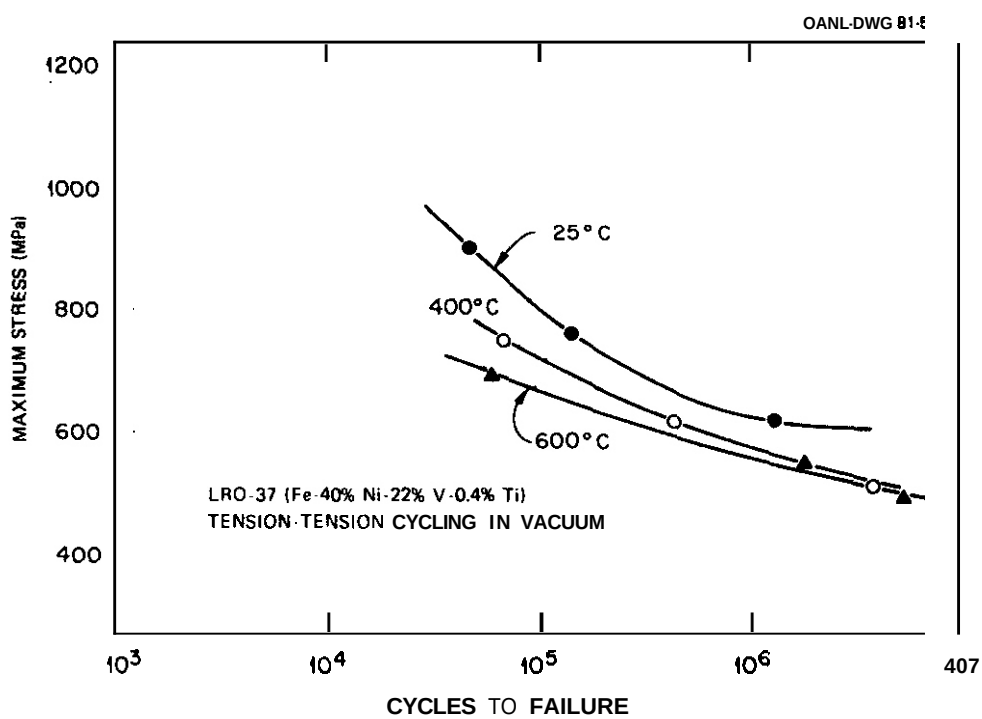

Fig. 6.2.1. Dependence of the High Cycle Fatigue of Alloy LRO-37 on Temperature.

fatigue resistance with temperature, contrary to previous experience with the cobalt-base alloy LRO-1 (Co-17% Fe-23% V). Figures 6.2.2 and 6.2.3 compare the fatigue properties of LRO-37 with commercial alloys. These comparisons show that LRO-37 is superior to type 316 stainless steel, Inconel 617, and Hastelloy X near 600°C, (Fig. 6.2.2) and to Inconel 617 near 400°C and at 25°C (Fig. 6.2.3).

Scanning electron microscropy (SEM) micrographs of fatigue fracture surfaces in LRO-37 are shown in Fig. 6.2.4. Fracture surfaces of LRO-37 revealed a very faceted appearance at 25, 400, and 600°C. This faceted appearance is partially due to cracking along annealing twin boundaries. Examination by SEM of the surface of tested samples showed that the cracks follow both twin bands, Fig. 6.2.5(a) and (c), and slip bands, Fig. 6.2.5(b).

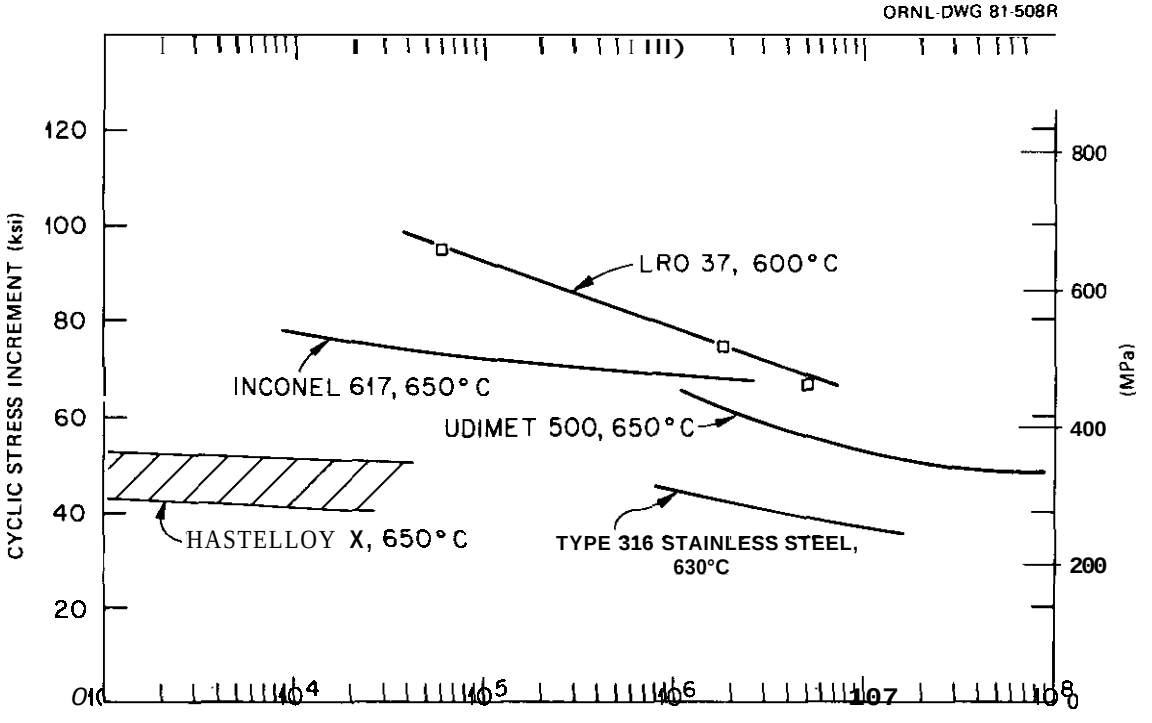

Fig. 6.2.2. Comparison of High Cycle Fatigue Data for Alloy LRO-37 and Several Commercial Alloys for Tests Near 600°C.

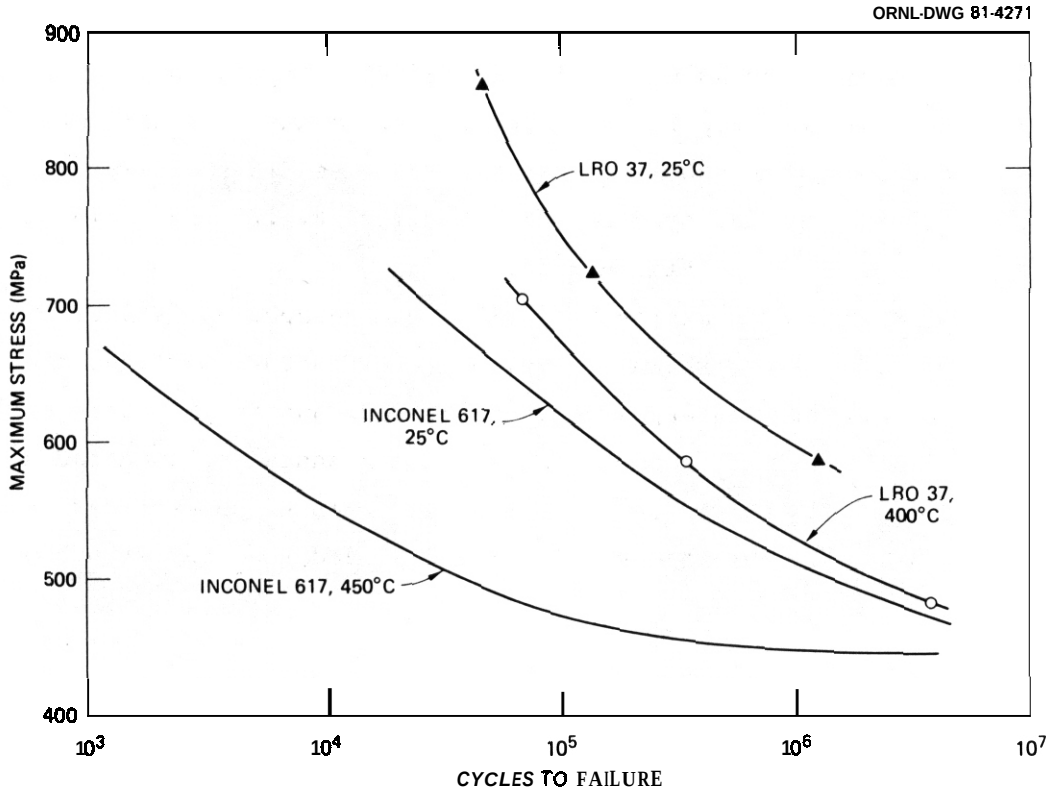

Fig. 6.2.3. Comparison of High Cycle Fatigue for Alloys LRO-37 and Inconel 617 at 25°C and 400 to 450°C.

6.2.5 Conclusions and Future Work

The creep behavior and fatigue properties of iron-base LRO alloys were characterized as functions of stress, temperature, and alloy composition. Creep tests indicate that formation of long-range order in the LRO alloys lowers the steady-state creep rate by more than 3 orders of magnitude. As a result, the alloys show excellent resistance to creep deformation in the ordered state. The ordered LRO alloy exhibited a rupture ductility of 3.7 to 5.6% at temperatures below T_c. Detailed examination of the failure mode is in progress.

Fatigue properties of LRO-37 (Fe–22% V–40% Ni–0.4% Ti) have been evaluated. High-frequency fatigue tests indicate only a small decrease in fatigue resistance with increasing test temperature. Comparison of this fatigue data with data on commercial alloys shows that LRO-37 is superior to type 316 stainless steel, Inconel 617, and Hastelloy X near 600°C, and to Inconel 617 near 400°C and at 25°C. Fractographic features of

Y-178846

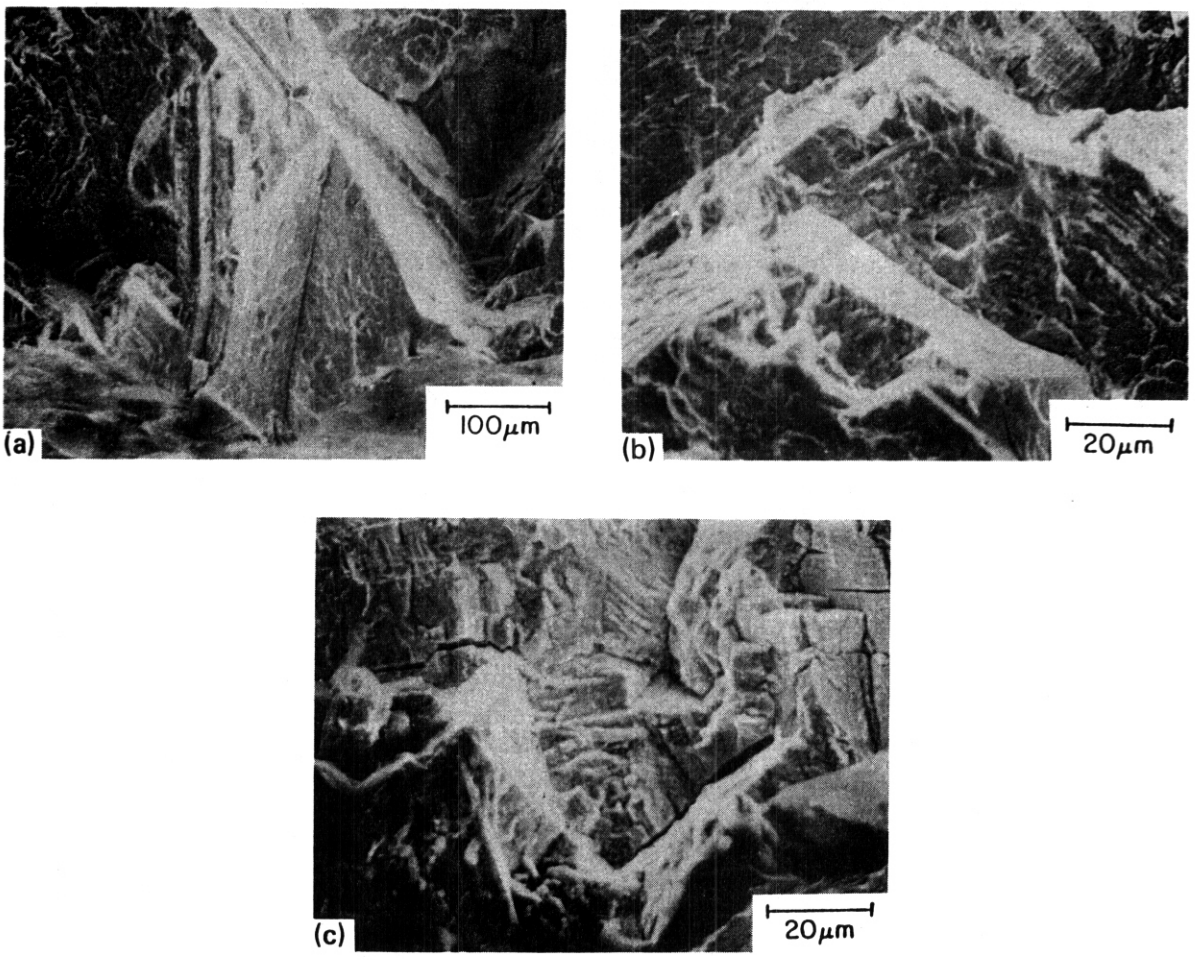

Fig. 6.2.4. Fatigue Fracture Surfaces of Alloy LRO-37 Tested at (a) 25°C, (b) 400°C, and (c) 600°C. (Rensselaer Polytechnic Institute prints.)

Y-178847

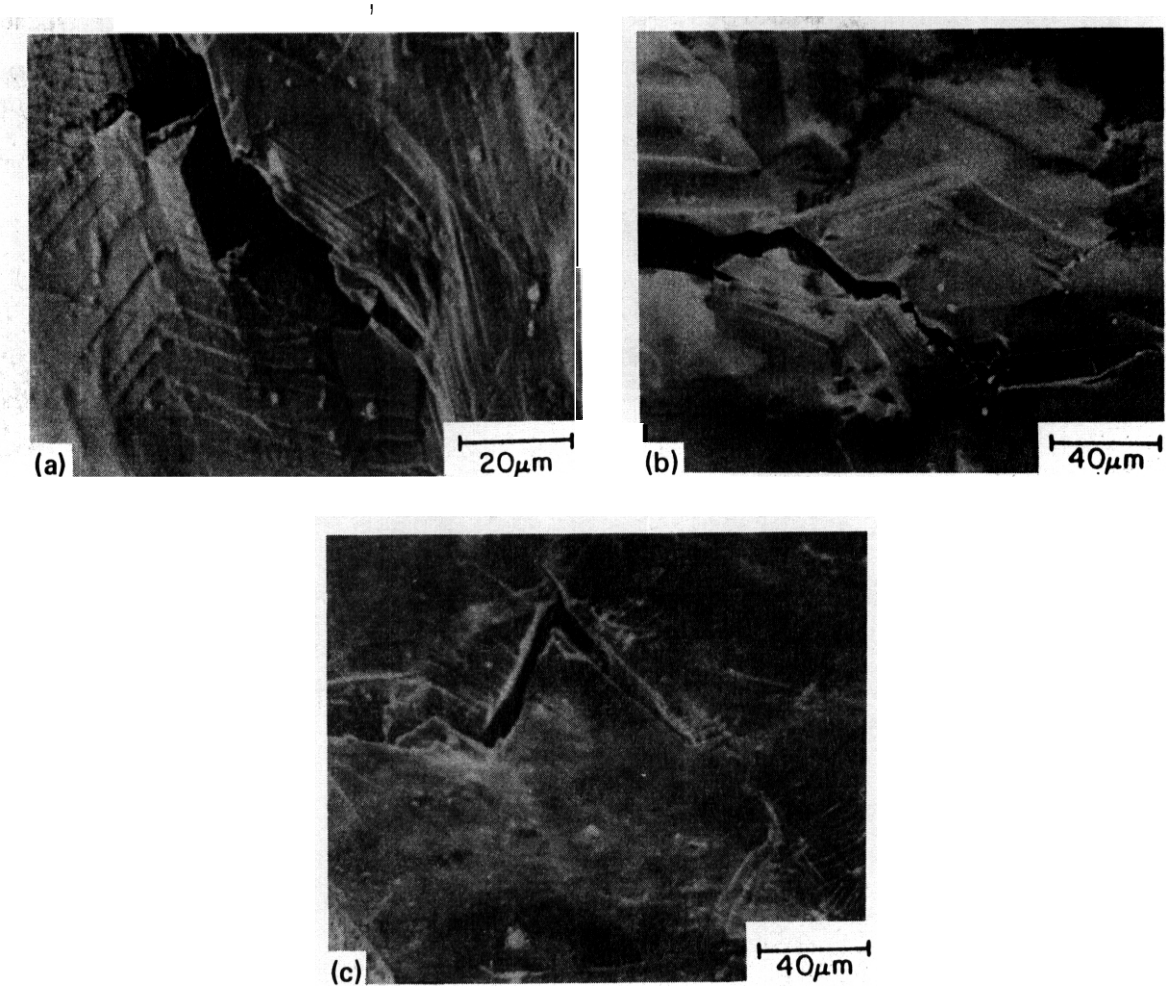

Fig. 6.2.5. Fatigue Cracks *on* the Surface of Cyclic Teated Specimens of Alloy LRO–37 Tested at (a) 25°C, (b) 400°C, and (c) 600°C. (Rensselaer Polytechnic Institute prints.)

fatigue fracture surfaces in LRO-37 revealed a very faceted appearance at 25, 400, and 600°C. This faceted appearance is partially due to cracking along annealing twin boundaries. Further characterization of fatigue properties will involve the determination of heat-to-heat variation in the iron-base LRO alloys.

626 References

1. N. S. Stoloff and R. G. David, "The Mechanical Properties of Ordered Alloys," *Prog. Mater. Sci.* 13(1): 1-84 (1966).

2. B. H. Kear, C. T. Sims, N. S. Stoloff, and J. H. Westbrook, Eds., *Ordered Alloys — Structural and Physical Metallurgy, Proc. 3d Bolton Landing Conf., Lake George, N.Y., Sept. 8–10, 1969,* Claiter's Publishing Division, Baton Rouge, La., 1970.

3. C. T. Liu and H. Inouye, "Control of Ordered Structure and Ductility of $(Fe,Co,Ni)_3V$ Alloys," *Metall. Trans.* 10A(10): 1515–25 (1979).

4. C. T. Liu, "Development of Ductile Long-Range Ordered Alloys for Fusion Reactor Systems," J. *Nucl. Mater.* 85&86: 907–11 (1979).

6.3 SCALE-UP OF AN IRON-BASE LONG-RANGE-ORDERED ALLOY — T. K. Roche and and C. T. Liu (Oak Ridge National Laboratory)

6.3.1 ADIP Task

ADIP Task I.D.l, Materials Stockpile for Magnetic Fusion Energy Programs.

6.3.2 Objective

The objective of this work is to perform semiproduction scale-up of an iron-base long-range-ordered alloy to gain some commercial experience with this class of developmental alloy. The activity will provide material for irradiation, mechanical property, compatibility, and other property tests to evaluate the potential of the alloy class for use in fusion energy systems.

6.3.3 Summary

A contract has been negotiated for the semiproduction scale-up of an iron-base long-range-ordered alloy by a commercial source. Three ingots, each weighing approximately 18 kg (40 lb), will be supplied with nominal composition: Fe-39.5 Ni—22.4 W.4 Ti (wt %). Three thicknesses of sheet, and ingot material for later processing, will be produced.

6.3.4 Progress and Status

Long-range-ordered alloys of the system $(Fe,Ni)_3(V,Ti)$ have been developed on a laboratory scale at ORNL. These alloys have unique properties that make them attractive as structural materials for advanced energy systems. The alloy development program has now reached the important phase of alloy scale-up.

Specifications have been prepared for the semiproduction scale-up of one alloy, LRO-37, with nominal composition: Fe—39.5 Ni—22.4 V—0.4 Ti (wt %) [Fe-37.5 Ni—24.7 W.5 Ti (at. %)], and a contract has been negotiated with High Technology Materials Division, Cabot Corporation, to produce the material. A total of three ingots, each weighing approximately 18 kg (40 lb), will be produced by two different melt practices — electron beam melting using high purity starting stock (one *ingot),* and

electroslag melting using commercial grade materials (two ingots). The vendor will process three thicknesses of sheet, 3.3-, 1.6-, and 0.7-mm (0.130-, 0.065-, and 0.030-in.) thirk, from these ingots. In addition, a small portion of each ingot will be made available to ORNL for processing. This alloy scale-up is expected to be completed before the end of FY 1981.

7. PATH E ALLOY DEVELOPMENT — FERRITIC STEELS

7.1 THE EFFECT OF AUSTENITIZING TIME AND TEMPERATURE ON THE MICROSTRUCTURE OF A 12 Cr-1 Mo-0.3 V STEEL (HT-9) — L. D. Thompson and T. A. Lechtenberg (General Atomic Company)

To be reported in the next quarterly report.

7.2 TENSILE PROPERTIES OF FERRITIC STEELS AFTER LOW-TEMPERATURE HF'IR IRRADIATION — R. L. Klueh and J. M. Vitek (Oak Ridge National Laboratory)

7.2.1 ADIP Task

ADIP Tasks are not defined for Path E, ferritic steels, in the 1978 program plan.

7.2.2 Objective

The goal of this project is to evaluate the properties of irradiated ferritic steels. Irradiation in the High Flux Isotope Reactor (HFIR) is used to produce both displacement damage and transmutation helium at levels relevant to fusion reactor service.

7.2.3 Summary

Tensile specimens from small heats of ferritic (martensitic) steels based on 12 Cr-1 MoVW, 9 Cr-1 MoVNb, and the low-alloy ferritic 2 1/4 Cr-1 Mo steel have been irradiated at coolant temperature in HF'IR to displacement-damage levels of up to 9.3 dpa and helium contents of 10 **to** 82 at. ppm. The base compositions and similar alloys to which nickel had been added for helium production are included in the irradiations.

During the present reporting period, irradiated specimens from a heat of 9 Cr-1 MoVNb and two heats of 9 Cr-1 MoVNb with 2% Ni were tensile tested at **room** temperature and 300°C. Yield strength and ultimate tensile strength of the irradiated samples displayed considerable hardening over the unirradiated condition. The increased strength was accompanied by **a** decreased ductility. Indications are that the hardening resulted only from the displacement damage and was not affected by the transmutation helium formed during irradiation. These results are similar to those for the 12 Cr-1 MOW-base alloys, which were previously reported.

7.2.4 Progress and Status

The HFIR-CTR-33 irradiation experiment was designed to determine the effect of transmutation helium on the tensile properties of 12 Cr-1 MoVW and 9 Cr-1 MoVNb ferritic (martensitic) steels. Nickel was added to the

base compositions to produce helium during HFIR irradiation. When these steels contain approximately 2% Ni, they can be irradiated in HFIR to obtain about the same helium production rate as the original chromium–molybdenum alloys (without nickel) would develop during first–wall fusion reactor service with a neutronic wall loading near 3 MW/m^2. The displacement production rate in HFIR is also appropriate for this wall loading. Last quarter we reported on the tensile behavior of the 12 Cr-1 MoVW alloys after irradiation;[1] in this report we will present similar properties for the 9 Cr-1 MoVNb steels.

7.2.4.1 Alloys Irradiated

Details on the chemical composition, heat treatment, and microstructure for the eight heats of steel irradiated were given in previous reports.[2,3] For the 9 Cr steels of interest in this report, a base 9 Cr-1 MoVNb alloy was irradiated, along with an alloy with the base composition, but with 2% Ni added. A third heat was prepared with 2% Ni, but with the net chromium equivalent adjusted to be approximately the same as that of the steel without nickel.[2] For the 9 Cr-1 MoVNb alloys, more chromium and molybdenum were added to maintain the chromium equivalence. The result was an alloy with a composition similar to the adjusted 12 Cr-1 MoVW alloy, where the adjusting additions were chromium, molybdenum, and tungsten.[1] The composition of the 9 Cr-1 MoVNb alloys discussed in this report are given in Table 7.2.1.

7.2.4.2 Experimental Procedure

Sheet tensile specimens in this experiment were of an SS-1 type, with a reduced gage section 20.32 mm long by 1.52 mm wide by 0.76 mm thick (Fig. 7.2.1). Three normalized–and–tempered specimens from each of the three heats of the 9 Cr steels were irradiated at about 50°C. The maximum total fluence was 5.0×10^{26} neutrons/m^2 and the fast fluence 1.3×10^{26} neutrons/m^2 (>0.1 MeV).[1,3] After immersion density measurements, the specimens were tensile tested at room temperature and 300°C. Tests were conducted in a vacuum chamber on a 44-kN capacity Instron universal testing machine at a strain rate of 4.2×10^{-5}/s.

Table 7.2.1. Composition of 9 Cr-1 MoVNb Heats of Steel

Element	Concentration,[a] wt %		
	9 Cr-1 Mo (XA-3590)	9 Cr-1 Mo + 2% Ni (XA-3591)	9 Cr-1 Mo + 2% Ni Adjusted (XA-3593)
C	0.09	0.064	0.067
Mn	0.36	0.36	0.36
P	0.008	0.008	0.008
S	0.004	0.004	0.004
si	0.08	0.08	0.10
Ni	0.11	2.17	2.24
Cr	8.62	8.57	12.30
Mo	0.98	0.98	1.70
V	0.209	0.222	0.29
Nb	0.063	0.066	0.074
Ti	0.002	0.002	0.002
co	0.013	0.015	0.017
cu	0.03	0.04	0.03
Al	0.013	0.015	0.016
B	<0.001	<0.001	<0.001
W	0.01	0.01	0.01
As	<0.001	<0.001	<0.001
Sn	0.003	0.003	0.003
Zr	<0.001	<0.001	<0.001
N	0.050	0.053	0.059
0	0.007	0.006	0.007

[a]Balance iron.

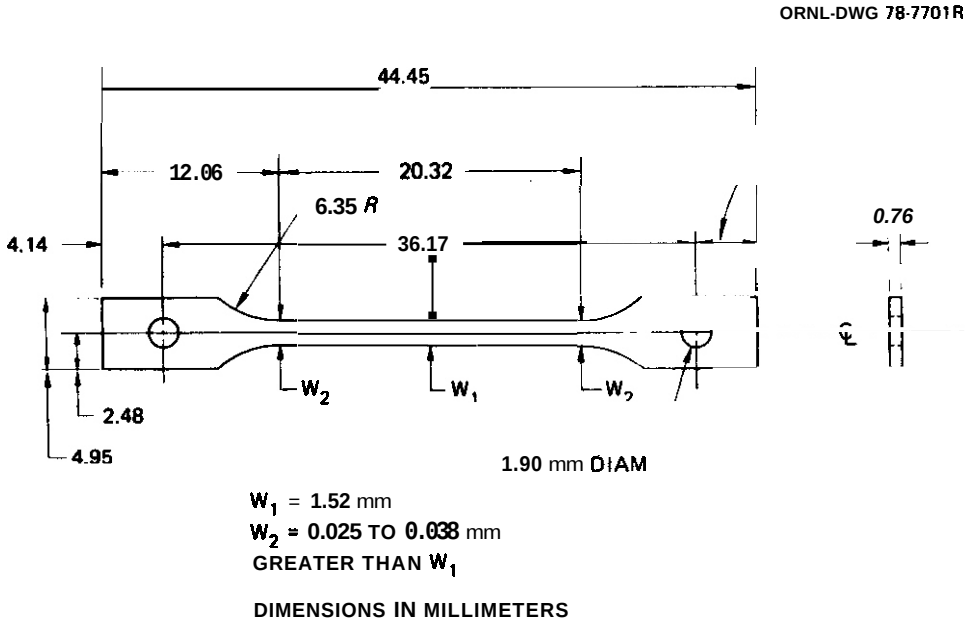

Fig. 7.2.1. The SS-1 Type Tensile Specimen.

7.2.4.3 Results

As reported last quarter,[1] there was no detectable change in the density of the specimens caused by the irradiation.

Room temperature and 300°C tensile tests were made on irradiated and unirradiated (control) specimens from the three heats of 9 Cr-1 MoVNb with compositions given in Table 7.2.1. The irradiation parameters, test conditions, and measured tensile properties for each specimen tested are given in Table 7.2.2.

Because 2% Ni lowered the Ac_1 temperature, it was necessary to use long-time, low-temperature tempering procedures on the two alloys with 2% Ni. The results for the unirradiated specimens show that after tempering the strength of the 2% Ni and 2% Ni (adjusted) alloys were still considerably higher than for the steels with no nickel (Figs. 7.2.2 and 7.2.3). It was also found that the unirradiated strength of the 2% Ni (adjusted) alloy was stronger than that of the 2% Ni alloy.

All of the room-temperature tests were made on specimens irradiated to 9.3 dpa; the sperimens tested at 300°C were irradiated to 7.6, 8.6, and 7.9 dpa for the alloys with 0% Ni, 2% Ni, and 2% Ni (adjusted), respectively (Table 7.2.2). The helium concentrations depended on the nickel concentration and the fluence (position of the sample in the capsule).

The strength data for a given heat were connected by a straight line; only one line was used for the yield strength and ultimate tensile strength values for the irradiated alloys with 2% Ni and 2% Ni (adjusted).

An effect of irradiation is immediately obvious. Irradiation inrreased both the yield strength (Fig. 7.2.2) and the ultimate tensile strength (Fig. 7.2.3) and decreased the uniform and total elongation (Fig. 7.2.4). The changes were similar at both test temperatures. The rate of derrease in strength with temperature between room temperature and 300°C was greater for the irradiated sperimens than for the unirradiated material. Similar rates (approximately similar slopes) were observed for the different heats (irradiated or unirradiated). These observations were similar to those made on the 12 Cr-1 MoVW alloys.[1]

Before irradiation there was a substantial differenre between the yield strength and the ultimate tensile strength of 2% Ni and 2% Ni (adjusted) alloys. However, after irradiation there was essentially no

Table 7.2.2. Tensile Properties of Unirradiated and Irradiated[a] Normalized-and-Tempered[b] 9 Cr-1 MoVNb Steels

Fluence, >0.1 MeV (neutrons/m^2)	Displacement Level (dpa)	Helium Concentration[c] (at. ppm)	Test Temperature (°C)	Strength (MPa)		Strength Ratio[d]		Elongation (%)	
				Yield	Ultimate	R_Y	R_U	Uniform	Total
			9 Cr-1 MoVNb (XA-3590)						
0			25	541	656			5.11	9.61
1.3 × 10^{26}	9.3	11	25	878	878	1.62	1.34	0.23	3.23
0			300	483	581			3.59	7.13
1.1	7.6	10	300	716	716	1.48	1.23	0.22	3.70
			9 Cr-1 MoVNb-2 Ni (XA-3591)						
0			25	734	851			3.74	7.50
1.3	9.3	80	25	1289	1297	1.76	1.52	0.36	1.60
0			300	650	757			2.29	5.29
1.2	8.6	72	300	1088	1107	1.67	1.46	0.41	2.72
			9 Cr-1 MoVNb-2 Ni (adjusted) (XA-3593)						
0			25	817	927			3.44	7.46
1.3	9.3	82	25	1286	1298	1.57	1.40	0.48	2.63
0			300	766	878			3.57	6.59
1.1	7.7	63	300	1093	1114	1.43	1.27	0.51	2.31

[a]Irradiation was in HFIR at 50°C.

[b]All heats were normalized by heating 0.5 h at 1040°C, then rapidly cooled in flowing helium. Heat XA-3590 was tempered 1 h at 760°C; heats XA-3591 and XA-3593 were tempered at 700°C for 5 and 8 h, respectively.

[c]Calculated level of helium from ^{58}Ni and ^{10}B. [Each alloy was assumed to contain 0.0007 wt % B (total)].

[d]R_Y = ratio of irradiated-to-unirradiated yield strengths; R_U = ratio of irradiated-to-unirradiated ultimate tensile strengths.

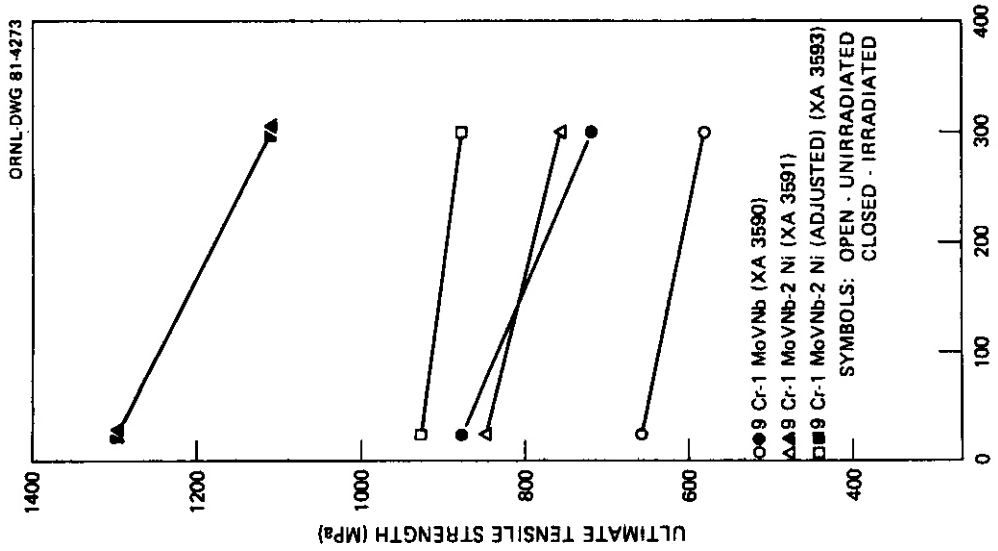

Fig. 7.2.3. The Ultimate Tensile Strengths of 9 Cr-1 MoVNb Steels.

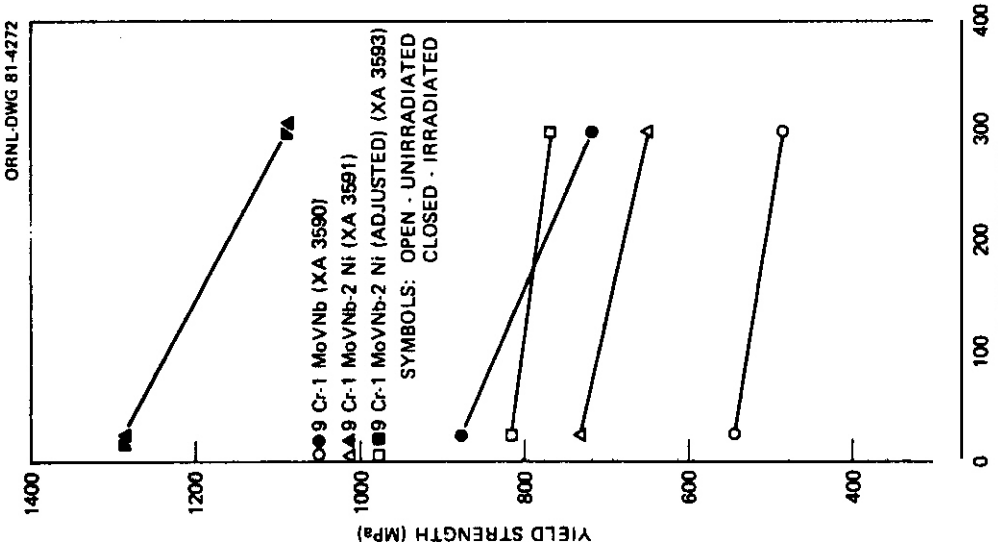

Fig. 7.2.2. The 0.2% Yield Strengths of 9 Cr-1 MoVNb Steels Unirradiated and After HFIR Irradiation to Produce up to 9.3 dpa and 10 to 80 at. ppm He.

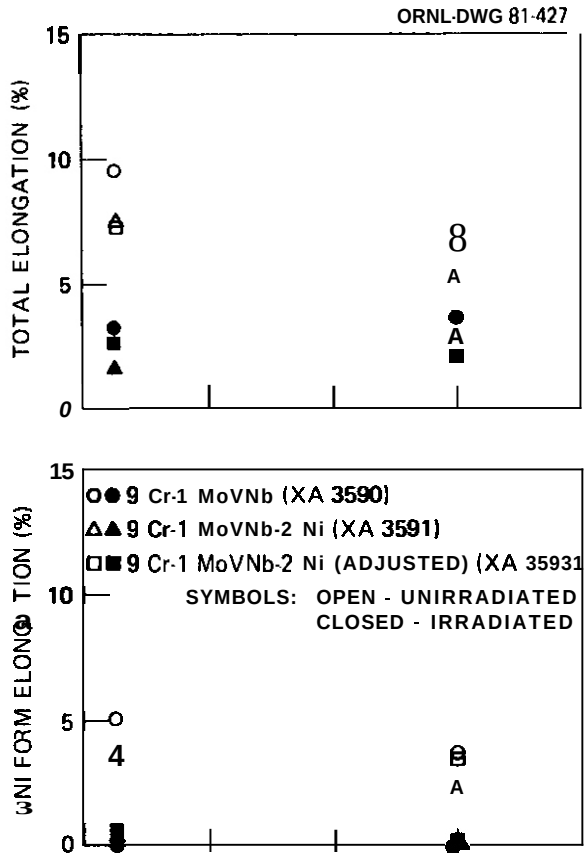

Fig. 7.2.4. The Uniform and Total Elongation of 9 Cr-1 MoVNb Steel Unirradiated and after Irradiation in HFIK to Produce up to 9.3 dpa and 10 to 80 at. ppm He.

difference. When the strength of the 2% Ni (adjusted) alloy from the present tests was compared with the 12 Cr-1 MoVW-2% Ni (adjusted) alloy previously tested,[1] there was little difference. As pointed out above, there is only a slight difference in the chemical composition of these two alloys (the major difference was that the nickel-adjusted 12 Cr alloy contained about 1.3% more chromium and 0.6% W).

We previously concluded that there was little or no effect of helium on the properties of the 12 Cr steels irradiated under the conditions of this experiment.[1] A similar conclusion follows for the 9 Cr steels when the effect of the unirradiated strength differences is eliminated. Qualitatively, this can be seen by calculating the following ratios:

$$Ry = Y_i/Y_u \text{ and } R_U = U_i/U_u \ ,$$

where Y_i and Y, are the irradiated and unirradiated yield strengths and U_i and U_u the irradiated and unirradiated ultimate tensile strengths.

For a given temperature the values of R_Y and R_U are reasonably constant for the three steels (Table 7.2.2), regardless of the helium content. Although the calculated values of these ratios for the 2% Ni alloy are larger than those for the other two steels, the maximum difference is less than 20%. This simplified comparison of the effect of irradiation on the steels suggests that the helium has little effect. Essentially all the hardening must result from the displacement damage.

The changes in uniform and total elongation also give no indication of a helium effect. The only unusual value is the low uniform elongation value for the irradiated specimen to which no nickel has been added. As was the case for the 12 Cr-1 MoVW alloys,[1] the strength and ductility of the three 9 Cr-1 MoVNb alloys both decrease in going from room temperature to 300°C. For irradiated material the strength again decreases, but the elongation shows a slight increase or remains unchanged between room temperature and 300°C.

7.2.5 Future Work

In the future we shall report results for the irradiated 2 1/4 Cr-1 Mo steel, and compare the behavior of the three steels (i.e., 12 Cr-1 MoVW, 9 Cr-1 MoVNb, and 2 1/4 Cr-1 Mo steels).

One of the objectives of this study is to determine the effect of helium on mechanical properties. No effect has thus far been observed for tests at room temperature and 300°C. For most alloys, small amounts of helium cause a loss of ductility at elevated temperatures. To determine if this also occurs in the ferritic steels, we will test the remaining 9 Cr and 12 Cr alloys at 700°C.

7.2.6 References

1. R. L. Klueh and J. M. Vitek, "Tensile Properties of Ferritic Steels After Low-Temperature HIFR Irradiation," *ADIP Quart. Prog. Rep. Dec. 31, 1980*, DOE/ER-0045/5, pp. 218-25.

2. M. L. Grossbeck, V. K. Sikka, T. K. Roche, and R. L. Klueh, "Preparation of Nickel-Doped Ferritic Alloys for HFIR Irradiation to Produce Helium," *ADIP Quart. Prog. Rep. Dec. 31, 1979,* DOE/ER-0045/1, pp. 100-04.

3. M. L. Grossbeck and J. W. Woods, "An Irradiation Experiment to Scope the Tensile Properties of Ferritic Alloys - HFIR-CTR-33," *ADIP Quart. Prog. Rep. June 30, 1980,* DOE/ER-0045/3, pp. 30-34.

7.3 PREPARATION OF ALLOY HT-9 AND MODIFIED ALLOY 9Cr-1Mo REFERENCE PLATES FOR UNIRRADIATED AND IRRADIATED CONDITION FRACTURE RESISTANCE STUDIES – J. R. Hawthorne (Naval Research Laboratory)

7.3.1 ADIP Task

The Department of Energy (DOE)/Office of Fusion Energy (OFE) has stated the need to investigate ferritic alloys under the ADIP program task. Ferritic Steels Development (Path E).

7.3.2 Objectives

Objectives of the present research tasks were to heat treat two sections of Alloy HT-9 plate from the Fusion Ferritic Program reference heat and to perform initial notch ductility and strength tests of this plate and a plate from the modified Alloy 9Cr-1Mo reference heat in the unirradiated condition.

7.3.3 Summary

Alloy HT-9 and modified Alloy 9Cr-1Mo are being evaluated for potential applications as first wall materials in magnetic fusion reactors. One objective of the current investigations is the assessment of material notch ductility and static fracture toughness in the preirradiation and postirradiation conditions.

Two sections of 1.7 cm thick plate from the HT-9 reference melt were heat treated by normalizing at 1050°C for 0.5 hours and tempering at 780°C for 2.5 hours. Good agreement of tensile test values with prior results for other plate sections from the melt was observed. Yield strength, tensile strength and Charpy-V (C_V) upper shelf energy levels, however, are lower than those for material (rod) from the Alloy HT-9 reference melt of the Cladding/Duct Alloy Development Program.

Tensile and C_V test results for a 1.3 cm thick plate from the modified Alloy 9Cr-1Mo melt are also reported.

1.3.4 Progress and Status

7.3.4.1 Introduction

Alloy HT-9 and Alloy 9Cr-1Mo (modified) are two ferritic stainless steel compositions being assessed for possible first wall applications in magnetic fusion reactors by the Magnetic Fusion Materials Program and for duct application in liquid metal fast breeder reactors by the Cladding/Duct Alloy Development Program of the Department of Energy. For these proposed uses, fracture resistance properties before and after elevated temperature irradiation are being investigated. Specimen types include C_v specimens for notch ductility determinations, fatigue precracked Charpy-V (PCC_V) specimens for dynamic fracture toughness (K_J) determinations and compact tension (CT) specimens for static fracture toughness determinations.

Current studies are aimed at exploratory evaluation of the 288 and 100°C radiation resistance of Alloy HT-9 plate material from the Fusion Ferritic Program reference heat and the evaluation of unirradiated condition, fracture resistance properties of a modified Alloy 9Cr-1Mo plate from a second reference heat. Plate stock for the Alloy HT-9 investigations was supplied to NRL in the nonheat treated condition. Progress for this material includes the performance of the required heat treatment, the fabrication of specimens for both unirradiated and irradiated condition studies, and the conduct of initial tests to characterize as-heat-treated mechanical properties. The material for the Alloy 9Cr-1Mo investigations was supplied in the fully heat treated condition. Initial characterization tests for this alloy were also performed during this quarter.

7.3.4.2 Materials

The Alloy HT-9 plate sections received by NRL were 24.1 x 50.8 x 1.7 cm and 24.1 x 30.5 x 1.7 cm in size and were produced from Electralloy Corporation Heat No. 9607.[1] Processing of the slab by Jessop Steel Company has been described by Stevenson.' The plate section of modified Alloy 9Cr-1Mo reported on here was 35.6 x 11.6 x 1.3 cm in size and was obtained from Cartech Heat No. 30176.[3] This material was previously heat treated at the Oak Ridge National Laboratory by normalizing at 1039°C (1900°F) for 1 hour with air cooling and tempering at

760°C (1400°F for 1 hour and air cooling.

7.3.4.3 Heat Treatment of Alloy HT-9 Plate

The plate sections were heat treated for NRL by the Armco Steel Corporation (courtesy E. Denhard, K. Crooks and B. Manke). Heat treatment specifications are indicated in Table 7.3.1. Actual plate temperatures during heat treatment are also listed and were determined using thermocouples (3 per plate). Thermocouple junctions were buried in the plates to monitor internal temperatures. Both plate sections were heat treated in air in the same furnace but were heat treated separately. Operations for section 1 (larger) and section 2 were the same except that section 2 was tempered in two steps instead of one. The first tempering period was one half hour in duration and the second tempering was two hours in duration for a total tempering time of 2.5 hours. Prior to the heat treatment at Armco Steel Corporation, section 1 was briefly heated to temperatures not more than 985°C while checking temperature gradients in an NRL furnace. (Gradients in excess of ± 14°C were observed, necessitating the use of an offsite furnace).

Table 7.3.1. Heat Treatment Conditions for Alloy HT-9 Plate

Heat Treatment	Specification	Temperature Measurements (°C)[a] Plate Section 1	Plate Section 2
Normalize	1050°C +14°C-0.5 hr, air cool	1041, 1052, 1054	1050,1054,1058
Temper	780°C +14°C-2.5 hr, air cool	782, 782, 783	776, 778, 779 (779 - 782)[b]

[a] Individual thermocouple indications.

[b] Range during second tempering period.

7.3.4.4 Unirradiated Condition Mechanical Properties (Alloy HT-9)

Tensile tests were performed at 24°C and at 232°C, using 5.7 mm diameter x 31.8 mm gage length specimens from plate section 1. Results are given in Table 7.3.2. Strength values are noted to be in good

Table 7 3 Z - Tensile Properties

Material	Temperature °C	Temperature °F	Yield Strength[a] MPa	Yield Strength[a] ksi	Tensile Strength MPa	Tensile Strength ksi	R.A. (%)	Elongation (%) (in.25.4 mm)
Alloy HT-9								
Plate Section 1	24	75	561	81.4	779	113.0	56.9	22.3[b]
	232	450	483	70.0	675	97.9	60.5	20.0[b]
G.A. Tests[c]	24	75	553	80.2	789	114.4	56.4	22.5
Sandvik Spec.	ZC	75	490	71.0	690	100	-	17.0
			min.	min.	841	122		min.
Rod (Heat 91354)[c,d]	25	7[illegible]	653	94.7	823	119.4	60.5	16.4
	Z32	C50	575	83.4	714	103.6	63.8	12.4
Alloy 9Cr-1Mo ((Mod.)								
Plate 1[e]	ZC	75	612	88.8	748	108.5	71.8	18.6

[a] 0.2% offset, average of duplicate LT orientation tests.

[b] Elongation in 12.7 mm

[c] Average of duplicate LT and TL orientation tests.

[d] Cladding/Duct Alloy Development Program

[e] 1.3 cm plate

agreement with values reported by General Atomic for other plate section and are shown to satisfy Sandvik specifications.[2] Strength values, however, are somewhat lower than those obtained for a 33 mm diameter rod from the HT-9 Melt No. 91354 of the Cladding/Duct Alloy Development Program.

Full temperature range C_V tests were performed. Results are given in Table 7.3.3 and can be compared to results for the 33 mm diameter rod from Melt 91354 in Fig. 7.3.1. Upper shelf levels for longitudinal and transverse test orientations are significantly lower than the upper shelf level for the rod. The C_V 41J transition temperatures, on the other hand, are similar.

Figure 7.3.2 illustrates the martensitic microstructure of the plate. Some banding is evident. Microstructure comparisons with Alloy HT-9 materials (different melts) are planned for a future report.

7.3.4.5 Unirradiated Condition Mechanical Properties (Modified Alloy 9Cr-1Mo)

Tensile test results for the modified Alloy 9Cr-1Mo plate are included in Table 7.3.2. Charpy-V notch ductility data are given in Table 7.3.4. The plate microstructure is illustrated in Fig. 7.3.3. Differences as well as similiarities in properties between this material and the Alloy HT-9 reference plate can be seen in the tabulated data. In particular, a much higher Charpy-V upper shelf energy level is observed which would provide a larger toughness reserve against radiation induced change.

7.3.4.6 Additional Specimen Fabrication

The full complement of C_V, PCC_V and 0.1 J specimens of the Alloy HT-9 required for the scheduled 288 and 100°C reactor experiments has been obtained. Individual specimen designs were described in the previous report.[5] In addition, J specimens in 0.1, 0.25 and 0.5 in. thicknesses for unirradiated condition test comparisons were fabricated during this quarter. The inventory of C_V, PCC_V and J specimens for unirradiated condition studies of the modified 9Cr-1Mo steel (1.3 cm thick plate stock) has also been completed.

Table 7.3.3. Charpy–V Notch Ductility of Alloy HT–9 Plate (Fusion Ferritic Program Heat[a], Unirradiated Condition)

Temperature (°C)	Temperature (°F)	Energy[b] (J)	Energy[b] (ft-lb)	Lateral Expansion (mm)	Lateral Expansion (mils)
–62	–80	18	13	.25	10
–40	–40	27	20	.41	16
-34	–30	31	23	.51	20
-18	0	48	35	.64	25
– 7	20	65	48	.91	36
4	40	75	55	1.02	40
		73[c]	54[c]		
		57[b,c]	42[b,c]		
27	80	77	57	1.09	43
49	120	88	65	1.27	50
93	200	95	70[b]	1.37	54
		77	57[b]		
		79	58[b]		
		100[c]	74[c]		
		73[b,c]	54[b,c]		
149	300	95	70	1.47	58
216	420	96	71	1.50	59
		95	70	1.40	55
427	800	102	75	1.65	65

[a] Electroalloy Heat 9607.

[b] Transverse test orientation.

[c] Plate section 2 data

Table 7.3.4. Charpy-V Notch Ductility of Modified Alloy 9Cr-1Mo Plate (Fusion Ferritic Program Heat, Unirradiated Condition)

Temperature (°C)	Temperature (°F)	Energy (J)	Energy (ft-lb)	Lateral Expansion (mm)	Lateral Expansion (mils)
-62	-80	14	10	.10	4
-51	-60	26	19	.31	12
-46	-50	27	20	.33	13
-34	-30	58	43	.76	30
-18	0	61	45	.84	33
-12	10	94	69	1.12	44
4	40	152	112	1.78	70
27	80	140	103	1.73	68
49	120	164	121	1.98	78
121	250	172	127	2.08	82
204	400	180	133	2.08	82

[a]Cartech Heat 30176.

[b]Longitudinal test orientation.

7.3.5 Conclusions

Two plate sections of Alloy HT-9 have been heat treated and specimens fabricated for irradiation studies. Tensile strength properties for the heat treated condition compare favorably with standard specifications for the alloy.

Charpy characterization tests of the Alloy HT-9 plate and the modified Alloy 9Cr-1Mo plate indicate a large (2:1) difference in upper shelf energy level between the plates but similar 41 J transition temperatures.

7.3.6 References

1. T. A. Lechtenberg, R. D. Stevenson, S. N. Rosenwasser, B. E. Thurgood, and L. D. Thompson, "Procurement of National 12Cr Heat and Evaluation of Welding Procedures for Irradiation Specimens," ADIP Quart. Prog. Rep. April 1980, DOE/ER-0045/2, pp. 109-131.

2. R. D. Stevenson, B. E. Thurgood and S. N. Rosenwasser, "Procurement and Conversion of the National Fusion-Ferritic Steel Program 12Cr (HT-9) Heat," ADIP Quart. Prog. Rep. July 1980, DOE/ER-0045/

3, pp. 192-200.

3. V. K. Sikka and R. E. McDonald, "Modified 9Cr-1Mo Steel Development Program Progress Report for Period Ending September 30, 1979," ORNL/BRP-80/1, p. 2.6.

4. F. A. Smidt, Jr., J. R. Hawthorne, and V. Provenzano, "The Fracture Resistance of HT-9 After Irradiation at Elevated Temperature," in Effects of Radiation on Structural Materials, ASTM STP 725, American Society for Testing and Materials, Feb. 1980.

5. J. R. Hawthorne, "Fracture Resistance Testing of Alloy HT-9 in the Unirradiated Condition," ADIP Quart. Prog. Rep. January 1981, DOE /ER-0045 /5, pp. 127-141.

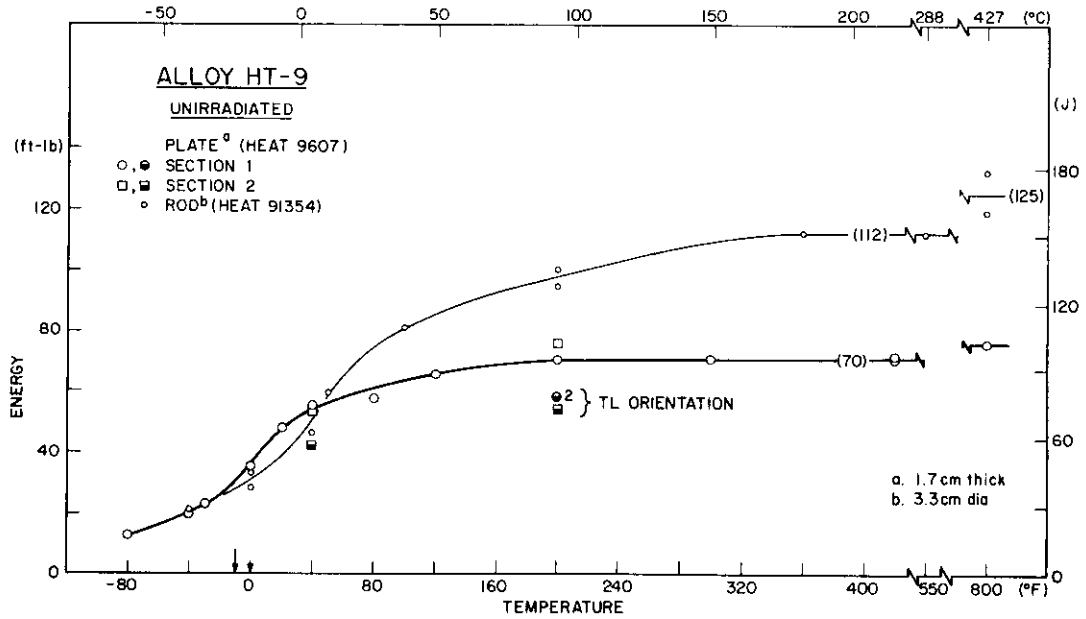

Fig. 7.3.1. Charpy-V notch ductility of Alloy HT-9 plate. Data for an Alloy HT-9 rod from the Cladding/Duct Alloy Development Program are also shown.

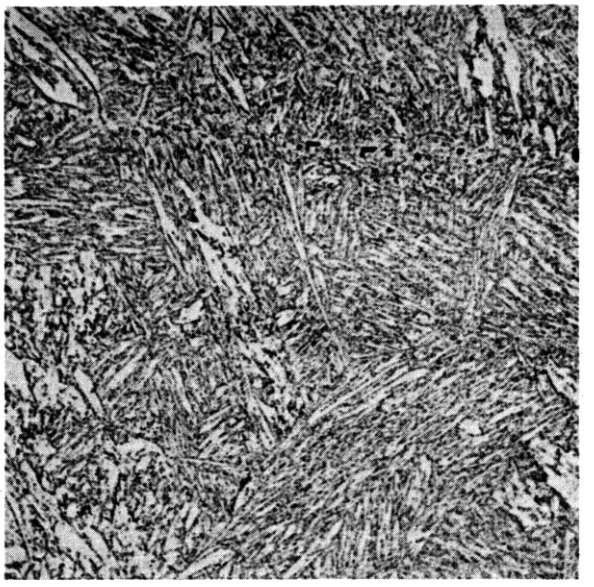

Fig. 7.3.2. Microstructure of the Alloy HT-9 Plate (electrolytic etch, 500X).

Fig. 7.3.3. Microstructure of the modified Alloy 9Cr-1Mo Plate (electrolytic etch, 500X).

7.4 MICROSTRUCTURAL EXAMINATION OF A SERIES OF COMMERCIAL FERRITIC ALLOYS IRRADIATED TO MODERATE FLUENCE - D. S. Gelles (Hanford Engineering Development Laboratory).

7.4.1 ADIP Task

The Department of Energy (DOE)/Office of Fusion Energy (OFE) has cited the need to investigate ferritic alloys under the ADIP program task, Ferritic Steels Development (Path E). The tasks involved are akin to task number 1.C.2, Microstructures and Swelling in Austenitic Alloys and task number l.C.l, Microstructural Stability.

7.4.2 Objective

The objective of this work is to provide guidance on the applicability of ferritic stainless steels for fusion reactor structural materials by examining a series of ferritic alloys (not including the Path E candidate alloy) as a function of irradiation fluence in a fast breeder reactor.

7.4.3 Summary

A series of five commercial ferritic alloys 2¼Cr-1Mo, €I-11, EM-12, 416 and 430F have been examined by transmission electron microscopy following irradiation at 425°C to 5.05 x 10^{22} n/cm^2 (E >0.1 MeV) in order to provide estimates for precipitation kinetics in this class of alloys based on comparison with earlier work on similar specimens irradiated to higher fluence. Results demonstrate that Mo_2C in 2¼Cr-1Mo and 11-11 and an as yet unidentified phase in 416 develop very rapidly. Chi phase in EM-12 and α' phase in 430F develop more sluggislily. Therefore postirradiation mechanical property changes may be expected to saturate in 2¼Cr-1Mo, H-11 and 416 by 5 x 10^{22} n/cm^2 at 425°C but changes can be expected to continue beyond 5 x 10^{22} n/cm^2 in EM-12 and 430F.

7.4.4 Progress and Status

7.4.4.1 Introduction

In the previous quarter, a series of commercial ferritic alloys

covering the composition range 2 to 17 percent chromium were examined by transmission electron microscopy following irradiation to very high fluence (14 to 17.6 x 10^{22} n/cm^2, E >0.1 MeV) in the Experimental Breeder Reactor II, Idaho Falls, Idaho.(1) The present effort is intended to examine the same alloys following irradiation to a lower fluence of 5.05 x 10^{22} n/cm^2 (E >0.1 MeV) at 425°C. The purpose of this effort is to provide information on the kinetics of in-reactor precipitation. Such precipitates are expected to have a major impact on changes in postirradiation mechanical properties and therefore information on the fluence dependence of precipitation will allow prediction of the change in postirradiation mechanical properties with fluence. The reader is referred to the previous report(1) for the necessary experimental details, procedures and microstructural background information.

7.4.4.2 Experimental Procedure

Specimens selected for transmission electron microscopy were those alloys which had been examined previously but in this case irradiated at 425°C to a lower fluence of 5.05 x 10^{22} n/cm^2 (E >0.1 MeV). The specimen identification codes were 94L3, 93L3, 98L3, 64L3 and 91L3 corresponding to alloys 2¼Cr-1Mo, H-11, EM-12, 416 and 430F respectively. Specimen preparation and examination procedures are as previously described.(1)

7.4.4.3 Results

7.4.4.3.1 2¼Cr-1Mo. Irradiation to 5.1 x 10^{22} n/cm^2 (E >0.1 MeV) at 425°C caused significant microstructural changes in 2¼Cr-1Mo, (condition 94L3). Void swelling was not observed but extensive Mo_2C and M_6C precipitation was found. Figure 7.4.1(a) provides comparison of this structure in a ferrite grain with that following irradiation to 15.8 x 10^{22} n/cm^2 as shown in Figure 7.4.1(b). The higher fluence condition does contain void swelling and the Mo_2C and M_6C have grown to larger size, but the major changes to mechanical properties can be expected to have occurred by 5 x 10^{22} n/cm^2 at 425°C in 2¼Cr-1Mo.

7.4.4.3.2 H-11. Irradiation to 5.1 x 10^{22} n/cm^2 (E > 0.1 MeV) at 425°C caused significant microstructural changes in H-11. Mo_2C had developed extensively and M_6C was present primarily on martensite lath boundaries and grain boundaries. The structure was very similar to that observed following irradiation to 15.8 x 10^{22} n/cm^2 as shown in Figure 7.4.2. Therefore, it may be anticipated that postirradiation mechanical property changes in H-11 occur prior to fluences on the order of 5 x 10^{22} n/cm^2 (E > 0.1 MeV).

7.4.4.3.3 EM-12. Voids and Chi phase precipitate had developed in EM-12 following irradiation to 5.1 x 10^{22} n/cm^2. Voids were found at low number density but the void swelling was negligible. Chi phase precipitate particles appeared as equiaxed particles in linear arrays. An example of this structure is given in Figure 7.4.3(a) and the structure obtained following irradiation to 15.8 x 10^{22} n/cm^2 is shown in Figure 7.4.3(b) for comparison. Analysis of the dislocation structure following irradiation to moderate fluence demonstrated the presence of both $a\langle 100\rangle$ and $\frac{a}{2}\langle 111\rangle$ Burgers vectors, with the precipitate arrays coupled to $\frac{a}{2}\langle 111\rangle$ dislocations. It is therefore presumed that precipitation is occurring on dislocations present prior to irradiation. Figure 7.4.3 clearly shows that significant changes in precipitate development occur between 5 and 16 x 10^{22} n/cm^2 and therefore changes in EM-12 postirradiation mechanical properties as a function of fluence can be predicted to be more sluggish than those of 2¼Cr-1Mo and H-11.

7.4.4.3.4 416. No voids were found in 416 following irradiation to 5.1 x 10^{22} n/cm^2 but extensive precipitation had developed. The precipitate was similar in shape and size and had similar electron diffraction characteristics to that which was present following irradiation to 15.8 x 10^{22} n/cm^2 but no further attempt was made to identify the phase. An example is provided in Figure 7.4.4 comparing the precipitate structure of 416 at 5.1 x 10^{22} n/cm^2 in Figure 7.4.4(a) with that at 15.8 x 10^{22} in Figure 7.4.4(b). It is apparent that the unidentified precipitate which forms in 416 during irradiation at 425°C forms very rapidly and changes in postirradiation mechanical properties can be expected to saturate quickly with fluence.

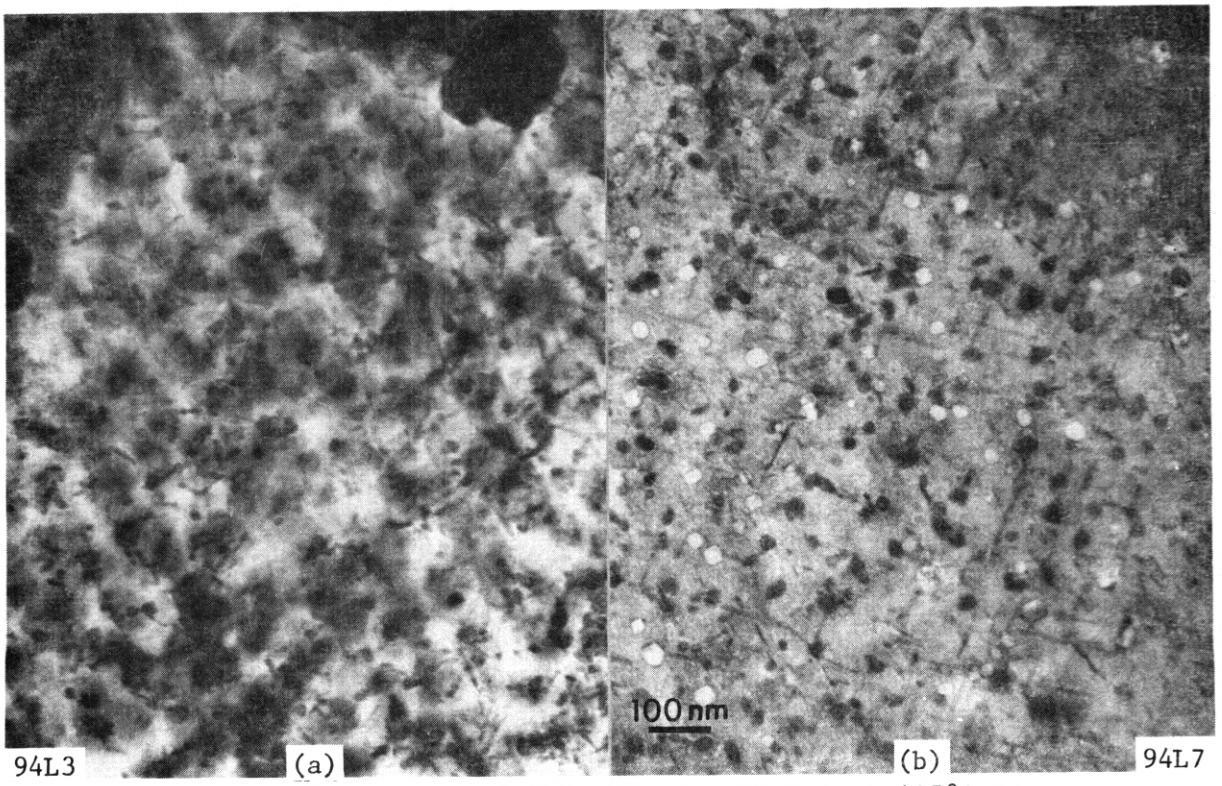

Fig. 7.4.1. Comparison of 2¼Cr-1Mo irradiated at 425°C to (a) 5.1 x 10^{22} n/cm^2 and (b) 15.8 x 10^{22} n/cm^2.

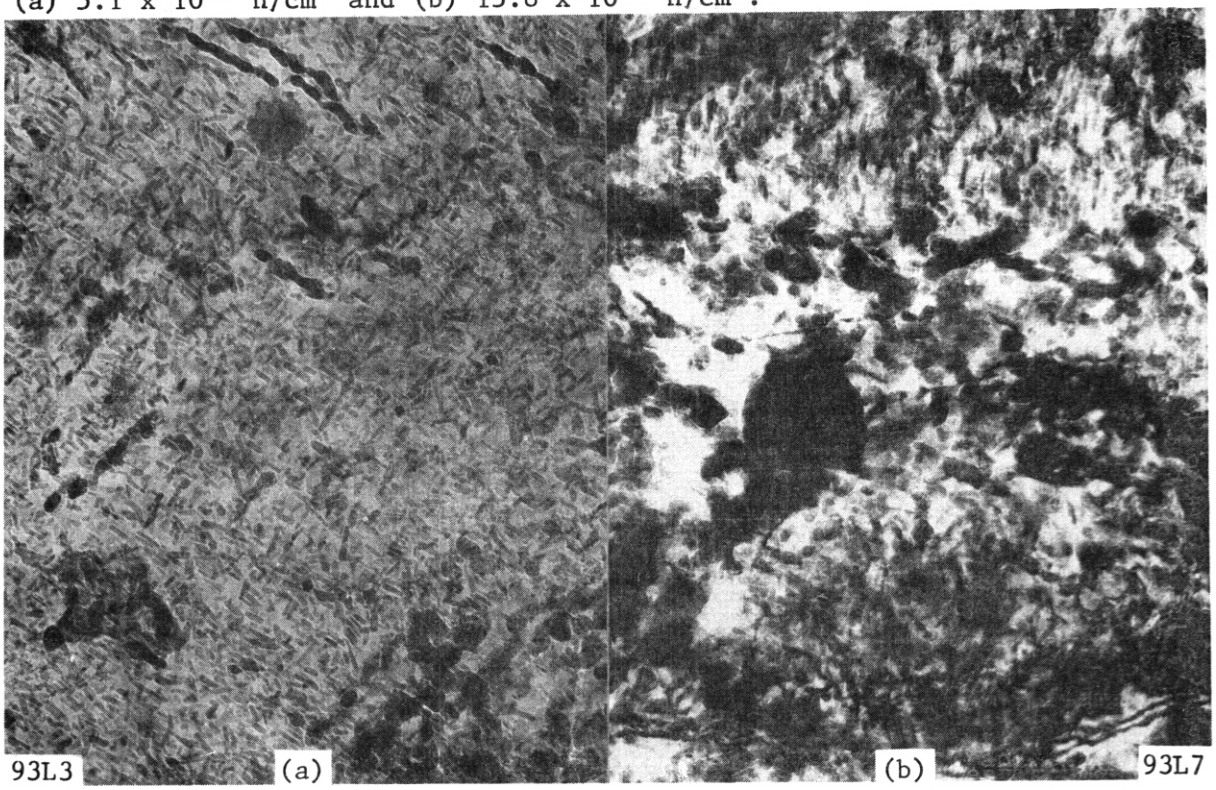

Fig. 7.4.2. Comparison of H-11 irradiated at 425°C to (a) 5.1 x 10^{22} n/cm^2 and (b) 15.8 x 10^{22} n/cm^2.

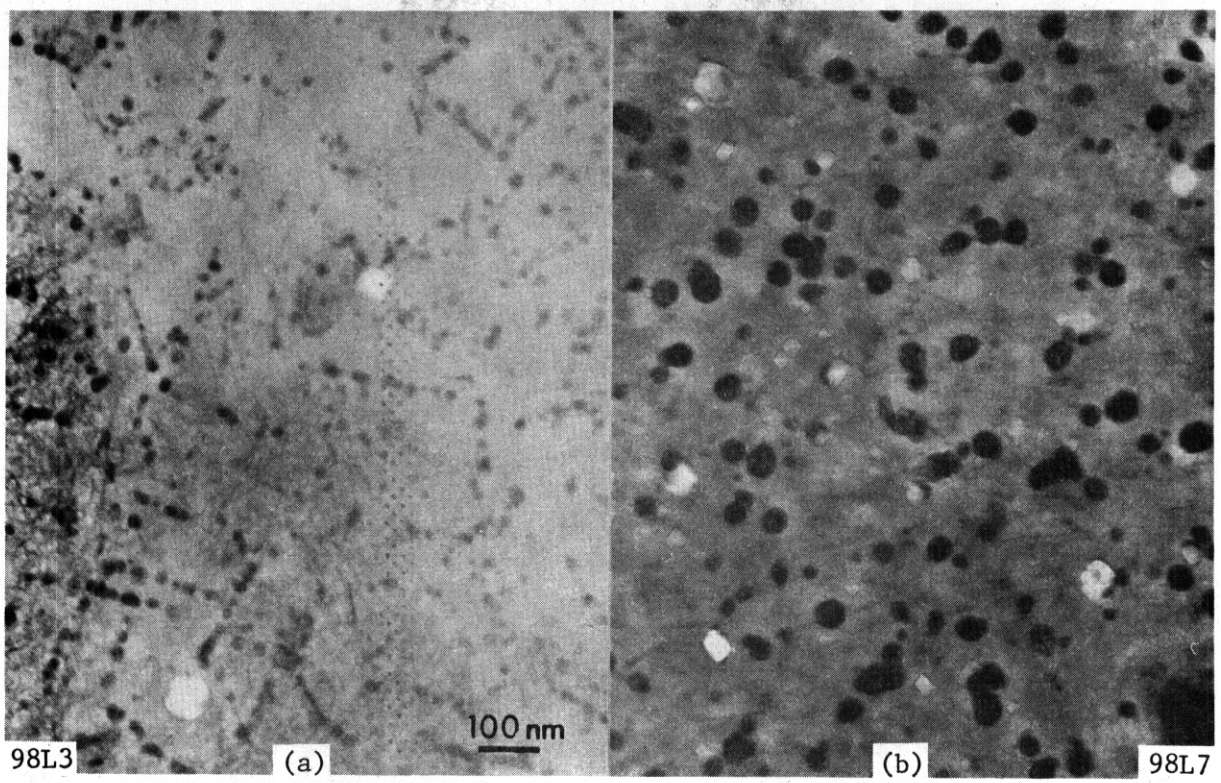

Fig. 7.4.3. Comparison of EM-12 irradiated at 425°C to (a) 5.1 x 10^{22} n/cm^2 and (b) 15.8 x 10^{22} n/cm^2.

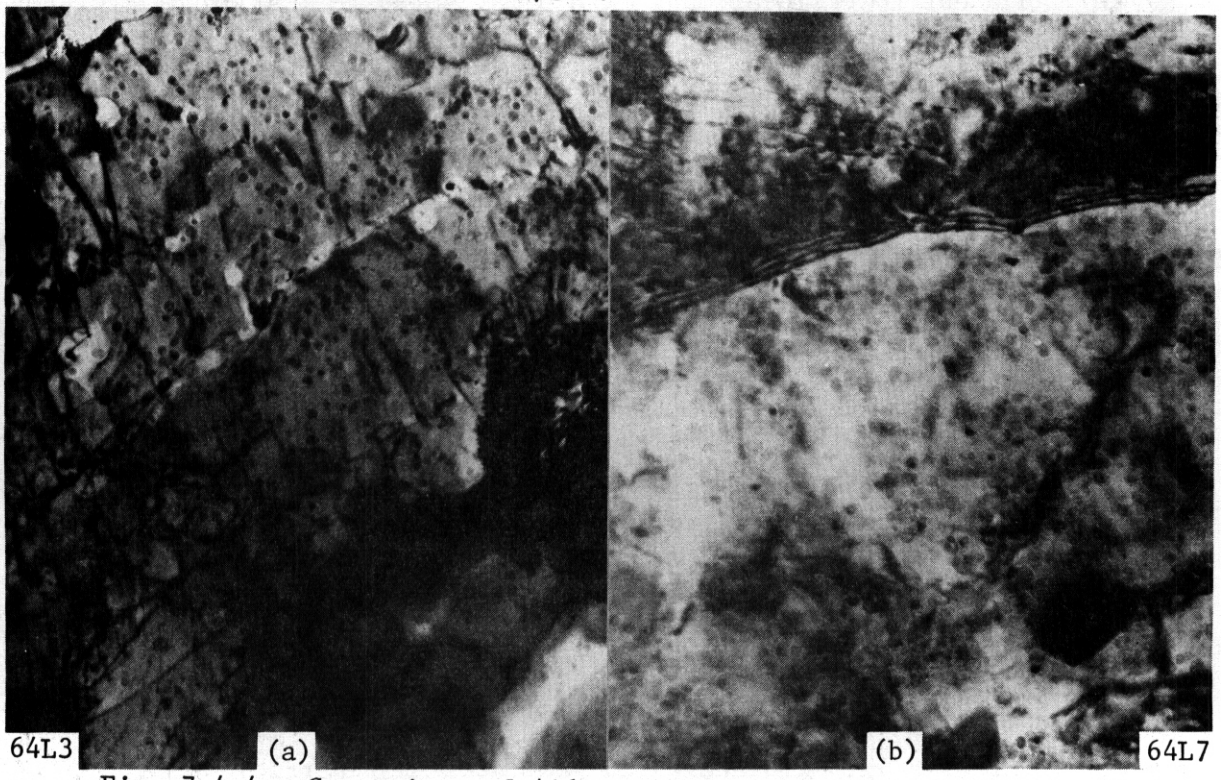

Fig. 7.4.4. Comparison of 416 irradiated at 425°C to (a) 5.1 x 10^{22} n/cm^2 and (b) 15.8 x 10^{22} n/cm^2.

7.4.4.3.5 430F. Evidence for effects of precipitation were found in 430F following irradiation at 425°C to 5.1 x 10^{22} n/cm^2 but the precipitation was much less extensive than that observed following irradiation to 15.8 x 10^{22} n/cm^2. $M_{23}C_6$ precipitates could be readily identified but the presence of the a' phase was very difficult to detect. a' could be seen in strain or thickness fringe contrast as a fine mottling with particles on the order of 60 Å but was very difficult to detect otherwise. This was very different from the high fluence condition. The precipitate structure in 430P as a function of fluence is shown in Figure 7.4.5(a) and (b). a⟨100⟩ dislocation loops, $M_{23}C_6$ and the fine mottling due to a' can be identified in Figure 7.4.5(a) whereas in Figure 7.4.5(b), the a' imaging obscures the other features. Weak beam dark field dislocation contrast which provides the optimum procedure to identify the a' phase gives the unexpected result that only a' precipitate particles at the surface can be seen following irradiation to moderate fluence as can be demonstrated withtheweak beam dark fieldstereo pair shown in Figures 7.4.5(c) and (d). Also from the stereo pair, it may be noted that zones denuded of a' develop adjacent to dislocations. (This may be an indication of preferential segregation of iron to dislocations.) Thus, a' precipitation at 425°C appears to be sluggish in 430F.

7.4.4.4 Discussion

The kinetics of precipitate development observed in this series of commercial ferritic alloys following irradiation at 425°C may be compared as follows. The unidentified phase which develops in 416 and the Mo_2C phase which is found in 2¼Cr-1Mo and €I-11 stabilize by fluences of 5 x 10^{22} n/cm^2. If one had to differentiate between them, the 416 phase may be considered more rapid based on the further increase in length of Mo_2C precipitates with increasing fluence as can be seen in Figure 7.4.1. The precipitation kinetics of Chi in EM-12 and a' in 430F are considerably slower with large changes in precipitate size demonstrated between fluences of 5 and 16 x 10^{22} n/cm^2. It is more difficult to estimate which phase develops more rapidly. The number density of the a' phase clearly decreases with fluence which indicates that particle size changes by a coarsening mechanism. In comparison the number density of

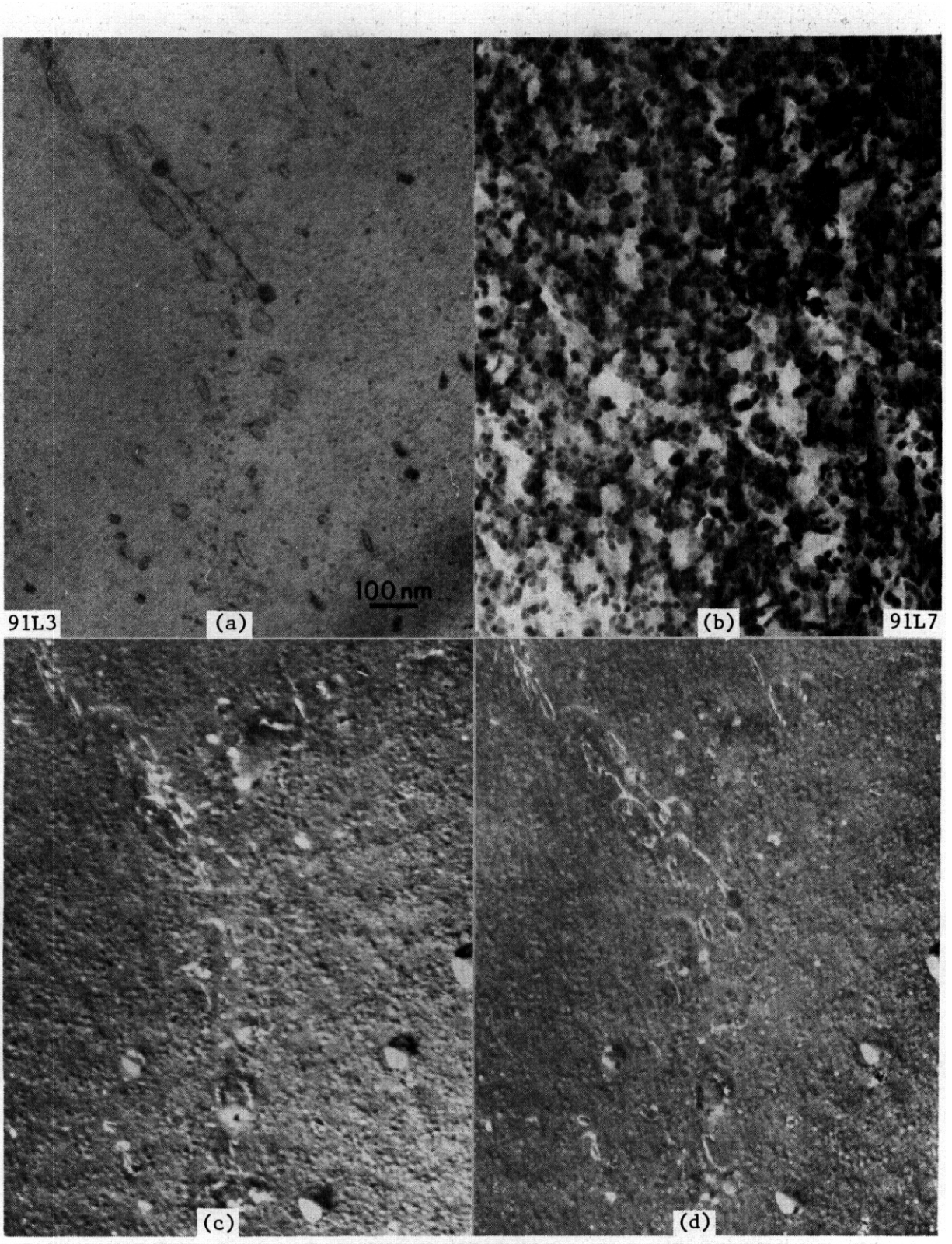

Fig. 7.4.5. Comparison of 430F irradiated at 425°C to (a) 5.1 x 10^{22} n/cm^2 and (b) 15.8 x 10^{22} n/cm^2. A g = 110 dark field stereo pair (c) and (d) is shown for the area of (a).

the Chi phase remains fairly constant demonstrating that particle size changes are controlled by a growth mechanism. As a growth mechanism should be much faster than a coarsening mechanism, it may be inferred that the α' forms more rapidly than does Chi. Therefore, in order of decreasing kinetics, precipitation in the ferritic alloy class during irradiation at 425°C may be ranked as follows: (1) the unidentified phase in 416, (2) Mo_2C, (3) a' and (4) Chi.

The Path E candidate alloy is HT-9, an alloy somewhat different in composition from all of the above alloys. The alloy composition is such that Mo_2C development is not expected to be significant in HT-9. However. the other three phases may develop. Chi and a' can be expected to have considerable effects on postirradiation mechanical properties if the low temperature phase found in 416 does not develop in HT-9. Therefore, a testing program for the candidate alloy must be continued to fluences in excess of 5 x 10^{22} n/cm^2 at 425°C in order to demonstrate that formation of α' and Chi phase will not so adversely affect postirradiation mechanical properties for the alloy as to make it unusable.

7.4.5 Conclusions

Precipitation in the ferritic alloy class during irradiation can occur very rapidly as in the case of Mo_2C inlowchromium alloys and the as yet unidentified phase in 416. However, kinetics for precipitation of α' and Chi are slower requiring fluences well in excess of 5 x 10^{22} n/cm^2 for stabilization. Therefore, irradiation experiments for Path E alloys should be extended well beyond 5 x 10^{22} n/cm^2 (E >0.1 MeV) or 25 dpa.

7.4.5.1 Future Work

This effort will shift to HT-9 and will include postirradiation examination from OFE experiments and low fluence irradiation creep effects.

7.4.6 References

1. D. S. Gelles, "Microstructural Examination of a Series of Commercial Ferritic Alloys Irradiated to Very High Fluence," DOE/ER-0045/5, (10-12/1980).

7.5 MICROSTRUCTURAL EXAMINATION OF POSTIRRADIATION DEFORMATION IN 2¼Cr-1Mo

D. S. Gelles, W. J. Mills and L. A. James (Hanford Engineering Development Laboratory).

7.5.1 ADIP Task

The Department of Energy (DOE)/Office of Fusion Energy (OFE) has cited the need to investigate ferritic alloys under the ADIP program task, Ferritic Steels Development (Path E). The tasks involved are akin to task number 1.B.13, Tensile Properties of Austenitic Alloys, task number 1.C.2, Microstructures aad Swelling in Austenitic Alloys and task number 1.C.1, Microstructural Stability.

7.5.2 Objective

The objective of this work is to provide guidance on the applicability of ferritic stainless steels for fusion reactor structural materials by providing mechanistic understanding of the effect of microstructure on postirradiation deformation.

7.5.3 Summary

Microstructural examinations using transmission electron microscopy have been performed on a tensile specimen of 2¼Cr-1Mo in the thermal annealed condition irradiated to 6.1 x 10^{22} n/cm^2 (E >0.1 MeV) at 400°C following postirradiation deformation. It is found that large increases in yield strength and ultimate tensile strength are a result of extensive precipitation of Mo_2C in weak ferrite grains and that effects of precipitation saturate by 10^{22} n/cm^2 or 5 dpa.

7.5.4 Progress and Status

7.5.4.1 Introduction

Ferritic stainless steels appear to provide attractive alternatives to austenitic stainless steels for fusion reactor applications. This has resulted in the establishment of the ADIP program task E, Ferritic Steels Development. A major concern regarding the application of such alloys in a fusion machine is the impact of irradiation on mechanical properties,

and in particular on fatigue and fracture toughness. As yet, little effort has been made to understand the phenomena which control these properties in ferritic stainless steels. It is therefore the intent of the present limited study to provide some understanding regarding the microstructural features which control postirradiation mechanical deformation in a ferritic steel, 2¼Cr-1Mo.

Irradiation and mechanical testing of the 2¼Cr-1Mo steel were performed under the auspices of the LMFBR Program. Microstructural analysis of postirradiation deformation was performed under OFE. Therefore, this effort represents an example where both programs gain substantially by cooperative effort.

7.5.4.2 Experimental Procedure

A tensile specimen of 2¼Cr-1Mo was made available for microstructural examination under the auspices of OFE following postirradiation testing. The specimen, #T453, was in the thermal annealed preirradiation condition (927°C for 30 minutes, cooled to 316°C at a rate slower than 55.5°C per hour and then air cooled). It had been irradiated in row 7 of the Experimental Breeder Reactor 11, Idaho Falls, Idaho at approximately 400°C to a fluence of 6.1 x 10^{22} n/cm^2 (E > 0.1 MeV). Uniaxial tensile testing at 425°C gave the following results: 0.2% offset yield strength, 624 MPa; ultimate tensile strength, 627 MPa; uniform elongation, 0.9%; total elongation, 4.1%. This yield strength represented a 170% increase over that of an unirradiated specimen. Specimens suitable for transmission electron microscopy were prepared from both the gauge and grip sections. Preparation and examination procedures were standard, as previously described.[1]

7.5.4.3 Results

7.5.4.3.1 Preirradiation Microstructure. The thermal anneal microstructure in 2¼Cr-1Mo is duplex, containing ferrite and cellular M_6C precipitation in ferrite often referred to as pearlite. Ferrite regions did contain occasional Mo_2C needles and regions adjacent to pearlite could be found containing higher densities of Mo_2C needles. The dislocation structure in both regions was low to moderate.

7.5.4.3.2 Unstressed Postirradiation Microstructure. Specimens from the grip section of tensile specimen T453 were examined following deformation to provide unstressed microstructural information. Irradiation to 6.1 x 10^{22} n/cm^2 (E >0.1 MeV) at 400°C produced significant amounts of void swelling, precipitation and dislocation development. Void swelling was highest in regions containing pearlite due to a higher density of larger voids but void swelling was found in ferrite regions as well. Also of note were high densities of smaller voids located at precipitate/ferrite interfaces. However, the total void swelling is low, estimated at less than 0.5%.

Precipitate structures present prior to irradiation remained stable but irradiation resulted in extensive further precipitation. This precipitation occurred predominantly in ferrite regions and consisted of needle shaped particles 30 nm long by 3 nm in diameter at a high number density (on the order of 2 x 10^{16} cm^{-3}). Electron diffraction analysis was consistent with identification as Mo_2C.

The dislocation structure was found to consist primarily of dislocation loops. The density varied as a function of precipitate density, with a higher density of small loops developing in ferrite regions containing the fine Mo_2C needles. Where Mo_2C was not present, such as in pearlite or adjacent to large precipitate particles in ferrite, the dislocation structure more closely resembled a tangle characteristic of extensive irradiation-induced dislocation climb. The radiation-induced dislocation structure is inferred to consist of a $\langle 100 \rangle$ Burgers vectors. It may be noted that dislocation imaging was significantly complicated by the presence of the fine Mo_2C precipitates. Dark field imaging techniques were found to be undecipherable necessitating that only bright field imaging techniques be used.

Examples of the unstressed postirradiation microstructures are given in Figures 7.5.1 and 7.5.2. Figure 7.5.1 compares a region in ferrite in void contrast (a), bright field dislocation contrast (b) and two variants of Mo_2C dark field contrast (c) and (d). *Two* large precipitate particles formed prior to irradiation can be seen at the lower right hand side and adjacent to these particles regions can be identified with enhanced void swelling, a lower dislocation density and reduced Mo_2C concentrations.

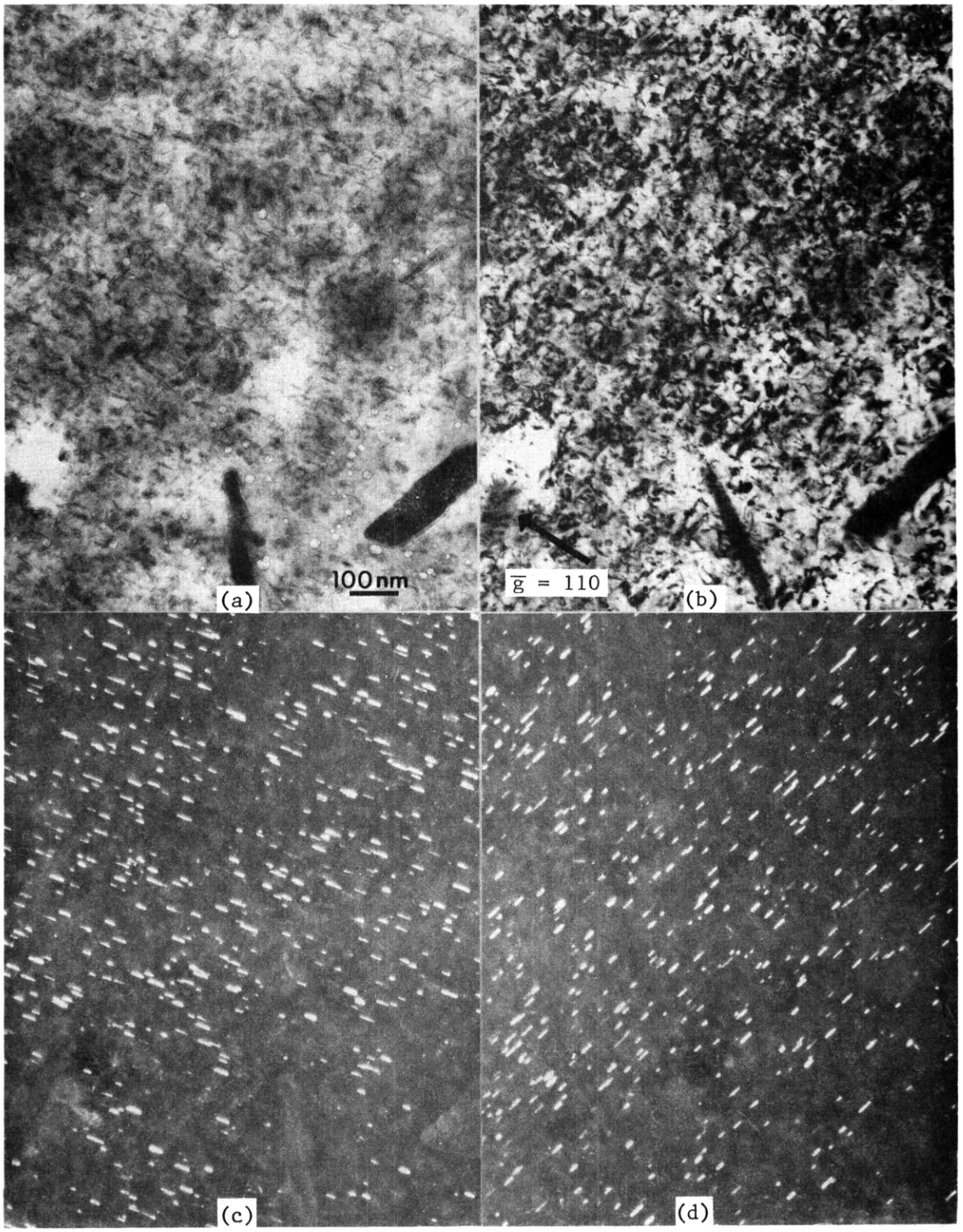

Fig. 7.5.1. Microstructure in ferrite *of* unstressed 2¼Cr-1Mo following irradiation to 6.1 x 10^{22} n/cm^2 (E >0.1 MeV) at 400°C in (a) void contrast, (b) dislocation contrast and (c), and (d) dark field constrast of two variants of Mo_2C.

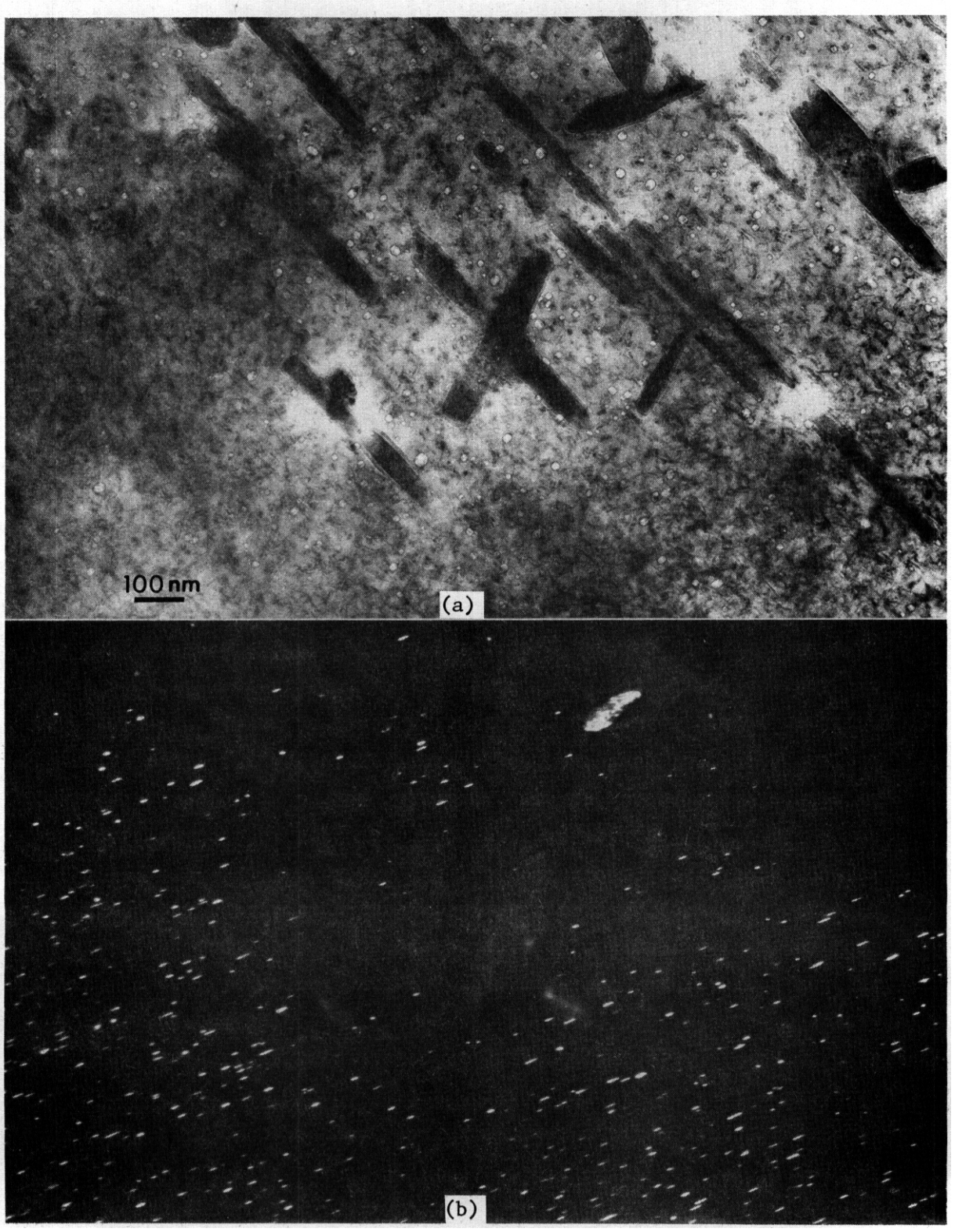

Fig. 7.5.2. Mo_2C development near M_6C cellular precipitation in (a) void contrast and (b) Mo_2C dark field contrast.

Figure 7.5.2 provides comparison of Mo_2C distributions in pearlite and adjacent ferrite. The structure is shown in void contrast in Figure 7.5.2(a) and the same area is imaged in Mo_2C dark field contrast in Figure 7.5.2(b). From Figure 7.5.2, it is further emphasized that the Mo_2C forms in ferrite but not in pearlite. The Mo_2C phase therefore appears to be responsible for reduced void swelling and dislocation development and can be expected to affect postirradiation mechanical properties.

7.5.4.3.3 Postirradiation Deformation Microstructure. The deformed microstructure appeared very similar to the undeformed microstructure. Void and precipitate development appeared identical and dislocation structures were very similar. An example is given in Figure 7.5.3 showing a region adjacent to a grain boundary in bright field void contrast (a) and bright field dislocation contrast (b). Close inspection of Figure 7.5.3(b) will reveal that between the arrows a dislocation slip band may be identified. Along that band two dislocation loops (marked A and B) and a void of unusual shape (c) can be identified. Therefore, it may be concluded that deformation is restricted to slip on individual slip planes and is probably localized in regions adjacent to pearlite where in-reactor Mo_2C precipitation does not occur.

7.5.4.4 Discussion

This microstructural examination of postirradiation deformation in 2¼Cr-1Mo reveals that significant microstructural changes have occurred as a result of irradiation which can account for observed changes in properties. Extensive precipitation of Mo_2C has developed and glissile dislocation loops have evolved. Both features will cause large increases in yield strength by inhibiting dislocation slip and will lead to a tendency for dislocation channeling. In regions where Mo_2C is reduced and dislocation structures are less dense, for example, in pearlite regions, a weaker microstructure results. Nonuniform deformation restricted to such regions will result in reduced plasticity.

Further understanding of the impact of irradiation-induced microstructural development on postirradiation yield strength can be obtained by reviewing earlier unpublished results from this study. Figure 7.5.4

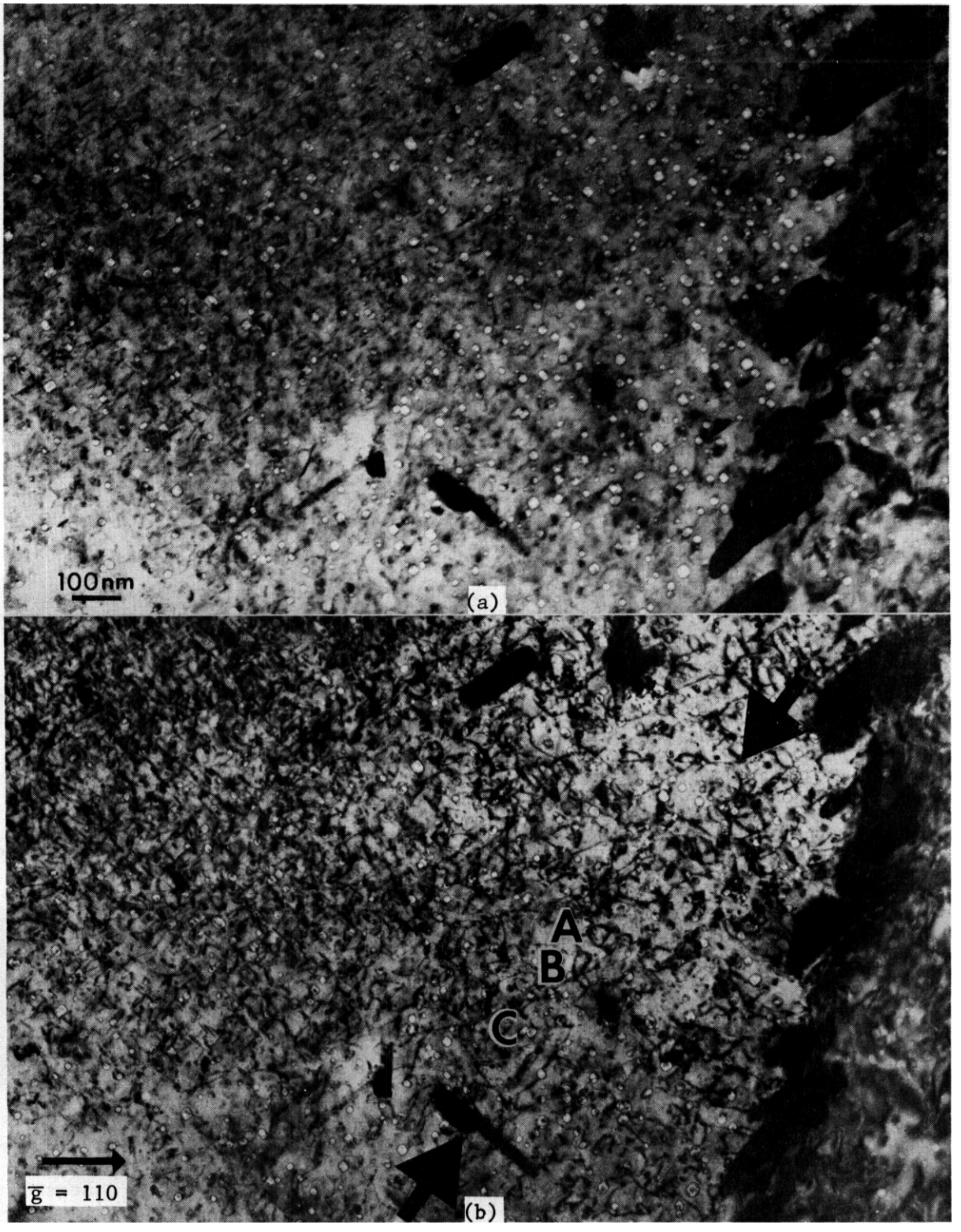

Fig. 7.5.3. Microstructure near a grain boundary in deformed 2¼Cr-1Mo following irradiation to 6.1 x 10^{22} n/cm^2 (E >0.1 MeV) at 400°C in (a) void contrast and (b) dislocation contrast. The arrows define a slip band with sheared loops at A and B and a distorted void at C.

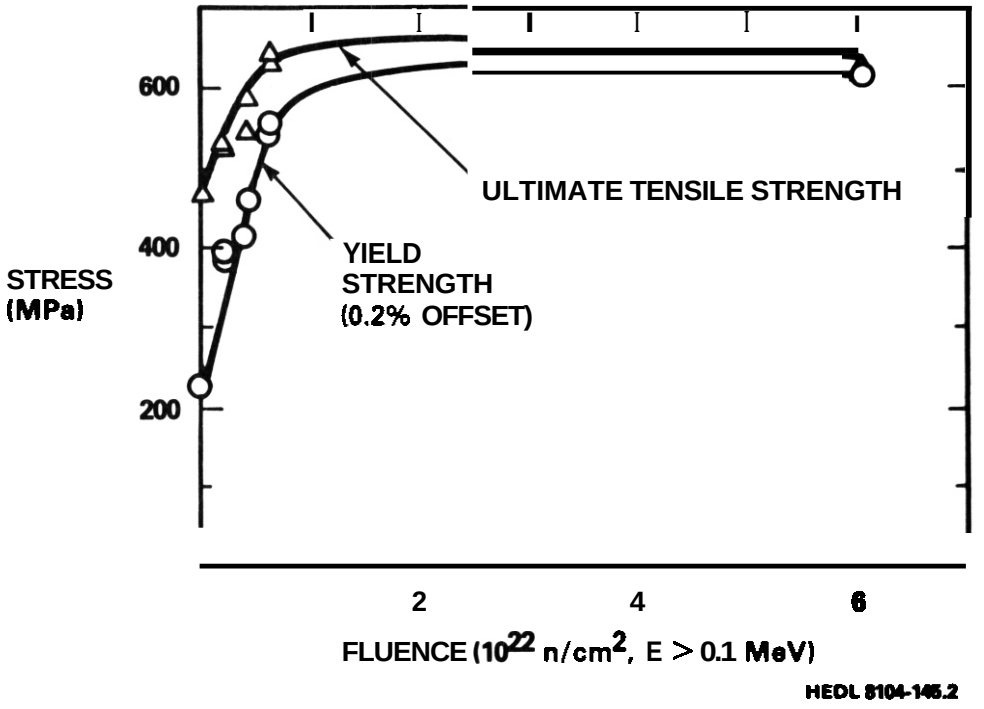

Fig. 7.5.4. Yield and ultimate tensile strength in 2¼Cr-1Mo as a function of fluence.

presents low fluence yield strength and ultimate tensile strength results in comparison with the present results as a function of fluence. From Figure 7.5.4, it may be demonstrated that yield strength and ultimate tensile strength increase rapidly as a function of fluence and then saturate at fluences on the order of 10^{22} n/cm^2. Such response indicates (1) void and dislocation structures are not having a large effect on strength because point defect agglomeration will not saturate with increasing fluence. (2) The large increase in strength must be attributed to precipitation of Mo_2C which results in large strength increases in the weak ferrite grains. (3) The kinetics of Mo_2C are extremely rapid; the precipitation process is completed after 10^{22} n/cm^2.

7.5.5 Conclusions

Extensive precipitation of Mo_2C in weak ferrite grains produces rapid increases in yield and ultimate tensile strength as a result of irradiation at 400°C in 2¼Cr-1Mo in the thermal annealed condition. Fluences on the order of 10^{22} n/cm^2 or 5 dpa result in saturation of the behavior.

7.5.5.1 Future Work

This effort will shift to HT-9 and will include postirradiation examination from OFE experiments and low fluence irradiation creep examinations.

7.6 EVIDENCE OF SEGREGATION TO MARTENSITE LATH BOUNDARIES IN A TEMPERED-EMBRITTLED 12 Cr-1 Mo-0.3 V STEEL (HT-9) — T. A. Lechtenberg (General Atomic Company)

To be reported in the next quarterly report.

7.7 ENVIRONMENTAL EFFECTS ON PROPERTIES OF FERRITIC STEELS – O. K. Chopra and D. L. Smith (Argonne National Laboratory)

7.7.1 ADIP Task

ADIP tasks are not defined for ferritic steels in the 1978 program plan.

7.7.2 Objective

The objective of this program is to investigate the influence of chemical environment on the compatibility, corrosion, and mechanical properties of ferritic steels under conditions of interest in fusion reactors. Test environments to be investigated include lithium, water, and helium as well as candidate solid breeding materials and neutron multipliers. Emphasis will be placed on the combined effect of stress and chemical environment on corrosion and mechanical properties of ferritic steels. Tests have been formulated to determine the (1) effect of a liquid lithium environment on fatigue and creep-fatigue properties of ferritic steels and (2) compatibility of structural materials with liquid lithium and candidate solid tritium-breeding materials.

7.7.3 Summary

Several continuous-cycle fatigue tests have been conducted on Type 304 stainless steel at 755 K in lithium containing ~700 wppm nitrogen. The test specimens show secondary cracks along the entire gauge length. Similar behavior was observed for HT-9 alloy tested in lithium containing ~1400 wppm nitrogen. Secondary cracks are generally not observed in ferritic and stainless steels tested in a low-oxygen sodium environment. These results indicate that the concentration of nitrogen in lithium has a strong effect on the fatigue behavior of ferritic as well as austenitic steels. A 3.6-Ms (1000-h) exposure of an HT-9 specimen under constant stress in lithium at 755 K has been completed. The specimen is being examined metallographically to evaluate the combined effects of constant stress and lithium environment on the corrosion behavior of HT-9 alloy. Compatibility tests were

carried out to investigate the reactivity of candidate solid breeding materials, i.e., Li_2O, $LiAlO_2$, Li_2SiO_3, Li_2ZrO_3, and Li_2TiO_3, with HT-9 alloy and Type 316 stainless steel. Metallographic evaluation of the specimens is in progress.

7.7.4 Progress and Status

7.7.4.1 Fatigue Tests

The effects of a liquid lithium environment on the fatigue properties of ferritic steels are being investigated. Several continuous-cycle fatigue tests have been conducted on HT-9 alloy at 755 K in a flowing lithium environment of controlled purity. The results show that the concentration of nitrogen in lithium has a large effect on the fatigue behavior of HT-9 alloy.' The fatigue life in lithium containing >1000 wppm nitrogen is a factor of 2 to 5 lower than that in a low-oxygen sodium environment. The specimens tested in high-nitrogen lithium showed partial intergranular fracture and considerable internal corrosive penetration.

The high nitrogen concentration in lithium also resulted in extensive corrosion and mass transfer in the stainless steel loop. The loop was shut down twice owing to plugging of the flowmeter and pump sections of the cold-trap purification system. Metallographic examination of the residue collected from the plugged sections indicated that plugging was caused by trapping of the nickel-manganese and iron-nickel-manganese crystals under the magnetic pump coil and flowmeter magnet.

During the present reporting period, four continuous-cycle fatigue tests were performed on solution-annealed Type 304 stainless steel in lithium at 755 K for a comparative evaluation of the fatigue behavior of ferritic and austenitic steels. The tests were conducted in flowing lithium containing ~700 wppm nitrogen. The strain-life data are shown in Fig. 7.7.1. The best-fit curve for tests conducted in air is also included in the figure. The results show that the fatigue life of Type 304 stainless steel in a lithium environment is

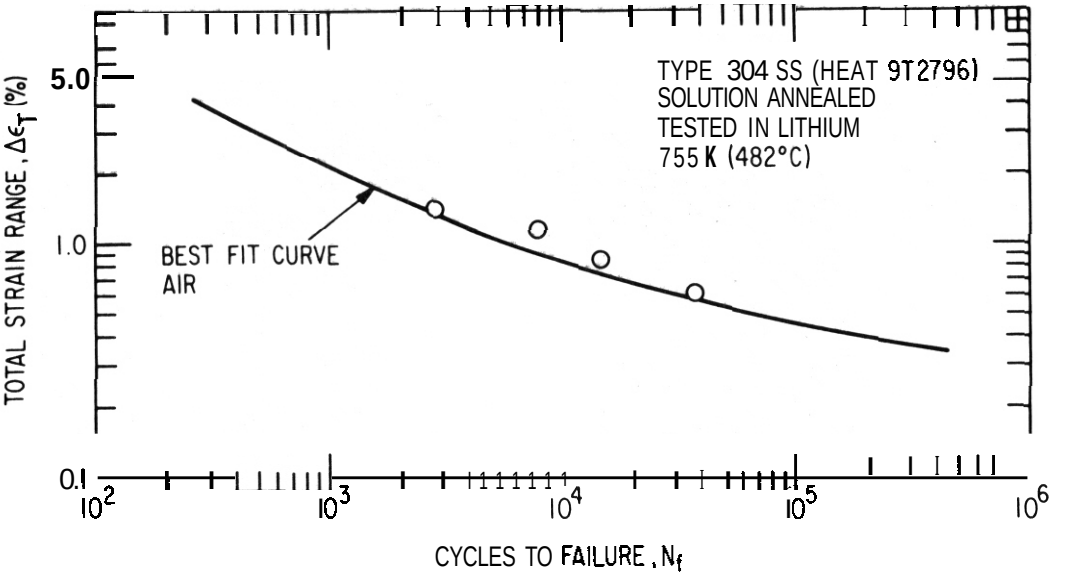

Fig. 7.7.1. Total Strain Range vs Cycles to Failure for Type *304* Stainless Steel Tested in Lithium at 755 K.

the same as or slightly greater than that in air. Metallographic examination of the specimen tested in lithium at a total strain range of 0.61% revealed several secondary cracks at the surface. Figure 7.7.2 shows a micrograph of the longitudinal section of the test specimen. Similar behavior was observed in the HT-9 specimens tested in lithium containing >1000 wppm nitrogen. Secondary cracking is virtually absent in ferritic and stainless steels tested in a low-oxygen sodium environment.

Although these tests indicate that the fatigue life of Type 304 stainless steel in lithium is similar to that in air, secondary cracks in the specimens suggest that a high nitrogen concentration in lithium can influence the fatigue life of Type *304* stainless steel. Fatigue data obtained in a low-oxygen sodium environment should be used as a reference for the evaluation of the influence of lithium on the fatigue behavior of materials. Fatigue tests on Type *304* stainless steel will be conducted in a flowing sodium environment at 755 K for comparison.

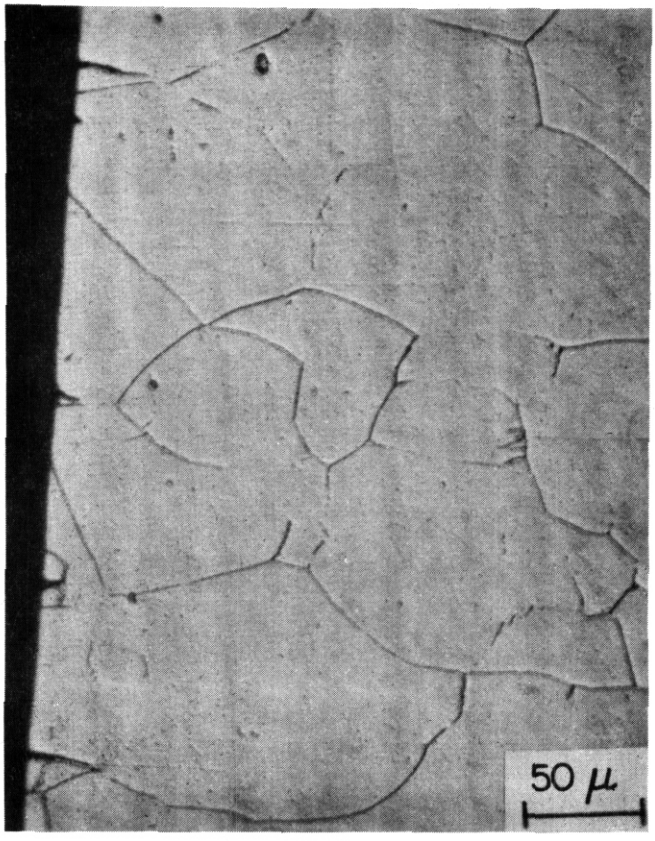

Fig. 7.7.2. Micrograph of the Longitudinal Section of Type *304* Stainless Steel Specimen Tested in Lithium at 755 K.

7.7.4.2 Compatibility

The combined effects of constant stress and liquid lithium environment on the corrosion behavior of ferritic steels are being evaluated by exposing monotonically stressed specimens of HT-9 alloy to flowing lithium. For this investigation, a dead load is applied to tapered specimens (with ~2.2-mm minimum and ~6.3-mm maximum diameter). A 3.6-Ms exposure of an HT-9 specimen in lithium at 755 K has been completed. For this test, the applied stress was in the range of 15 and 137 MPa. Metallographic examination of the specimen is in progress.

7.7.4.3 Solid Breeding Materials

A comparative evaluation of the compatibility of HT-9 alloy, Type 316 stainless steel. and Inconel 625 exposed in contact with pellets of Li_2O, γ-$LiAlO_2$, or Li_2SiO_3 tritium-breeding materials was presented in an earlier report.[1] The results indicated that Li_2O is the most reactive of the three breeding materials. The interaction zone between the HT-9 alloy and Li_2O ceramic contained Li_5FeO_4 and $LiCrO_2$ compounds, whereas $Li_2Ni_8O_{10}$ and $LiCrO_2$ were observed on the Inconel 625 specimen. For this test, the various reaction couples were retained in a common stainless steel test apparatus. The formation of volatile compounds, e.g., Li_5FeO_4 and $LiCrO_2$, resulted in cross-contamination between the different reaction couples. A subsequent test was therefore designed to use isolated reaction couples. Tube specimens of HT-9 alloy and Type 316 stainless steel were individually packed with five different ceramic materials, i.e., Li_2O, $LiAlO_2$, Li_2SiO_3, Li_2ZrO_3, or Li_2TiO_3, and sealed. The tube specimens were encapsulated in a quartz tube and annealed at 973 K for 3.6 and 7.2 Ms. Metallographic evaluation of the specimens is in progress.

7.7.5 References

1. O. K. Chopra and D. L. Smith, "Environmental Effects on Properties of Ferritic Steels," ADIP Quarterly Progress Report, December 31, 1980.

7.C THE EFFECT OF INTERNAL HYDROGEN ON THE MECHANICAL PROPERTIES OF HT-9: ROOM TEMPERATURE - J. M. Hyzak and R. E. Stoltz (Sandia National Laboratories, Livermore, CA)

7.8.1 ADIP Task

The Department of Energy (DOE) Office of Fusion Energy (OFE) has cited the need for these data under the ADIP Program Task, Ferritic Alloy Development (Path E).

7.8.2 Objective

The goal of this study is to evaluate the hydrogen compatibility of 12Cr-1Mo ferritic/martensitic steel for use in first wall and blanket structures. This report summarizes preliminary data on the effect of internal hydrogen on the room temperature tensile properties of HT-9.

7.8.3 Summary

Tensile testing of quench and tempered HT-9 in 0.10 MPa (15 psi) external hydrogen at room temperature has previously been shown to cause a reduction in ductility and change in fracture mode compared to tests in air. This report summarizes preliminary results on the effect of internal hydrogen, introduced by cathodic charging, on the tensile properties of both as-quenched and quench and tempered HT-9. Tensile specimens were cathodically charged at (0.003 A/cm^2) and (0.006 A/cm^2) for up to 150 minutes, immediately copper plated, and tested at room temperature. There was no appreciable effect of internal hydrogen on the tensile properties of quench and tempered BT-9. The hydrogen levels were believed to be greater than 30 ppm compared to 1-5 ppm in the previous gas phase testing. For the higher strength, quenched microstructure, the same charging conditions resulted in fracture mode from cup-cone centerline cracking and void coalescence to more brittle surface crack initiation. These results support the earlier gas phase test results that hydrogen embrittlement of quench and tempered HT-9 is not a serious concern. However, at strength levels above 700 MPa (produced here by eliminating the temper treatment) large hydrogen effects are manifest. The data reconfirm the need for hydrogen testing of irradia-

tion hardened samples.

7.8.4 Progress and Status

7.8.4.1 Experimental Details

Tensile tests were performed on samples cathodically charged with hydrogen, and copper-plated to retard outgassing. The charging solution was 4 percent sulfuric acid containing 5mg of sodium arsenate. The current densities employed were 0.003 A/cm^2 (0.02 A/in^2) and 0.006 A/cm^2 (0.04 A/in^2) for 8 and 150 minutes (Table I). Specimens were copper plated in a acid copper bath immediately after charging, and aged at room temperature for 24 hours before testing in order to evenly distribute the hydrogen. The internal hydrogen concentrations resulting from the different charging conditions have not as yet been fully determined, but preliminary data indicates that even the least severe condition (.003 A/cm^2/8 minutes) would result in hydrogen levels greater than 10 ppm.

All tests were performed on samples taken from a pipe section supplied by General Atomics (Ref. 1). Material was tested in both the quenched and quench and tempered conditions. All specimens were austenitized at 1040°C/30 min. and air cooled; the tempered specimens were further heat treated at 750°C for 60 minutes. Both microstructures were fully martensitic. Tensile bars had a nominal 0.287 cm (0.113 in) gage diameter and a 1.27 cm (0.500 in) gage length. All tests were run at 0.13 cm/min. (0.05 in/min.) extension rate. Following completion of the tensile tests, the fracture surfaces were examined by SEM.

7.8.4.2 Results

The results of all the tensile tests are given in Table I. For the quench and tempered microstructure, there was no significant effect of internal hydrogen on the ductility, as measured by the reduction in area (R_A) after fracture. However, there did appear to be a small but consistent increase in both yield and ultimate strength as a result of hydrogen charging. The fracture process for both the charged and un-

Table I

Mechanical Properties of HT-9 Subject to Cathodic Charging

Spec #*	Charging Cond.**	Yield Strength MPa (ksi)	Ultimate Strength MPa (ksi)	Reduction in Area (%)	Total Elongation (%)
Q&T 18	Uncharged	650 (94.3)	792 (114.9)	58.8	16.9
Q&T 16	.003 A/cm^2-8 min.	656 (95.2)	823 (119.4)	62.1	17.8
Q&T 20	.003 A/cm^2-150 min.	676 (98.0)	816 (118.4)	59.6	16.5
Q&T 23	.006 A/cm^2-150 min.	673 (97.6)	836 (121.3)	60.0	17.2
Q 17	Uncharged	980 (142.2)	1676 (243.1)	28.0	8.8
Q 15	.003 A/cm^2-8 min.	943 (136.7)	1616 (234.4)	27.1	8.0
Q 19	.003 A/cm^2-150 min.	1261 (182.9)	1564 (226.9)***	6.7	1.7
Q 26	.003 A/cm^2-150 min.	1225 (177.6)	1731 (251.0)***	7.2	3.7
Q 24	.006 A/cm^2-150 min.	554 (80.3)***		6.0	.1

*Q&T-Quench & Temper Microstructure

Q-As-Quenched Microstructure

**Current Density (amps/cm^2) and Charging Time

***Fracture Stress

charged specimens was the same, classical cup-cone failure. The fracture surfaces were rough with many large secondary cracks in the interior surrounded by a uniform shear lip (Fig. 1a). The fracture mode in the central section was dimpled rupture (Fig. 1b). Examination of metallographic cross-sections of the fracture surfaces revealed that fracture occurred in the tensile (rolling) direction along lath boundaries (Fig. 2a) as the result of nucleation and growth of voids at tempered carbides and stringers (Fig. 2b).

The as-quenched microstructure had an uncharged yield strength substantially higher than that of the quench and tempered condition, 980 MPa versus 650 MPa. There was also a much larger effect of hydrogen charging on the tensile properties in the quenched material compared to the quench and tempered condition. Charging at 0.003 A/cm^2 for 2.5 hours increased the yield strength by 260 MPa and reduced the ductility by 78%, from 28% to 7%. Charging for comparable times at twice that current density caused further embrittlement; the specimen failed at 554 MPa (80.3 ksi), before general yielding occurred.

The fracture appearance of the as-quenched specimens differed in both the charged and uncharged conditions from that observed for the quench and tempered speicmens. The uncharged specimen with the as-quenched microstructure had a cup-cone type failure with a blocky topography on the fracture surface and some secondary cracking (Fig. 3a). The fracture surface exhibited regions of both dimpled rupture and a more brittle faceted fracture (Fig. 3b). Observations of cross-sections of the fracture surfaces suggested that fracture was transgranular proceeding mainly along untempered martensitic lath boundaries. Cracking along prior austenitic grain boundaries and stringers in the tensile stress direction also contributed to the "tortuous" fracture topography.

Fracture of the highly charged samples (Q19, Q24, Q26) was much more flat and brittle. Specimen Q19 failed in a cup-cone mode (Fig. 4a), but the fracture surface was dominated by faceted fracture along untempered lath boundaries (Fig. 4b). Specimen Q24 which was the most severely charged exhibited surface crack initiation and no shear lip (Fig. 5). The fracture initiated at surface flaws associated with the machining process.

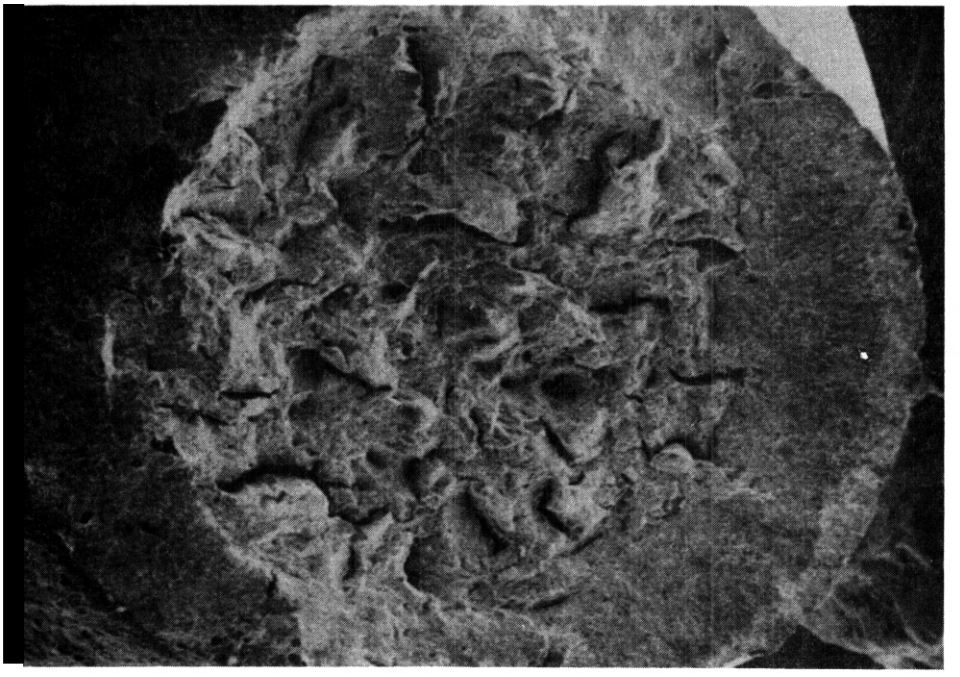

(a)

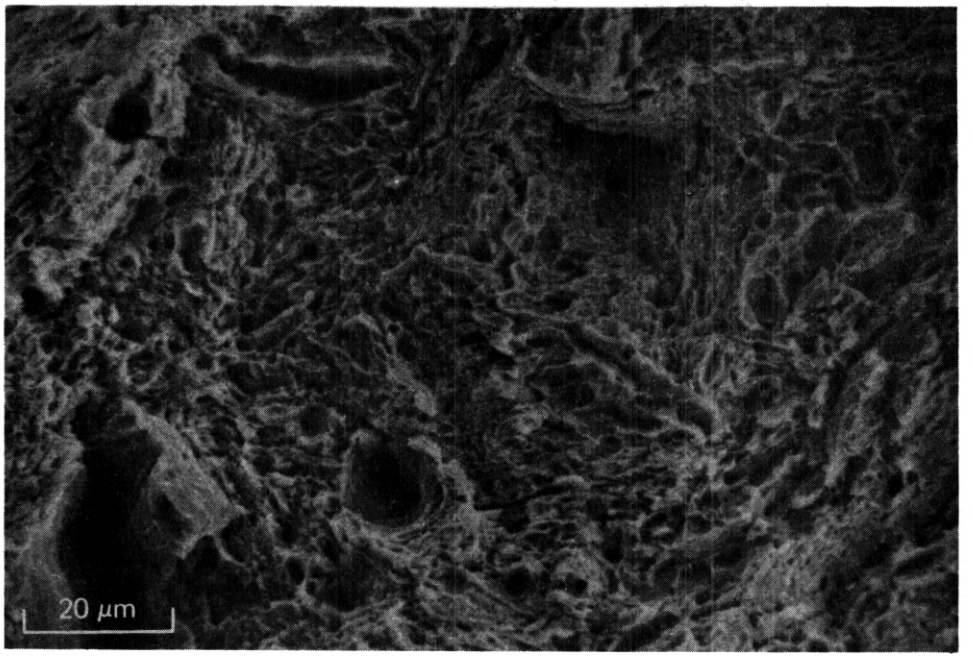

(b)

Figure 1. Tensile fracture of cathodically charged HT-9 quench and tempered specimen tested in air: (a) low magnification of cup-cone fracture; (b) higher magnification showing dimpled rupture fracture morphology.

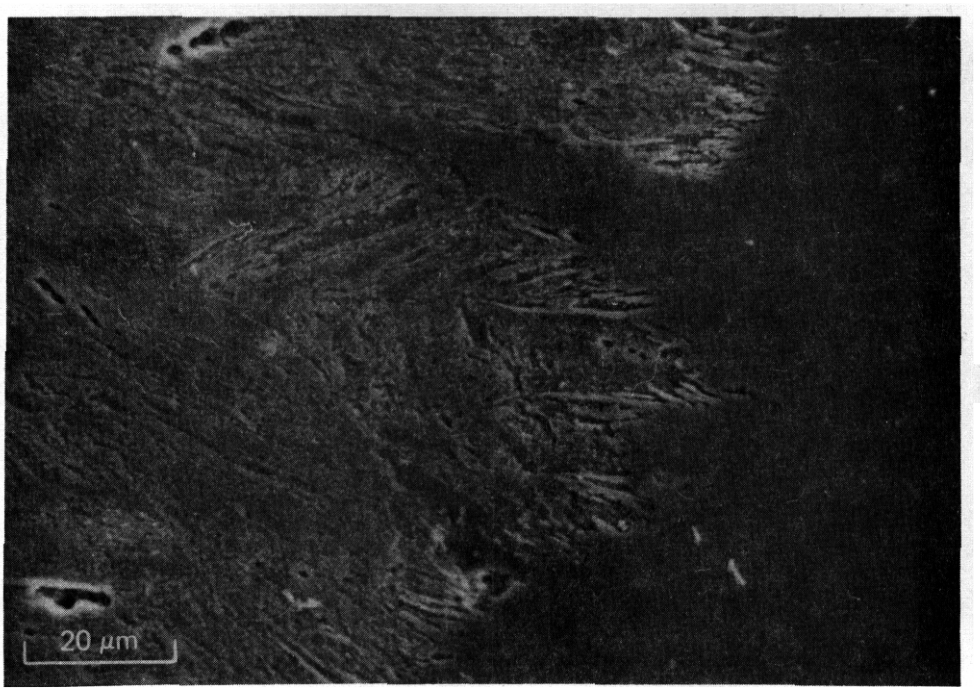

(a)

(b)

Figure 2. Nickel-plated cross-sections *of* uncharged €IT-9 quench and tempered tensile fracture: (a) fracture along martensite lath boundaries; (b) void nucleation at tempered carbides and inclusion stringers. Tensile direction is horizontal.

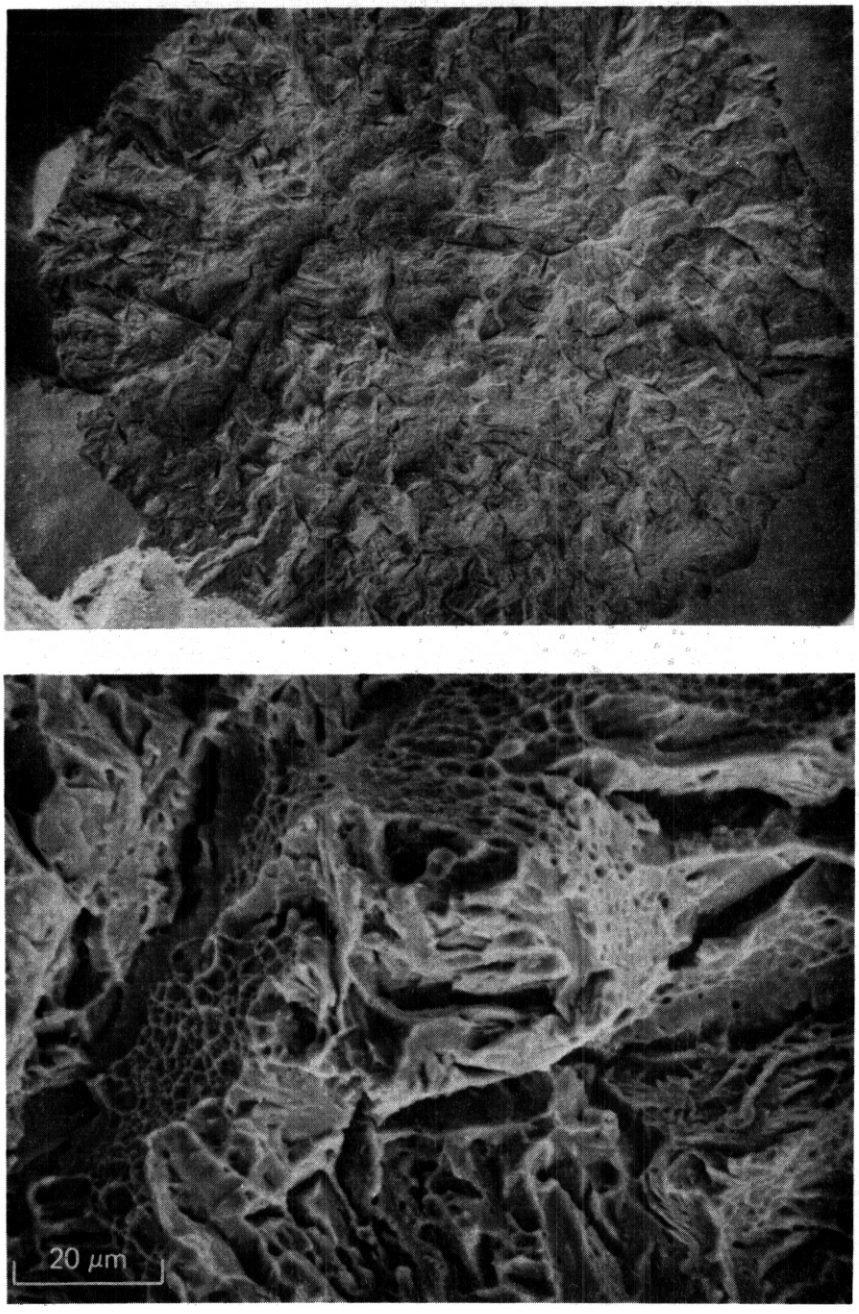

Figure 3. Surface of uncharged HT-9 as quenched tensile specimen: (a) low magnification photo *of* cup-cone failure mode with rough, blocky fracture topography; (b) higher magnification showing combination of dimpled rupture and faceted fracture in center region.

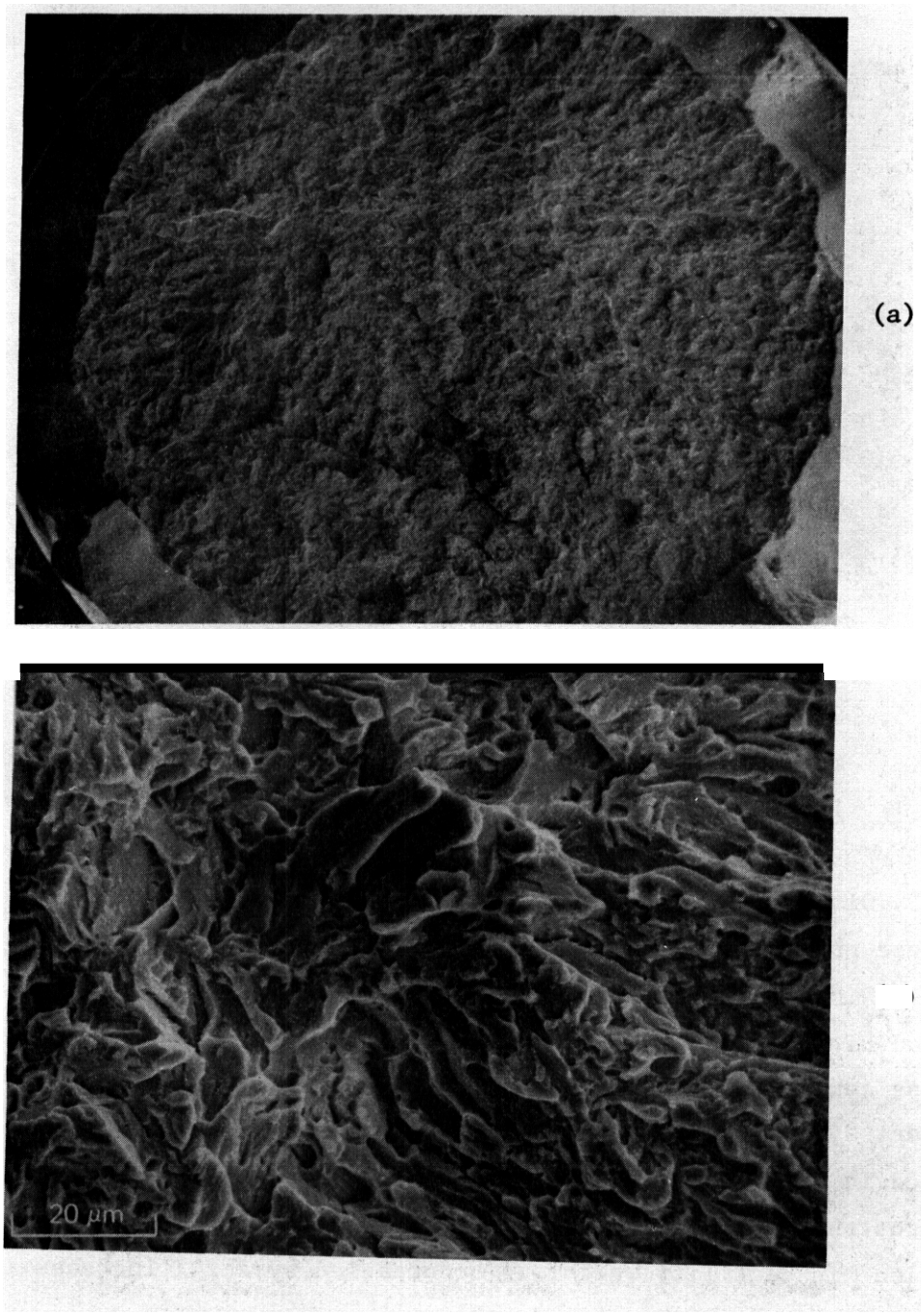

Figure 4. Surface of cathodically charged (.003 A/cm^2, 150 min.) HT-9 as-quenched tensile specimen: (a) low magnification of relatively flat, brittle fracture; (b) higher magnification of faceted brittle fracture mode.

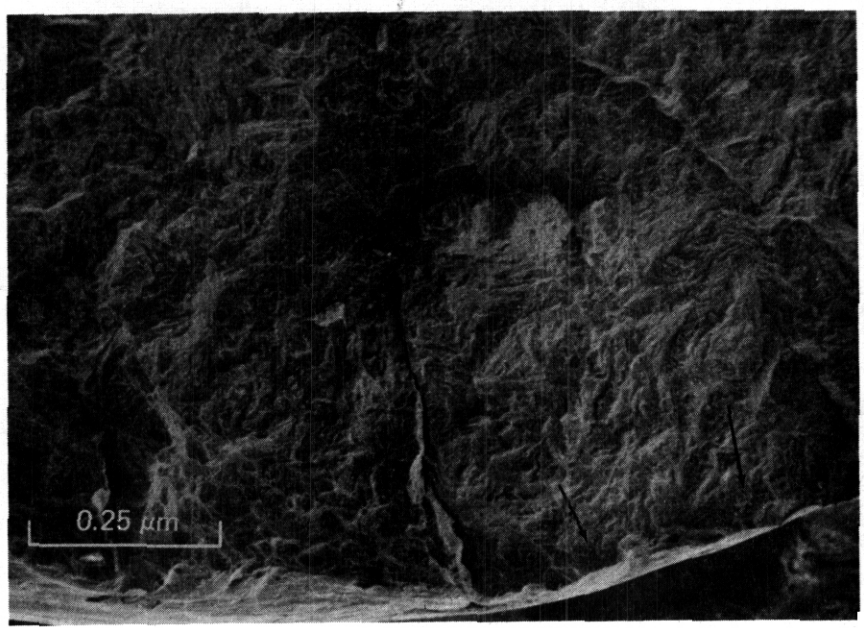

Figure 5. Fracture surface of cathodically charged (.006 A/cm^2, 150 min.) HT-9 as quenched tensile specimen with surface crack initiation sites (arrows) and no shear lip.

7.8.4.3 Discussion

These preliminary results indicate that there is no appreciable effect of internal hydrogen on the tensile properties of quench and tempered HT-9 in the 620-690 MPa (90-100 ksi) yield strength regime. Charging conditions up to 0.006 A/cm^2 for 2½ hours were imposed; the resultant hydrogen concentrations are believed to be well above those expected in HT-9 first wall structures[2]. For the higher strength quenched microstructure, however, similar charging conditions resulted in a 78% reduction in ductility which was accompanied by a 24% increase in yield strength.

In a previous report (Ref. 1) it was shown that testing in a gaseous hydrogen environment can reduce the tensile properties of quench and tempered HT-9. Specimens tested at 25°C in the presence of 0.10 MPa (15 psi) hydrogen showed a ductility decrease from 68% to 58% with a corresponding change in fracture mode. These tests had an overall hydrogen concentration of 1-5 ppm whereas the least severe cathodic charg-

ing condition (0.003 A/cm^2, 8 minutes) is believed to result in greater than 10 ppm hydrogen with concentrations greater than 30 ppm for the other charging levels. The difference in behavior between internal hydrogen (cathodic charge) and external hdyrogen (gaseous environment) is thought to be due to their respective influences on the failure origins. Gaseous hydrogen introduces a large hydrogen surface concentration into the tensile sample, and as a result shifts the initiation location from the interior (cup-cone fracture) to the surface. Hydrogen assisted crack growth intervenes and causes failure before the normal ductile-rupture process is complete. Internal hydrogen, however, is more generally distributed through the gage diameter, and at nominally the same overall hydrogen concentration as for the gaseous hydrogen, surface crack initiation does not occur and the ductility is maintained.

The internal hydrogen concentration did affect the fracture location for the higher strength HT-9 as quenched samples. At the lower charging levels, cup-cone fracture occurred. However, specimen Q24 which was the most severely charged sample, failed from surface initiated cracks at only *554* MPa (80 ksi) with less than 0.1% total elongation. These results indicate that increasing the internal hydrogen concentration can increase the likelyhood of surface initiated failures which in turn interrupts the cup-cone, centerline initiation process and enhances embrittlement. The data also show that this decrease in defect tolerance with increasing hydrogen concentration is more of a concern with higher strength alloys.

The quenched specimens which had a higher strength level than the quench and tempered microstructure were used to simulate the yield strength increases observed following irradiation. The present results indicate that hydrogen effects are magnified at strength levels greater than 690 MPa (100 ksi). There are certain important differences, however, between quench hardened and irradiation hardened samples. Irradiation would introduce a large number of hydrogen traps along with the increase in strength. In this case, the traps may reduce the susceptibility of the irradiated alloy to hydrogen embrittlement by binding the hydrogen to innocuous sites. This is the same type of process that is thought to give the quench and tempered microstructure its relative immunity

to hydrogen embrittlement. However, hydrogen testing of irradiated material is critical to understanding this process, and should be pursued.

7.8.5 Conclusions

Preliminary studies of the effect of internal hydrogen on HT-9 have shown:

1. Cathodic charging at levels up to 0.006 A/cm^2 for 150 minutes (>30 ppm hydrogen) did not effect significantly the tensile properties of quenched and tempered HT-9 (620-690 MPa yield strength).

2. Similar charging of as-quenched HT-9 (965-1035 MPa yield strength) reduced its ductility 78% and resulted in a change in fracture mode. With increasing hydrogen concentration, the failure mode changed from centerline crack initiation and void coalescence (cup-cone mode) to surface initiated cracking.

3. Surface initiated failure which is associated with a high local hydrogen concentration results in increased embrittlement compared to centerline cracking and cup-cone failure. Surface crack initiation, which represents a decrease in defect tolerance, is promoted by gas phase testing and charging to high internal hydrogen levels. Susceptibility is also greater in higher strength alloys.

7.8.6 References

1. R. E. Stoltz, "Mechanical Property Measurements of HT-9 in Hydrogen: 25 to 400°C", ADIP Quarterly Progress Report, March 31, 1980, DOE/ER-0045/2, pp. 88-97.

2. R. E. Stoltz, M. I. Baskes, and G. W. Look, "Calculations of Hydrogen Isotope Loading in HT-9 First Wall Structures", ADIP Quarterly Progress Report, September 30, 1980, DOE/ER-0045/4, pp. 151-159.

7.9 TEMPERING BEHAVIOR OF LASER WELDS IN HT9 - J. C. Lippold (Sandia National Laboratories, Livermore, CA)

7.9.1 ADIP Task

The Department of Energy (DOE)/Office of Fusion Energy (OFE) cited the need for these data under the ADIP Program Task, Ferritic Alloy Development (Path E).

7.9.2 Objective

This phase of the ongoing investigation of the welding metallurgy of HT9 addressed the tempering response of autogenous laser welds. The formation of untempered martensite in both the fusion zone and heat-affected zone (HAZ) seriously compromises the structural integrity of the alloy and necessitates a postweld heat treatment to restore adequate mechanical properties. Presently, a postweld heat treatment of 2 hours at 760°C (1400°F) is being considered for use in construction of the Fusion Engineering Device (FED). Selection of this heat treatment was based primarily on mechanical property data gathered from high heat input and/or high deposition rate processes (such as the gas tungsten-arc or gas metal-arc process). Since laser welding is a low energy input, high energy density process, the tempering response of laser welds may be somewhat different due to variations in the weld microstructure relative to the high energy input welds. The main objective of this study was to determine if a less stringent postweld heat treatment could be utilized in order to impart comparable structural integrity to laser welded components.

7.9.3 Summary

The effect of postweld heat treatment on both the microstructure and properties of laser welds in HT9 was evaluated. High depth-to-width ratio laser welds made at a power level of 6 kW and a travel speed of 2.96 mm/sec (70 in/min) were heat treated for 1 and 2 hours at 400, 600, and 800°C (750, 1110, and 1470°F). Heat treated weldments tempered at 400°C exhibited little variation in either microhardness or microstructure relative to the as-welded properties.

Tempering at 600°C markedly reduced the hardness in both the fusion zone and HAZ. The decrease in hardness was associated with the initial stages of martensite tempering and the simultaneous precipitation of alloy carbides. Heating to 800°C reduced the hardness in all regions of the weldment to the level of the base metal. Comparison of the tempering response of the laser welds with the previously reported behavior of gas tungsten-arc welds indicated that the postweld heat treatment necessary to restore adequate mechanical properties to the weld region is relatively insensitive to the welding process which is employed.

7.9.4 Progress and Status

The analysis of the properties and microstructure of HT9 laser welds is the final stage in the Sandia effort to investigate and define the welding metallurgy of the 12Cr-1Mo-0.3V martensitic stainless steel system. The data base which has been established will provide baseline information for future studies of HT9 weldments in actual operating conditions. These studies will evaluate the behavior and influence of weld microstructures in both hydrogen and irradiation environments.

7.9.4.1 Experimental Approach

The composition of the base material which was provided by General Atomic is listed in Table 1. Prior to welding the as-received material was austenitized for 30 minutes at 1040°C (1905°F) and subsequently tempered for 1 hour at 750°C (1380°F). The hardness of the heat treated material was R_C 22-24.

Table I
Chemical Composition (wt%)

C	Si	Mn	Cr	Ni	V	P	S
0.22	0.38	0.52	11.3	0.50	0.27	.019	.006

Laser welds were performed at the Naval Research Laboratory through the courtesy of Dr. Ed Metzbower and Dr. Deug Moon. The welds used in the heat treatment study were made at a power level of 6 kW and a travel speed of 2.96 mm/sec (70 in/min). These parameters were the minimum

necessary to achieve full pkaetration through the 6.35 mm (0.25 in) plate. The plates were not preheated prior to welding.

Heat treatment coupons sectioned transverse to the welding direction were tempered at 400, 600, and 800°C (750, 1110, and 1470°F) for 1 and 2 hours in air. Following the tempering treatment the samples were mounted and metallographically polished to reveal microstructural details and to facilitate microhardness evaluation. Samples were surface ground prior to polishing in order to ensure the removal of the decarburization layer which results from the heat treatment in air. All samples were etched with Vilella's Reagent to reveal microstructural details and inspected using both a conventional light microscope and the scanning electron microscope (SEM). Microhardness data was obtained with the aid of a Kentron Microhardness Tester fitted with a Knoop diamond indenter.

7.9.4.2 As-Welded Properties

The as-welded microstructure and properties of laser welds in HT9 were documented in a previous report[1]. The results of the study revealed that regions of high hardness existed in both the fusion zone and a fully transformed region of the HAZ adjacent to the fusion line. The low heat input and resultant high cooling rates experienced by the weld region promoted the formation of an untempered martensite with a hardness in excess of R_c55. A microstructural montage of the pertinent regions of the laser weld with the accompanying hardness levels of these regions is shown in Fig. 1. Note that the hardest region of the microstructure is located in the slightly grain coarsened region adjacent to the fusion line (F.L.). A complete hardness traverse of the weld region is shown in Fig. 2. The rapid decrease in hardness in the HAZ results from the steep temperature gradient which exists in this regioh during welding. Only portions of the microstructure which have been heated above thk lower critical temperature (~840°C) will exhibit an increase ih hardness relative to the base material.

The microstructures of the particular regions of the laser weld are shown at higher magnification in Fig. 3. The fusion zone con-

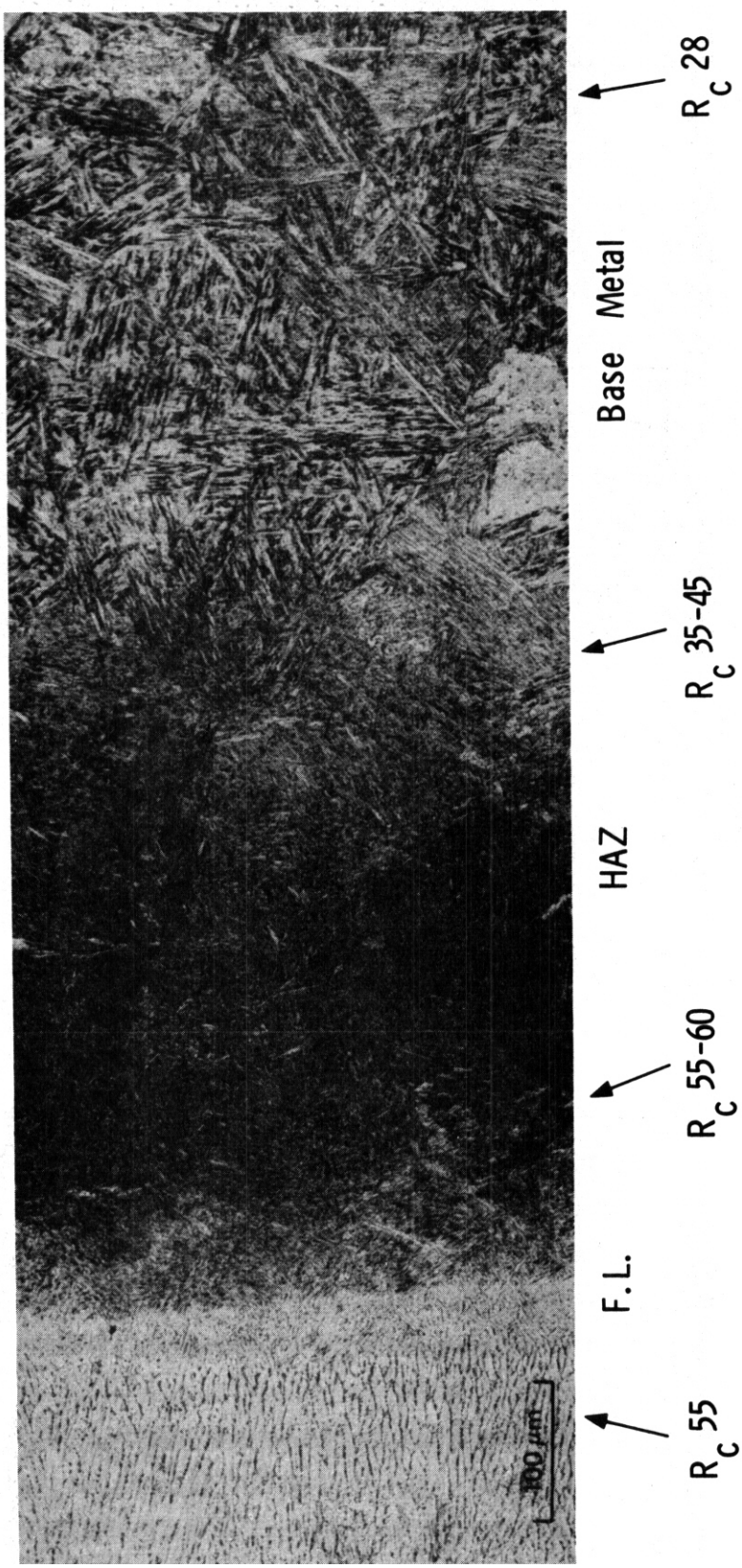

Figure 1. Microstructural Montage of the Weld Region of an HT9 Laser Weld.

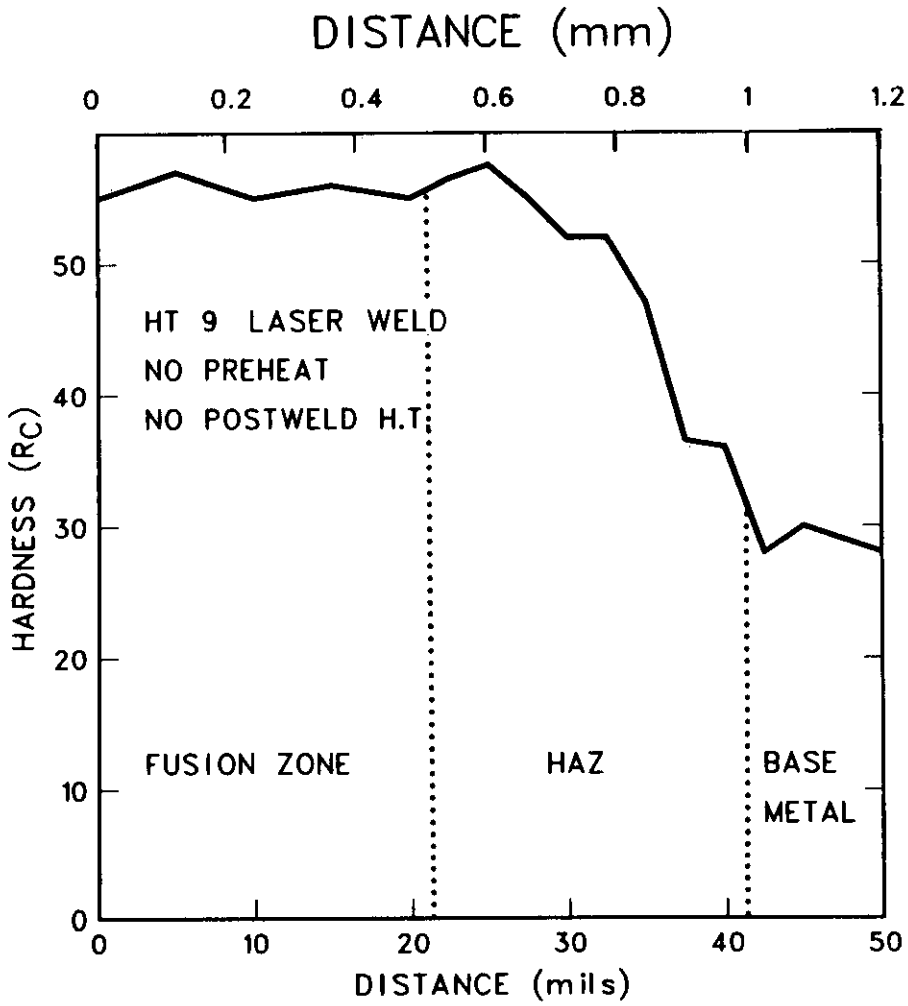

Figure 2. Microhardness Traverse Across the Weld Region in an HT9 Laser Weld.

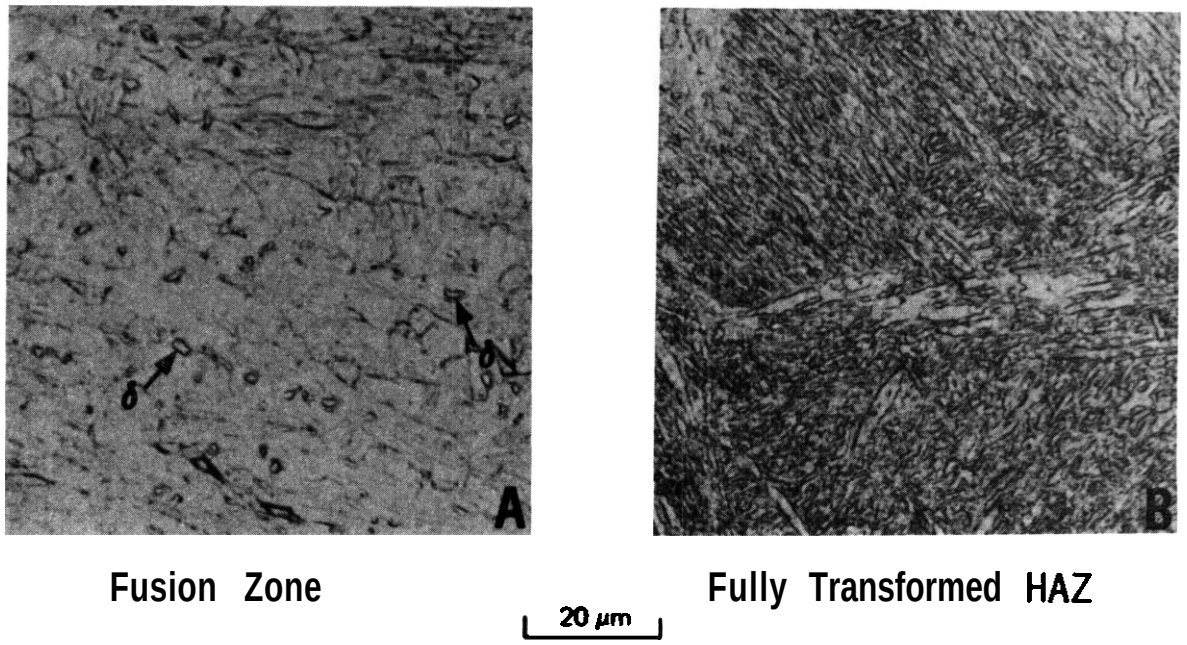

Figure 3. Microstructural Regions in an HT9 Laser Weld in the As-Welded Condition.

sists of untempered martensite and delta ferrite which is distributed along the boundaries of the original solidification substructure (arrows in Fig. 3). The presence of the ferrite slightly reduces the hardness of this region relative to the adjacent HAZ.

A narrow region in the HAZ approximately 0.3 mm (0.012 in.) wide immediately adjacent to the fusion line exhibited the highest hardness measured on the as-welded specimens. During the weld thermal cycle this region is rapidly heated to temperatures significantly above the lower critical temperature (A_{c_1}). The reversion of the tempered base metal martensite to austenite is accompanied by the nearly complete dissolution of the carbides. Upon cooling, the entire structure within this narrow band transforms to untempered martenite and exhibits the lath-like morphology shown in Fig. 3b. Since the hardness of the martensite is a function of the amount of carbon in solution in the austenite the nearly complete dissolution of the carbides during welding assures that the maximum hardness of the weld will occur in this region.

The perceptible drop in hardness which was observed at the fusion line in gas tungsten-arc (GTA) welds was not detected in the laser welds. The rapid heating and cooling cycles experienced in this region minimizes the length of time spent in the austenite plus ferrite phase field and precludes the transformation of austenite to ferrite which was found to be responsible for the hardness drop in the GTA welds.

In regions of the HAZ more remote from the fusion line the decrease in hardness relative to the fully transformed region adjacent to the fusion line is associated with the incomulete dissolution of the carbides. Although the reversion to austenite occurs rapidly on heating above the A_{c_1}, the decomposition of the carbides is more sluggish, particularly at temperatures only slightly above the lower critical temperature. As a result, the amount of carbon in solution during reaustenization is less than that present in regions closer to the fusion line and, thus, the potential hardness of the martensite will be lower. The as-welded microstructure in this region consists of a mixture of untempered martensite and carbides as shown in Fig. 3c. The base metal microstructure, shown in Fig. 3d, exhibits a relatively coarse lath martensite morphology interspersed with secondary carbides.

7.9.4.3 Effect of Tempering on Hardness

The macrostructures of the HT9 laser welds tempered for 1 hour at 400, 600, and 800°C are shown in Fig. 4. Porosity is evident in many of the cross sections and has been commonly observed in other laser welds[1]. The location of the microhardness surveys can also be seen in Fig. 4. All surveys were performed perpendicular to the fusion line in a region where the width of the HAZ would be approximately equal for each heat treatment.

The results of the hardness surveys are presented in Fig. 5. Tempering at 400°C had little effect in reducing the as-welded hardness particularly in the fully transformed region of the HAZ. After tempering at 600°C both the fusion zone and the HAZ exhibited a hardness of approximately R_c40. Finally, a 800°C heat treatment reduced the hardness of the weld region to nearly base metal levels. Tempering for 2 hours had little effect on further reducing the hardness relative to the 1 hour treatment.

7.9.4.4 Microstructural Changes During Tempering

Microstructural evaluation of the heat treated samples revealed that significant changes occur in both the fusion zone and fully transformed region of the HAZ during tempering. Changes in the partially transformed region of the HAZ were more subtle and not as easily detected metallographically.

The microstructural changes which occur during tempering of the fusion zone are illustrated in Fig. 6. Both the as-welded microstructure and the tempered structure at 400°C appear to be similar, suggesting that neither softening of the martensite nor precipitation of secondary carbides has occurred to any noticeable degree. In addition, the distribution and morphology of the non-equilibrium ferrite (arrows) exhibits little variation. At 600°C the initial stage of carbide precipitation is manifested by the slightly darker-etching appearance of the microstructure. The precipitation phenomenon is concomitant with the martensite tempering reaction, whereby carbon diffuses to interlath sites where it is available to form alloy carbides. The ferrite distribution is similar to that of both the as-welded and 400°C microstructure.

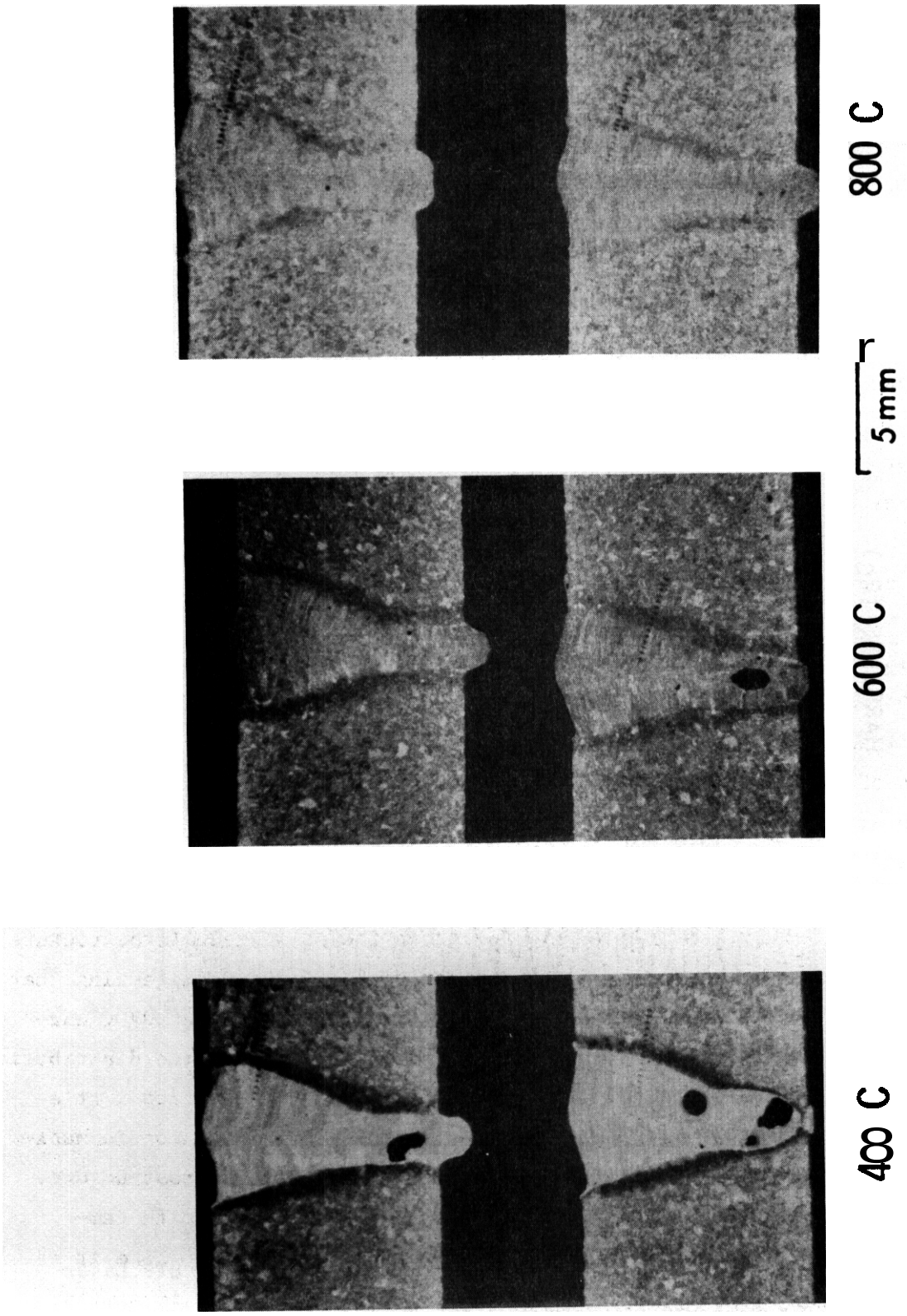

Figure 4 Macrostructure of HT9 Laser Welds Tempered for 1 (top) and 2 (bottom) Hours at 400, 600 and 800°C.

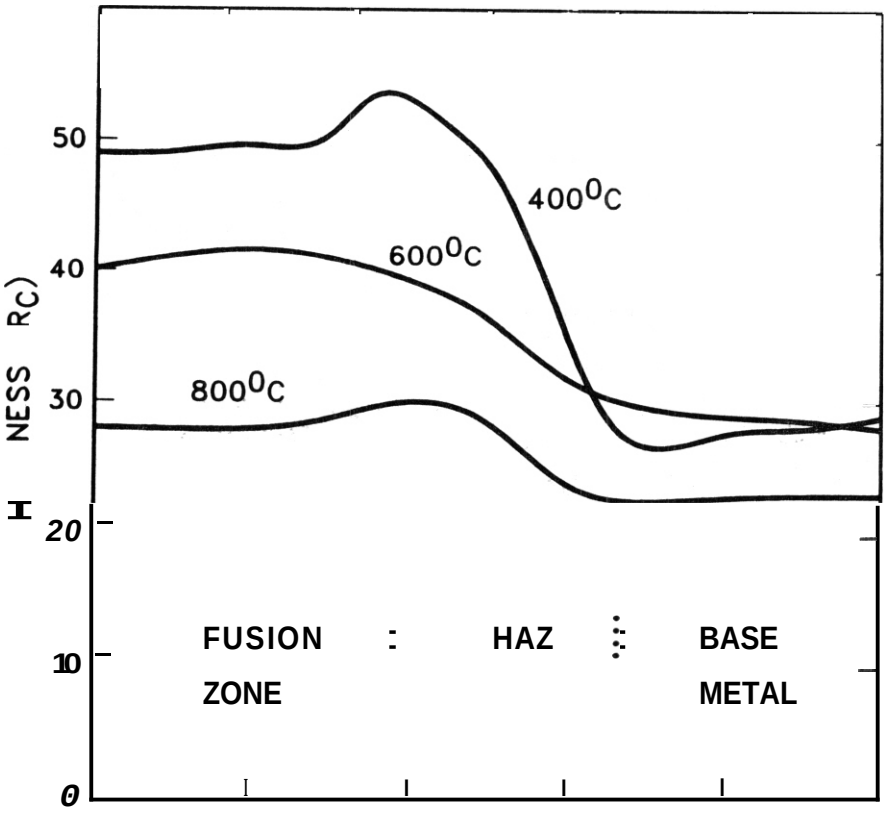

Figure 5. Microhardness Traverses Across the Weld Region in HT9 Laser Welds Tempered at 400, 600, and 800°C.

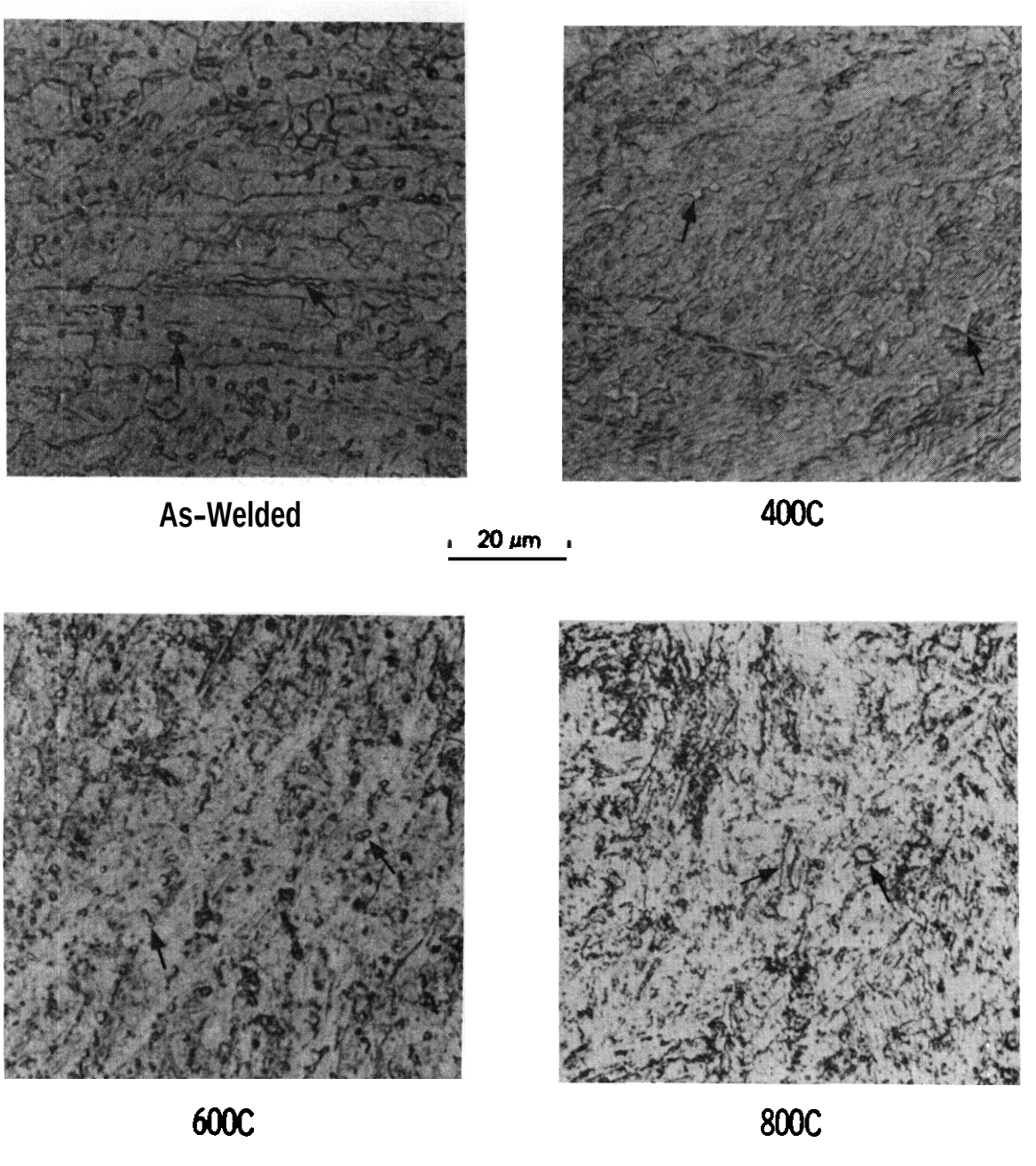

Figure 6. Tempering Response of the Fusion Zone in HT9 Laser Welds.

Tempering at 800°C accelerates both the precipitation kinetics and the martensite softening reaction, as evidence by the discrete carbide particles distributed along lath boundaries in Fig. 6. The reduction in the proportion of ferrite in the microstructure indicates that ferrite dissolution is significant at 800°C and that the rate of ferrite decomposition is quite rapid at this temperature. Despite the difference in appearance of this microstructure relative to the base metal microstructure shown previously in Fig. 3 the individual hardness values are nearly identical.

Significant microstructural transitions during tempering also occur in the fully transformed region of the HAZ as illustrated by the photomicrographs in Fig. 7. Tempering at 400°C has essentially no effect on the martensite lath morphology relative to the as-welded microstructure. The presence of secondary carbides is evident at both 600 and 800°C and again marks the onset of martensite softening.

The variation in microstructure within the weld region after tempering at 800°C is illustrated in Fig. 8. Although the hardness values are roughly comparable both the fusion zone and fully transformed region of the HAZ exhibit finer martensite lath morphologies than either the partially transformed region or the unaffected base metal. The prior austenite grain size is nearly equivalent throughout the weld region, indicating that grain growth resulting from the weld thermal cycle is negligible.

7.9.4.5 Comparison of Laser to GTA Welds

The characteristic high energy density, low energy input properties of the laser welding process results in relatively steep thermal gradients in the HAZ which effectively minimizes the extent of thermally modified microstructure surrounding the fusion zone. A microstructural investigation of GTA welds has shown that the HAZ in these higher heat input welds is more extensive but that the microstructure and properties are similar to distinct regions in the HAZ of the laser welds. As a result, regions of hard, untempered martensite are indigenous to the fusion zone and portions of the HAZ in both GTA and laser welds.

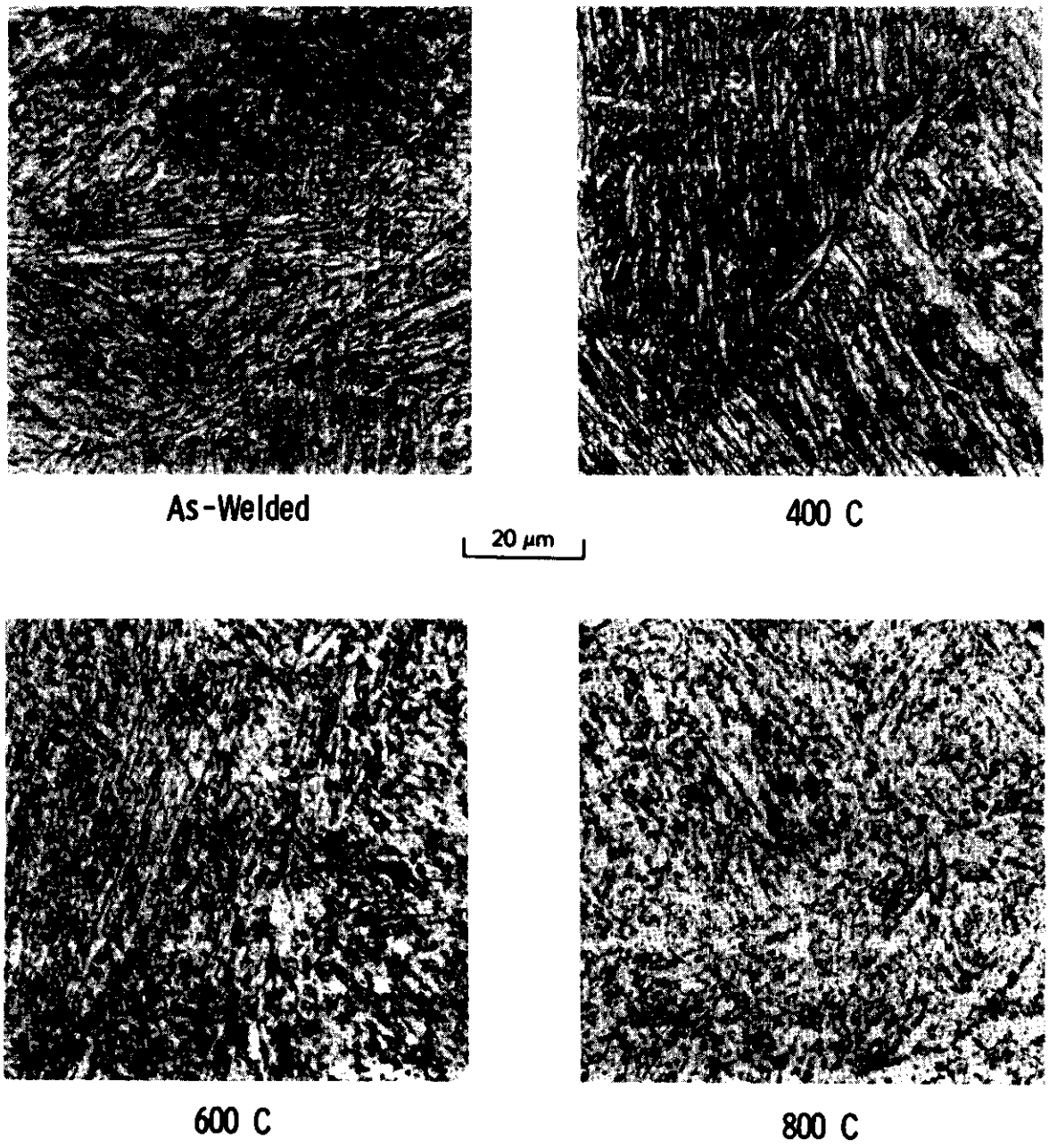

Figure 7. Tempering Response of the FUlly Transformed Region of the HAZ in HT9 Laser Welds.

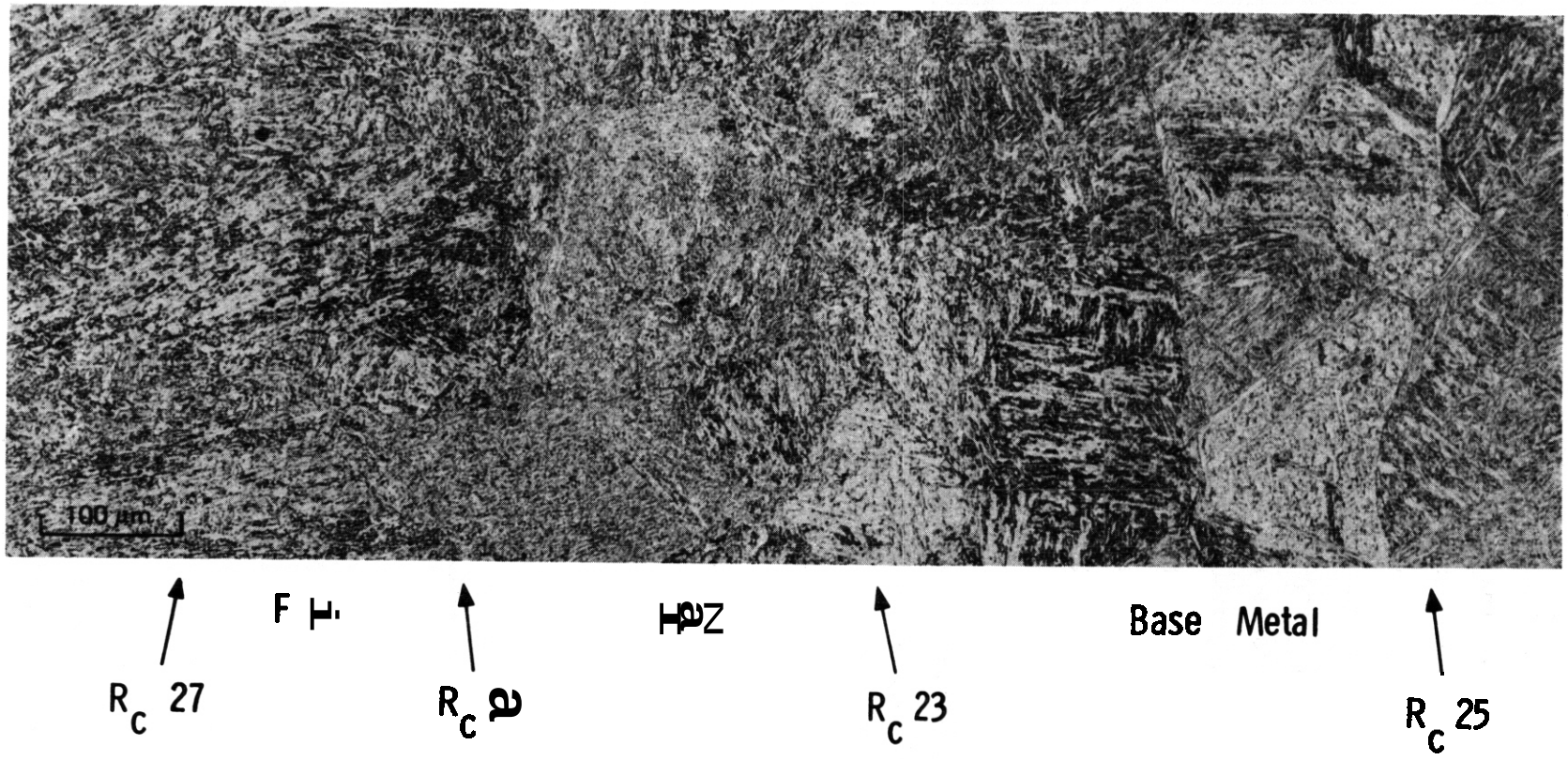

Figure 8 Microstructural Montage of an XT9 Laser Weld Tempered for 1 Hour at 800°C

Examination of the untempered lath martensite morphology has shown that the lath spacing is much smaller in both the fusion zone and HAZ of laser welds, but that this refined structure does not accelerate either the tempering response or the precipitation kinetics of the secondary carbides. Maximum hardness values in both the fusion zone and the fully transformed region of the HAZ after tempering at *400,* 600, and 800°C have been plotted in Fig. *9* on a tempering curve determined from an earlier study of GTA welds[2]. At *400* and 600°C the hardness in both regions exceeds that of similar regions in the GTA welds. It should be noted, however, that the as-welded hardness of the laser weld was somewhat greater than that of the GTA weld (for example, R_C60 versus R_C52 in the fully transformed region). At 800°C the tempered hardness of both regions approaches the curve and indicates that the tempering response at higher tempering temperatures is relatively insensitive to the morphology of the as-welded microstructure.

The results of this investigation have shown that from a metallurgical standpoint the utilization of laser welding offers no advantage over the more conventional GTA welding. The formation of a brittle, untempered martensite in both the fusion zone and a narrow region in the HAZ can be effectively minimized but not completely eliminated in the as-welded microstructure. As a result, both welding procedures will require a postweld heat treatment to restore adequate mechanical properties to the weld region. A future report will provide a more comprehensive evaluation of welding procedures which will ensure the integrity of the weld region during service conditions.

7.9.5 Conclusions

1. Regions of untempered martensite exhibiting a hardness of R_C55-60 were found in the as-welded laser welds both in the fusion zone and in a narrow band in the HAZ adjacent to the fusion line.

2. Tempering at 400°C had little effect on either the as-welded hardness or the microstructure of the weld region.

3. Tempering at 600 and 800°C promoted both a martensite softening reaction and a simultaneous precipitation of alloy carbides.

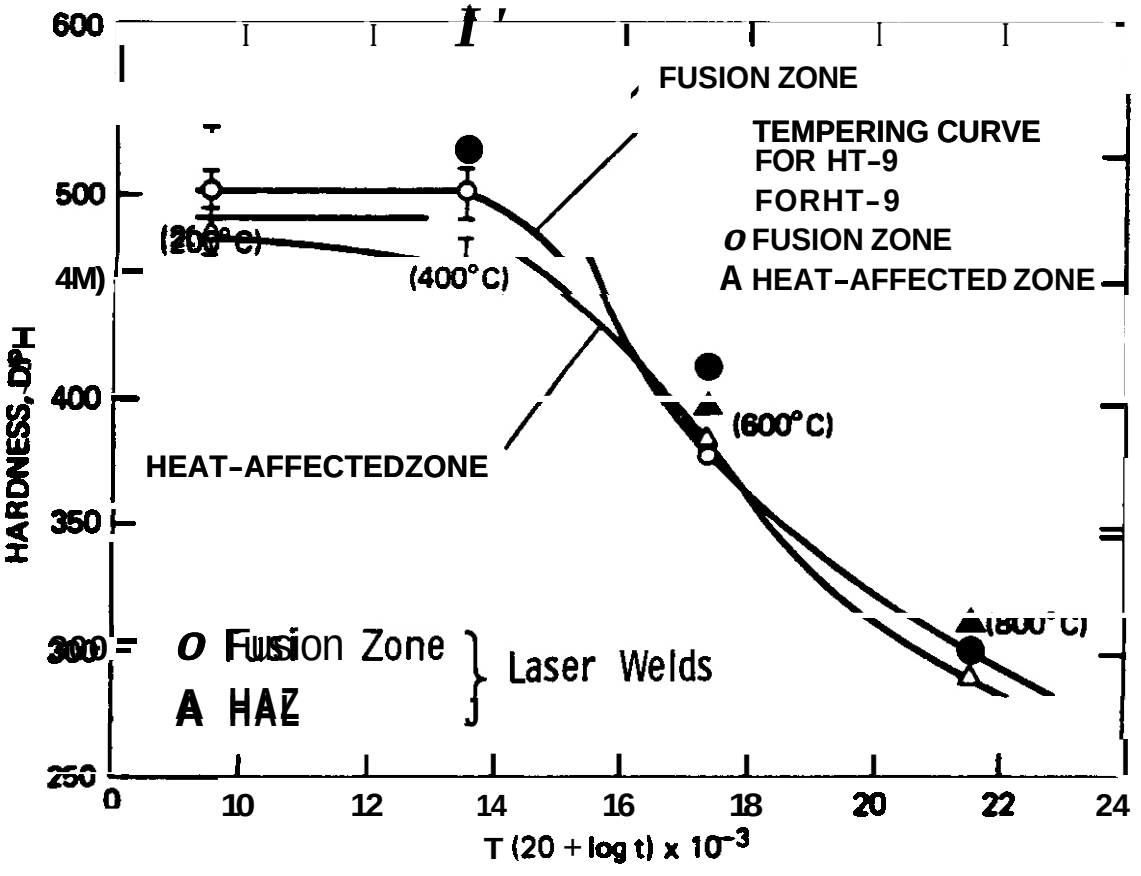

Figure 9. Microhardness Values of the HAZ and Fusion Zone of Tempered HT9 Laser Welds Superimposed on a Tempering Curve for GTA Welds in HT9.

4. Increasing the tempering time from one to two hours at a given temperature had little effect on either the microstructure or properties of the individual weld regions.

5. Dissolution of the metastable ferrite in the fusion zone is relatively sluggish at 400 and 600°C but proceeds more rapidly at 800°C.

6. The microstructural variation between GTA and laser welds has little effect on the relative tempering behavior of distinct regions in the individual weldments.

7.9.6 References

1. Lippold, J. C., "Analysis of Laser Welds in HT9", ADIP Quarterly Progress Report for period ending September 30, 1980, pp. 126-139.

2. Lippold, J. C., "Tempering and Transformation Behavior of HT9 Weldments", ADIP Quarterly Progress Report for period ending June 30, 1980, pp. 216-225.

7.10 AN AUGEK SPECTRASCOPLC ANALYSIS OF AN HT-9 SUPERHEATER TUBE IN-SERVICE AT 600°C FOR 80,000 HOURS — T. A. Lechtenberg (General Atomic Company)

To be reported in the next quarterly report.

8. STATUS OF IRRADIATION EXPERIMENTS AND MATERIALS INVENTORY

8.1 IRRADIATION EXPERIMENT STATUS AND SCHEDULE

There are a large number of planned, in-progress, or completed reactor irradiation experiments that support the ADIP program. Table 8.1.1 presents a summary of the parameters that describe experiments that have been completed. Experiments that have been removed from the reactor only recently, are currently undergoing irradiation, or are planned for future irradiation are included in the schedule bar charts of Table 8.1.2.

Experiments are now under way in the Oak Ridge Research Reactor (ORR) and the High Flux Isotope Reactor (HFIR), which are mixed spectrum reactors and in the Experimental Breeder Reactor (EBR-II), which is a fast reactor.

During the reporting period experiments HFIR-MFE-T1 and HFIR-MFE-T2 were installed in the target region of HFIR. Both experiments contain tensile and fatigue specimens of ferritic steels. Thermocouple repairs were made on experiment ORR-MFE-4A, and this experiment has been reinserted in the ORR and is now operating successfully. The in-reactor crack growth experiment, ORR-MFE-5 was removed because of an unexpected drop in load. This experiment is expected to yield useful results upon disassembly and examination. The first disk irradiation experiment, HFIR-CTR-32, has completed its scheduled irradiation and has been removed from the reactor. The experiment has been disassembled and specimens are being sorted and identified. Specimen shipment to participating laboratories will begin next quarter.

Table 8.11. Descriptive Parameters for Completed Reactor Irradiation Experiments

Experiment	Major Objective	Alloy	Reactor			Helium (at. ppm)	Duration (month)	Date Completed
ORR-MFE-1	Scope the effects of composition and microstructure on tensile, fatigue, and irradiation creep	Paths A, B, C	ORR	250–600	2		4	6/78
ORR-MFE-2	Scope the effects of composition and microstructure on tensile, fatigue, and irradiation creep	Paths A, □, C	ORR	300–600	6		15	4/80
Subassembly X-264	Effect of preinjected helium on microstructure, tensile properties, and irradiation creep	316, PE-16, V–20% Ti, V–15% Cr–5% Ti, Nb–1% Zr	EBR-II	500–825	8		4	1/77
AA-X Subassembly X-287	Effect of preinjected helium on microstructure, tensile properties, and irradiation creep	316, PE-16, V–20% Ti, V–15% Cr–5% Ti, Nb–1% Zr	EBR-II	400–700	20		23	12/78
Subassembly X-217D	Stress relaxation	Titanium alloys	EBR-II	450	2		1	1/78
Pins B285, B286, and B284	Swelling, fatigue, crack growth, and tensile properties	Titanium alloys	EBR-II	370–550	25		14	9/79
HFIR-CTR-3	Swelling and tensile properties	PE-16, Inconel 600	HFIR	300–700	4.3–9		3	2/75
HFIR-CTR-4	Swelling and tensile properties	PE-16	HFIR	300–700	2.2–4.5		2	3/77
HFIR-CTR-5	Swelling and tensile properties	PE-16, Inconel 600	HFIR	300–700	4.3–9		3	4/75

Experiment	Major Objective	Alloy	Reactor	Temperature (°C)	Displacement Damage (dpa)	Helium (at. ppm)	Duration (month)	Date Completed
HFIR-CTR-6	Swelling and tensile properties	PE-16, Inconel 600	HFIR	300–700	4.3–9	350–1800	3	4/75
HFIR-CTR-7	Swelling and tensile properties	PE-16	HFIR	300–700	9–18	1250–3000	7	8/77
HFIR-CTR-8	Swelling and tensile properties	PE-16	HFIR	300–700	9–18	1250–3000	7	8/77
HFIR-CTR-9	Swelling and tensile properties	316, 316 + Ti	HFIR	280–680	10–16	400–1000	6	5/77
HFIR-CTR-10	Swelling and tensile properties	316, 316 + Ti	HFIR	280–680	10–16	400–1000	6	5/77
HFIR-CTR-11	Swelling and tensile properties	316, 316 + Ti	HFIR	280–680	10–16	400–1000	6	5/77
HFIR-CTR-12	Swelling and tensile properties	316, 316 + Ti	HFIR	280–680	7–10	200–500	4	2/77
HFIR-CTR-13	Swelling and tensile properties	316, 316 + Ti	HFIR	280–680	7–10	200–500	4	2/77
HFIR-CTR-14	Fatigue	316	HFIR	430	9–15	400–1000	7	12/7
HFIR-CTR-15	Fatigue	316	HFIR	550	6–9	200–400	4	10/7
HFIR-CTR-16	Weld characterization, swelling and tensile properties	316 Welds in 316 PE-16 Inconel 600	HFIR	55	6–9	150–2700	4	8/77
HFIR-CTR-17	Weld characterization	Welds in 316	HFIR	280–620	7–13	180–460	5.5	10/7
HFIR-CTR-18	Swelling and tensile properties	316 PE-16	HFIR	280–700	17–27	1600–5600	12	6/78
HFIR-CTR-19	Weld characterization	Welds in 316	HFIR	280–620	7–10	200–500	4	12/7
HFIR-CTR-20	Fatigue	316	HFIR	430	6–9	200–400	4	1/78
HFIR-CTR-21	Fatigue	316	HFIR	550	9–15	400–1000	7	7/78
HFIR-CTR-22	Fatigue	316	HFIR	430	6–9	200–400	4	3/78
HFIR-CTR-23	Fatigue	PE-16	HFIR	430	6–9	370–1000	3.5	2/79
HFIR-CTR-24	Temperature calibration, and tensile properties	316	HFIR	300–620	2.2	30	1	12/7

Table 8.1.2. Objectives and Schedule for Current and Planned ADIP Program Reactor Irradiation Experiments

Experiment Designation	Major Objective
A. Oak Ridge Research Reactor	
ORR-MFE-3	[1] Effect of irradiation on postirradiation fatigue crack growth in representative path A, B, and C alloys.
ORR-MFE-4	[2] Effect of irradiation on tensile, fatigue, and irradiation creep of path A PCA (*Prime Candidate Alloy*) and path B base research alloys. Spectral tailoring to maintain correct He/dpa ratio. Irradiation on continuing basis. 330–600°C
ORR-MFE-5	In-reactor fatigue crack growth experiment. 325–460°C
ORR-MFE-6	In-reactor fatigue crack growth experiment 325–460°C

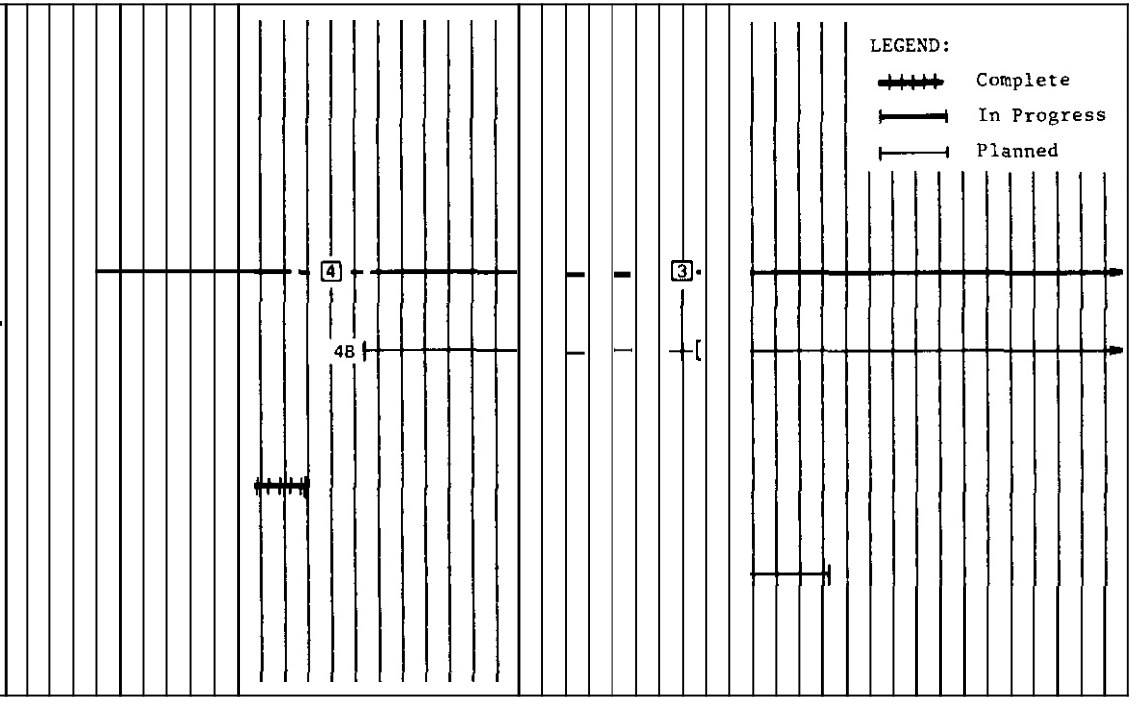

[1] Delayed for undetermined period.

[2] MFE-4A operates at 330 and 400°C. MFE-4B will operate at 500 and 600°C.

[3] Approximate schedule for specimen charge out.

[4] Removed from reactor for thermocouple repairs.

Table 8.1.2. (Continued)

Experiment Designation	Major Objective	1980 J F M A M J J A S O N D	1981 J F M A M J J A S O N D	1982 J F M A M J J A S O N D	1983 J F M A M J J A S O N D
B. Experimental Breeder Reactor (EBR-II)					
Experiment plan depends on alloy availability. EBR-II space not yet identified.	Effect of irradiation on swelling, tensile, fatigue, and crack growth properties of V and Nb scoping alloys. 370, 450, 550, and 650°C. Position in reactor not finalized, therefore no fluence estimate. [1]				
AD-2 (6 pins in separate subassemblies of row 4)	To supplement present EBR-II data on ferritic alloys with data on crack growth, fatigue, and fracture toughness. Temperature 390, 450, 500, and 550°C. 19 and 38 dpa.		[2]		

[1] Delayed for undetermined period.

[2] Interim examination. Experiment out of reactor.

Table 8.1.2. (Continued)

Experiment Designation	Major Objective
C. High Flux Isotope Reactor (HFIR)	
HFIR-CTR-25	Temperature calibration, tensile properties of MFE ref. 316, 2.25 dpa, 30 at. ppm He [1]
HFIR-CTR-26	Swelling and tensile properties of MFE ref. 316, 32 dpa, 1900 at. ppm He
HFIR-CTR-27	Swelling and tensile properties of MFE ref. 316, 56 dpa, 3450 at. ppm He
HFIR-CTR-28	Swelling and tensile properties of MFE ref. 316, 32 dpa, 1900 at. ppm He
HFIR-CTR-29	Swelling and tensile properties of MFE ref. 316, 56 dpa, 3450 at. ppm He
HFIR-CTR-30	Swelling and tensile properties, Paths A, B, and D microstructural variations, 40 dpa, 2500 at. ppm He (Path A)
HFIR-CTR-31	Swelling and tensile properties, Paths A, B and D microstructural variations, 20 dpa, 1200 ppm He (Path A)
HFIR CTR-32	Swelling and tensile properties, Paths A, B and D microstructural variations, 10 dpa, 500 ppm He (Path A)
HFIR-CTR-33	Swelling and tensile properties, Path E alloys, 10 dpa, 50°C

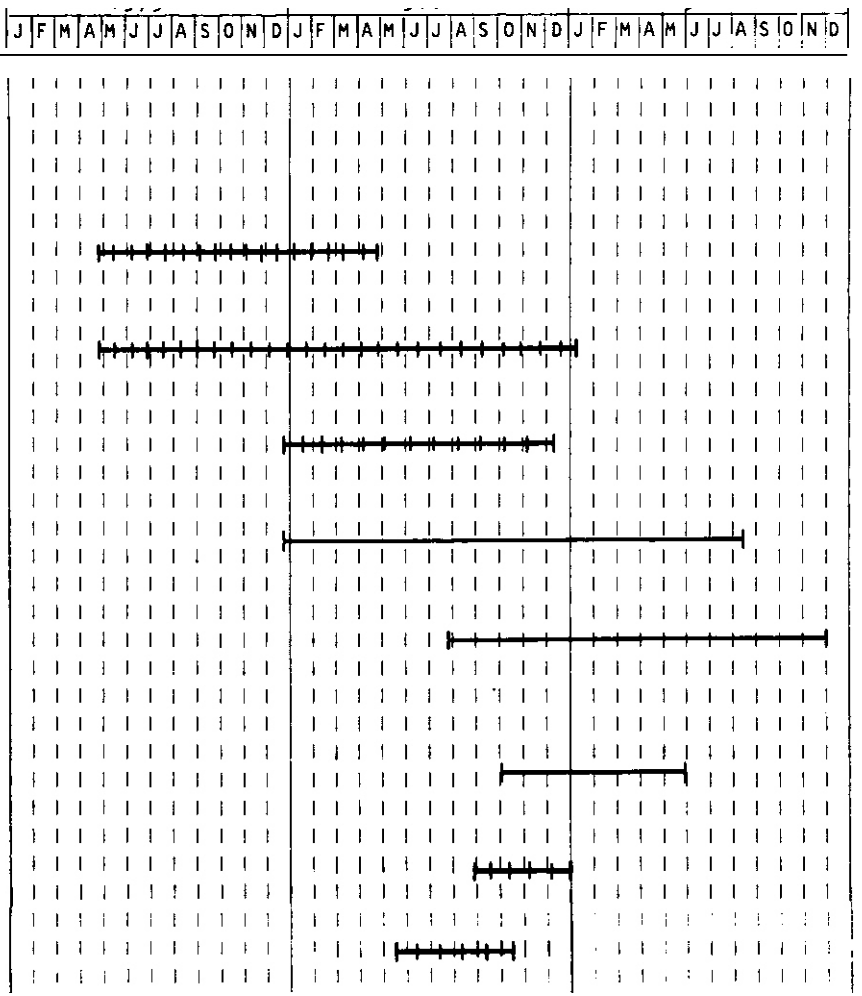

[1] Delayed for undetermined period.

Table 8 1 Z (Continued)

Experiment Designation	Major Objective
HFIR-MFE-T1	Swelling, tensile properties, and fatigue of path E alloys. 70 dpa, up to 650 ppm He depending upon alloy, 55°C.
HFIR-MFE-T2	Swelling, tensile properties, and fatigue of path E alloys. 10 dpa, up to 75 ppm He depending upon alloy, 55°C.
HFIR-MFE-T3	Impact properties of path E alloys. 10 dpa, up to 75 ppm He depending upon alloy, 55°C.
HFIR-MFE-RB1	Swelling, microstructure, crack growth, fracture toughness, impact, tensile, and fatigue properties of path E alloys, 55°C.
HFIR-MFE-RB2	Similar to HFIR-MFE-RB1.

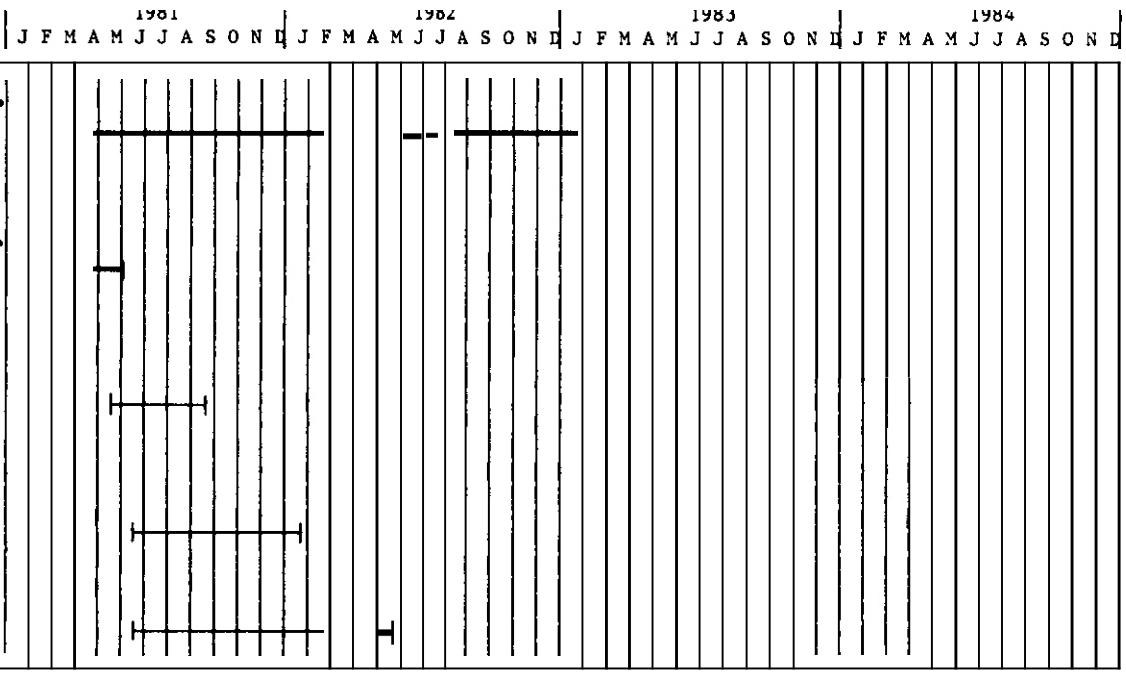

8.2 ETM RESEARCH MATERIALS INVENTORY — F. W. Wiffen, T. K. Roche (Oak Ridge National Laboratory) and J. W. Davis (McDonnell Douglas)

8.2.1 ADIP Task

ADIP Task I.D.1, Materials Stockpile for MFE Programs.

8.2.2 Objective

The Office of Fusion Energy has assigned program responsibility to ORNL for the establishment and operation of a central inventory of research materials to be used in the Fusion Reactor Materials research and development programs. The objective is to provide a common supply of materials for the Fusion Reactor Materials Program. This will minimize unintended materials variables and provide for economy in procurement and for centralized recordkeeping. Initially this inventory is to focus on materials related to first-wall and structural applications and related research, but various special purpose materials may be added in the future.

The use of materials from this inventory for research that is coordinated with or otherwise related technically to the Fusion Reactor Materials Program of DOE, but which is not an integral or directly funded part of it, is encouraged.

8.2.3 Materials Requests and Release

Materials requests shall be directed to ETM Research Materials Inventory at ORNL (Attention: F. W. Wiffen). Materials will be released directly if:

(a) The material is to be used for programs funded by the Office of Fusion Energy, with goals consistent with the approved Materials Program Plans of the Materials and Radiation Effects Branch.

(b) The requested amount of material is available, without compromising other intended uses.

Materials requests that do not satisfy both (a) and (b) will be discussed with the staff of the Materials and Radiation Effects Branch, Office of Fusion Energy, for agreement on action.

8.2.4 Records

Chemistry and materials preparation records are maintained for all inventory material. All materials supplied to program users will be accompanied by summary characterization information.

8.2.5 Summary of Current Inventory and Material Movement During Period Jan. 1 to Mar. 31, 1981

A condensed, qualitative description of the content of materials in the ETM Research Materials Inventory is given in Table *8.2.1.* This table indicates the nominal diameter of rod or thickness of sheet for product forms of each alloy and also indicates by weight the amount of each alloy in larger sizes available for fabrication to produce other product forms as needed by the program. Table *8.2.2* lists materials distributed from the inventory during this reporting period. No material was received.

Alloy compositions and more detail on the alloys and their procurement and/or fabrication are given in earlier ADIP quarterly progress reports.

Table 8.2.1 Summary Status of Material Availability in the ETM Research Materials Inventory

Alloy	Product Form: Ingot or Bar,[a] Weight (kg)	Rod,[b] Diameter (mm)	Sheet,[c] Thickness (mm)	Thin-Wall Tubing, Wall Thickness (mm)
		Path A Alloys		
Type 316 SS	900	16 and 7.2	13 and 1.9	0.25
Path A PCA[d]	490	12	13	0.25
USSR — Cr-Mn Steel[e]	0	10.5	2.6	0
		Path B Alloys		
PE-16	140	16 and 7.1	13 and 1.6	0.25
B-I	180	0	0	0
B-2	180	0	0	0
8-3	180	0	0	0
B-4	180	0	0	0
8-6	180	0	0	0
		Path C Alloys		
Ti-64	0	0	2.5 and 0.76	0
Ti-6242s	0	63	6.3, 3.2, and 0.76	0
Ti-5621s	0	0	2.5 and 0.76	0
Ti-38644	0	0	0.76 and 0.25	0
Nb-1% Zr	0	6.3	2.5, 1.5, and 0.76	0
Nb-5% Mo-1% Zr	0	6.3	2.5, 1.5, and 0.76	0
V-20% Ti	0	6.3	2.5, 1.5, and 0.76	0
V-15% Cr-5% Ti	0	6.3	2.5, 1.5. and 0.76	0
Vanstar-7	0	6.3	2.5, 1.5, end 0.76	0
		Path D Alloys — No Material in Inventory		
		Path E Alloys		
HT9	0	0	4.5 and 18	0
HT9 + 1% Ni	0	0	4.5 and 18	0
HT9 + 2% Ni	0	0	4.5 and 18	0
HT9 + 2% Ni + Cr adjusted	0	0	4.5 and 18	0
T-9 modified	0	0	4.5 and 18	0
T-9 modified + 2% Ni	0	0	4.5 and 18	0
T-9 modified + 2% Ni + Cr adjusted	0	0	4.5 and 18	0
2 1/4 Cr-1 Mo	0	0	f	0

[a] Greater than 25 mm, minimum dimension.

[b] Less than 25 mm in diameter. Some Path A and Path B alloys are available in two different diameters.

[c] Less than 15 mm thick. Some Path A, Path B, and Path C alloys are available in two or three different thicknesses.

[d] Prime Candidate Alloy.

[e] Rod and sheet of a USSR stainless steel supplied under the U.S.-USSR Fusion Reactor Materials Exchange Program.

[f] Material is thick-wall pipe, rerolled as necessary to produce sheet or rad.

Table 8.2.2. EMT Research Materials Inventory, Fusion Reactor Program, Disbursements 1-1-81 to 3-31-81

Alloy	Heat	Product Form	Dimensions[a]		Quantity				Sent to
			(mm)	(in.)	(m)	(in.)	(m^2)	($in.^2$)	
Path A Alloys — Austenitic Stainless Steels									
Type 316 SS[b]	X-15893	Rod	7.4 diam	0.290 diam	5.08	200			Metals Processing Group, ORNL
Path A-PCA[c]	K-280	Tubing	4.57 OD × 0.254 wall	0.180 OD × 0.010 wall	1.57	62			HEDL[d]
Path A-PCA	K-280	Sheet	0.25 thick	0.010 thick			0.06	99	University of California, Santa Barbara
Path E Alloys — Ferritic Steels									
HT-9	ESR-XAA-3587-4	Sheet	0.76 thick	0.030 thick			0.1	160	Radiation Effects Group, ORNL
HT-9 + 1% Ni	ESR-XAA-3588-9	Sheet	0.76 thick	0.030 thick			0.1	160	Radiation Effects Group, ORNL
HT-9 + 2% Ni	ESR-XAA-3589-9	Sheet	0.76 thick	0.030 thick			0.1	160	Radiation Effects Group, ORNL
T-9 modified	ESR-XA-3590-9	Sheet	0.76 thick	0.030 thick			0.1	160	Radiation Effects Group, ORNL
T-9 modified + 2% Ni	ESR-XA-3591-9	Sheet	0.76 thick	0.030 thick			0.1	160	Radiation Effects Group, ORNL

[a]Characteristic dimension — thickness for plate and sheet, diameter for rod and tubing.

[b]Program reference material.

[c]Prime Candidate Alloy.

[d]Hanford Engineering Development Laboratory.

9. MATERIALS COMPATIBILITY AND HYDROGEN PERMEATION STUDIES

9.1 COMPATIBILITY STUDIES OF FERRITIC STEELS EXPOSED TO STATIC LITHIUM AND TYPE 316 STAINLESS STEEL EXPOSED TO STATIC Pb–17 at. % Li –

P. F. Tortorelli and J. H. DeVan (Oak Ridge National Laboratory)

9.1.1 ADIP Task

ADIP Task I.A.3, Perform Chemical and Metallurgical Compatibility Analyses.

9.1.2 Objective

The purpose of this program is to determine the chemical compatibility of fusion reactor candidate materials with possible coolants and tritium breeding materials. Specimens are exposed to static lithium and lithium–lead melts to identify the kinetics and mechanisms that govern corrosion. Specific program objectives include (1) to determine the effects of N, C, H, and O on apparent solubilities of metals in lithium and lithium–lead; (2) to determine the carbon and nitrogen partitioning coefficients between alloys and lithium; (3) to determine the effects of soluble (Ca, Al) and solid (Y, Zr, Ti) active metal additions on corrosion by lithium; and (4) to determine the tendencies for mass transfer between dissimilar metals.

9.1.3 Summary

The thermodynamic tendency for carbon transfer between ferritic steels and lithium is described. The treatment predicts a much greater driving force for decarburization of 2 1/4 Cr-1 Mo steel than for Sandvik HT9 exposed to lithium, which is consistent with our experimental findings. However, the amount of carbon loss from the 2 1/4 Cr-1 Mo steel exposed to lithium would probably not be severe in the temperature range of 2 1/4 Cr-1 Mo steel application. Furthermore, decarburization by lithium can be minimized by use of a stabilized 2 1/4 Cr-1 Mo steel. Preliminary results from exposures of type 316 stainless steel to Pb–17 at. % Li at 300, 400, and 500°C indicated a significant corrosion rate at 500°C but no detrimental effects on the tensile properties of the steel.

9.1.4 Progress and Status

In preceding reports,[1,2] we have reported the effects of lithium exposures to 2 1/4 Cr-1 Mo steel and Sandvik HT9. Significant decarburization of the 2 1/4 Cr-1 Mo steel by lithium occurred at higher temperatures (500–600°C), whereas there was no evidence of decarburization of HT9 by lithium at 500°C. We have recently evaluated the thermodynamic tendency for the transfer of carbon from the steel to the lithium by calculating the equilibrium ratio (distribution coefficient) of the carbon content in lithium to that in the steel. In general, the carbon distribution coefficient is dependent on the relative magnitudes of the carbon activity coefficients of the lithium and the steel. More specifically, we can write expressions for the following reactions:

$$Li + C = 1/2\ Li_2C_2 \ , \tag{1}$$

$$23/6\ Cr + C = 1/6\ Cr_{23}C_6 \ , \tag{2}$$

where $Cr_{23}C_6$ is one of the principal long-term precipitates in the normalized and tempered 2 1/4 Cr-1 Mo steel.

The standard free energy of formation for reaction (1) allows us to calculate the activity of carbon in lithium at the saturation limit (carbon standard state = graphite):

$$\Delta F_{1/2Li_2C_2} = -RT \ln \frac{\left(a_{Li_2C_2}\right)^{1/2}}{a_{Li} a^{\circ}_{C(Li)}} = RT \ln a^{\circ}_{C(Li)} \ , \tag{3}$$

where $a_{Li_2C_2}$ and a_{Li} are the activities of the Li_2C_2 and lithium in the lithium, respectively, and are equal to 1; and $a^{\circ}_{C(Li)}$ is the activity of the carbon in the lithium at the solubility limit.

Similarly, for reaction (2),

$$\Delta F_{1/6Cr_{23}C_6} = -RT \ln \frac{\left(a_{Cr_{23}C_6}\right)^{1/6}}{\left[a_{Cr(s)}\right]^{23/6} \cdot a^{\circ}_{C(s)}} \tag{4}$$

$$= RT\left[(23/6) \ln a_{Cr(s)} + \ln a^{\circ}_{C(s)}\right] ,$$

where

$a_{Cr_{23}C_6}$ = 1,

$a^{\circ}_{C(s)}$ = activity of carbon in the steel at the solubility limit,

$a_{Cr(s)}$ = activity of chromium in the 2 1/4 Cr-1 Mo steel.

$$a_{Cr(s)} \approx 0.02 . \tag{5}$$

The value for a_{Cr} was obtained by equating the activity with the atom fraction of the chromium in the 2 1/4 Cr-1 Mo ferrite solid solution.[3]

Subtracting Eq. (3) and (4),

$$\frac{a^{\circ}_{C(s)}}{a^{\circ}_{C(Li)}} = \left(a_{Cr}\right)^{-23/6} \exp\left(\frac{\Delta F^{\circ}_{1/6Cr_{23}C_6} - \Delta F^{\circ}_{1/2Li_2C_2}}{RT}\right) . \tag{6}$$

Assuming that Henry's law is obeyed to the saturation limit of carbon in the steel and in the lithium, the carbon activities can be expressed as

$$a^{\circ}_{C(s)} = K_1 N^{\circ}_{C(s)} , \tag{7}$$

$$a^{\circ}_{C(Li)} = K_2 N^{\circ}_{C(Li)} , \tag{8}$$

where N°_{C} = saturation atom fraction of carbon in the respective metals. Substituting **Eqs.** (7) and (8) into Eq. (6),

$$\frac{K_1}{K_2} = \frac{N^{\circ}_{C(Li)}}{N^{\circ}_{C(s)}} \left(a_{Cr}\right)^{-23/6} \exp\left(\frac{\Delta F^{\circ}_{1/6Cr_{23}C_6} - \Delta F^{\circ}_{1/2Li_2C_2}}{RT}\right) . \tag{9}$$

At equilibrium,

$$a_{C(s)} = a_{C(Li)} \tag{10}$$

or,

$$K_1 N_{C(s)} = K_2 N_{C(Li)} , \tag{11}$$

$$\frac{K_1}{K_2} = \frac{N_{C(Li)}}{N_{C(s)}} . \tag{12}$$

Therefore, combining Eqs. (9) and (12) and converting to weight fractions:

$$\frac{C_{C(s)}}{C_{C(Li)}} = \left(a_{Cr}\right)^{23/6} \frac{C^{\circ}_{C(s)}}{C^{\circ}_{C(Li)}} \exp\left(\frac{\Delta F^{\circ}_{1/2Li_2C_2} - \Delta F^{\circ}_{1/6Cr_{23}C_6}}{RT}\right) , \tag{13}$$

where C_C = solubility of carbon in parts per million by weight in the respective metals. At 500°C,

$$\Delta F^{\circ}_{1/2Li_2C_2} = -9673 \text{ J/mol } (-2312 \text{ cal/mol}) ,$$

$$\Delta F^{\circ}_{1/6Cr_{23}C_6} = -73{,}291 \text{ J/mol } (-17{,}517 \text{ cal/mol}) ,$$

$$C^{\circ}_{C(Li)} \approx 440 \text{ ppm} ,$$

and

$$C^{\circ}_{C(s)} \approx 47 \text{ ppm} .$$

Substituting these values and Eq. (5) into Eq. (13),

$$C_{C(s)}/C_{C(Li)} = 6.6 \times 10^{-4} . \quad (14)$$

Equation (14) will be inexact to the extent that changing concentrations of nitrogen and chromium in the lithium affect the Henry's law constant for carbon in lithium. However, Eq. (14) predicts that carbon transport should occur from the steel to the lithium, given the normal carbon concentrations in the metals at the start of test, and this is in agreement with our experimental observations.

The weight change and tensile data for HT9 exposed to static lithium indicated that this alloy does not decarburize in "as-purified" lithium.[2] This is consistent with the above thermodynamic treatment because, assuming the same initial carbide concentration and carbon saturation limit as for 2 1/4 Cr-1 Mo steel,[3] the estimated a_{Cr} for HT9 (~0.11) yields, by Eq. (13), a distribution coefficient of 0.4, which is 3 orders of magnitude greater than that for the 2 1/4 Cr-1 Mo steel-lithium system [Eq. (14)]. Thus, the extent of carbon transfer required to attain equilibrium between HT9 and lithium with nominal carbon impurities is much less than that required for 2 1/4 Cr-1 Mo steel. This dependence of carbon transfer on the chromium content of ferritic steels has also been observed in sodium systems.[4,5]

Although the above treatment predicts a greater tendency for decarburization of 2 1/4 Cr-1 Mo steel by lithium relative to HT9, it should be noted that, at the service temperatures proposed for 2 1/4 Cr-1 Mo steel (400–450°C), the decarburization rate would be low, as was seen from our 400°C data.[1] Furthermore, carbon loss from the 2 1/4 Cr-1 Mo steel can be reduced by adjusting the processing history of the steel to attain the maximum chemical stability of carbides in the matrix.[6] Also, a carbon-stabilized 2 1/4 Cr-1 Mo steel (with Nb, V, or Ti as alloying elements) would be more resistant to decarburization by lithium.

Lead-lithium molten alloys provide one possible alternative to molten lithium for tritium-breeding in fusion reactors.[7] We have therefore initiated a study of the compatibility of candidate structural alloys with

molten lead–lithium by exposing tensile specimens of type 316 stainless steel to the low melting point (235°C) eutectic composition of Pb–17 at. % Li. The experimental conditions were similar to those used for pure lithium static tests. Type 316 stainless steel specimens were sealed with appropriate amounts of lead and lithium under argon in type 316 stainless steel capsules. The specimens (two in each capsule) were anchored so as to prevent them from floating to the Pb-Li/Ar interface. Specimens were exposed at 300, 400, and 500°C, respectively. At present, we have completed 1000– and 3000–h tests at 300 and 400°C and 1000–h exposures at 500°C. Results from these experiments are given in Table 9.1.1. Weight loss rates were low at 300 and 400°C, but were significant (7.6 $mg/m^2 \cdot h$) at 500°C. However, we observed no changes in the tensile properties of the type 316 stainless steel exposed to Pb–17 at. % Li relative to specimens exposed to argon for the same exposure temperatures and times. (Metallographic examinations are not yet complete.) Longer term (5000 h at 300 and 400°C; 3000 and 5000 h at 500°C) experiments are currently in progress.

9.1.5 Conclusions

1. Although thermodynamic equilibrium in lithium requires significant carbon loss from 2 1/4 Cr-1 Mo steel compared to HT9, the kinetics of decarburization are relatively slow at the proposed service temperature (400–450°C) of this steel. Additionally, the decarburization rate can be minimized by using a stabilized 2 1/4 Cr-1 Mo steel.

2. Preliminary results from exposures of type 316 stainless steel to static Pb–17 at. % Li at 300, 400, and 500°C showed significant corrosion rates only at the highest temperature. No changes in the tensile properties of the type 316 stainless steel exposed to Pb–17 at. % Li relative to exposures in argon were observed at any of the temperatures, however.

9.1.6 References

1. P. F. Tortorelli, J. H. DeVan, and C. T. Liu, "Compatibility of Static Lithium with Fe–Ni–V and Fe-Cr-Mo Alloys," *ADIP Quart. Prog. Rep.* Sept. 30, 1980, DOE/ER-0045/4, pp. 182–90.

2. P. F. Tortorelli and J. H. DeVan, "Compatibility of Ferritic Steels with Static Lithium and Li—5 wt % Al," *ADIP Quart. Prog. Rep. Dec. 31, 1980,* DOE/ER-0045/5, ppo. 250—55.

3. R. L. Klueh, "Heat Treatment Effects on the Tensile Properties of Annealed 2.25 Cr-1 Mo Steel," *J. Nucl. Mater.* 68: 294—307 (1977).

4. K. Matsumoto et al., "Carbon Transfer Behavior of Materials for Liquid-Metal Fast Breeder Reactor Steam Generators," *Nucl. Technol.* 28: 452—70 (1976).

5. O. K. Chopra, K. Natesan, and T. F. Kassner, "Compatibility of Fe—9 Cr-1 Mo Ferritic Steels in a Sodium Environment," *Proc. 2d Int. Conf. Liquid Metal Technol. in Energy Conversion,* J. M. Dahlke, Ed., published by USDOE, Washington, D.C., CONF-800401-P1, pp. 17-26—17-34, 1980.

6. R. L. Klueh and J. M. Leitnaker, *An Analysis of the Decarburization and Aging Processes in 2 1/4 Cr—1 Mo Steel,* ORNL-TM-4799 (March 1975).

7. D. K. Sze, R. Clemmer, and E. T. Cheng, *LiPb, A Novel Material for Fusion Applications,* University of Wisconsin Report, UWFDM-378 (October 1980).

9.2 CORROSION OF AN IRON-BASE LONG-RANGE-ORDEKED ALLOY IN FLOWING LITHIUM — P. F. Tortorelli and J. H. DeVan (Oak Ridge National Laboratory)

9.2.1 ADIP Task

ADIP Task I.A.3, Perform Chemical and Metallurgical Compatibility Analyses.

9.2.2 Objective

The purpose of this task is to evaluate the corrosion resistance of candidate first-wall materials to flowing lithium in the presence of a temperature gradient. Corrosion rates (in both dissolution and deposition) are measured as functions of time, temperature, additions to the lithium, and flow conditions. These measurements are combined with chemical and metallographic examinations of specimen surfaces to establish the mechanisms and rate-controlling processes for dissolution and deposition reactions.

9.2.3 Summary

Data are reported on the corrosion of the long-range-ordered (LRO) alloy Fe—31.8 Ni–22.5 W . 4 Ti (wt %) exposed to lithium in type 316 stainless steel thermal-convection loops (TCLs) at 600 and 570°C for up to 1500 h. Corrosion rates that include a contribution from dissimilar-metal transfer of nickel from the alloy to the stainless steel are much greater than those of type 316 stainless steel previously exposed in these loops. A loosely adherent layer was observed on the LRO coupons in one of the two loops and may indicate additional complicating effects due to the dissimilar loop material.

9.2.4 Progress and Status

We previously found[1,2] that an LRO alloy composed of Fe—31.8 Ni—22.5 W—0.4 Ti (wt %) was unaffected by exposure to static lithium at elevated temperatures, while commercial Fe-Cr-Ni alloys with similar and higher nickel concentrations were readily attacked under the same exposure conditions. We therefore initiated experiments to assess the corrosion resistance of this LRO alloy to flowing lithium. Because of a lack of

sufficient LRO material, the tests are being conducted in type 316 stainless steel TCLs that are designed[3] so that lithium samples can be taken and corrosion coupons can be withdrawn and inserted without altering loop operating conditions. The use of a dissimilar loop material imposes a severe chemical gradient between the LRO specimens and the lithium, especially considering that surfaces of the loops' hot legs have been preferentially leached of nickel from prior exposures to lithium. Such an arrangement provides the worst case for the dissolution of the LRO alloy in flowing lithium. The LRO coupons were placed in the two hottest positions (600 and 570°C) of two type 316 stainless steel TCLs. In the preceding quarterly,[4] it was reported that the corrosion rates of the LRO alloy after 500 h of exposure to flowing lithium were much greater than those of type 316 stainless steel previously exposed in the two loops. We have continued to expose the LRO coupons and the updated results for the 600°C specimens are shown in Fig. 9.2.1. The weight losses for the LRO specimens in both TCLs (2B and 3B) are very much greater than comparable measurements of type 316 stainless steel. Also,

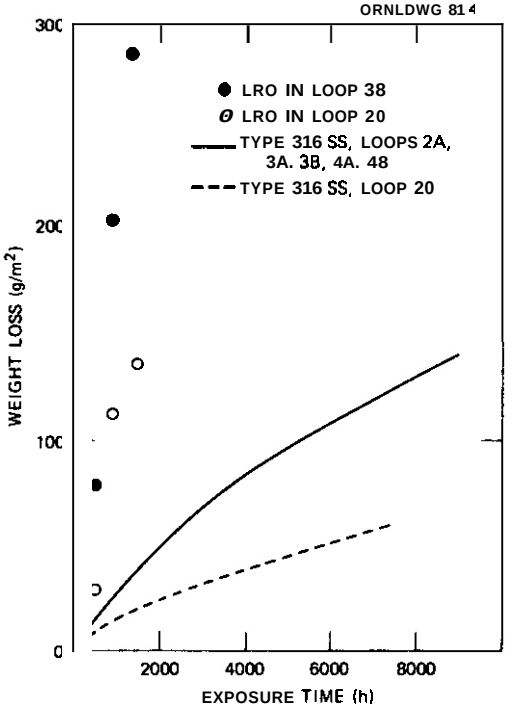

Fig. 9.2.1. Weight Loss Versus Exposure Time.

as was noted previously,[4] despite similar operating conditions, the weight losses are different between the two loops. The difference is consistent with the trend established earlier when coupons of type 316 stainless steel were exposed in these two loops:[4] lower weight losses in loop experiment 2B (with respect to five other similar experiments) resulted after replacement of the loop's cold-leg section, which had operated for 5000 h. (Data for the 5000 h period fell within the uncertainty of the average of the four other tests.) This pattern was not repeated in the second of these two loops, whose cold-leg section was also replaced (see Fig. 9.2.1). Although there is a difference between the corrosion rates in the two loops, the weight losses of the LRO coupons in type 316 stainless steel loops are definitely much greater than those of type 316 stainless steel.

After 1000 h of exposure, the coupon exposed at 570°C in loop 2B was found to have a loosely adhering layer (see Fig. 9.2.2). (Weight losses were measured after the layer had been removed.) A portion of the layer was analyzed by scanning electron microscopy (SEM) and energy dispersive x-ray analysis. The material was composed principally of iron with a significant amount of chromium (not originally present in the alloy) and small concentrations of nickel and vanadium. The reason for this layer is unclear. It did not appear on the specimens in loop 3B (which showed the greater weight losses) but did occur again in loop 2B after 1500 h. It, therefore, may be related to the more rapid mass transfer of iron in loop 3B compared to loop 2B and to the deposition of iron on the LRO surfaces. Another possibility is that this layer represents a near-surface zone that has spalled after being depleted of certain elements by exposure to the lithium. This would explain the very small amount of nickel in the layer but not the depletion in vanadium. In either case, the formation of the layer had to be accompanied by a transfer of chromium to the coupons, since the only source of chromium is the type 316 stainless steel loop itself. Although the layer is foil-like and homogeneous in appearance, it is quite porous when observed by SEM (see Fig. 9.2.3). Obviously, a metallographic examination of the LRO specimen surface is required to ascertain the origin of the layer, and this will be completed

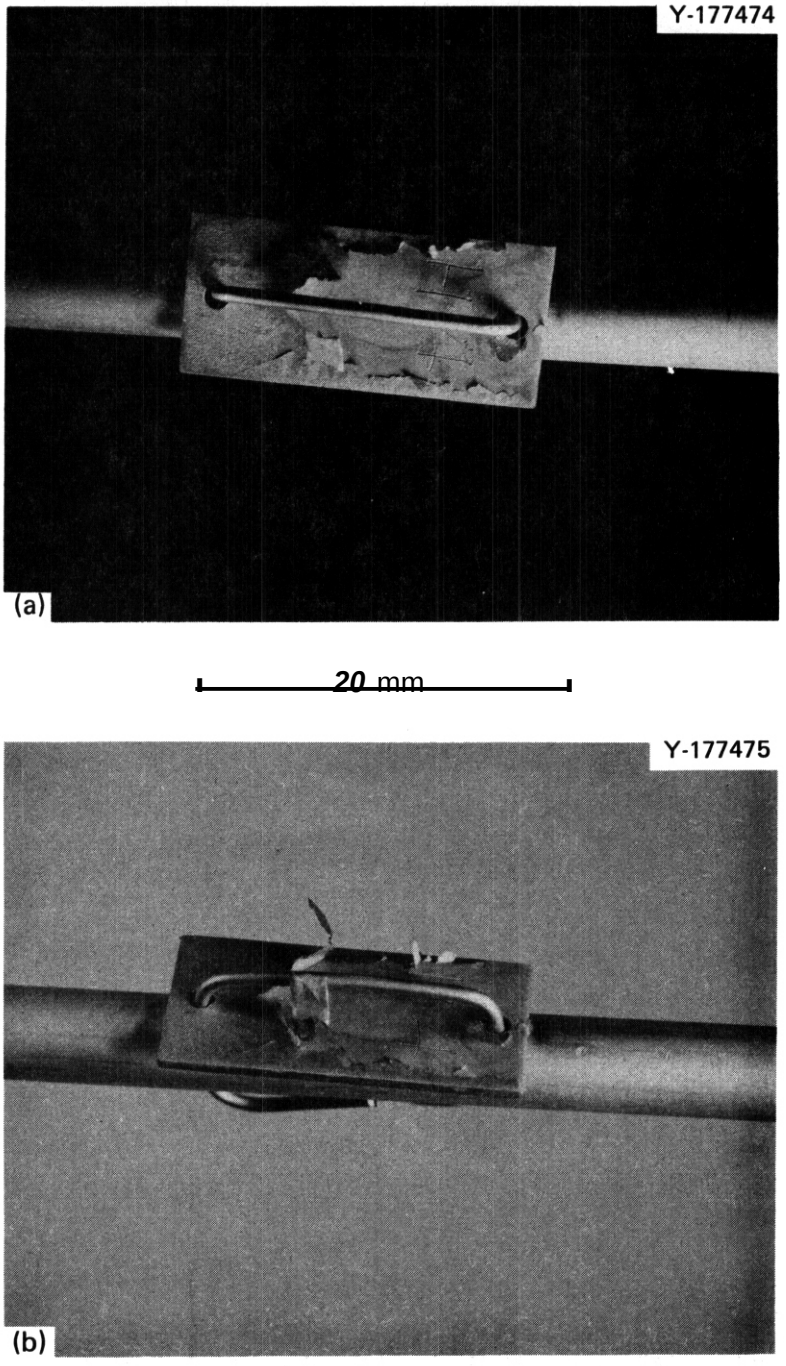

Fig. 922. Long-Range-Ordered **Alloy [Fe-31.8 Ni-22.5** *W . 4* **Ti** (wt %)] **After Exposure to Lithium in Loop 2B for 1000 h at** 570°C.

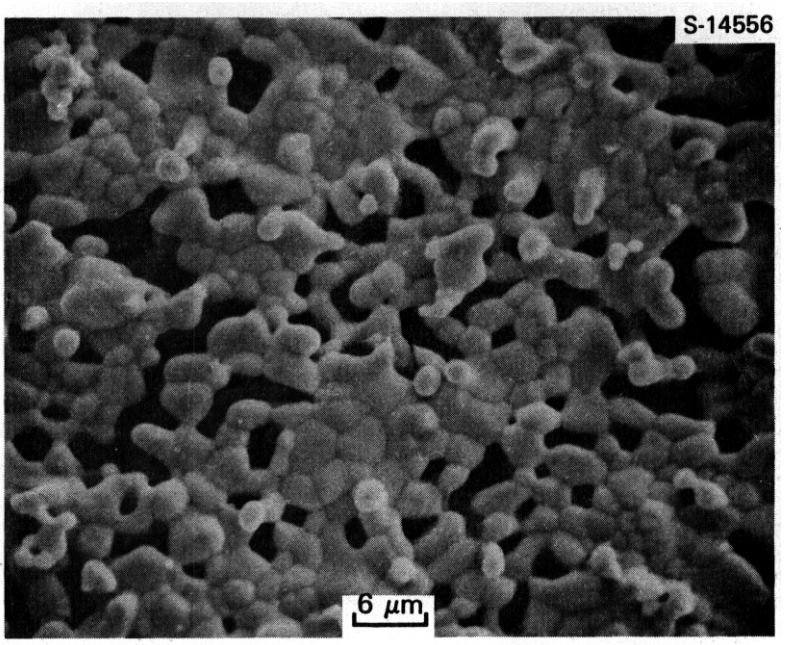

Fig. 9.2.3. Scanning Electron Micrograph of a Piece of the Loosely Attached Layer on the LRO Alloy Coupon Exposed to Lithium in Loop 2B for 1000 h at 570°C.

at the next determination of weight change. By establishing the origin of the layer, we can better understand to what extent the differences in composition between loop and specimens have accentuated the weight losss of the specimens.

9.2.5 Conclusions

1. The corrosion rates of a LRO alloy of Fe-31.8 Ni-22.5 V-0.4 Ti (wt %) in lithium-type 316 stainless steel TCLs are much greater than those of type 316 stainless steel previously exposed in these loops. However, there is some evidence that dissimilar-metal transfer may have an effect in the process in addition to acceleration of nickel transfer.

9.2.6 References

1. P. F. Tortorelli, J. H. DeVan, and C. T. Liu, "Compatibility of Static Lithium with a Long-Range-Ordered Fe-Ni-V Alloy and 2 1/4 Cr-1 Mo Steel," *ADIP Quart. Prog. Rep. June 30, 1980*, DOE/ER-0045/3, pp. 328-36.

2. P. F. Tortorelli and J. H. DeVan, "Corrosion of Fe–Ni–Cr and Fe–Ni–V Alloys in Static Lithium," *ADIP Quart. Prog. Rep. Dec. 31, 1979*, DOE/ER-0045/1, pp. 152–57.
3. J. H. DeVan and J. R. DiStefano, "Thermal–Convection Loop Tests of Type 316 Stainless Steel in Lithium," *Alloy Development for Irradiation Performance Quarterly Progress Report January–March, 1981*, DOE/ET-0058/1, pp. 200–08.
4. P. F. Tortorelli and J. H. DeVan, "Corrosion of Type 316 Stainless Steel and a Long–Range–Ordered Fe–Ni–V Alloy in Naturally Convective Lithium," *ADIP Quart. Prog. Rep. Dec. 31, 1980*, DOE/ER-0045/5, pp. 256–62.

DOE/ER-0045/6
Distribution
Category
uc-20, 20c

DISTRIBUTION

1-4. Argonne National Laboratory, 9700 South Cass Avenue, Argonne, IL 60439

L. Greenwood
V. Maroni
D. L. Smith
H. Wiedersich

5-6. Battelle-Pacific Northwest Laboratory, P.O. Box 999, Richland, WA 99352

J. L. Brimhall
D. Dingee

7. Brookhaven National Laboratory, Upton, NY 11973

C. L. Snead, Jr.

8. Carnegie-Mellon University, Schenley Park, Pittsburgh, PA 15213

J. C. Williams

9-204. Department of Energy, Technical Information Center, Office of Information Services, P.O. Box 62, Oak Ridge, TN 37830

For distribution as shown in TID-4500 Distribution Category, UC-20 (Magnetic Fusion Energy), and UC-20c (Reactor Materials)

205-210. Department of Energy, Office of Fusion Energy, Washington, DC 20545

M. M. Cohen
T. C. Reuther, Jr. (5 copies)

211. Department of Energy, Oak Ridge Operations Office, P.O. Box E, Oak Ridge, TN 37830

Office of Assistant Manager for Energy Research and Development

212. General Atomic Company, P.O. Box 81608, San Diego, CA 92138

D. I. Roberts

213–221. Hanford Engineering Development Laboratory, P.O. Box 1970, Richland, WA 99352

H. R. Brager
D. G. Doran
F. A. Garner
D. S. Gelles
G. L. Wire
R. E. Nygren
E. C. Opperman
R. W. Powell
J. L. Straalsund

222–224. Lawrence Livermore Laboratory, P.O. Box 808, Livermore, CA 94550

E.N.C. Dalder
M. Guinan
C. M. Logan

225–228. Massachusetts Institute of Technology, Cambridge, MA 02139

O. K. Harling
N. J. Grant
D. J. Rose
V. B. Vander Sande

229–230. McDonnell Douglas Astronautics Company, Fast, P.O. Box 516, St. Louis, MO 63166

J. W. Davis
D. L. Kummer

231–233. Naval Research Laboratory, Washington, DC 20375

Superintendent, Materials Science and Technology Division
J. A. Sprague
H. Watson

234-267. Oak Ridge National Laboratory, P.O. Box X, Oak Ridge, TN 37830

Central Research Library (2 copies)
Document Reference Section
Laboratory Records Department (2 copies)
Laboratory Records Department, RC
ORNL Patent Section
E. E. Bloom (10 copies)
D. N. Braski
J. H. DeVan
T. A. Gabriel

M. L. Grossbeck
M. R Hill (3 copies)
R. L. Klueh
K. C. Liu
P. J. Maziasz
C. J. McHargue
T. K. Roche
J, L. Scott
K. R Thoms
P. F. Tortorelli
J. M. Vitek
F. W. Wiffen

268. Rensselaer Polytechnic Institute, Materials Engineering Department, Roy, NY 12181

N. Stoloff

269–270. Sandia National Laboratories, Livermore Division 8316, Livermore, CA 94550

J. Swearengen
W. Baller

271. University of California, Department of Chemical, Nuclear, and Thermal Engineering, Los Angeles, CA 90024

R. W. Conn

272. University of California, Santa Barbara, CA 93106

G. R. Odette

273. University of Missouri, Department of Mechanical and Aerospace Engineering, Columbia, MO 65211

M. Jolles

274. University of Virginia, Department of Materials Science, Charlottesville, VA 22901

W. A Jesser

275. University of Wisconsin, 1500 Johnson Drive. Madison, WI 53706

W. G. Wolfer

276. Westinghouse Electric Company, Fusion Power Systems Department, P.O. Box 10864, Pittsburgh, PA 15236

R. E. Gold

☆U.S. GOVERNMENT PRINTING OFFICE: 1981-740-062/111